

**Study of detachment and the
processes involved in its dynamics
in MAST-U and Magnum-PSI via
radiation and emission analysis**

Fabio Federici, MSc.

Doctor of Philosophy

University of York

Physics

January 2023

Abstract

The process of divertor detachment in tokamaks is associated with the reduction of power and particles to the targets. This is deemed necessary to limit damage and erosion of solid surfaces and preserve the target.

The evolution of the radiation profile is studied in MAST-Upgrade, thanks to the novel Infra Red Video Bolometer (IRVB) diagnostic. The IRVB was optimised to observe the lower x-point and divertor and was successfully calibrated and verified post installation.

The movement of the radiation along the divertor legs and inner separatrix was compared with other metrics of detachment. In MAST-U L-mode plasmas, progress of radiative detachment happens in the same sequence as in large aspect ratio tokamaks. Inner leg detachment is gradual, appearing to be contrary to expectations from theory, which is beneficial to detachment control.

The IRVB, in combination with spectroscopic measurements, was used to infer that in MAST-U, during detachment of a super-x plasma, hydrogenic emission dominates radiation on the outer leg. This is in stark contrast with another carbon machine, TCV, where carbon dominates instead.

ELM-like pulses have been reproduced on the linear machine Magnum-PSI at DIFFER. The target chamber neutral pressure was increased to simulate detachment of the steady state plasma. In some cases the ELM-like pulse energy was completely dissipated in the volume. This can potentially translate to tokamaks, if the ionisation front has sufficiently receded from the target.

Despite significant radiative losses, most of the plasma energy losses are due to potential energy exchange. Both molecular assisted recombination and dissociation are important, with the latter being a more efficient path to dissociation than electron impact dissociation.

Studying detachment in both machines it is determined that, when the plasma temperature drops below $\sim 5\text{eV}$, it is necessary to include molecular assisted reactions to accurately model the plasma's power and particle balance.

Contents

Abstract	2
List of Tables	7
List of Figures	8
Acknowledgements	28
Declaration	31
Executive summary	32
1 Introduction	35
1.1 Fusion energy	35
1.2 Plasma confinement	36
1.3 H-mode	39
1.4 The exhaust problem	40
1.5 Divertor shaping	41
1.6 Radiative dissipation scenario	42
1.7 Detachment	43
1.8 The x-point radiator	45
1.9 Effect of X-point radiator	46
1.10 ELMs and XPR	50
1.11 Analytic models	51
1.11.1 Two Point Model	51
1.11.2 Thermal front Model	54
1.12 Goals and objectives of the thesis	56

<i>CONTENTS</i>	4
2 MAST-U IRVB hardware activities	60
2.1 Motivation	60
2.2 IRVB basics	61
2.3 MAST-U IRVB design	63
2.4 System calibration	74
2.4.1 Counts to temperature model	74
2.4.2 Temperature calibration	75
2.4.3 Foil model	80
2.4.4 Foil calibration	81
2.4.5 Etendue	86
2.4.6 Viewing geometry validation	86
2.5 MU01 Line integrated results	91
2.6 Summary	97
3 MAST-U IRVB scientific exploitation	99
3.1 Tomography	100
3.2 Inversion techniques	102
3.2.1 Truncated singular value decomposition (SVD)	102
3.2.2 Tikhonov regularization	103
3.2.3 Simultaneous algebraic reconstruction technique	104
3.2.4 Bayesian method	104
3.2.5 Regularisation optimisation	107
3.2.6 Comparison between SART and Bayesian method	110
3.2.7 Inversions in the SXD chamber	116
3.3 MU01 tomographically inverted results	120
3.3.1 Metrics from diagnostics	120
3.3.2 L-mode and detachment characteristics	125
3.3.3 H-mode and detachment characteristics	132
3.3.4 IRVB and MWI correlation in SXD discharges	139
3.4 Summary	145
4 Magnum PSI activities	147
4.1 Motivation	147

4.2	Experimental setup	149
4.2.1	Experimental conditions	150
4.2.2	Diagnostics	151
4.3	Fast camera	155
4.3.1	Steady state	155
4.3.2	Effect of ELM-like pulses	156
4.4	Thomson scattering	161
4.5	IR camera	163
4.6	Role of molecular assisted reactions	168
4.6.1	Analysis steps	171
4.6.2	Analysis limitations due to restrictions on measured Balmer lines . . .	179
4.6.3	Bayesian analysis results	180
4.7	Summary	190
5	Overall summary	193
5.1	MAST-U	193
5.2	Magnum-PSI	197
6	Conclusions	199
6.1	MAST-U	199
6.2	Magnum-PSI	200
6.3	Outlook	202
A	Details on the Magnum-PSI study	204
A.1	Sampling strategy	204
A.2	OES data interpretation	206
A.3	Target temperature profile interpretation	208
A.4	Details on the Bayesian calculations	214
A.4.1	Priors from B2.5 Eunomia	214
A.4.2	Priors from AMJUEL	218
A.4.3	Priors range optimization	219
A.4.4	Emissivity	219
A.4.5	Balance over the plasma column	222

<i>CONTENTS</i>	6
A.4.6 Power balance	224
A.4.7 Particle balance	228
A.4.8 Plasma column power balance	230
A.4.9 Reactions	231
List of References	231

List of Tables

4.1	Table of the experimental conditions of Magnum-PSI for the experiments presented in this work. Common parameters are: steady state source current 140A to generate the background plasma, 31.2mm target to OES/TS distance, TZM (a molybdenum alloy) target. ID 1-4 are referred to as weak pulse conditions while ID 5-10 are referred to as strong pulses. The stages are 1-3 and correspond to: fully attached (1), partially detached (2) and fully detached (3) as it will be defined in Section 4.3.	151
A.1	Reactions whose rates and reference coefficients were sourced from the ADAS database. [1,2]	231
A.2	Reactions whose rates and reference coefficients were sourced using the Yacora collisional radiative code. [3,4]	232
A.3	Reactions whose rates and reference coefficients were sourced from the AMJUEL database. [5-7]	232
A.4	Reactions whose rates and reference coefficients were sourced from the Janev database. [8]	232

List of Figures

1.1	Average binding energy per nucleon [9]	36
1.2	Schematic of the main components of a tokamak [10]	38
1.3	The poloidal cross section of a limited (left) and diverted (right) plasma. [9] .	38
1.4	Example of different divertor configurations. Left: Standard Vertical Plate Divertor (SVPD), Super-X Divertor (SXD) and X-point Divertor (XPTD). Right: Long Vertical Leg Divertor (LVLD) [11]	41
1.5	Loss function data from the Atomic Data and Analysis Structure (ADAS) data base (solid lines) for the different elements [12]	42
1.6	Different radiation profiles with the clear presence of an X-point radiator for different impurities [13]	49
1.7	Schematic of how the poloidal SOL geometry can be straightened into a 1D one. 'u' indicates the location of the upstream location where core plasma enters the SOL. Adapted from [14] and the JET image database.	51
2.1	Schematic representation of the main components of a IRVB diagnostic . . .	61
2.2	Top view of the lower half of MAST-U, showing the positioning of the IRVB inside the vacuum vessel respect to other features. The numbers identify the sectors, assigned clockwise in the toroidal direction.	63
2.3	IRVB components overview: exploded view showing all internal components before welding and assembly.	65

2.4 IRVB components overview: (a) photograph of the exterior of the foil assembly inside the tube, (b) the view port side of the tube installed in MAST-U and (c) the camera installed on the flange respectively. Photographs taken 2018/07/23, 2018/12/03, 2021/05/14 respectively. To change pinhole size and foil pinhole distance the tube must be removed while the camera is always accessible. 66

2.5 Radiated power deposited on foil, modelled with CHERAB, from a homogeneous toroidal emitter of radius 8cm located at R=0.55m and Z=-1.2m, emitting a total of 0.5MW (equivalent to $\sim 7.2kW/m^3$) for the combinations of pinhole diameter and stand-off length considered. The power deposited on the foil below $100W/m^2$ is not shown, as that is the minimum desired signal level. In black are overlaid the projection of relevant features of MAST-U structure on the foil for reference. 68

2.6 Radiated power deposited on foil, modelled with CHERAB, of two tori of 4 cm minor radius separated by 16cm in vertical position with uniform emissivity such as to total 0.5MW of radiated power, located at the expected x-point location. The pinhole size was varied from 4mm (a) to 6mm (b) to illustrate the loss of spatial resolution. The power deposited on the foil below $100W/m^2$ is not shown, as that is the minimum desired signal level. Only the relevant section of the foil is shown. In black are overlaid the projection of relevant features of MAST-U structure on the foil for reference. 69

2.7 Radiated power deposited on foil, modelled with CHERAB, with a 4mm diameter pinhole and (a) 45mm and (b) stand-off between pinhole and foil, for the case of the core and divertor regions emitting homogeneously at a level of $50kW/m^3$. The white regions do not receive any radiation from the plasma, in black are overlaid the projection of relevant features of MAST-U structure on the foil for reference. 70

2.8 Approximate view inside MAST-U as if the IRVB operates as a camera. Blue labelling is used to highlight the various sectors and the fuelling locations in the IRVB field of view (FOV). At the bottom of the image is the coil P6 obstructing the field of view. 71

2.9 (a) Poloidal view of MAST-U showing the comparison of the resistive bolometer system LOS (magenta) with a colour plot obtained by scanning all the voxels with a $1W/m^3$ emitter and integrating the power absorbed by the foil, indicating the regions of higher sensitivity of the IRVB. (b) Top view of MAST-U showing the position of neutral beam injectors (NBI, green), of the co- and counter-NBI resistive bolometer LOSs and the IRVB FOV (yellow, mostly counter-NBI). Adapted from [15]. For reference the separatrix of a typical plasma is shown as an overlay of a blue dashed line. The resistive bolometer LOSs that will be used in the later analysis are here identified. The LOSs not operational in MU01 are red rather than magenta. The location of CH9 in b indicates where the entire core poloidal fan is located. 72

2.10 Photographs of the foil in relation of the pinhole (a) and of all the identifying markings (b), taken 23/07/2018. 73

2.11 Schematic of the calibration setup. The NUC plate and the IR window are located at the same distance from the camera as when installed and as per design. Effort is made to keep the window with the same rotational orientation. See the marking for the view port alignment in the detail. 76

2.12 Example of non uniformity of the counts of the IR camera when aimed at the NUC plate at room temperature. Shown are the images without the view port (a) and with (b). The same scale is applied to both plots and there was a 2ms integration time. The black cross indicates two reference points (inside/outside the narcissus) that will be used in later analysis. c shows the position of the foil (the red square) inside the camera field of view. Around the foil are the bolts that lock the foil in between the two copper plates, that can be used to identify the foil orientation. 77

2.13 (a) Shown are the IR camera counts at 41.9°C minus the counts at room temperature, scaled up such that the average across the foil is the same as at high temperature. In black is highlighted the region corresponding approximately to the IRVB foil and the two reference points defined in Figure 2.12. The vertical orientation is here bottom to top, with the top of the image being up. (b) Peak temperature difference between the temperature deriving from the counts at high temperature and the counts at room temperature scaled up as previously mentioned. 78

2.14 Comparison of the temperature calibration curves for a pixel at the centre of the narcissus (red) with one on its side (blue). The legend gives the fit parameters (a_1 proportional and a_2 additive components), their uncertainties, and the coefficient of determination of the fit. 79

2.15 a_1 and a_2 coefficients of Equation 2.3 obtained via calibration with the NUC plate. In black is highlighted the region corresponding approximately to the IRVB foil and the two reference points defined in Figure 2.12. The vertical orientation during this calibration is right to left, with the top on the left. 80

2.16 Photograph (a) and CAD model (b) of the bench-top setup used for the foil calibration. In the CAD model the re-entrant tube is shown in white and the foil assembly is on the left side. The photograph, taken on 02/08/2018, shows the laser used to illuminate the foil, as well as the diode and aperture used to calibrate the laser and vacuum system. 83

2.17 Examples of the power absorbed by the foil and its components (total absorbed power P and its components black body radiation P_{BB} , conduction $P_{\Delta T}$ and temperature variation $P_{\frac{\partial T}{\partial t}}$; peaks and troughs of P running average, P_h and P_l ; peak input power P_{in}) with the laser at maximum intensity for a focused low frequency case (a), a focused high frequency case (b) and a defocused low frequency one (c). 84

2.18 Variation of the measured power compared to the expected values with laser intensity (top) and frequency (bottom). The blue colour indicates the defocused cases while the red the focused ones. P_h and P_l are the inferred high and low power level of the laser square wave, $area$ is the area of the foil receiving laser light, P_{in} is the known peak laser power density. 85

2.19 Field of view of the high speed visible light camera indicating the sector numbers. In yellow the locations of the outlets of the gas valve HFS_MID_L08 are indicated. In red is shown the location of the outlets of the gas valve HFS_MID_U02, dashed because they are on the other side of the central column, hidden from view. 88

2.20 Example of the radiation caused by the valve HFS_MID_L08 from shot 45295. (a) brightness data from IRVB at 132ms. Shown in dashed blue is the poloidal projection of the separatrix. The toroidal traces of x-point and strike points are shown in solid red, and in dashed red is the magnetic axis. The outlet of the valve HFS_MID_L08 in the IRVB FOV, marked by a black cross and a yellow arrow, is clearly visible in the IRVB image. In (b) a cropped image of the raw data from the high speed visible light camera (HSV) for the same shot at 50ms. The two bright spots correspond to the two outlets from the valve, both in the HSV FOV, marked as in (a). Note: this data is affected by saturation. In (c), the relative average of the readings inside the dashed regions that are outlined in a and b, and the programmed flow for the HFS_MID_L08 valve. 89

2.21 IRVB Brightness image of the plasma from shot 45295, 388ms, at a time when high field side valves are off and the target is radiatively detached. In blue a tangential projection the separatrix from EFIT++ magnetic reconstruction overlaid on the image using nominal IRVB design geometry. The toroidal traces of x-point and strike points are shown in solid red, and in dashed red, is the magnetic axis. 90

2.22 Image of foil temperature increase due to the disruption of the plasma in shot 45225. No temporal or spatial binning of the data applied. Indicated in white is the demarcation line between the region of the foil that receives any radiation or none from an homogeneous emitter in the core and divertor region from Figure 2.7a. 91

2.23 Changes in brightness pattern in a density ramp for a conventional divertor, L-mode, Ohmic plasma (shot 45473, Double-null and 650KA). All MU01 shots have ion ∇B drift downward. First the inner target is radiatively attached (a), then it starts detaching (b) to form an x-point radiator (c) and finally a radiation MARFE-like structure on the high field side (HFS) midplane (d). Further increasing the density the structure moves inward (e) leading to a disruption. Note that the all images have different colour bar ranges. The average brightness in the regions marked by the dashed lines (green: outer target, violet: inner target, brown: x-point, pink: midplane, grey: control) will be used for later analysis. 93

2.24 Comparison of the measurements from different diagnostics for the shot 45473. In (a) is the IRVB brightness averaged inside the regions indicated with dashed lines of matching colours around the x-point and other regions in Figure 2.23 while the vertical black lines indicate the time corresponding to the images in Figure 2.23. In (b) is the core line averaged density, (c) is the Greenwald density ratio and (d) is the brightness from the resistive bolometer core toroidal channel 9. 94

2.25 Changes in brightness pattern in a density ramp for a conventional divertor, H-mode, beam heated plasma (shot 45401, Double-null and 750kA). All MU01 shots have ion ∇B drift downward. First, the inner target is radiatively attached (a). Then, it detaches and forms an x-point radiator (b) and finally a radiation MARFE-like structure on the HFS midplane (c). In this shot the density was decreased after this point and this resulted in the peak radiation to move back towards the x-point (d). The bright region at the top left of (a) is likely due to the foil being heated by a particle flux rather than radiation from the plasma. In (d) are overlaid in dashed red and numbered, the resistive bolometer LOS through similar regions as included in the IRVB brightness image shown. Note that all images have different colour bar ranges. The average brightness in the regions marked by the dashed lines (green: outer target, violet: inner target, brown: x-point, pink: midplane, grey: control) will be used for later analysis. 96

2.26	Comparison of the measurements from different diagnostics for the shot 45401. In (a) is the IRVB brightness averaged inside the regions indicated with dashed lines in Figure 2.25 while the black lines indicate the time corresponding to the images in Figure 2.25. In (b) is the core line averaged density, (c) is the Greenwald density ratio and (d) is the brightness from the resistive bolometer core toroidal channel 9, 13 and 14, where the first corresponds to the midplane while the others to the intermediate regions of the IRVB.	97
3.1	Path for forward modeling, left to right, and for experimental data analysis, right to left.	100
3.2	Example of power density distribution on the foil from the shot 45401, showing the region of the foil used for Ohmic discharges (green) and that which is excluded when the NBI is used (red)	102
3.3	Typical amplitude of the eigenvalues in an undetermined inversion problem. .	108
3.4	(a), (b): types of Laplacian operators commonly used for tomographic inversions. [16] (c): Laplacian operator corresponding to the real 2D second degree derivative used to analyse IRVB data.	109
3.5	Typical L-curve shape. On the horizontal axis is the residual norm, on the vertical the penalty norm. Adapted from [17].	109
3.6	Emissivity distribution for the MDS+ SOLPS simulation 69590 corresponding to a MAST-U conventional plasma with the NBIs injecting a total of 10MW (configuration investigated for a future upgrade) characterised by a large radiated power. The approximate location of the separatrix is shown by the dashed blue line.	110
3.7	Power density (a) and power density uncertainty (b) generated by the emissivity pattern as per Figure 3.6. Of these only the area defined by the green line in Figure 3.2 is used.	111
3.8	Power absorbed by the foil excluded by Bayesian method because it is attributed to the region close to the pinhole (outside the black solid line and close to the green cross in Figure 3.6) or due to offsets (see Equation 3.9). This plot is restricted to the section of the foil used as per Figure 3.2.	112

3.9	Tomographic reconstructions from the SOLPS phantom (Figure 3.7) using SART (left: a, c, e) and the Bayesian method (right: b, d, f). L-curve (a, b) and respective curvature (c, d). The blue point in the L-curve and curvature represent the selected optimal regularisation. The green and red points represent respectively a low and high regularisation coefficient. In (d) the dashed lines indicate the maximum and minimum acceptable regularisation coefficient for the peak of the L-curve curvature. Note that the α regularisation coefficients are not equivalent between SART and the Bayesian method. (e, f) tomographically inverted emissivity. The approximate location of the separatrix is in dashed blue. The same colour scale as Figure 3.6 is used. . . .	113
3.10	Power density (a) and power density uncertainty (b) from the conventional Ohmic shot 45473 at 511ms.	114
3.11	Tomographically inverted emissivity using SART (a) and the Bayesian method (b) for data from shot 45473 at 511ms.	115
3.12	Tomographically inverted emissivity using SART (a) and the Bayesian method (b) for data from shot 45473 at 511ms. The same colour scale as Figure 3.11b is used.	116
3.13	Emissivity profiles for 3 toroidal phantoms occupying 9 voxels (indicated by the solid black square) with fixed emissivity of $1.26 MW/m^3$. The radiation from the phantoms is forward modelled to the foil power density, foil temperature and camera counts and then inverted to emissivity with a fixed regularisation coefficient $\alpha = 5 \cdot 10^{-3}$. Inside of the SXD chamber the radiation is elongated along the IRVB LOS. The dashed black line indicates the centre of different phantoms located as to follow the typical shape of the separatrix in a super-x plasma. The green indicates the different shape for a conventional plasma separatrix (the shape at smaller radii is shared with the super-x case so not repeated). In magenta is a scan of location close to the target (surface, surf) to evaluate the precision at the strike point.	117
3.14	Impact of the location of the toroidal phantom centre on the capability to reconstruct its location (distance of peak emissivity and phantom locations). The location of the phantom is moved along 3 paths identified in Figure 3.13.	117

3.15 Movement of the peak radiation (marked by the 'x') compared to the phantom centre (marked by the circle), indicated by the arrows. In the region right of the blue dashed line the position of the emissivity is considered unreliable. 118

3.16 Impact of the location of the toroidal phantom centre on the capability to reconstruct its location (error in total radiated power relative to the input). The location of the phantom is moved along 3 paths identified in Figure 3.13. 119

3.17 How the metric for the movement of the peak radiation along the separatrix is defined. $(L_{peak} - L_{target})_{sep}$ is the distance between the position on the separatrix closest to the peak of the radiation and the target, calculated along the separatrix. $(L_{x-point} - L_{target})_{sep}$ is the same calculated for the x-point. The region where the peak is selected is within 10cm of the inner separatrix. For the radiation at the x-point not to affect the location of the peak radiation, the observed region is first limited to 10cm away from the x-point. When the peak reaches the region of the x-point then the region is extended to the entire separatrix. The same is done on the outer separatrix. 120

3.18 Location of the working (green) and broken (red) Langmuir probes for MU01. The probes are in two toroidal locations (sector 4 and 10) but are shown overlapped. 122

3.19 Regions in which the plasma volume is divided similar to [14]: red = x-point (radius of 10cm around x-point), green = core, yellow = inner SOL, light blue = inner leg and SOL below the x-point, blue = outer leg and SOL below the x-point, magenta = outer SOL. The distinction between inner and outer leg region is made via the extension of the line between magnetic axis and x-point. The radiation within 10cm of the legs and out of the x-point region is also separately accounted for. The green dashed line indicates the left limit of the SXD chamber region limit; that is also the limit below which the radiation distribution is considered unreliable. The red dashed line indicates the upper limit of the MWI diagnostic FOV. 124

3.20 Changes in emissivity distribution in a density ramp for a conventional divertor, L-mode, Ohmic plasma (shot 45473, Double-null and 650KA), same as Figure 2.23. First both inner and outer target are radiatively attached (a), then the inner detaches (b) to form an x-point radiator while the outer detaches too (c) and finally a radiation MARFE-like structure on the high field side (HFS) midplane (d). Further increasing the density the structure moves inward (e) leading to a disruption (the radiation peak is here too close to the midplane and out of view). Note that the all images have different colour bar ranges. The limit below which the radiation distribution is considered unreliable is marked in dashed green. 126

3.21 Results from different diagnostics related to detachment for a conventional divertor, L-mode, Ohmic plasma (shot 45473, Double-null and 650KA). (a): movement of the peak radiator along the separatrix as per the scaling defined in Section 3.3.1 for the inner and outer separatrix. The vertical dashed lines indicate the time that corresponds to the data in Figure 3.20. (b): Components of the global power balance: input power defined as the sum of Ohmic and NBI minus the variation in stored energy. The IRVB power is obtained by adding all voxels at $Z < 0$ then multiplying by 2, therefore assuming up/down symmetry. The divertor region is obtained adding the inner leg + SOL and outer log + SOL region (see Figure 3.19). (c): particle flux from Langmuir probes at the outer targets. The oscillation on the lower target is due to a strike point sweep close to a dead probe. (d): brightness for the tangential LOSs CH25, CH26 and CH27 (CH25 and CH26 scaled up to match CH27 integration path length) and (red) the ratio of the two, showing the growth of the MARFE. The vertical red line corresponds to when the CH27/CH26 ratio starts to grow. (e): averaged core density (\bar{n}_e) and upstream density from TS as per Section 3.3.1 (n_u). 128

3.22 Variation of the C_1 parameter as per Equation 1.24 in the shot 45473 for a front position from target ($\hat{L}_f=0$) to x-point ($\hat{L}_f=1$). Solid lines for the inner leg, dashed for the outer. 129

3.23 Data from the high speed visible camera for shot 45473 showing the minor up/down symmetry in a shot fuelled only by the midplane HFS_MID_U02 valve at the beginning of the formation of the MARFE-like structure (a). At the end of its growth (b) the up/down asymmetry is more significant and centred close to the fuelling location (see Figure 2.19). 130

3.24 Comparison of the target current, providing the detachment condition from particle flux roll over, with the movement of the emission radiator, indicating radiative detachment. The vertical coloured dashed line indicates the beginning of the growth of the MARFE-like structure on the HFS midplane. . . . 132

3.25 Changes in emissivity distribution in a density ramp for a conventional diverter, H-mode, NBI heated plasma (shot 45401, Double-null and 750kA), same as Figure 2.25. First both inner and outer target are radiatively attached (a), then the outer starts detaching (b) and closely after the inner to form an x-point radiator (c). Then a radiation MARFE-like structure forms on the high field side (HFS) just below the midplane (d) and moves slightly back towards the x-point for decreasing core density (e). A disruption then follows. Note that the all images have different colour bar ranges. The colour range in (b) was adapted to show the early detachment of the outer leg. The limit below which the radiation distribution is considered unreliable is marked in dashed green. 134

3.26	Results from different diagnostics related to detachment for a conventional divertor, H-mode, NBI heated plasma (shot 45401, Double-null and 750kA). (a): movement of the peak radiator along the separatrix as per scaling defined in Section 3.3.1 for the inner and outer separatrix. The vertical dashed lines indicate the time that corresponds to the data in Figure 3.25. (b): Components of the global power balance: input power defined as the sum of Ohmic and NBI minus the variation in stored energy. The NBI power is already scaled by the corrective factors 0.4 and 0.8 for SW and SS respectively. The IRVB power is obtained by adding all voxels at $Z < 0$ then multiplying by 2, therefore assuming up/down symmetry. The divertor region is obtained by adding the inner leg + SOL and outer log + SOL region (see Figure 3.19). (c): particle flux from Langmuir probes at the outer targets. (d): brightness for the tangential LOSs CH25, CH26 and CH27 (CH25 and CH26 scaled up to match CH27 integration path length), (red) the ratio of the two, showing the growth of the MARFE, and poloidal LOSs CH4 and CH13. The vertical red line corresponds to when the CH27/CH26 ratio starts to grow. (e): averaged core density ($\overline{n_e}$) and upstream density from TS as per Section 3.3.1 (n_u).	135
3.27	Data from the high speed visible camera for shot 45401 showing the level of up/down symmetry when only the midplane HFS_MID_U02 valve is used (a), the valve LFSD_BOT_L0102 is initially used (b) and when the core density decreases (c).	136
3.28	Hydrogen D_α emission from the midplane, used to assess the type of ELM regime of the H-mode. Each zoomed section can be identified by the colour.	137
3.29	Electron temperature and density profiles from core TS before, during and after the small ELM highlighted in Figure 3.28, showing the small decrease of n_e at the outer midplane separatrix. ρ is obtained from EFIT magnetic reconstructions.	138

3.30 Changes of emissivity distribution in a density ramp for a super-x divertor, L-mode, Ohmic plasma (shot 45371, Double-null and 650KA). After the outer leg is moved into the super-x configuration the inner one is already radiatively detached and significant radiation is present in the SXD chamber (a). Then fuelling is increased and radiation inside the super-x decreases (b) up to becoming negligible and the radiation climbs the inner separatrix (c). Then fuelling is cut and the radiation starts to come back towards the strike point (d). Note that the all images have different colour bar ranges. The limit below which the radiation distribution is considered unreliable is marked in dashed green. 140

3.31 Results from different diagnostics related to detachment for a super-x divertor, L-mode, Ohmic plasma (shot 45371, Double-null and 650KA). (a): Components of the global power balance: input power defined as the sum of Ohmic and NBI minus the variation in stored energy. The IRVB power is obtained by adding all voxels at $Z < 0$ then multiplying by 2, therefore assuming up/down symmetry. The regions indicated are defined as per Figure 3.19. The vertical dashed lines indicate the time that corresponds to the data in Figure 3.30. (b): averaged core density (\bar{n}_e) and upstream density from TS as per Section 3.3.1 (n_u). (c): gas flow programmed for the valves used to fuel the plasma. There is no measurement of the effective gas flow produced by a valve setting. . . . 141

3.32 Number of photons per MWI target emission line radiated in the SXD chamber relative to the maximum level from MWI, compared to the power radiated in the same region from IRVB. The number of photons is smoothed with a running average of the same length of the temporal resolution of the IRVB data ($\sim 37ms$). The arrow in the legend indicates to which y axis each line refers to. The number of photon axis is scaled so that 1 corresponds to the peak level of the SXD chamber power. 143

4.1 Schematic of Magnum-PSI linear plasma machine. $z = 0$ corresponds to the surface of the target, Thomson scattering and Optical Emission Spectroscopy (OES) are located at $z = -31.2\text{mm}$. The TS view is composed of 50 evenly spaced LOS orthogonal to the plasma column length (z). The OES view is composed of 40 LOS perpendicular to the column length. The fast camera, for measuring integrated light emission from the plasma, has a radial view of the plasma through a lateral viewport of the vacuum vessel of diameter $\sim 75\text{mm}$. The IR camera has a radial view that is converted to looking at the target surface by a mirror outside the target chamber. The mirror angle can be adapted to maintain the view of the target when moved in z 150

4.2 Visible fast camera brightness images corresponding to a steady state plasma in conditions similar to this work from an experiment by Akkermans [18] (1.2T, 120A, $\text{H}\alpha$ filter present), (a) is affected by overexposure in the black region near the target. The target chamber neutral pressure is increased to induce detachment and corresponds to 0.29Pa (a), 2.01Pa (b) and 17.3Pa (c). The shaded region indicates the position of the target. The OES and TS measurement locations in z are indicated by the 2 vertical lines. The fast camera view is through a lateral viewport, giving a useful FOV of $\sim 75\text{mm}$ diameter. 155

4.3 Radial average of the visible fast camera brightness for the steady state cases in Figure 4.2. The longitudinal position axis is cut after the target. The brightness decreases towards the source as the plasma exits the field of view of the camera. 157

4.4 Fast visible camera images of the ELM-like obtained by averaging temporally over the pulse duration. The images show a plasma which is increasingly detached and corresponds to ID 5 (a), 10 (b), 4 (c) in Table 4.1 ((a) and (b) are effected by overexposure in the black region near the target). The fast camera view is through a lateral viewport, giving a useful FOV of $\sim 75\text{mm}$ diameter. 157

4.5 Radial and temporal average of the visible fast camera brightness for the neutral pressure scan with strong ELM-like pulses, where we observe the transition from Stage 1 to 2. (ID 5-10 in Table 4.1). 159

4.6	Radial and temporal average of the visible fast camera brightness for the neutral pressure scan with weak ELM-like pulses, where we observe the transition from Stage 1 to 3 (ID 1-4 in Table 4.1).	159
4.7	Typical source power (top), Thomson scattering T_e (mid) and n_e (bottom) measurement for strong pulses in Stage 1 (a), Stage 2 (b) and weak pulses in Stage 3 (c) (ID 5, 10, 4 in Table 4.1 respectively). TS data is smoothed over time and radius in order to match the same steps of OES.	161
4.8	Comparison of plasma peak T_e , n_e and p_e smoothed over $700\mu s$ for a neutral pressure scan with strong pulses (dashed lines, $B=1.3T$, pulse energy= $48J$), corresponding to Figure 4.5 and weak (solid lines, $B=0.6T$, pulse energy= $10.3J$), corresponding to Figure 4.6 (ID 5-10 and 1-4 respectively in Table 4.1)	162
4.9	Comparison of the measured and fitted time dependence of the peak target temperature: (a) Stage 1 case, (b) Stage 2 case (ID 5 and 10 in Table 4.1 respectively). The black curve is the target peak temperature. The green dashed line (colour online only) is the temperature fit using the entire temperature curve. The red dashed line corresponds to fitting the temperature only for the time $1.5ms$ after the temperature peak. The curve is then plotted over the entire time domain using the fit parameters. In both cases the analytical model used is Model3 (Equation A.4 in Section A.3). The fit parameters are shown in the figure legend.	163
4.10	Results of analysis of the IR data for the variations in target chamber neutral pressure. In this figure we focus on the case of strong pulses ($48J$ at the source) and higher magnetic field that yields higher plasma pressure background plasma (ID 5 to 10 in Table 4.1). Analysed data displayed are: target temperature before the ELM (blue), temperature increase during the ELM (red), ELM energy reaching the target (solid green) estimated with Model3 fitted after $1.5ms$ of the temperature peak and the steady state heat flux (dashed green).	166
4.11	Results of analysis of the IR data for the variations in target chamber neutral pressure. In this figure we focus on the case of weak pulses ($10.3J$ at the source) and lower magnetic field that yields lower plasma pressure background plasma (ID 1 to 4 in Table 4.1). Line colours and styles are the same as Figure 4.10.	166

- 4.12 Sketch illustrating how the initial guess of each parameter Θ_i is done. With *link* are marked items that link different parts of the global bayesian routine together. *measurement* indicate quantities measured experimentally and *external input* represents inputs from simulations or reaction rates libraries. 171
- 4.13 Sketch illustrating how the prior probability distribution is determined given the parameter grid. *Bayesian output* indicates groups of quantities that are collected for all the parameter space and with the likelihood will return their PDF. 172
- 4.14 Sketch illustrating how the likelihood distribution is determined comparing the line emission with the expected values and adding the prior log-probability, to refine the parameter grid and calculate the outputs PFD. 176
- 4.15 Density ratio of hydrogen excited states to p=4 for different processes for typical $T_e = 1eV, n_e = 4 \cdot 10^{21} \# / m^2$ plasma. The similarity of the profile shape for H_2^+ dissociation and H^+ mutual neutralisation is maintained for all the T_e, n_e range of interest. 179
- 4.16 Most likely values of the radiated power via EIE (a), recombination (b) and molecular processes (c) for the same conditions of Figure 4.7b, ID 10 in Table 4.1. The noise shown in these figures arises from the fact that the analysis is independent for each radial and temporal location (no regularisation applied). 181
- 4.17 Example of the radial sum of the power radiated via excitation for ID 5 in Table 4.1 at 0.4ms. Only the radial locations that are more relevant are here shown. The power density (W/m^3) at each location is multiplied by the volume it pertains to determine the x coordinate. 181

4.18	Stacked area plot of the most likely values for the terms of the power balance as per Section A.4.6 for the lowest (a) and highest (b) pressure conditions for strong pulses. The data below zero corresponds to energy that released by recombination reactions heating the plasma. The potential energy from interactions with molecules is split in its positive and negative components. As <i>molecules</i> is here intended any reaction with exchange of potential energy different to EIR and ionisation (see Section A.4.9). <i>volume sinks-sources</i> corresponds to the net local power balance while <i>removed from plasma</i> indicates the contribution to the plasma column power balance as per Section A.4.8. The colours in the legend of (b) apply to both plots.	182
4.19	Energy dissipated radiatively per mechanism for increasing neutral pressure (ID 5 to 10 in Table 4.1) obtained with the Bayesian analysis.	183
4.20	Results from the Bayesian analysis for strong ELM-like pulses with increasing neutral pressure (ID 5 to 10 in Table 4.1). Total energy input (blue), energy removed from the plasma column (approximated with the hydrogenic radiative losses, red), energy absorbed by the target from IR camera analysis in Section 4.5 (orange), estimated maximum energy removed from CX (grey) and H_2 elastic (black) collisions. CX and H_2 elastic have already been multiplied by the corrective factors found in Section 4.6.1.3 by comparison with B2.5-Eunomia.	185
4.21	Plasma particle balance on the plasma column from the Bayesian analysis for strong ELM-like pulses with increasing neutral pressure (ID 5 to 10 in Table 4.1). Total particle input from the plasma source estimated from Section A.4.5 and A.4.7 ($(nv)_{H^+,in}$). Number of plasma particles created during the duration of the ELM-like pulse by type of reaction. MAR and MAI are defined as ensemble of multiple reactions that, starting from neutrals, first create a molecular precursor (H_2^+ , H^-) then further react with the end result of the two consecutive reactions being plasma recombination or ionisation respectively. [19] We note that there can be a discrepancy between $netH^+$ and $nete^-$, which appears to be an analysis artefact.	186

4.22 Atomic hydrogen particle balance on the plasma column from the Bayesian analysis for strong ELM-like pulses with increasing neutral pressure (ID 5 to 10 in Table 4.1). It is assumed no atomic hydrogen enters the plasma column from the source thanks to differential pumping so only volumetric sources/sinks and interactions with the surface (not inferred here) are possible. Number of particles created during the duration of the ELM-like pulse by type of reaction. MAD is defined as ensemble of multiple reactions that, starting from neutrals, first create a molecular precursor (H_2^+ , H^-) then further react with the end result of the two consecutive reactions being exclusively H_2 dissociation. [19] 188

A.1 Sampling strategy for TS and OES. At the top is indicated the progressive reading of the camera rows, with the integration time of TS is indicated. Below are each of the ELM-like pulses. It is shown how the trigger of the capacitor bank is shifted in time and all the pulses are split in two scans. Dashed lines indicate an interruption of the space or time scale. 205

A.2 Example of a raw image from the OES. The readout starts from the bottom so higher rows represent later times. In the figure are indicated rows/times corresponding to different stages of the ELM-like pulse 206

A.3 Example of decomposed time frame showing the symmetry of the image to the vertical pixel ~ 600 , likely representing the location of the plasma column axis. 207

A.4 (a): example of a fit of the OES line integrated brightness and relative SNR with 3 Gaussians for the $n = 4 \rightarrow 2$ line. In magenta the profile of the fitted Gaussian, in thin black the found location of the plasma column centre. (b): SNR of the line integrated brightness. 208

A.5 Measured and fitted peak target temperature for a discharge in Stage 1 (ID 5 in Table 4.1). In dashed green the fit of the temperature profile using the triangular Gaussian pulse model for $t > 1.5\text{ms}$ and in solid green the whole profile. The black dashed line indicates the cooling from the previous pulse and the thin solid black one is the peak target temperature not corrected for this. 211

A.6	Peak temperature of the target for low neutral pressure (ID 5 in Table 4.1). To estimate the effect of the ELM-like pulse only the second half of the pulses is used, when the target is close to a steady state.	211
A.7	Comparison of the peak power density profiles (b) result of fitting the peak temperature curve (a) the with different analytical solutions for the lowest available neutral pressure conditions (ID 5 in Table 4.1). All find adequate values for the energy density even with radically different peak durations. Dashed lines are obtained fitting from 1.5 to 30ms while solid ones from -20 to 30ms. In magenta 1.5ms after the temperature peak.	212
A.8	Peak target temperature evolution (a) calculated with the MSC.Marc/Mentat® code from a known heat flux profile made to be similar to the one caused by the CB in Magnum-PSI (b) (solid black lines). That is fit with different an- alytical solutions and the inferred heat flux compared to the input. Dashed lines are obtained fitting from 1.5 to 30ms while solid ones the entire time axis. In magenta 1.5ms after the temperature peak.	213
A.9	Peak temperature increase distribution over the steady state on the target. (a) low neutral pressure conditions showing a clear confined peak (ID 5 in Table 4.1). (b) high neutral pressure case showing the temperature increase is not localized, possibly consistent with reflections of volumetric radiation or radiation of other origin (ID 10 in Table 4.1). The black dashed line is the circular side of the cylindrical target. The arrow indicates where the source is outside the camera view.	214
A.10	Correlation between molecular hydrogen and plasma density with temperature from B2.5-Eunomia modelling. The coloured dashed lines are obtained with a linear log log fit for the single cases. The solid black line is obtained averaging the fitting parameters obtained.	215
A.11	Correlation between atomic hydrogen and plasma density with temperature from B2.5-Eunomia modeling. The coloured dashed lines are obtained with a linear log log fit for the single cases. The solid black line is obtained averaging the fitting parameters obtained.	216
A.12	Correlation between atomic hydrogen and electron temperature from B2.5- Eunomia modeling	217

A.13 Correlation between H_2 and electron temperature from B2.5-Eunomia modelling. The coloured dashed lines are obtained with a linear log log fit for the single cases. The solid black line is obtained averaging the fitting parameters obtained. This is assumed to be the same as H_2^+ temperature, while to obtain H^- temperature 2.2eV are added to account for the H_2 dissociation energy. .	217
A.14 Residuals from fitting T_{H_2} with the scaling from Figure A.13 and their weak dependence on the plasma density. The linear log log scaling in black is obtained by fitting all points at once.	218
A.15 Correlation between H^+ and electron temperature from B2.5-Eunomia modelling. The dashed line indicates $T_{H^+} = T_e$	218
A.16 Schematic of the plasma column model used. This schematic is useful to correlate local properties (at TS/OES location) to global ones like the total input power. Simplifications as constant densities and temperatures along the magnetic field and constant flow speed are used.	221

Acknowledgments

This work was only possible thanks to the support of my supervisor Bruce Lipschultz; my “unofficial” supervisor Matthew Reinke; CCFE exhaust group; the collaborators from CCFE and DIFFER; the staff of the YPI; the engineers and technicians of MAST-U and Magnum-PSI, and all my PhD colleagues in and out of the CDT, to all of which I’m very thankful.

First of all, I would like to thank Bruce for his support in these years. The project had its ups and downs, not helped by a pandemic in its middle, but we did the best we could to navigate towards our goals. It must have been difficult to manage a student based in a different lab, with a background in engineering rather than physics and eager to always fall in the newest rabbit hole, but he did a very good job. I’m also thankful for Bruce taking care of the organisational hiccups sometimes arising from the hardware work, providing the critical push for things to follow through.

I would like to thank Matt, as he made the entire PhD possible and was responsible for engineering and procuring the hardware, with all the headaches it implies. He taught me how to design, calibrate and use an IRVB diagnostic and his help was necessary in interfacing with a device as complicated as MAST-U. He taught me the care and thoughtfulness necessary to operate on a machine as complex as MAST-U and didn’t get angry when “magic smoke” was accidentally released. Matt was often helpful to smooth the discussion and was always seeking tangible results.

Plenty of others have helped me during these 5 years but they would not fit on these few pages. I can explicitly mention only a few, so I apologize in advance for who is not here, but I’m still grateful to.

I thank Tom Farley, whose help was necessary to manage the multitude of interfaces between the IRVB and MAST-U and helped to deal with the documentation. This team work was vital and I wish him and his family the best. I would like to thank Gijs Akkermans for providing the first contact that made the collaboration with DIFFER possible, his teachings on spectroscopy, and allowing me to meet so many wonderful people. I thank Ray Chandra for his help in including B2.5-Eunomia results and Tijs Wijkamp for the MWI data.

I want to thank everyone that helped me progress towards my results in MAST-U, and

among many in particular Andrew Thornton, Jack Lovell, Richard Martin, James Harrison, Peter Ryan, Joe Allcock, Mike Robson, Kandan Balamurugan, Nigel Thomas-Davies and all the MAST-U team. I also want to thank those who helped me navigate through the different environment of DIFFER like Ivo Classen, Thomas Morgan, Jonathan van den Berg and all the Magnum-PSI operations team.

I can't thank Kevin Verhaegh enough, whose spectroscopy and operations knowledge was instrumental, together with help from Daljeet Singh Gahle, to steer the work on molecules towards its scientific objectives. Chris Bowman was invaluable in providing support for everything Bayesian.

I'm infinitely grateful to Yoshika Terada who gave me the courage to seek and start the PhD in the first place. She supported me all these years, from Massa Lombarda to Oxford, and has always believed in me. She also helped me in developing the tools to analyse the raw and processed data.

I would like to thank all the people that made my stay in the UK a lot more fun, and I'm happy to have had the chance to meet, of which I would like to mention Omkar, Hasan, Eduardo, Steve, Charlie, Lena, Tom N, Jack, Sam, Simon, Joe, Michail and all the Fusion CDT group. I thank in particular Andrew for his support and willingness to adapt to the Italian ways; Nick for editing this thesis; Mads for introducing me to caving; Yacopo and Nicola to bring Italian vibes in this far away land. I'm thankful for all the great people I met in The Netherlands and are part in making it a *beautiful* place, like Aaron, Michele, Luca, Qin, Devyani, Bob, Ana, Artur and all the Pineapples.

I'm thankful to Vittorio Colombo, who first taught me about plasmas and, many years later, helped me secure the PhD.

Last but not least I would like to thank my family and all my friends in Italy that have always supported me.

Voglio ringraziare i miei amici d'infanzia, che sono da sempre al mio fianco e che sono sempre felice di incontrare: Diego, Lorena, Bert. Voglio anche ringraziare i miei amici dell'università, con sono ancora vicino e il cui successo mi ha motivato per intraprendere il dottorato: Alberto, Viola, Benny, Fedè.

Voglio anche ringraziare Massimo Foresti e tutti gli ex-colleghi dell'Elettrotecnica Imolese che, nonostante per iniziare il dottorato abbia dovuto lasciare l'azienda, mi sono sempre stati amici.

Infine voglio ringraziare la mia famiglia, che nonostante la scelta di intraprendere il dottorato più tardi della norma e di stare così lontano da casa mi ha sempre voluto bene e sostenuto.

Support for M. L. Reinke's contributions was in part provided by Commonwealth Fusion Systems.

This work has been carried out within the framework of the EUROfusion Consortium, funded by the European Union via the Euratom Research and Training Programme (Grant Agreement No 101052200-EUROfusion). Views and opinions expressed are, however, those of the author(s) only and do not necessarily reflect those of the European Union or the European Commission. Neither the European Union nor the European Commission can be held responsible for them.

The authors wish to also acknowledge Byron J. Peterson for providing the blackened and calibrated platinum foil used as absorber in the IRVB.

This work was supported in part by the DIFFER institute.

Declaration

This thesis has not previously been accepted for any degree and is not being concurrently submitted in candidature for any degree other than Doctor of Philosophy of the University of York. This thesis is the result of my own investigations, except where otherwise stated. All other sources are acknowledged by explicit references.

Portions of this thesis are based on manuscript which has been published to peer-reviewed journals. I am the first author of this manuscript. Where appropriate, this work has been referenced. The vast majority of the work has been done by the main author and is explicitly stated otherwise. The manuscript is:

F. Federici, M. L. Reinke, B. Lipschultz, A. J. Thornton, J. R. Harrison, J. J. Lovell, and M. Bernert. Design and implementation of a prototype infrared video bolometer (IRVB) in MAST Upgrade. *Review of Scientific Instruments*, 2023. Also cited in this work as [20].

Executive summary

The changes of radiation profile due to detachment were characterised in MAST-U. This was enabled by the new infra red video bolometer (IRVB) diagnostic. The diagnostic was originally designed by Matthew Reinke, based on previous work on NSTX-U. [21] The field of view (FOV) of the IRVB is designed to accurately measure the radiated power profiles around the lower x-point region, where large spatial gradients of emissivity are expected. The FOV includes a poloidal view of the plasma covering $\sim 2/3$ of the foil and a tangential view over the rest. The diagnostic was optimised using the ray tracing code CHERAB and fully characterised prior to installation. Due to restricted vessel access, the match between design and real FOV was verified using known features of the plasma itself, like the silhouette of the central column, highlighted by disruptions, and bright spots corresponding to fuelling locations. This verification is a difficult task for foil bolometers, as the minimum signal that can be detected is of brightness similar to the plasma, so they cannot be calibrated with long exposure images like other camera diagnostics.

In parallel to the hardware and calibration activities, an inversion algorithm was developed to obtain the emissivity distribution. This follows a Bayesian approach where, given a set of priors (limited negative emissivity and regularity), the uncertainties of the components of the IRVB are propagated so as to find the most likely radiation distribution that yields the measurements. The radiated power inferred has a spatial resolution of the order of few cm, difficult to achieve in the x-point and divertor region, and unprecedented in spherical tokamaks. This demonstrates the viability of the IRVB to measure radiation in a region other than the core, for which they are usually employed.

In MAST-U the IRVB was used to determine that, in a conventional divertor L-mode plasma, radiative detachment follows the same progression as in large aspect ratio tokamaks: the inner target detaches first, followed by the outer, then the radiation climbs the inner

separatrix to form a MARFE-like structure at the midplane that can then penetrate into the core. In MU01 no extrinsic impurities were fed to the plasma, and the radiation was not observed to penetrate the core from the x-point, as was previously observed in other devices. [13] The radiation on the inner leg was observed with unprecedented resolution and it was determined that its movement from target to x-point is gradual, appearing to be contrary to expectations from theory. [22] The IRVB was also used, in conjunction with the MWI and other spectroscopic measurements, to infer that, after the particle flux roll over in a super-x plasma, the radiation is mainly dominated by hydrogenic radiation, unlike in the comparable carbon wall devices TCV. It is inferred that, after the ionisation front recedes from the target and the plasma cools, radiation from molecular effects becomes dominant.

As part of a collaboration with The DIFFER institute, ELM-like pulses were reproduced in the linear machine Magnum-PSI. The steady state plasma was progressively detached by increasing the neutral pressure in the target chamber, simulating the burn through in a tokamak divertor. It was observed that by increasing the neutral pressure it was possible to reduce the energy delivered to the target, up to complete shielding in extreme cases. This is associated with a reduction of the heat flux factor, a measure of the effect of heat transients on wall components. This observation could potentially be applicable for tokamaks, as the connection length between the radiation front and the target can be of the order of meters (in deep detachment) while the pressure can reach a few tens of Pa, as it was in Magnum-PSI. This can be further improved if the divertor is baffled, so that the neutral compression is enhanced, and an advanced divertor configuration like the super-x is adopted, resulting in a much longer connection length.

The optical emission spectroscopy (OES) setup was upgraded by the author and Gijs Akkermans in order to acquire intra-ELM data. The OES is composed by a series of parallel poloidal lines of sight, so that Balmer line emission can be determined radially. This was used, together with a crude model of the plasma column, to infer the processes in the plasma via a Bayesian inference. For this study the effect of molecular reactions was accounted for in terms of line emission and in both the particle and power balance. It is observed that even if radiative losses are significant, exchanges of potential energy dominate the plasma energy losses. Of the molecular reactions, the path to molecular assisted dissociation is the most important, as it is more efficient than electron impact dissociation. Molecular assisted recombination is also important, especially at intermediate temperatures, but electron ion

recombination dominates for cold plasmas. It is found that ionisation dominates for temperatures above $\sim 5\text{eV}$ while molecular processes become important in colder plasmas and electron ion recombination dominates below $\sim 1.5\text{eV}$.

The results from both devices indicate that in deep detachment and during the burn through, when plasmas interact with colder neutrals and molecules, the effect of molecular reactions becomes important at mid to low temperatures. This is a useful insight for the development of models used to estimate the plasma energy losses during detachment or removed from ELMs before they reach the target.

Chapter 1

Introduction

In this section I will describe the background and the current status of the fusion energy research related to this PhD thesis.

1.1 Fusion energy

In a fusion reaction two light nuclei fuse and a heavier nucleus is generated. The energy released in the reaction depends on how strongly protons and neutrons are bound in the nucleus of reactant and products. This strength is expressed by the average binding energy per nucleon, that is the energy necessary to decompose one nucleus divided by the number of nucleons. The energy released by the nuclear reaction is given by the difference of the total binding energy in the products minus the reactants. [Figure 1.1](#) shows that it is possible to obtain energy in two ways: fusion and fission. In fusion, the lighter the reactants the larger the energy released per nucleon tends to be.

Another factor to consider in comparing different fusion reactions is the likelihood of the reaction to happen. This is characterised by the fusion cross section, which depends on the kinetic energy of the incident particle. Considering an ensemble of particles this kinetic energy translates to temperature. The lower the temperature for which the cross section reaches its peak, and the higher the peak, the easier it is to achieve fusion. For this and other reasons the reaction that is the main focus of current research is the fusion of deuterium and tritium to helium: [\[23\]](#)



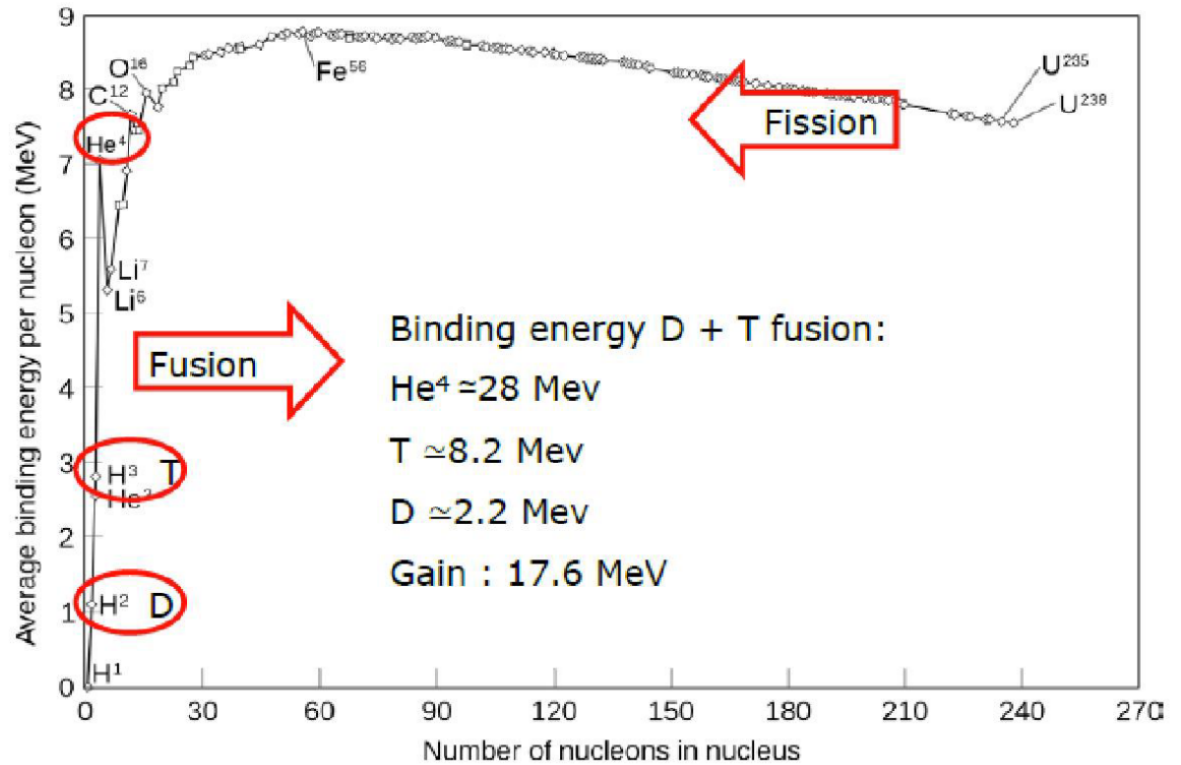


Figure 1.1: Average binding energy per nucleon [9]

In this reaction 3.5MeV kinetic energy is released to the α particle and 14.1MeV to the neutron. Tritium is not available in nature because it is radioactive with a short half life, so it must be produced. It is envisaged that it will be produced using the neutron released in reaction 1.1 in reactions 1.2 and 1.3



The initial fuels in this cycle then are deuterium and lithium, both widely available in nature.

1.2 Plasma confinement

The temperatures that are relevant for fusion applications are measured in keV, corresponding to millions of °C. At these temperatures matter is in the state of plasma, meaning that

atoms are ionised and nuclei and electrons can move freely. These temperatures are of the same order of magnitude as the centre of the Sun. No material can withstand them so special techniques must be adopted to confine the reactant long enough for a significant fraction to fuse. The most important figure of merit of the achieved confinement is the fusion triple product, related to the Lawson criterion, that gives the minimum product of plasma density, temperature and confinement time required to achieve ignition (Equation 1.4). Ignition is the condition when the fusion power output is sufficient to maintain a constant temperature against all losses without external heating.

$$n_e \tau_E T_e \geq 5 \cdot 10^{21} m^{-3} s keV \quad (1.4)$$

The most viable way to maintain this environment is expected to be through magnetic confinement fusion (MCF), and specifically the tokamak. In MCF the fuel is confined in plasma state thanks to its behaviour when exposed to electromagnetic fields. Every electrically charged particle is subject to the Lorentz force:

$$F = q(E + v \times B) \quad (1.5)$$

In the presence of a magnetic field the particle gyrates with a circular motion in the direction perpendicular to field lines and is unperturbed in the parallel direction. In a tokamak the plasma is arranged in a doughnut shape, closely surrounded by two main sets of coils. The toroidal field coils generates a magnetic field that is closed in on itself, so that charged particles can be maintained in circular spiralling motion. This toroidal geometry, though, causes an up/down drift in the plasma that would cause it to quickly reach the walls and cool down. This is prevented with a current through the plasma, induced by a central solenoid with a time varying current, that generates the poloidal magnetic field. To further stabilise the plasma and shape it as requested other coils are added to this basic configuration. [24] The magnetic field generated in this way is composed of concentric flux surfaces expanding out to the coils. The final configuration is outlined in Figure 1.2. Shown in pink is a magnetic flux surface, the surface on which a magnetic field line lies. JET is currently the largest tokamak and has achieved triple products higher than $10^{21} m^{-3} s keV$ in 1997 [25] and recently achieved the record for fusion energy produced, at 59MJ. [26]

The plasma can move freely along the field lines and slowly across it, so in time it drifts

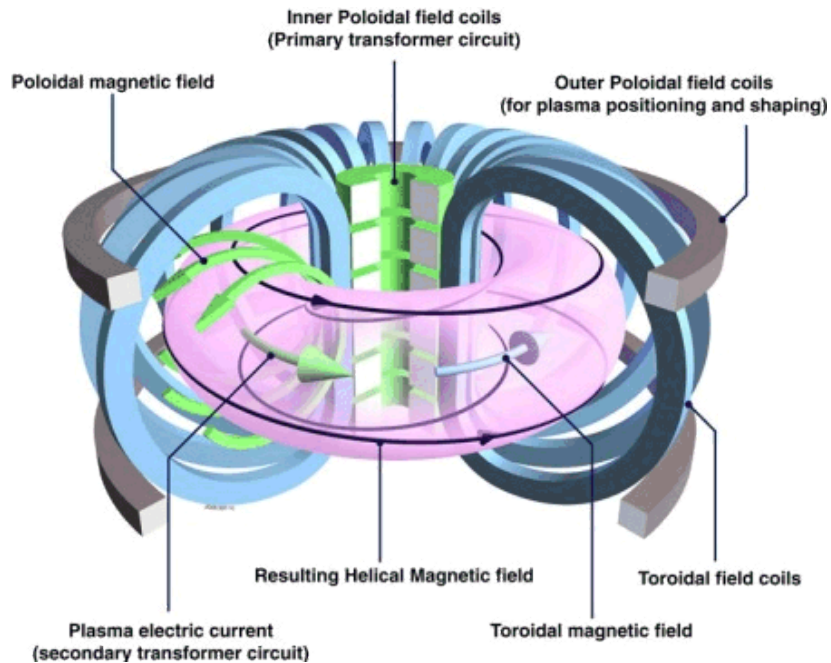


Figure 1.2: Schematic of the main components of a tokamak [10]

from the centre toward the wall via cross field transport caused by collisions and turbulence. One of the important evolutions of the tokamak design is to add a coil parallel to the plasma with a current in the opposite direction. This changes the magnetic configuration in such a way that the core of the plasma is no longer in direct contact with a solid limiter, as shown in Figure 1.3. The first magnetic surface that crosses a solid surface, adjacent the Last Closed

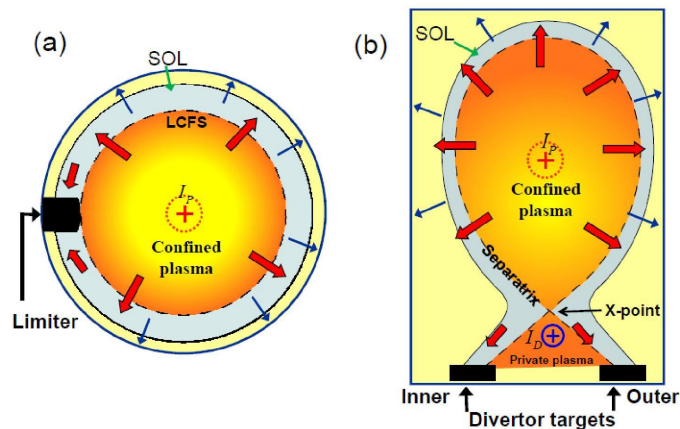


Figure 1.3: The poloidal cross section of a limited (left) and diverted (right) plasma. [9]

Flux Surface (LCFS), is referred as separatrix, and where the poloidal field goes to zero is known as the x-point. The region below the lower x-point (and above the upper in the double null configuration) is called the divertor. The separatrix crosses the solid surfaces in well

defined regions, called divertor targets. The plasma that escapes from the core (the position of which is usually referred to as "upstream") reaches the separatrix and then follows the magnetic field around the core and eventually reaches the targets. In this way the core is shielded from the impurities generated by the plasma/surface interaction and can efficiently expel the fusion products. This motion along field lines is much faster than across them and is associated with a layer beyond the LCFS called the Scrape-Off Layer (SOL). The time a particle needs to cross the plasma from the centre and reach the wall defines the confinement time.

1.3 H-mode

A way to limit cross field transport in the core region and move towards ignition is to operate in the so called high-confinement mode (H mode), as opposed to the low-confinement mode (L mode). This regime is reached when the energy flux across the separatrix is increased over a threshold that depends on the discharge conditions. [27] The physics behind the specific value of the L-H threshold is still not fully understood, but its effect is to induce a transport barrier at the edge of the core plasma. This barrier strongly reduces the anomalous transport due to turbulence in a thin region around the core, allowing for a better energy and particle confinement there. One drawback of the H-mode is that it causes cycles of accumulation of energy in the core (up to 10% of the core plasma thermal energy [28]) that is then released in sub millisecond bursts of hot plasma. These so called Edge Localised Modes (ELMs) cause a temporary increase of particle and thermal flux on the target of 2-3 orders of magnitude, which is not expected to be tolerable in a large tokamak. [29] The transport barrier is also very effective in confining impurities and fusion products in the plasma core. [30] This leads to a dilution of the fusion fuel and a possible radiative collapse of the plasma. ELMs are beneficial in this context as they provide a mechanism to transport impurities across the transport barrier. [31]

Various solutions to the ELM problem have been put forward, in the form of different operational regimes where the instabilities that cause the ELMs are prevented or limited, but such solutions usually involve some degree of degradation of the confinement properties typical of the ordinary ELMy scenario, or a limitation of the operational space. Another solution is to cause intentionally more frequent and smaller events that can release part of

the accumulated energy and particles in a more controlled and gradual manner. [31]

In order to sustain the H-mode a certain amount of power must cross the separatrix, otherwise the H-L back transition can occur. This constitutes a lower bound to the heat and particles that need to be dissipated from the separatrix to the target.

1.4 The exhaust problem

A consequence of the divertor configuration is that the SOL is very narrow, of the order of mm [32, 33], therefore all the exhaust heat is delivered to the small area of the target in contact with the SOL. The situation is even worse in H-mode, as even more power crosses the separatrix and is exhausted via the SOL. For ITER, a fusion device in construction in France that will be a step closer to a power production device, the heat flux parallel to field lines is in the order of GW/m^2 . [34] The maximum power that can be removed from a surface with current technologies is $10 - 20 MW/m^2$. [35, 36] If the heat to the target is not mitigated this will pose a serious limitation on its lifetime and the amount of impurities reaching the plasma, making profitable operations impossible.

Sputtering is the phenomenon of emission of one or multiple atoms from a solid surface caused by interaction with an ion. This happens even for heat fluxes much lower than those required for melting the surface. [37] There are various types of possible interactions but, as a whole, the larger the energy of the ion, the larger the number of atoms that are sputtered from the surface. The local interaction of the plasma with a solid surface creates a sheath where the ions are accelerated towards the surface, exacerbating sputtering. The flow velocity at the sheath entrance amounts to $v_{se} \geq \sqrt{\frac{kT_e + \gamma kT_i}{m_i}}$ with m_i the ion mass, k the Boltzmann constant, $\gamma = 5/3$, T_e and T_i electron and ion temperature respectively, and is higher than the plasma sound speed $c_s \approx \sqrt{\frac{2kT}{m_i}}$. The sputtered atoms can end up in the plasma, polluting it, or be redeposited to the target, changing its composition and properties. Sputtering can be so severe as to be the main limiting factor of the lifetime of the plasma facing components.

This work fits into the broader effort of reducing the heat flux to the target and associated sputtering to acceptable levels while maintaining an acceptable performance. This is important both during the plasma steady state phase (to which the work in [Chapter 2](#) and [3](#) is mostly concerned) and during transients (for which [Chapter 4](#) is more relevant) as will

be explained later.

1.5 Divertor shaping

The heat and particle flux can be reduced by tilting the target with respect to the separatrix, by locally reducing the magnetic field, thus spreading the heat over a larger surface, and by moving the strike points to a larger radius to spread the heat over a larger surface. Different divertor designs are under investigation (see some on [Figure 1.4](#)) with the purpose, among others, of easing the thermal burden on the target.

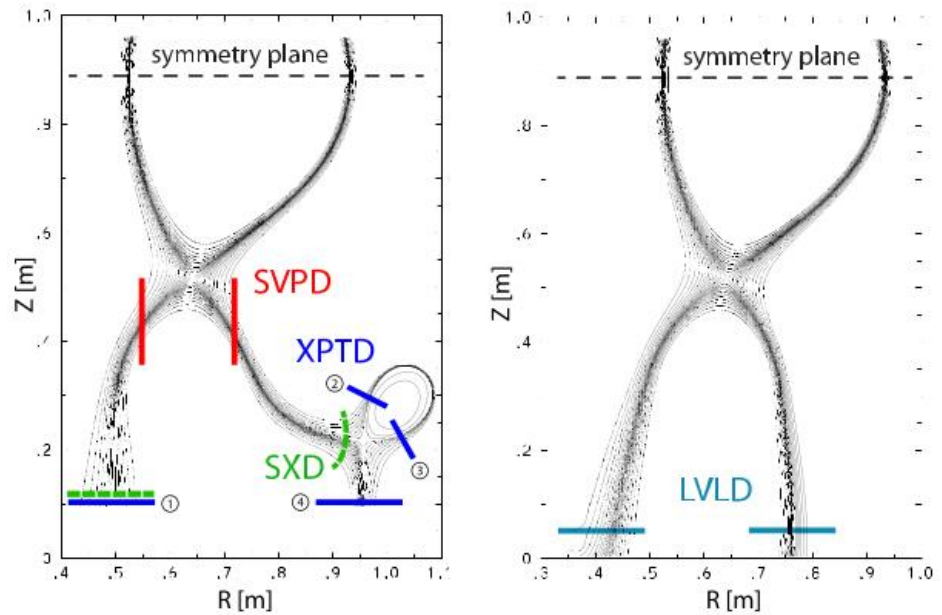


Figure 1.4: Example of different divertor configurations. Left: Standard Vertical Plate Divertor (SVPD), Super-X Divertor (SXD) and X-point Divertor (XPTD). Right: Long Vertical Leg Divertor (LVL) [11]

The above mentioned mitigations combined lead to a reduction of the heat flux density of around 20 times for a tokamak of Standard Vertical Plate Divertor (SVPD) divertor type, such as will be implemented on ITER, still short of the additional 10 times reduction needed to respect the $10 - 20 MW/m^2$ limit. The divertor configuration introduces an asymmetry in the poloidal geometry due to the two targets being located at different radii. In terms of energy and particle redistribution in the SOL the inner target will receive a higher ion flux and lower energy flux compared to the outer one. As will become clear later, on the inner target this causes stronger recycling and eases the thermal load, while the outer target is normally subjected to more severe conditions. [[38] and references therein]

1.6 Radiative dissipation scenario

Another way to decrease the heat flux to the target is to induce radiation in the SOL. Radiation occurs naturally in plasmas and it depends greatly on the temperature and density of each species. When an atom is not yet fully ionised its electronic levels can be excited by collision and de-excite emitting a photon. The ionised atoms can recombine with free electrons and release a photon too. The energies at which these effects are more likely correspond to the peaks in the curves in Figure 1.5. If the temperature is so high that atoms are fully ionised, then the only radiative mechanism is Bremsstrahlung radiation that is much less efficient. This corresponds to the monotonically increasing right-hand-side part of the curves in Figure 1.5.

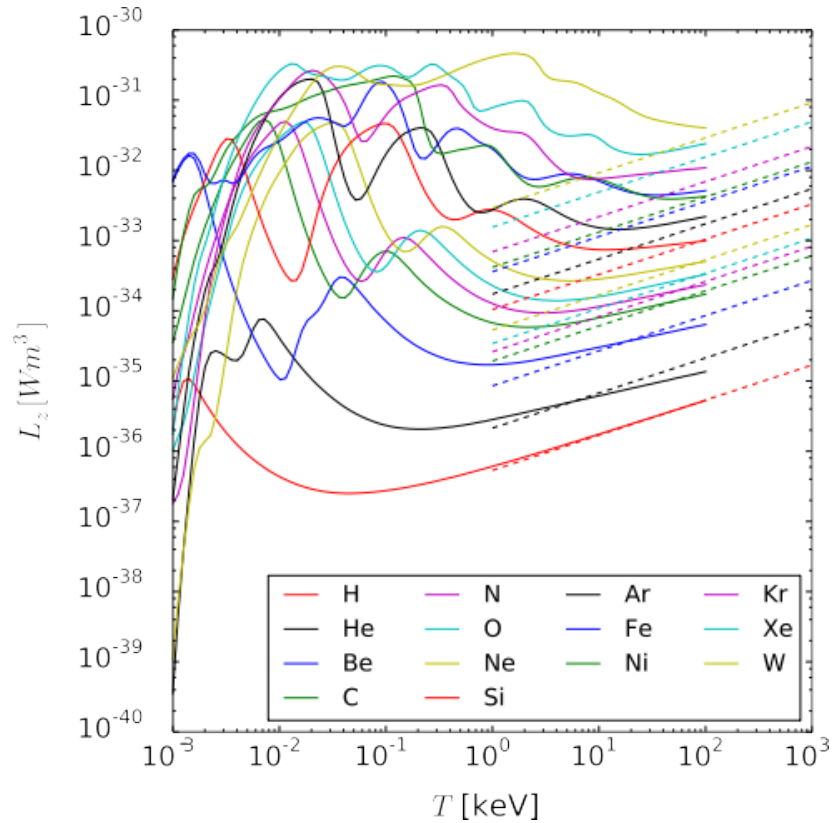


Figure 1.5: Loss function data from the Atomic Data and Analysis Structure (ADAS) data base (solid lines) for the different elements [12]

At the temperatures of interest in the SOL (100s of eV [39]) hydrogen is fully ionised and radiates weakly. With the addition of impurities sputtered from the wall, or specifically seeded in the discharge, energy can be transferred from the plasma to the impurities and then radiated. This mechanism can be exploited to dissipate a significant amount of power

from the core and edge of the plasma, but also the SOL. This regime is referred to as the radiative scenario.

1.7 Detachment

At low upstream densities the plasma that enters the SOL can flow relatively unimpeded towards the target. The temperature in the SOL is about constant and the particle flux is limited only by the sheath condition (e.g. "sheath-limited"). By increasing the core and SOL density, plasma heat flux conductivity decreases (e.g. "conduction limited"), leading to negative temperature gradients and positive density gradients, with an almost uniform pressure. The heat flux to the target is the sum of the component parallel to field lines q_{par} , the orthogonal one q_{ort} , and a component given by the energy released with recombination q_{rec} , given by [Equation 1.6](#).

$$\begin{aligned} q_{par} &= n_{e,t} c_s \gamma_{sh} k_B T_{e,t} \propto p_{e,t} T_{e,t}^{0.5} \\ q_{ort} &= q_{par} \left(\frac{B_p}{B_\phi} \right)_t \propto p_{e,t} T_{e,t}^{0.5} \\ q_{rec} &= n_{e,t} c_s E_{pot} \propto p_{e,t} T_{e,t}^{-0.5} \end{aligned} \quad (1.6)$$

where γ_{sh} is the heat sheath transmission factor, $n_{e,t}$ and $T_{e,t}$ are the electron density and temperature in front of the target, c_s is the sound speed, B_p and B_ϕ are the poloidal and toroidal magnetic fields and $E_{pot} \approx 15.8eV$ is the potential energy released per ion when recombining to form neutral deuterium molecules on the target plate. [40] The temperature cannot be indefinitely reduced because of operational limits such as the Greenwald limit. [41] Moreover, a reduction of the temperature does not alone guarantee a decrease of the heat flux. One possible solution to achieve it is to cause gradients of temperature and pressure along the field lines in the SOL. This should be done in such a way to minimize the impact on the core plasma.

A way to achieve this is to induce plasma detachment. This phenomenon has been observed in a series of tokamaks [[40] and references therein] and can be induced by impurity seeding or fuelling. In Alcator C-Mod [42] and AUG [43] it was shown to significantly reduce target heat flux in conditions scalable to burning plasmas like ITER.

In an attached regime the plasma streams through the SOL and reaches the target. At the target the charged particles recombine and become neutrals. These are generated in an

excited state and, therefore, there is strong radiation at the strike points. The neutrals are not bound by magnetic fields and can move freely until they collide with other neutrals or particles from the plasma. A neutral can then re-ionise and stream along field lines, returning to the target or entering the plasma again. This process is called recycling and the region of the leg where it occurs is called the ionisation or recycling region.

If the density in the SOL is high enough then the neutrals generated at the surface by the plasma will interact mainly in the SOL and the plasma will lose part of its energy and momentum on its way to the target via radiation and transport. [44] To further increase the energy loss, low Z impurities like Nitrogen can be seeded in the SOL: they will ionise only partially, radiating efficiently at a higher temperature than hydrogen or helium. The lower the temperature, the higher the energetic ionisation cost will be. This is because lower temperature means slower progressive excitation by collisions of the bound electron up to ionisation, with radiative losses in the process, instead of a single higher energetic collision directly to ionisation. This causes even more radiative cooling. In most cases volumetric ionisation from neutrals constitutes the main source of ions for the target flux. This effect is even stronger if the divertor is separated from the main chamber by a physical barrier, the baffle, that confines the neutrals increasing their density in the divertor, like in the Mega Amp Spherical Tokamak Upgrade (MAST-U) tokamak. [45–47] This is referred to as high recycling, where the recycling region constitutes a self-contained system that is supplied from upstream with the energy to ionise the neutrals. This is believed to be one of the most important differences between tokamak divertors and linear machines, where the main source of ions is usually the plasma source upstream. Simulations for the linear machine Pilot-PSI, characterised by a very high density, show that ionisation could account for up to a third of the plasma source, but in a region very close to the source itself. [48, 49]

From detachment experiments it is observed that the particle flux to the target increases with increasing core density. Increasing the density or seeding impurities causes the particle flux to reach a maximum and then decrease. This is called rollover and corresponds with the onset of detachment. Other metrics for detachment onset have been used, such as the decrease of the target temperature below a certain threshold [50, 51], but the Langmuir probe particle flux roll over constitutes a direct and simple measurement, hence their widespread use. Further increasing the density the particle flux decreases and saturates. In the case that the plasma loses all its kinetic or thermal energy it still maintains the energy absorbed

during its creation, the ionisation and dissociation energy, $15.8eV$. In a DEMO scale device this residual energy flux would be still high enough to exceed the $10 - 20MWm^{-2}$ limit on the target. [46] To reduce it even further the temperature must drop below $1eV$ to trigger volumetric recombination. This is accompanied by a strong radiation increase from where volumetric recombination occurs. The particle flux drop can continue up to the point that the measured plasma temperature at the target reaches a minimum and the radiating region (radiation front) recedes upstream along the field lines. [52] At different stages in this process different fronts will in turn detach from the target like the ionisation and thermal front. [22, 53, 54] The front's movement comes from the balance between the power and particles entering the SOL with dissipation by radiation and interaction with recycling neutrals.

1.8 The x-point radiator

When a discharge, either L-mode or H-mode, is close to the detachment threshold in a tokamak with a conventional divertor configuration, and the impurity or core density is increased, 4 stages of detachment are defined as per the description in [38, 40] (here detachment is intended to mean the particle flux roll over and deviation from what is expected in the attached case, see [Section 1.11](#)).

1. Onset of detachment: the inner target detaches inter-ELMs (both from impurity seeding and from upstream density increase), the outer target is attached
2. Fluctuating state: inter-ELM radiative fluctuations (of the order of kHz) appear at the X-point and, inter-ELMs, the inner target detaches
3. Partial detachment at outer target: inner target always detached, outer target detached inter-ELMs, strong radiation at the X-point, fluctuations frequency decrease to ELMs scale, ELM's amplitude decrease.
4. Complete detachment: inner and outer target always detached, sporadic ELMs, radiator moves from X-point further into the confined plasma

For this type of discharge the radiator close to the X-point appears when detachment starts at the inner target, while it is only enhanced by the detachment on the outer target.

Because the parameter of interest is the reduction of thermal flux on the outer target, a feature that will always be present in reactor relevant conditions is a strong radiator located close to the X-point.

If the density is further increased, the radiator can either move vertically upwards entering the core [55], or move along the inner separatrix up to the midplane and enter the core from there forming a MARFE. [56] In both cases a degradation of the confinement properties is observed.

1.9 Effect of X-point radiator

The X-point radiator (XPR) [55] or X-point MARFE [43] is a region of steep temperature gradient, where the temperature goes from that of the hot upstream plasma from the core to the cold region where ion / neutral interactions dominate. The presence of such a region at or inside the separatrix can lead to confinement degradation. In this context, what is referred to as confinement H98 is the ratio of the actual energy confinement time τ_{th} to a reference. The reference is a confinement time from a scaling law obtained by fitting the confinement time of many tokamak experiments in a certain operating mode. For ELMy H-mode the scaling law mostly used is the ITER Physics Basis (IPB) 98(y,2). [57] For L-mode the ITERL-97P scaling can be used. [58] The scalings are given by Equation 1.7 and 1.8. For spherical tokamaks an H-mode [59] and MAST L-mode [60] scaling are given in Equation 1.9, 1.10 respectively

$$H_{98} = \tau_{th} / \tau_{th,98y2}, \quad \tau_{th,98y2} = 0.0562 I_P^{0.93} B_t^{0.15} n_{19}^{0.41} P_L^{-0.69} R^{1.97} \varepsilon^{0.58} \kappa_a^{0.78} M^{0.19} \quad (1.7)$$

$$L_{97} = \tau_{th} / \tau_{th,97P}, \quad \tau_{th,97P} = 0.037 I_P^{0.74} B_t^{0.2} n_{19}^{0.24} P_L^{-0.75} R^{1.69} \varepsilon^{0.31} \kappa_a^{0.67} M^{0.26} \quad (1.8)$$

$$H_{ST} = \tau_{th} / \tau_{th,HST}, \quad \tau_{th,HST} = 0.066 I_P^{0.53} B_t^{1.05} n_{19}^{0.65} P_{heat}^{-0.58} R^{2.66} \kappa_a^{0.78} \quad (1.9)$$

$$L_{ST} = \tau_{th}/\tau_{th,LST}, \quad \tau_{th,LST} = 0.153 I_P^{1.01} B_t^{0.7} n_{19}^{-0.07} P_L^{-0.37} \quad (1.10)$$

with I_P plasma current in MA , B_t toroidal magnetic field in T , n^{19} averaged electron density in units of $10^{19} \#/m^3$, $P_L = P - dW/dt$ power loss in MW with P heating power and W stored energy, R major radius, a minor radius, $\varepsilon = a/R$ inverse aspect ratio, κ_a elongation, M ion mass number in amu . It is possible to calculate the energy confinement time from magnetic coil measurements and the energy transferred to the plasma as heating (P_{heat}). τ_{th} is defined by

$$\begin{aligned} \frac{dW}{dt} &= P_{heat} - \frac{W}{\tau_{th}}, \quad W = \frac{3}{2} \langle p \rangle V, \quad \langle p \rangle = \frac{\mu_0 I_p^2 \beta_p}{8\pi^2 a^2} \\ \beta_p &= \left\langle \frac{nk_B T}{B_p^2 / (2\mu_0)} \right\rangle, \quad P_{heat} = P_{ohmic} + P_{NBI} + P_{RF} \end{aligned} \quad (1.11)$$

With V plasma volume, $\langle p \rangle$ volume-averaged plasma kinetic pressure, β_p poloidal beta, B_p poloidal magnetic field, a minor radius, P_{ohmic} , P_{NBI} , P_{RF} , power transferred to the plasma by ohmic heating, neutral beam injector and radio frequency respectively. [61, 62] The confinement loss is usually determined by comparing the confinement before and after the appearance of the X-point radiator, or by comparing a series of discharges in similar conditions with and without X-point radiator. The confinement degradation can be due to direct cooling caused by the cold region (e.g. poloidal temperature gradients driving power to that location [63]) or to easier penetration of impurities in the core [22] and references therein]. The degradation significantly affects the outer part of the core region with significant reduction of temperature, pressure and an increase in density. [43] It was found on some experiments that the inner core (i.e. where the ratio of poloidal magnetic flux over poloidal magnetic flux at the separatrix $\rho_{pol} < 0.8 - 0.5$) is only marginally effected. [64] and references therein] It is therefore suggested that the reduction of the gradients in the pedestal region could be recovered in a portion of plasma $0.8 < \rho_{pol} < 0.95$. [40]

The X-point radiator will also have the effect of radiating a substantial fraction (75–90% of the heating power achieved [65]) of the power input to the core. This could reduce the power crossing the separatrix, causing the H-L transition. This is not a major risk for ITER and larger machines, because the power crossing the separatrix is expected to be significantly larger than the threshold requirement. In fact, seeding a higher-Z impurity into the plasma

to enhance core radiation (radiative mantle) and lower the power needed to be exhausted through the separatrix to about the minimum for the L-H transition, has been considered. Then a lower-Z impurity will be fed to radiate in the divertor. [[43, 64] and references therein]

There are two active areas of research to limit confinement losses with XPR.

One is in trying to achieve detachment while not allowing the radiator to move all the way to the X-point and cause confinement degradation. The main difficulty in achieving this is that, for standard divertor geometries, the operational window of any given control parameter to move the radiator from target to X-point is very narrow. Considerable effort has been put forward to find a predictive model. An early attempt is the two point model, a 1D model where the conditions outside the separatrix and at the target are correlated and some approximations on the heat and particle transport adopted. [66–72] The thermal front model proposed by Lipschultz [22] is an improved 1D model that, balancing input / output power on the thermal front (edge of the radiator toward the core), tries to identify the operational window of a control parameter and its stability for given plasma / magnetic configuration. This model finds that for all the control variables analysed, the operational window widens for an increasing ratio of X-point to target magnetic field B_x/B_t ; and increasing ratio of the connection length between X-point and target to upstream and target z_X/L . It is also found that increasing connection length should lower the detachment upstream density threshold. Stability analysis indicates that for decreasing z_X/L there is an increasing minimum B_x/B_t for a stable solution. [22]

This puts additional emphasis on research of different divertor designs. TCV in Switzerland and MAST-U in UK are the best suited for these type of investigations due to the flexibility of their divertor geometry. Recent data from TCV seems to prove that the sensitivity on control parameters decreases with flux expansion (larger operational window) but didn't verify the threshold dependence on connection length. [73]

A second strategy is to live with the radiator located at the X-point (it is further apart from the target and ELMs have to burn through more divertor volume before reaching the target) and try to understand and minimize the loss of confinement in the core. The reality of current conventional tokamaks is that the X-point radiator always appears if full detachment from the target is pursued, with different variations depending on the seeded impurity as can be seen in [Figure 1.6](#).

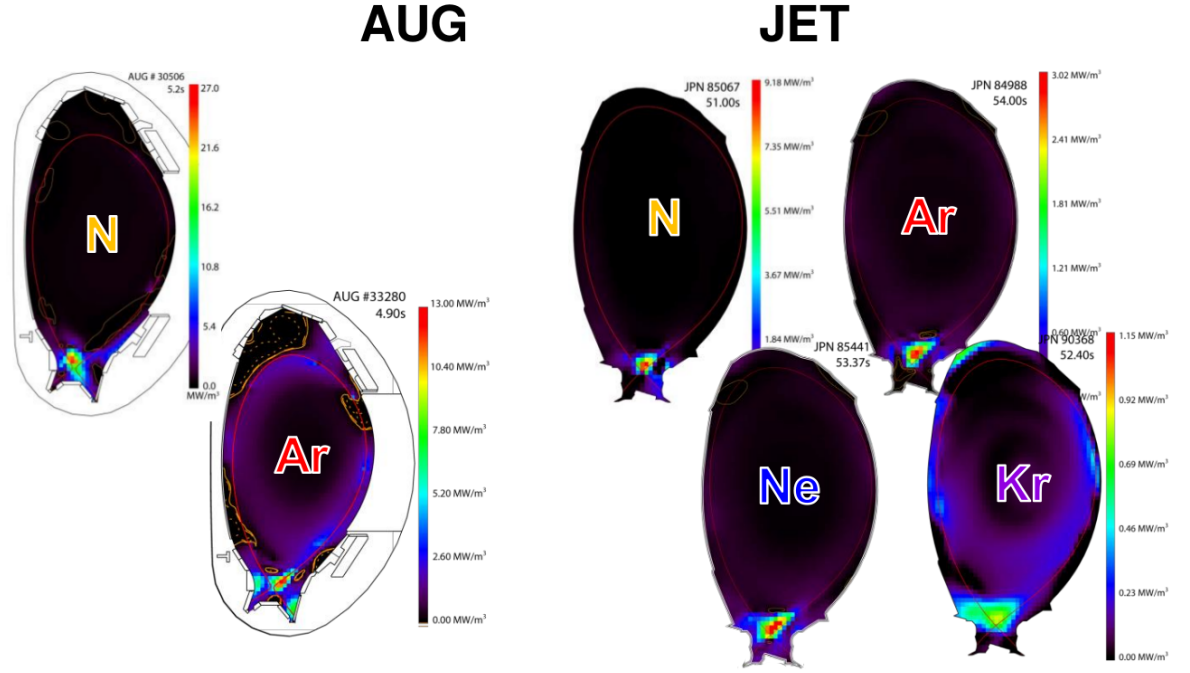


Figure 1.6: Different radiation profiles with the clear presence of an X-point radiator for different impurities [13]

The X-point radiator cannot be idealised as easily as the thermal front of detachment, because it is much more related to core and edge dynamics. Modeling its behaviour requires the use of codes that account for all atomic interactions, drifts, etc. such as SOLPS-ITER, EDGE2D-EIRENE, SOLEDGE2D-EIRENE [[37] and references therein]. The presence of the radiator significantly affects temperature, pressure and density distribution, especially in the pedestal, therefore it is likely to have an effect on the current distribution and MHD activity. In recent years a large effort has been put forward to characterise the behaviour of the X-point radiator and its macroscopic effects on the core / edge. This has been done mostly in conventional geometry tokamaks, both with metal and carbon walls.

A recent effort in the analytical modeling of the XPR with a simplified power and particle balance [74] allowed for discrimination between conditions conducive to the XPR compared to a MARFE at the midplane (which causes a significant loss of performance and often a disruption). The stability of the XPR strongly depends on the radiation curve (Wm^3 vs T_e) of the plasma. Due to the relatively high temperatures at the edge of the core, this dependence is influenced by the type of impurity present in the plasma. It was found that for carbon, which is an intrinsic impurity in machines with carbon walls, the transition from XPR to MARFE occurs at low plasma densities, such that a stable XPR is usually

not possible. In metal machines, it is easier to control the type of impurity, and if heavier elements like nitrogen are present, then the XPR is stable for a larger parameter space. This could be partially tested in MAST-U by seeding nitrogen, but carbon will always be present, sputtered by the graphite tiles.

1.10 ELMs and XPR

Another important feature of the XPR is the reduction in amplitude of ELMs. This can be attributed to the fact that the energy associated with an ELM first heats up the XPR and then moves toward the target. If the neutral density between the X-point and target, and in the radiator itself, is high enough then it could be possible to avoid ELM “burn through”, where the ELM penetrates the detachment front and reaches the target. [45] This can be further improved by alternative divertor configurations, like the super-x divertor with a long outer leg, since the ELM has more time to interact the cold gas and dissipate some of its energy. The burn through is a complex phenomenon because of the short time scale (hundreds of μs), complex geometry and complex interactions between the core plasma being expelled by the ELM with the neutrals.

Simulations with simplified atomic and neutral physics have been carried out with the code JOREK to study the dynamic of the burn through in MAST-U, showing a significant reduction of the peak target heat flux compared to empirical scalings. [75,76] Other attempts with the code SOL-KiT have shown the importance, given the short time scale of the burn through, of including kinetic effects and that the target flux could be underestimated with fluid models. [77] Attempts to better understand the physics of detachment and the burn through with a more detailed model that includes molecular reactions with simpler geometric approximations (SD1D) have revealed that molecular reactions are important for the plasma momentum balance and cause Balmer α radiation to increase at and after the roll over. [78] These attempts could recreate target power fluxes similar to experiments, but require significant refinement to return sensible results. [79] No simulation yet, to the knowledge of the author, includes a complete treatment of the molecular reactions that become relevant at the low temperatures typical of deep detachment ($< 5eV$) together with the 3D and kinetic effects that have been shown to be important.

1.11 Analytic models

1.11.1 Two Point Model

In order to qualify and characterise the evolution of detachment it is useful to build approximate analytical models for the properties of interest, like particle and power fluxes, depending on the upstream plasma conditions. The most widely model is the two point model (2PM) and its variations. [66–72] In it the complex 3D geometry of the SOL is translated to a simpler 1D system as shown in Figure 1.7.

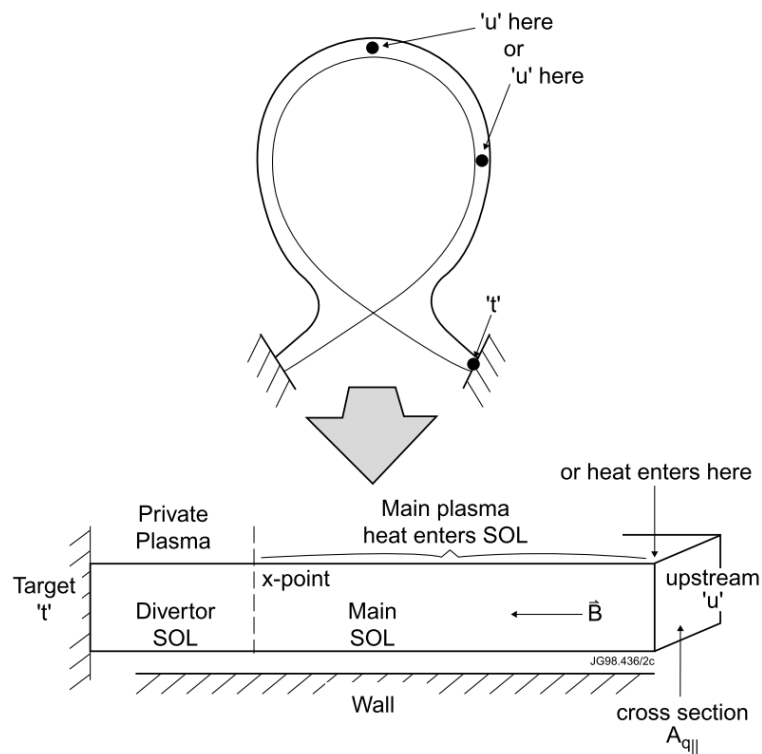


Figure 1.7: Schematic of how the poloidal SOL geometry can be straightened into a 1D one. 'u' indicates the location of the upstream location where core plasma enters the SOL. Adapted from [14] and the JET image database.

Then a series of assumptions are made:

- there are no power losses along the SOL
- ionisation does not affect the energy and flow profile
- heat is transported only via parallel heat conduction
- plasma pressure is considered constant in the entire SOL

- quasi neutrality, and the same temperature for electrons and ions ($n_e = n_i = n$, $T_e = T_i = T$)
- all the power to the SOL is transferred at the upstream location.

At the target surface the presence of the sheath accelerates the ions to the sound speed, so the local pressure given by the static and dynamic component p_t is

$$p_t = p_{static} + p_{dynamic} = 2n_t k T_t + n_t m_i c_{st}^2 \quad (1.12)$$

Upstream, the dynamic component of the pressure is assumed to be negligible so, $p_u \approx 2n_u k T_u$, so that if the pressure is considered uniform then this returns the first equation of the 2PM

$$2n_u k T_u = 2n_t k T_t + n_t m_i c_{st}^2 = 2n_t k T_t + 2n_t k T_t \rightarrow n_u T_u = 2n_t T_t \quad (1.13)$$

Since no volumetric power loss is considered, the heat transferred to the SOL is transported to the target, and it is determined by the sheath physics to be

$$q_{\parallel} = \gamma n_t k T_t c_{st} = \gamma n_t \sqrt{\frac{2(kT_t)^3}{m_i}} \quad (1.14)$$

returning the second equation of the 2PM.

This heat is carried to the target via conduction. In order to calculate it, using Spitzer conductivity ($\kappa_{\parallel} = \kappa T^{5/2}$) [72, 80], one should consider that the parallel heat conductivity for charged particle self-collisions is proportional to $n_s v_{th_s} \lambda_s \approx n_s v_{th_s}^2 / \nu_s$ with v_{th_s} the unidirectional thermal velocity of the species s , n_s species s density, λ_s the self-collision mean free path and ν_s the self-collision frequency. v_{th_s} is given by $\sqrt{8kT_s/m_s}$ while ν_s is proportional to $n_s/\sqrt{m_s T_s^3}$. The heat conductivity is then proportional to $T_s^{5/2}/m_s^{1/2}$. This indicates that, given the mass difference, electrons dominate the conduction heat transfer, and that there is a strong dependency on the temperature. The heat flux can then finally be written as per Equation 1.15 where the electron parallel heat conductivity coefficient κ is of the order of 2000. [72]

$$q_{\parallel} = -\kappa T^{5/2} \frac{dT}{ds_{\parallel}} \quad (1.15)$$

This equation can be integrated from upstream to target (amounting to the connection length L), and considering that q_{\parallel} is constant one can obtain the last equation of the 2PM model

$$T_u^{7/2} = T_t^{7/2} + \frac{7q_{\parallel}L}{2\kappa} \quad (1.16)$$

Assuming fixed q_{\parallel} , L , γ , m_i Equation 1.13, 1.14 and 1.16 contain 4 unknowns (n_t, n_u, T_t, T_u) and can be used to numerically solve for 3 when one is known or measured. If one assumes $T_u \gg T_t$ Equation 1.16 can be further simplified neglecting T_t and the 2PM reduces to

$$\begin{aligned} T_t &= \frac{q_{\parallel}^2}{n_u^2 T_u^2} \frac{2m_i}{\gamma^2 k^3} \\ n_t &= \frac{n_u^3 T_u^3}{q_{\parallel}^2} \frac{\gamma^2 k^3}{4m_i} \\ T_u &= \left(\frac{7q_{\parallel}L}{2\kappa} \right)^{2/7} \end{aligned} \quad (1.17)$$

The target particle flux can finally be calculated as the heat flux over the energy released by each particle (neglecting the energy from surface recombination) from Equation 1.14 as shown in Equation 1.18 (the arrow refers to the further simplification as per Equation 1.17).

$$\Gamma_t = \frac{q_{\parallel}}{\gamma k T_t} = n_t \sqrt{\frac{2kT_t}{m_i}} \rightarrow \frac{n_u^2 T_u^2}{q_{\parallel}} \frac{\gamma k}{2m_i} \quad (1.18)$$

This correlation is the one that has been used in the literature to find detachment. The particle flux from Langmuir probes and the expectation from this scaling roughly match for an attached target. Increasing the upstream density further, the particle flux plateaus and then starts to decrease, deviating from the expected trend. This can be quantified in the Degree of Detachment (DoD) given by the ratio of the two quantities. [54,72] Of relevance for the present work is that the depth of detachment increases with upstream density. This will be used to characterise density ramps in MAST-U during the first experimental campaign (MU01). It has also been demonstrated that the threshold for rollover is proportional to a certain value of the ratio $\frac{q_{rec}}{p_{up}}$ (q_{rec} is the specific energy flux into the hydrogen recycling region). [45,52,81]

This simple model can then be improved by including more of the true physics of the divertor and SOL such as: volumetric power and momentum losses due to interactions with

neutrals, volumetric radiated power losses, variation in q_{\parallel} and pressure along field lines, sharp transition regions from x-point to target (e.g. ionisation / density / radiation front), magnetic configuration, etc. [22, 72, 82, 83] This increase of sophistication also allows, depending on the model, the study of the conditions along the leg, and investigation of the relevance of different phenomena and the stability of the front's movement. The front's stability is particularly important because, as detached scenarios become more and more relied upon to provide the volumetric dissipation required for the target survival, it is paramount to be able to control their location.

1.11.2 Thermal front Model

Following the formulation in [22, 53] the thermal front is defined as the region with steep thermal gradients where the temperature transitions between the hot upstream, and the cold target region where ionisation, recombination and other neutral processes dominate. The front is thin in the direction parallel to magnetic field and is located in the divertor leg (between x-point and target). From the upstream side of the front (temperature T_h) to the midplane the pressure is approximated as constant, with the parallel heat flux driven entirely by conduction in the same fashion as for the 2PM (see Equation 1.15, this approximation will be later adopted within the front too). From the downstream side of the front to the target temperature is low ($\sim T_c$), in the eV level, and processes that can reduce the particle flux like recombination are possible.

Unlike before, Equation 1.15 is integrated from the upstream location to the front and the variation of q_{\parallel} along the field lines is considered. No power enters the SOL apart from upstream and no power losses are assumed in the SOL, so the conducted heat flux has a functional form $q_{\parallel}(s_{\parallel}) = q_{\parallel,u} \frac{B(s_{\parallel})}{B_u}$. The upstream temperature is then given, neglecting T_c , by

$$T_u \approx \left[\frac{7}{2\kappa} \int_{s_{\parallel,f}}^{L_{\parallel}} q_{\parallel}(s_{\parallel}) ds_{\parallel} \right]^{2/7} = \left[\frac{7q_{\parallel,u}}{2\kappa} \int_{s_{\parallel,f}}^{L_{\parallel}} \frac{B(s_{\parallel})}{B_u} ds_{\parallel} \right]^{2/7} \quad (1.19)$$

Now one can perform a power balance on the front. Assuming the power losses due to impurity radiation are dominant and no power enters the region other than via conduction, this results in

$$\frac{dq}{dz} = n_e n_I L_I(T) = f_I n_e^2 L_I(T) \quad (1.20)$$

with $q = q_{\parallel} \frac{B_u}{B} = -\kappa_{\parallel} \frac{B_u^2}{B^2} \frac{dT}{dz}$ a scaled form of the parallel heat flux, z a scaled version of the parallel distance such that $dz = \frac{B_u}{B} ds_{\parallel}$, I the main radiating impurity and L_I and f_I the electron cooling function and impurity fraction respectively. L_I is low at very low temperatures, as a minimum energy for an impacting electron is required to excite an atom, but is also low above the temperature that leads to the full ionisation. Therefore, depending on the specific impurity, there is a temperature range where its radiation is significant, identified with the T_c and T_h previously mentioned. T_h can be determined as the temperature at which L_I decreases below a set small fraction of its peak, usually around 60-80eV for nitrogen. [22] Multiplying Equation 1.20 by $q = -\kappa_{\parallel} \frac{B_u^2}{B^2} \frac{dT}{dz}$ and integrating between T_c and T_h one obtains

$$[q^2]_c^h = 2 \int_c^h f_I n_e^2 L_I(T) \kappa_{\parallel} \frac{B_u^2}{B^2} dT \quad (1.21)$$

Taking f_I and $p = n_e T_e = n_u T_u$ as constant inside the front as well as up to the upstream location, and assuming that the heat flux at the cold side of the front is negligible as most of the energy is radiated in the front, this reduces to

$$q_{\parallel,u}^2 = 2n_u^2 T_u^2 f_I \kappa \int_c^h \sqrt{T} L_I(T) \frac{B_u^2}{B^2} dT \quad (1.22)$$

Assuming the parallel distance between the *cold* and *hot* locations to be short, B inside the integral can be approximated with B_f , constant over T , and T_u can be replaced as per Equation 1.19 to finally obtain

$$q_{\parallel,u} = n_u \frac{B_u}{B_f} \left[\frac{7q_{\parallel,u}}{2\kappa} \int_{s_{\parallel,f}}^{L_{\parallel}} \frac{B(s_{\parallel})}{B_u} ds_{\parallel} \right]^{2/7} \sqrt{2f_I \kappa \int_c^h \sqrt{T} L_I(T) dT} \quad (1.23)$$

This equation contains variables that can be externally controlled while others depend on the magnetic configuration and the intrinsic characteristics of the plasma. Separating the two one can construct a lumped detachment parameter C as

$$C(s_{\parallel,f}) = \frac{n_u \sqrt{f_I}}{q_{\parallel,u}^{5/7}} = \underbrace{7^{-2/7} (2\kappa)^{-3/14} \left[\int_c^h \sqrt{T} L_I(T) dT \right]^{-1/2}}_{C_0} \underbrace{\frac{B_f}{B_u} \left[\int_{s_{\parallel,f}}^{L_{\parallel}} \frac{B(s_{\parallel})}{B_u} ds_{\parallel} \right]^{-2/7}}_{C_1} \quad (1.24)$$

The grouping indicated with C_0 is independent on the front location, therefore variations of external conditions will impact the front location as per C_1 . If C_1 increases from the target to the x-point, it means that if the front moves towards the upstream location (getting more detached) a lower $q_{\parallel,u}$ (as an example of one of the control variables) is required to maintain that location. If $q_{\parallel,u}$ doesn't change, the front will be pushed towards a more attached configuration, restoring the original front position. In this case, therefore, the front is stable.

If C_1 decreases from the target to the x-point, when the front moves upstream from equilibrium a higher $q_{\parallel,u}$ is required. If $q_{\parallel,u}$ doesn't change the front will move so as to make the target more detached, moving further towards the x-point in an unstable manner. This means that in a leg where this condition on C_1 is present, the model predicts that as soon as the conditions for the formation of the thermal front occur at the target, it should then rapidly move to the x-point.

In both standard and spherical tokamaks, when the inner leg goes from a region of high to low magnetic field from target to x-point, C_1 is often decreasing, leading to the prediction of an unstable detachment front movement. Meanwhile, on the outer leg, the possibility to vary the total and poloidal flux expansion allows for a greater range of outcomes. [22, 82] These predictions can be verified in MAST-U observing the movement of the peak radiation on the leg, as will be shown later.

1.12 Goals and objectives of the thesis

The main objectives of this work are related to the radiation distribution on MAST-U and its relation to detachment, with the ultimate goal of reducing heat and particle flux to the target. Of particular interest is: understanding the movement of the radiating regions compared to other metrics of detachment in MAST-U compared to other tokamaks; examining the feasibility of the XPR configuration; comparing the stability of the movement of the detachment front with theoretical expectations; analysing the plasma behaviour in the novel super-x regime. This is achieved by measuring the total radiated power profiles, with the

design, implementation, calibration, validation and use of the new infra-red video bolometer diagnostic in MAST-U. As will be shown in detail in [Chapter 2](#), the diagnostic is based on previous work on NSTX-U [\[21\]](#) and Alcator C-Mod [\[84\]](#) and its goal is to measure the radiation distribution in the lower section of MAST-U with particular emphasis on the x-point region.

Significant work was necessary to design the system and to balance the strength of the signal with the desire to maximize spatial resolution (see [Section 2.3](#)). For this, new and accurate ray tracing methods were used in order to accurately determine the intensity of the radiation from the plasma on the diagnostic.

Once the diagnostic was built it was necessary to calibrate it in order to convert the data to a form related to the power radiated by the plasma (see [Section 2.4](#)). This was done by characterising all parts of the diagnostic and by finally verifying its accuracy compared to a known source. Once installed on MAST-U the orientation and the field of view was verified using features of the plasma, obtaining good agreement with the original design.

Finally the data from MAST-U is collected and analysed (see [Section 2.5](#)). The changes of line integrated brightness in different region of the plasma correlated well with the progress of detachment. The measurements match observations from another diagnostic that observes the total radiated power (the resistive bolometry system), albeit being negatively affected by imperfections in the sensing element and a signal from the NBIs unrelated to the radiated power effecting part of the field of view.

In parallel to the hardware development, an effort was made to develop inversion routines capable to tomographically invert the line integrated brightness to emissivity (see [Section 3.2](#)). Different methods were tested and a probabilistic approach was adopted to take into account the uncertainties arising from the different parts of the system.

The results show, for the first time in a spherical tokamak, the changes of radiation distribution in relation with detachment with high spatial resolution (see [Section 3.3](#)). The movement of the radiation in the inner and outer leg can be compared with literature [\[38, 40, 55, 56\]](#) and it is found that the progression is similar to expectations for L-mode in large aspect ratio tokamaks. It was not possible to clearly determine a consistent behaviour for H-mode discharges (see [Section 3.3.3](#)). The progress of detachment in L-mode is compared to measurements from other diagnostics (see [Section 3.3.2](#)). The particle flux on the outer target is observed to consistently roll-over after the radiation is detached on the inner target and

at the same time as the outer target radiatively detaches. It is also shown that the radiation moves gradually on both the inner and outer legs, against expectations from analytical models [22, 82] that predict a sharp transition on the inner leg. The XPR regime is briefly observed after both legs detach, before a MARFE-like structure is observed on the high field side midplane. In MAST-U, where only the intrinsic impurity carbon was present in the first experimental campaign, this is only a transient phase, matching recent theoretical predictions. [74] The radiated power in the core region scales well with measurements from the resistive bolometry system while the total power radiated in the super-x chamber is used in conjunction with measurements of the hydrogen and carbon line emission to confirm recent results on the processes involved with detachment [85, 86] and the importance of molecular assisted reactions as an intermediate step between electron impact ionisation and electron-ion recombination (see [Section 3.3.4](#)).

A secondary goal of this work, developed thanks to a collaboration with the DIFFER institute in The Netherlands, is understanding the behaviour of ELM-like pulses during detachment and the role of atomic and molecular processes. This was achieved by conducting a series of experiments on the linear plasma machine Magnum-PSI, and upgrading the existing optical emission spectrometer to operate intra-shot measurements, as detailed in [Chapter 4](#).

Conditions similar to those at the end of the divertor leg in a tokamak were reproduced, changing the neutral pressure to cause the target to transition from attached to detached. Superimposed on this steady state regime, ELM-like pulses are recreated with a dedicated power supply system. This causes a sudden increase of the plasma temperature and density such that the heat flux increases transiently by half an order of magnitude. Temporally and spatially resolved measurements are taken with different diagnostics to understand the burn through process. This is difficult to do in a tokamak because of poor diagnostic access and reproducibility.

Direct measurements from a fast camera observing the burn through process tangentially and an infrared camera observing the target are used to determine that, when the neutral pressure is sufficiently high, the ELM-like pulse is prevented from effecting the target and the plasma is dissipated in the volume instead.

The measurements from the optical emission spectrometer were used in conjunction with other diagnostics to build a Bayesian algorithm capable of inferring the most likely properties of the plasma, poloidally and temporally resolved. This is used to show, similarly to what was

done in the study on MAST-U, the importance of molecular assisted reactions. Molecular processes are important in the exchange of potential energy, while less so in radiating the energy from the ELM-like pulse. It is also found that, for some conditions, the volumetric ionisation source is more important than the plasma input from the source, making these conditions closer than other linear machines to what observed in tokamaks.

Chapter 2

MAST-U IRVB hardware activities

2.1 Motivation

Parts of this chapter have been adopted from:

F. Federici, M. L. Reinke, B. Lipschultz, A. J. Thornton, J. R. Harrison, J. J. Lovell, and M. Bernert. Design and implementation of a prototype infrared video bolometer (IRVB) in MAST Upgrade. *Review of Scientific Instruments*, 2023.

As explained in [Chapter 1](#) the location of the radiating regions can have a significant impact on the core plasma. [\[40\]](#). It is important, therefore, to well characterise the power balance and radiated power profile in current machines to understand the stability and performance of strongly radiating plasmas and support predictions for future devices.

Key diagnostics are bolometers that usually operate by exposing a thin foil to plasma radiation and by monitoring its temperature. The subject of this chapter is a prototype infrared video bolometer (IRVB) installed on MAST-U to study x-point and divertor radiation. The IRVB concept has previously been demonstrated on tokamaks (Alcator C-Mod [\[84\]](#), HL-2A [\[87\]](#), JT-60U [\[88\]](#), KSTAR [\[89, 90\]](#)) and stellarators (LHD [\[91, 92\]](#), Heliotron J [\[93\]](#)) and its basic operating principles are well known. A thin foil is exposed to the plasma radiation through a pinhole aperture so that each point of the foil corresponds to a different line of sight (LOS). The foil heats up according to the radiation it receives and the change in foil temperature is measured via an infrared camera. The advantage, relative to discrete resistive bolometer sensors [\[94\]](#), lies in the very large number of LOS accessible with a single IRVB device and the capability to image very large or small portions of the plasma based on foil and pinhole relative position. The foil is also a completely passive component, potentially better

resistant to neutron irradiation therefore more reactor relevant, than in a resistive bolometer, where on the foil is glued the active resistors used to measure its temperature. The downsides are that the physics of thermal diffusion needs to be considered which introduces a limit in the time resolution of the diagnostic.

The IRVB technique is not new, but the current application in MAST-U represents the first successful implementation on a spherical tokamak. Additionally, in most cases, the IRVB is tuned to image the core plasma, while in this case the aim is to measure the radiated power profile in the vicinity of the lower x-point with high resolution. This choice also comes from the need to complement the MAST-U resistive bolometry system with a radiated power diagnostic with high resolution in a region of the plasma characterised by sharp variations. This chapter will detail the considerations that dictated this prototype design. The entire calibration procedure and the lessons learned from this implementation will also be presented. It will be shown how the line integrated data was analysed to extract the emissivity profile and early results from the first experimental campaign in MAST-U (MU01).

2.2 IRVB basics

A sketch of the IRVB in MAST-U is in [Figure 2.1](#).

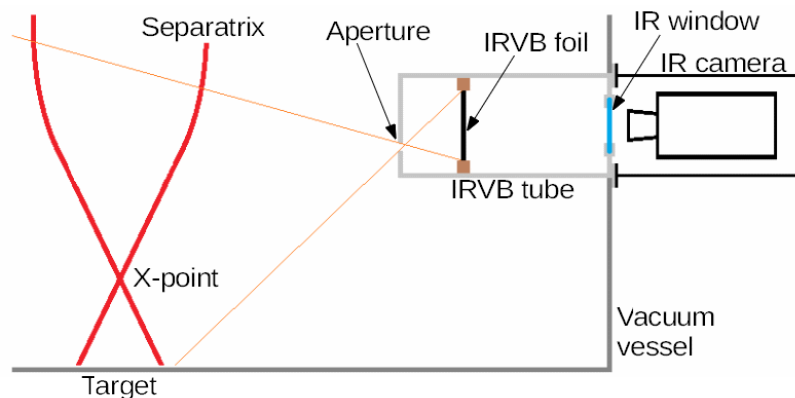


Figure 2.1: Schematic representation of the main components of a IRVB diagnostic

As mentioned above, the radiation from the plasma reaches the absorber through a pinhole. The radiation is absorbed by the foil and its temperature increases accordingly. Knowing the thermal characteristics of the foil the absorbed power can be calculated, then a tomographic inversion can provide the emissivity profile from the plasma. There are various

elements to consider in the design of the IRVB diagnostic as shown in [Figure 2.1](#).

Considering how thin a typical carbon coated foil is (composed of $10\mu\text{m}$ graphite + $2.5\mu\text{m}$ platinum + $10\mu\text{m}$ graphite as per [\[95\]](#) and their standard properties), when the temperature on one side is increased by a set amount it takes $\sim 7\text{ns}$ for the other side to reach the 99% of that increase. The heat transfer across the foil is so fast compared to the maximum frame rate of the infrared (IR) cameras available (tens of kHz) and the timescale of the phenomena of interest (1-10ms) that it permits treating heat diffusion as a 2D problem. The thinner the foil the lower the thermal inertia, allowing for a higher temperature rise for given input power. The thickness must nevertheless be large enough for the vast majority of the radiation to be absorbed. The foil must also (if a significant amount of neutrons are produced by the plasma) be made of a material weakly prone to neutron induced transmutation and vacuum compatible. [\[96\]](#) It is important that the foil has low reflectivity for the wavelength range of interest. Metals normally used in bolometers have low reflectivity for UV and shorter wavelengths, but high for longer as the majority of radiation from the plasma is emitted at VUV wavelengths. This is usually addressed by coating the foil with a thin layer of carbon (as done in our case), known as "blackening", that weakly absorbs and weakly reflects high energy photons but has low reflectivity and high absorption at low energies. [\[97\]](#) The coating does not significantly impact the reflectivity of radiation entering the diagnostic at shallow angles and reaching the foil supports. [\[98\]](#) This light would require multiple reflections to reach the foil and would, therefore, be scattered resulting in a weak offset in a large portion of the foil. This would not change its capability to observe sharp features from the plasma. The coating introduces an interface between materials that might impede heat transfer and increases the mass of the foil increasing its inertia. The coating could also, depending on the technique, be deposited non uniformly on the foil, adding to the non uniformity already present on the foil. The coating must also be stable and vacuum compatible. [\[99\]](#)

The infrared camera must be positioned as close as possible to the foil in order to increase the resolution and signal to noise ratio. If the neutron flux is significant, or there are mechanical constraints, mirrors or periscopes must be used. All apparatus must be suitable to transmit infrared radiation and properly coated to avoid reflections. The camera itself has to be suitable for measuring temperature differences of few K around room or vacuum vessel temperature. Of great importance in the design is the positioning and size of the pinhole aperture with respect of the foil. The distance and position impacts the field of view (FOV)

of the diagnostic, its spatial resolution and the radiation intensity.

2.3 MAST-U IRVB design

The entire IRVB hardware design and optimisation was originally done by Matthew Reinke, based on work previously done for NSTX-U. [21] The definition of the materials, verification of compatibility with MAST-U vacuum and magnetic environment, procurement as well as the initial training of the author on the calibration and assembly of an IRVB system was by Reinke. The design was then verified and confirmed by the author with the selection of the fine tuning hardware feature mentioned in this section.

Here it will be shown how the design was adapted to the specific geometry of MAST-U. The vertical location of the IRVB was dictated by the available ports on the machine. The one assigned to the IRVB is HE11-2, located in sector 11 and centred $0.7m$ below the midplane. The pinhole was placed as close as possible to the plasma to enable an unobstructed, wide field of view while being protected by the surrounding structures and safely outside the plasma scrape-off layer (SOL), at a radius of $1.55m$. The resulting positioning of the IRVB tube can be seen in [Figure 2.2](#).

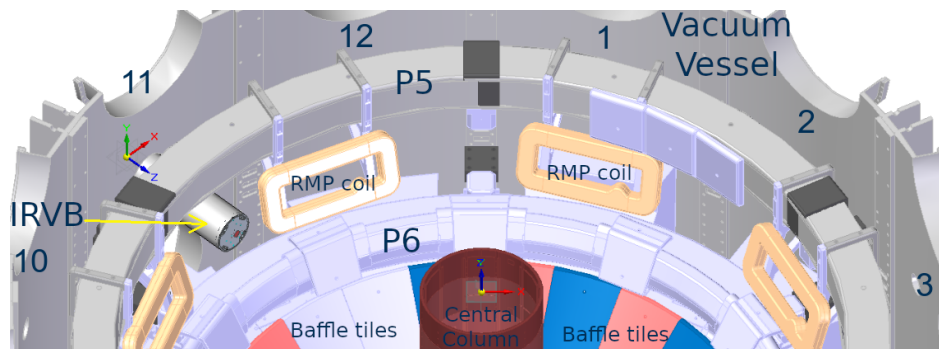


Figure 2.2: Top view of the lower half of MAST-U, showing the positioning of the IRVB inside the vacuum vessel respect to other features. The numbers identify the sectors, assigned clockwise in the toroidal direction.

With the above constraints, the pinhole was located off the centre of the foil so that the LOS starting from the x-point in the poloidal view of the plasma would land in the centre of the foil. The left two-thirds of the foil surface will have a mostly poloidal view of the plasma so that the radiation is integrated along the LOS mainly along field lines; the one-third of the foil on the right will have a mainly tangential view, with radiation integrated across field lines (see [Figure 2.8](#)). This was done to help the tomographic inversion that must then be

performed. The foil is composed of a $2.5\mu\text{m}$ platinum film coated with graphite on both sides of dimensions $9 \times 7\text{cm}$ as supplied by the National Institute for Fusion Science (NIFS), with the longer side aligned with the vertical axis of the machine to provide a large coverage in that direction. An exploded view of the components and their final appearance are shown in [Figure 2.3](#) and [Figure 2.4](#) respectively. In the design of the assembly, particular care was dedicated to:

1. The presence on the re-entrant and air side section of the diagnostic of features that can be used to align the view with the MAST-U geometry as intended.
2. The mechanical rigidity of the assembly and the increase of magnetic permeability due to welds. The tube has a weld along its length that was heat treated to reduce the relative magnetic permeability below 1.05.
3. Blackening all the surfaces that could cause reflections and direct light to the foil. The entire detector sub-assembly was blackened with Moly-Paul powder in an isopropanol solution (the same used within the MAST-U vacuum vessel (VV)) while it was deemed sufficient to grit blast the other surfaces.
4. The presence of cutouts in the tube to equalise the pressure within. The effect of rapid pressure changes was tested on a dummy foil created for this purpose in the benchtop setup (see [Figure 2.16](#)) causing no motion of the foil with depressurization of up to 0.05bar/s (only cooling due to ambient air decompression) and visible motion but no damage up to 0.2bar/s .
5. Maintaining electrical isolation between the tube and the absorber assembly (foil and copper plates) with PEEK isolation washers to avoid eddy currents through the absorber.
6. Use of vented screws for tapped holes to avoid trapping air and slowing down the vessel pump down.

The power density on the foil was estimated with [CHERAB \[100–102\]](#), a code that can perform ray tracing with the full geometry of MAST-U. Its advantage compared to simpler analytical techniques is that it can accurately account for the shape of the pinhole and the details of the machine geometry. The foil is assumed capable of fully absorbing radiation at all

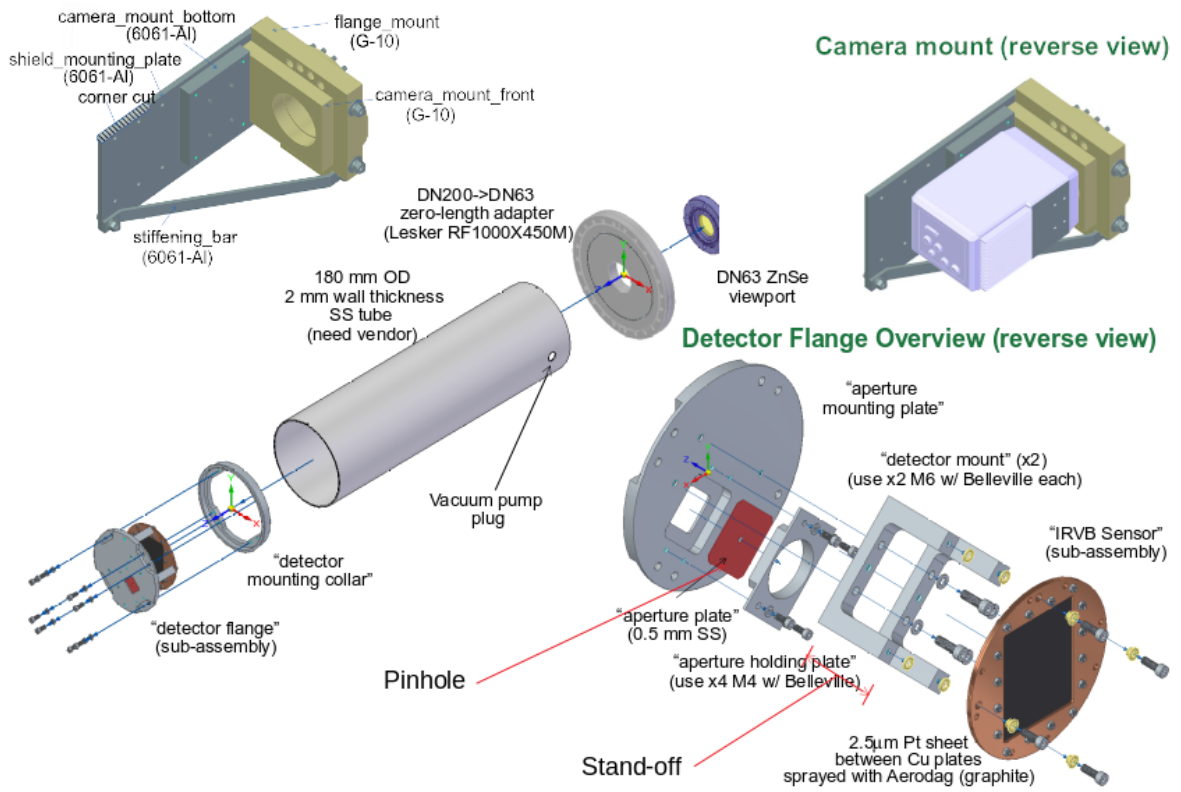


Figure 2.3: IRVB components overview: exploded view showing all internal components before welding and assembly.

the wavelengths relevant in MAST-U, as explained later. Based on prior experience with the IRVB on NSTX-U [103], the noise equivalent power density (NEPD) is expected to be in the region of $\sim 5W/m^2$, and so a desired signal of $\sim 100W/m^2$ was utilized in the pinhole camera design. Three possible diameter sizes have been evaluated for the circular pinhole in order to tune the signal strength and resolution: 4, 6, 8 mm. The larger the pinhole, the larger the fraction of the radiation that can reach the foil, but the radiation from neighbouring regions can overlap and decrease the spatial resolution. In order to tune the magnification of the system three possible lengths of the bracket that connects the foil assembly to the pinhole one (the stand-off) have been considered: 45, 60, 75 mm. The longer the stand-off, the more magnified the plasma image on the foil, so the better the spatial resolution, but the lower the signal. The results from the simulations of a homogeneous toroidal emitter of radius 8cm located at $R=0.55m$ and $Z=-1.2m$, emitting a total of 0.5MW (equivalent to $\sim 7.2kW/m^3$) for the 9 combination of configurations is shown in Figure 2.5. [104] The stand-off distances of 60 and 75cm allow the entire foil to observe the plasma and not be obscured by coils.

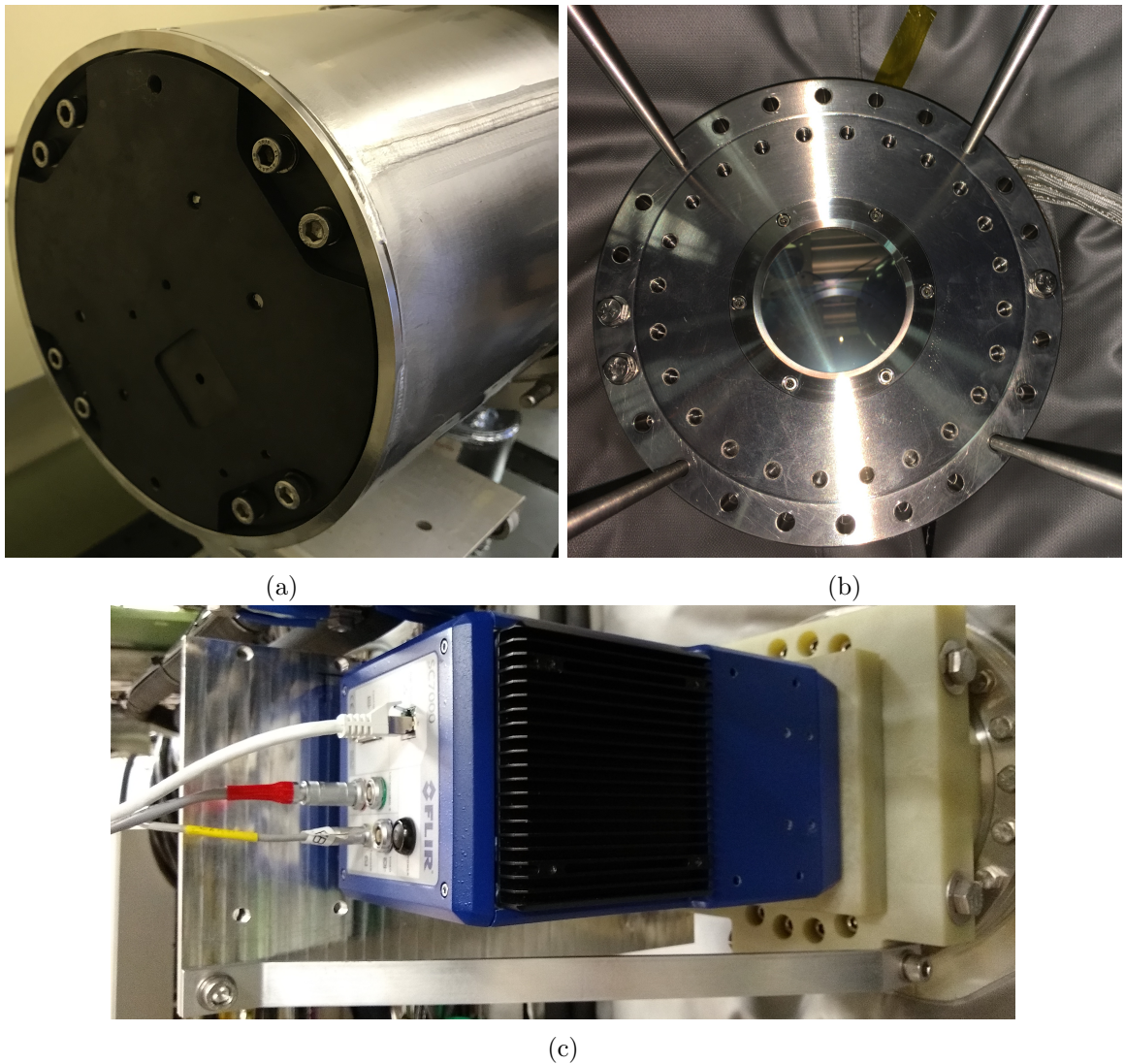


Figure 2.4: IRVB components overview: (a) photograph of the exterior of the foil assembly inside the tube, (b) the view port side of the tube installed in MAST-U and (c) the camera installed on the flange respectively. Photographs taken 2018/07/23, 2018/12/03, 2021/05/14 respectively. To change pinhole size and foil pinhole distance the tube must be removed while the camera is always accessible.

With a 75cm stand-off both a smaller fraction of the SXD chamber and of the outer leg in the tangential view (right side of the foil) would be out the FOV. Pinhole diameters of 6 and 8mm return a much larger signal than the desired minimum of $100W/m^2$. In [Figure 2.6](#) it is illustrated how, with a smaller pinhole, the signal level is lower but it is easier to identify close but distinct structures in the radiation distribution, even from the poloidal view alone (left side of the foil). For closer radiating structures it would be easier to distinguish them as separate in the tangential view with a smaller rather than large pinhole. For these reasons,

the configuration that includes in the FOV the features of interest and allows for the highest spatial resolution, while maintaining a sufficiently high SNR, is a stand-off of 60cm and pinhole diameter of 4mm. This equates to a minimum angle between the LOSs of adjacent infrared camera pixels of ~ 0.36 deg and an approximate solid angle per pixel of 3.5msr .

The power distribution on the foil was also simulated in the case of the entire plasma volume filled with a $50\text{kW}/\text{m}^3$ homogeneous emitter to establish the foil "wetted area", see [Figure 2.7](#). The bottom left region of [Figure 2.7a](#) is where no radiation can arrive. This was helpful for the prototype phase, because that area could be used as a reference where the power is zero. For this reason it has been decided to adopt a stand-off between pinhole and foil distance of 45mm for MU01, which covers the results shown in this work. This also returns an even larger radiation from the X-point. The MAST-U IRVB diagnostic has been returned to operation on MAST-U for the second campaign (MU02) with the optimal 60cm stand-off after re-evaluating the noise levels and the spatial resolution achievable (see [Chapter 3](#)).

An approximate view inside MAST-U, imagining that the IRVB operates as a camera to show the features and obstructions, is shown in [Figure 2.8](#). The view of the plasma is mainly poloidal on the left side of the central column, but the field of view is large enough to see both sides of the central column.

[Figure 2.9](#) displays the overlap between the coverage and views of the resistive bolometry system and that of the IRVB. The core resistive bolometer LOSs are mostly suited to measure the fairly homogeneous core emissivity profiles on a flux surface, as there is no overlap between the various LOS. The super-x chamber has a good coverage, but only between the strike point and the entrance to the divertor defined by the baffle. The IRVB is aimed to fill the gap between the two systems. It must be noted that the resistive bolometer sensor is not carbon coated, meaning it has a lower sensitivity to lower energy photons. [97] In detached conditions this was assessed to cause a reduction of the brightness of $\sim 15\%$. [105]

The assembly holding the foil is composed by a $2.5\mu\text{m}$ thick platinum foil from Nilaco, Japan, held between oxygen free copper plates and was originally prepared by NIFS. The foil is the same as that used in Alcator C-mod [84] where it is described in more detail. The foil thickness is optimised to stop photons with energies up to 8.2keV [92,98], higher than the few keV expected in MAST-U. The foil and its support frame have been spray blackened on both sides with Aerodag® G Graphite Aerosol and calibrated with a procedure analogous to the

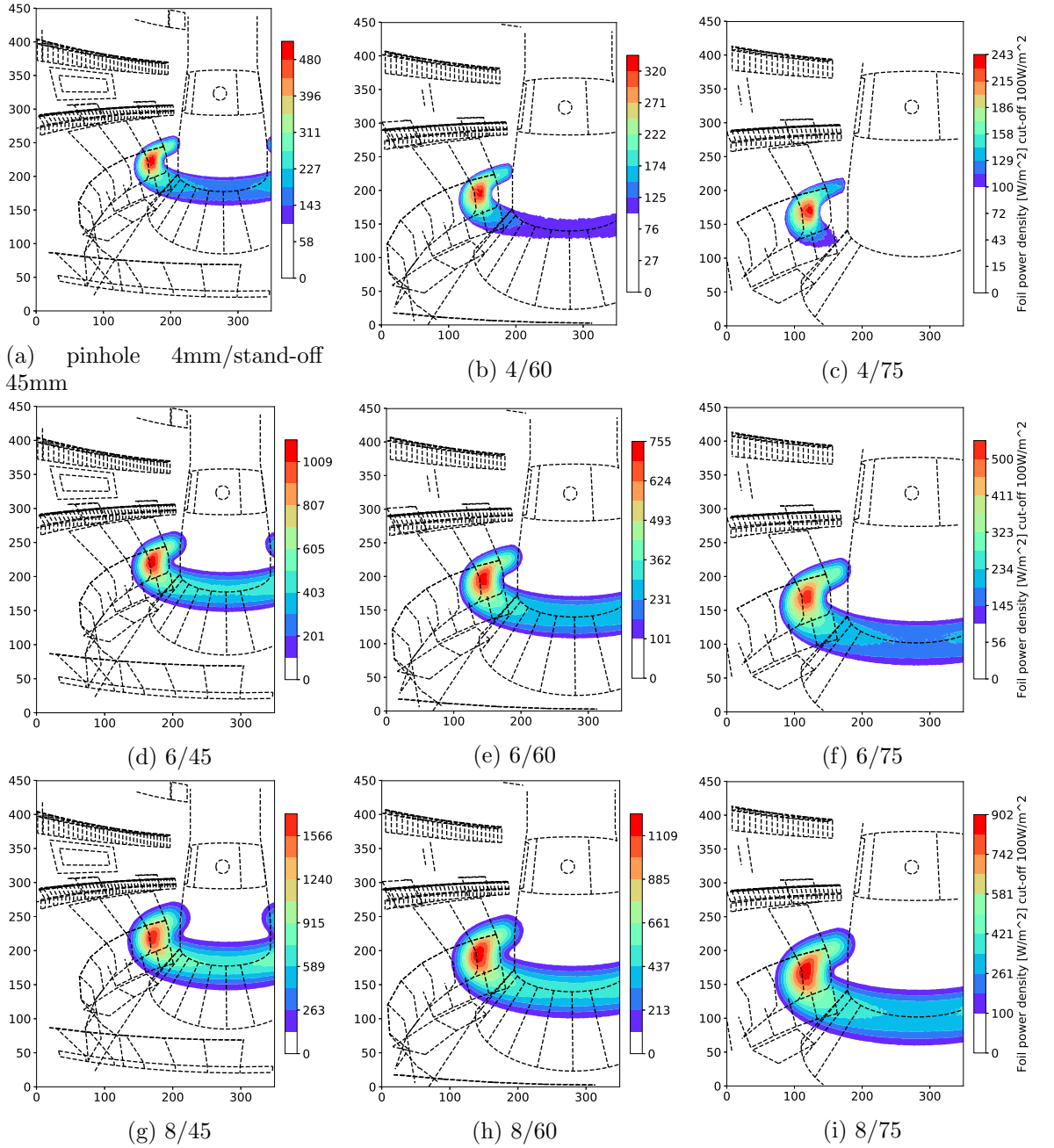


Figure 2.5: Radiated power deposited on foil, modelled with CHERAB, from a homogeneous toroidal emitter of radius 8cm located at $R=0.55\text{m}$ and $Z=-1.2\text{m}$, emitting a total of 0.5MW (equivalent to $\sim 7.2\text{kW}/\text{m}^3$) for the combinations of pinhole diameter and stand-off length considered. The power deposited on the foil below $100\text{W}/\text{m}^2$ is not shown, as that is the minimum desired signal level. In black are overlaid the projection of relevant features of MAST-U structure on the foil for reference.

one described in [106]. The layer of graphite helps to absorb radiation in the visible range, preventing reflection becoming significant for photon energies below $\sim 40\text{eV}$ [98]; even if its thickness is larger than the platinum layer [95] it should be thermally irrelevant. [97] Lower

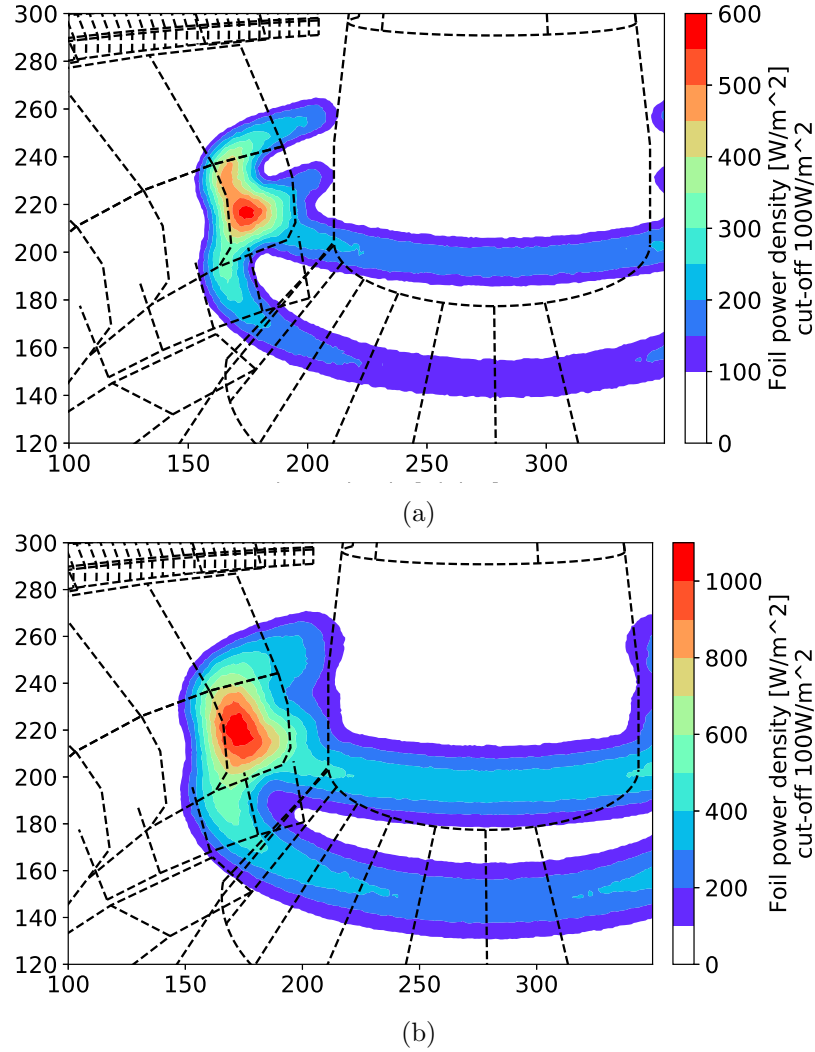


Figure 2.6: Radiated power deposited on foil, modelled with CHERAB, of two tori of 4 cm minor radius separated by 16cm in vertical position with uniform emissivity such as to total 0.5MW of radiated power, located at the expected x-point location. The pinhole size was varied from 4mm (a) to 6mm (b) to illustrate the loss of spatial resolution. The power deposited on the foil below $100\text{W}/\text{m}^2$ is not shown, as that is the minimum desired signal level. Only the relevant section of the foil is shown. In black are overlaid the projection of relevant features of MAST-U structure on the foil for reference.

energy photons like visible light represent a minor energy loss channel, but their relevance is expected to increase in deeply detached and cold plasmas, therefore the importance of the coating. [107] In [99] it is shown that this type of coating causes irregularities in the foil, leading to non uniform temperature increases. To alleviate this issue, the carbon layer can be deposited with a vacuum evaporation technique that guarantees reproducibility and uniformity, as done at LHD. [99] Given the prototype nature of the present implementation and the availability of a vacuum compatible certified absorber, this spray-blackened foil was

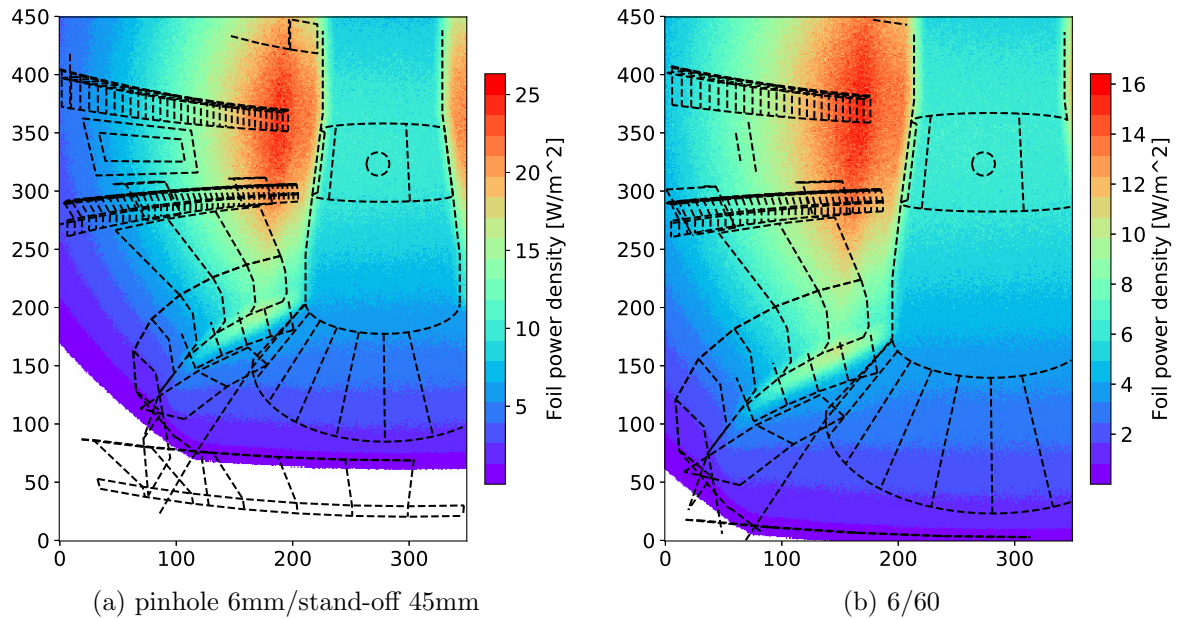


Figure 2.7: Radiated power deposited on foil, modelled with CHERAB, with a 4mm diameter pinhole and (a) 45mm and (b) stand-off between pinhole and foil, for the case of the core and divertor regions emitting homogeneously at a level of $50kW/m^3$. The white regions do not receive any radiation from the plasma, in black are overlaid the projection of relevant features of MAST-U structure on the foil for reference.

deemed sufficient.

To guarantee consistency in the positioning and orientation of the foil with respect to the pinhole, a series of markings were inscribed by NIFS on the copper plates as shown in [Figure 2.10](#). The yellow numerical markings are also used to define the thermal calibration supplied with the foil. The compatibility of the assembly with the thermal expansion caused by the MAST-U VV bake was studied. The bake causes the VV and internal components to reach $\sim 110^\circ C$ and 120 to $200^\circ C$ respectively, likely causing the absorber assembly to reach an intermediate temperature. The thermal expansion coefficients for Cu and Pt are $16\mu m/mK$ (similar to steel) and $9\mu m/mK$ respectively. This could have led to stress and thus tearing of the foil, but confidence was gained with the pressure test mentioned in [Section 2.3](#) on the mechanical resilience of the foil. Another item of concern related to the bake is the stability of the carbon coating on the absorber foil. The technical datasheet for Aerodag® G used for coating, indicates that it can be used as lubricant up to $200^\circ C$. Considering the possible failure modes, any piece of carbon detaching from the absorber assembly was expected to stay within the tube, posing no risk for MAST-U operations. The IRVB has ultimately undergone the entire bake cycle prior to MU01 and after inspection did

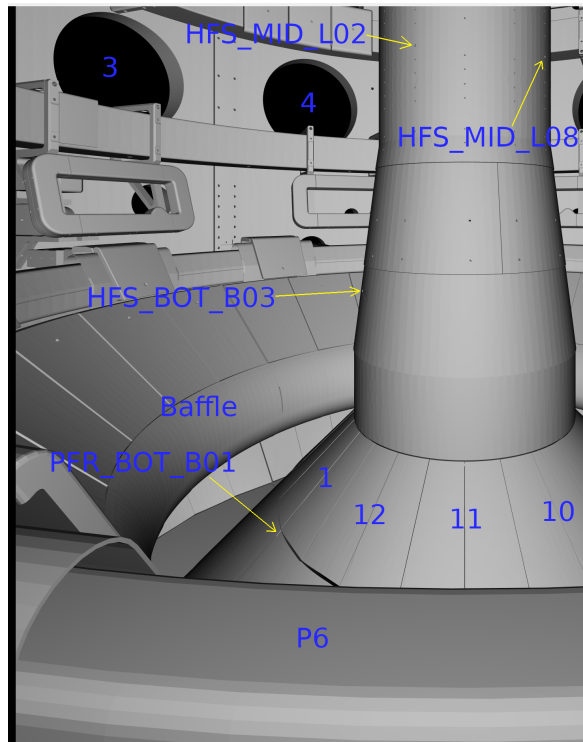


Figure 2.8: Approximate view inside MAST-U as if the IRVB operates as a camera. Blue labelling is used to highlight the various sectors and the fuelling locations in the IRVB field of view (FOV). At the bottom of the image is the coil P6 obstructing the field of view.

not seem to suffer any damage.

The tube where the foil is installed extends from the vacuum chamber wall to a position close to the plasma, but still safely outside the SOL and potential particle and power loads. The camera images the absorber foil through a 10mm thick ZnS view port from Crystran with $4 - 5\mu\text{m}$ and $8 - 10\mu\text{m}$ anti reflection coating on both sides and is bolted to the tube. The orientation of the view port with respect to the camera, even if it should not matter substantially, was maintained throughout the test and assembly phases for consistency. The view port assembly was leak checked before final installation with the setup in [Figure 2.16](#). The camera, a FLIR SC7500 with InSb detector array, is equipped with a $4 - 5\mu\text{m}$ pass band filter and has a spectral range of $1.5 - 5.1\mu\text{m}$. This model was selected so that the same could be adopted for other diagnostics in MAST-U and the same acquisition software could potentially be developed. This is inconvenient for the IRVB, as the optimal wavelength for a black body radiator around room temperature is around $10 - 14\mu\text{m}$. Considering that the volume between foil and camera is fully enclosed in the IRVB tube and that the temperature of the entire assembly does not deviate appreciably from room temperature during the short

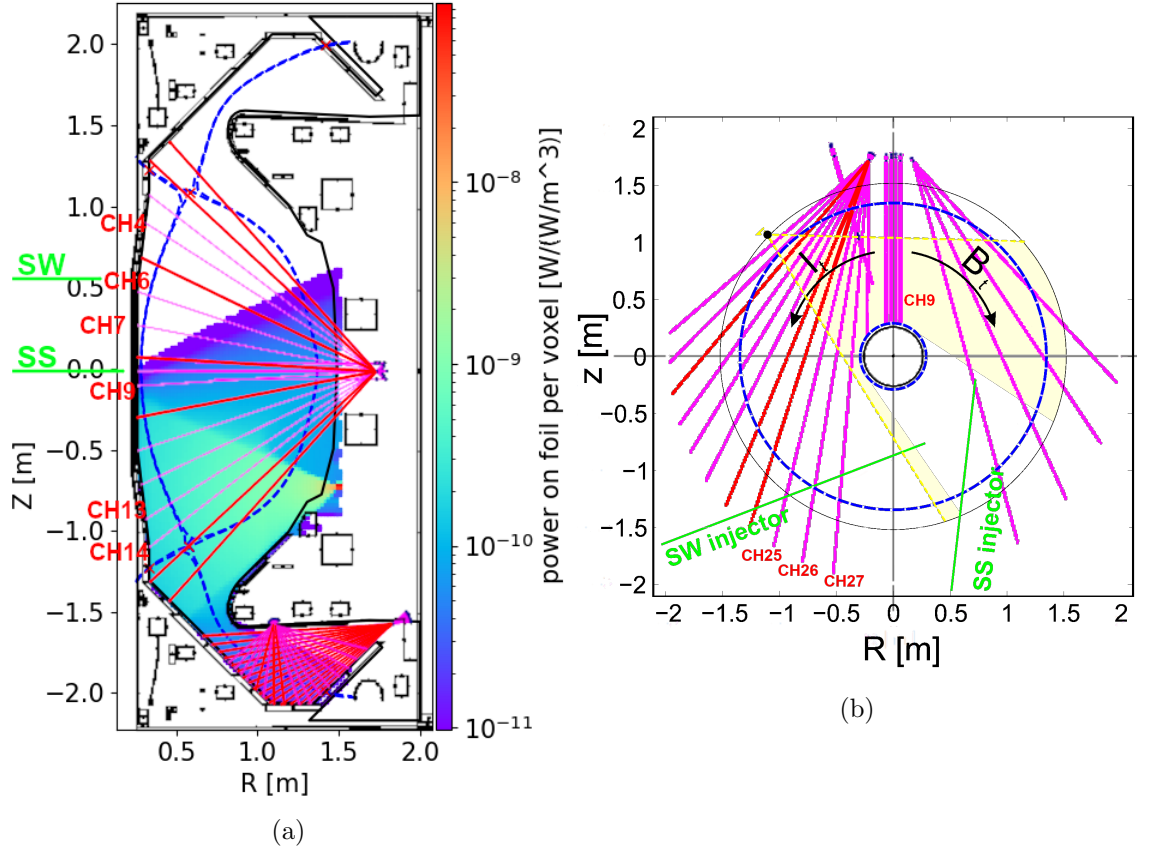


Figure 2.9: (a) Poloidal view of MAST-U showing the comparison of the resistive bolometer system LOS (magenta) with a colour plot obtained by scanning all the voxels with a $1W/m^3$ emitter and integrating the power absorbed by the foil, indicating the regions of higher sensitivity of the IRVB. (b) Top view of MAST-U showing the position of neutral beam injectors (NBI, green), of the co- and counter-NBI resistive bolometer LOSs and the IRVB FOV (yellow, mostly counter-NBI). Adapted from [15]. For reference the separatrix of a typical plasma is shown as an overlay of a blue dashed line. The resistive bolometer LOSs that will be used in the later analysis are here identified. The LOSs not operational in MU01 are red rather than magenta. The location of CH9 in b indicates where the entire core poloidal fan is located.

duration of the pulse, the use of the filter would not have prevented any stray light to effect the measurements. For this reason the camera was used without the internal filter, increasing the signal. At the maximum frame rate at full frame (383Hz) and 2ms integration time a signal around 11000 counts is measured at around room temperature (see Figure 2.14) with saturation at $2^{14} = 16384$ counts and a noise floor ~ 5 counts (noise equivalent temperature difference, NETD, $\sim 15mK$). During testing a design flaw of the present IRVB design was discovered. It became clear that, even with the presence of the anti reflection coating, the view port caused the so-called "narcissus effect". This happens when the camera can see its

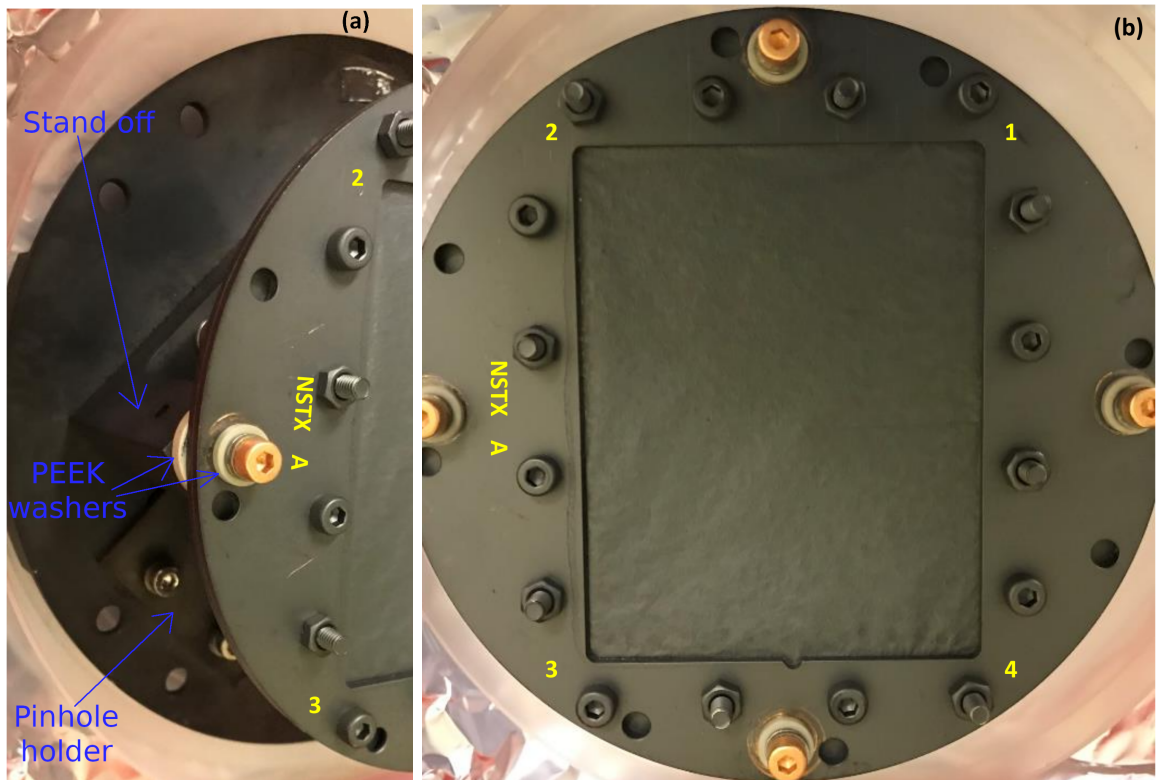


Figure 2.10: Photographs of the foil in relation of the pinhole (a) and of all the identifying markings (b), taken 23/07/2018.

own reflection on the view port, hence "narcissus". The view is orthogonal to the camera FOV, so at its centre is the image of the reflection of the sensor array. The detector array is cooled to about -203°C , while around it the body of the camera is slightly above room temperature. This causes a "dark spot" to appear at the centre of the image. The main difficulty in dealing with the effect arises from the inability to perfectly match the orientation of the view port during calibration and on the machine. Ultimately this systematic error, if stable intra-shot, does not effect the temporal and spatial temperature derivatives on which the analysis primarily relies. In future iterations of the diagnostic, the view port should be angled with respect to the camera so as to reflect light from an area with a more homogeneous temperature and emissivity.

The camera is bolted to aluminium plates cantilevered off an insulating G-10 piece that is connected directly to the vacuum vessel flange (to stop induced current loops) as shown in [Figure 2.4](#). The aluminium plates holding the camera have multiple holes so that the camera can be located at 4 fixed distances from the view port (8.7, 11.2, 13.7, 16.2cm), with the

closest being the one with the foil in focus. The ability to vary the camera location allowed us to progressively test the compatibility of the camera with magnetic field. That data was collected during the commissioning phase of the MAST-U magnets while the camera was first as far as possible from the VV. Once the maximum field was reached the camera was then progressively moved towards its final position whilst checking that no anomalies in its operation arose. The camera operated normally at all distances, making a magnetic shield around it unnecessary.

The IRVB tube was installed on MAST-U in November 2018 while all parts outside the vacuum vessel by early 2021. The calibration of the system was performed in 2018.

2.4 System calibration

Before scientific utilization, the IRVB diagnostic has to be properly calibrated. This includes the temperature response of the IR camera, the thermal response of the foil and spatial alignment of the pinhole and camera. Laboratory tests can be performed for the first two calibrations, while the third was verified during operation, using observed features inside the tokamak.

2.4.1 Counts to temperature model

The temperature calibration is the procedure used to convert the camera raw data from counts to temperature. It involves defining the mathematical model for the conversion and finding the coefficients required. Once defined it can be applied to MAST-U data to obtain the IRVB foil temperature. The surface of the foil is approximated as a black body emitter. The total number of photons emitted by a unitary BB source Φ_p within the camera integration time can be modelled as per [Equation 2.1](#)

$$\Phi_p(T) = \epsilon i \int_{\lambda_1}^{\lambda_2} \frac{2\pi c}{\lambda^4} \frac{1}{e^{\frac{hc}{\lambda kT}} - 1} d\lambda \quad (2.1)$$

where ϵ is the emissivity, i the integration time, λ the wavelength, $\lambda_1 - \lambda_2$ the wavelength range allowed by the camera or filter and T the surface temperature. To simplify the calculations the interpolators α and α_r are built to encapsulate the non linearity between temperature and photon flux, using [Equation 2.1](#), such that:

$$\frac{\Phi_p(T)}{T} = \alpha(T), T = \alpha_r(\Phi_p) \quad (2.2)$$

The number of photons reaching the camera is proportional to the number of photons emitted from the absorber foil (a_1), with an additional offset due to thermal photons originating from the view port and the air between sample and camera as well as their reflections (a_2). This offset will be approximately constant because it will not depend on the surface temperature observed by the camera. Assuming that the number of counts is proportional to the number of photons, and that this does not depend on the photon wavelength, the number of camera counts can be expressed as:

$$C = a_1 \cdot \Phi_p(T) + a_2 \quad (2.3)$$

where $a_1 \in [0, \infty]$ and $a_2 \in [-\infty, \infty]$ the proportional and constant components. Once a_1 is determined the temperature is calculated as:

$$T = \alpha_r(\Phi_p(T)) = \alpha_r\left(\frac{C - a_2}{a_1}\right) = \alpha_r\left(\frac{C - C_0}{a_1} + \Phi_p(T_0)\right) \quad (2.4)$$

T_0 and C_0 are the temperature and counts relative to the initial conditions at the beginning of the shot (approximated with the vacuum vessel temperature). The power absorbed by the IRVB foil is obtained using the temperature increase over the profile before the pulse so the constant offset from the calibration will not impact the results.

2.4.2 Temperature calibration

Given that the IRVB relies on measuring small temperature differentials with high precision it was necessary to calibrate all camera pixels independently. Given a black body source that could encompass the entire field of view with the image in focus was not available, the method employed was similar to the one by Reinke. [84]: A Sofradir non-uniformity correction (NUC) plate, built such that it emits black body radiation uniformly with an emissivity close to 1, was used. The plate was then heated in an oven to $\sim 70^\circ C$, then left to cool to room temperature while taking samples with the IR camera. Similarly, the plate was also cooled below room temperature and observed while heating up. The temperature of the plate was monitored with a thermocouple. For consistency, two cooling and heating temperature ramps were performed and the data fitted with the model in [Section 2.4.1](#).

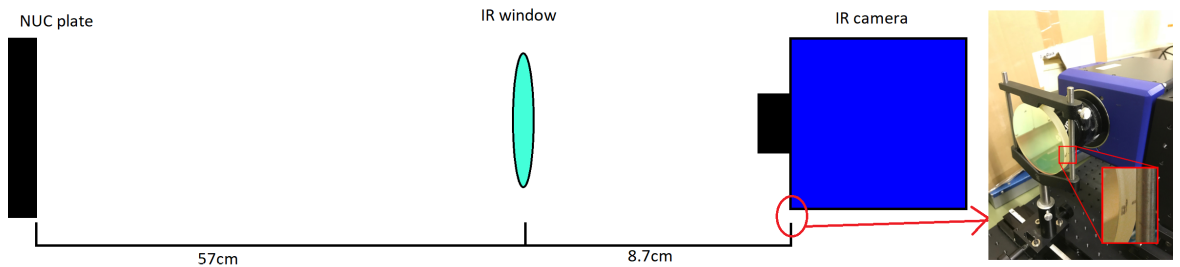


Figure 2.11: Schematic of the calibration setup. The NUC plate and the IR window are located at the same distance from the camera as when installed and as per design. Effort is made to keep the window with the same rotational orientation. See the marking for the view port alignment in the detail.

The infrared camera is equipped with two distinct digitizers therefore the calibration will be operated independently for each. This means that the two digitizers behave as two distinct instruments; the power absorbed by the foil will be calculated independently for each and then averaged, causing a reduction of the maximum (full frame) frame rate from 383 to 192Hz.

The geometry of the calibration is represented in [Figure 2.11](#). The relative distances are the same as when the camera is installed. The rotational orientation of the view port was maintained during calibration and on the machine thanks to markings on the side of the window. During testing the narcissus effect was clearly observed.

[Figure 2.12](#) displays the qualitative effect of the presence of the view port. [Figure 2.12a](#) shows the typical view when the camera images the NUC plate; vignetting due to the camera lenses is apparent. [Figure 2.12b](#) shows the effect of the window reflections. In [Figure 2.12c](#) the effect on the foil image is shown. The dark spot caused by the narcissus is at the centre of the image, decreasing the counts by ~ 200 counts at an integration time of $2ms$. This should be a systematic error and, therefore, should mostly impact the a_2 coefficient that ultimately doesn't impact the temperature measurement. During the temperature ramps it was observed that the NUC plate, albeit having a uniform emissivity, shows a non uniform temperature across the FOV due to heat transfer. The plate is naturally cooled/heated via conduction, convection and black body radiation. Air flows around the plate and can lead to uneven heat transport.

The temperature non uniformity across the image was estimated for different temperature ramps as shown in [Figure 2.13b](#) and it was found to be at most $0.3^\circ C$ on average in the temperature range of interest. As shown in [Figure 2.13a](#) the spatial variation of temperature

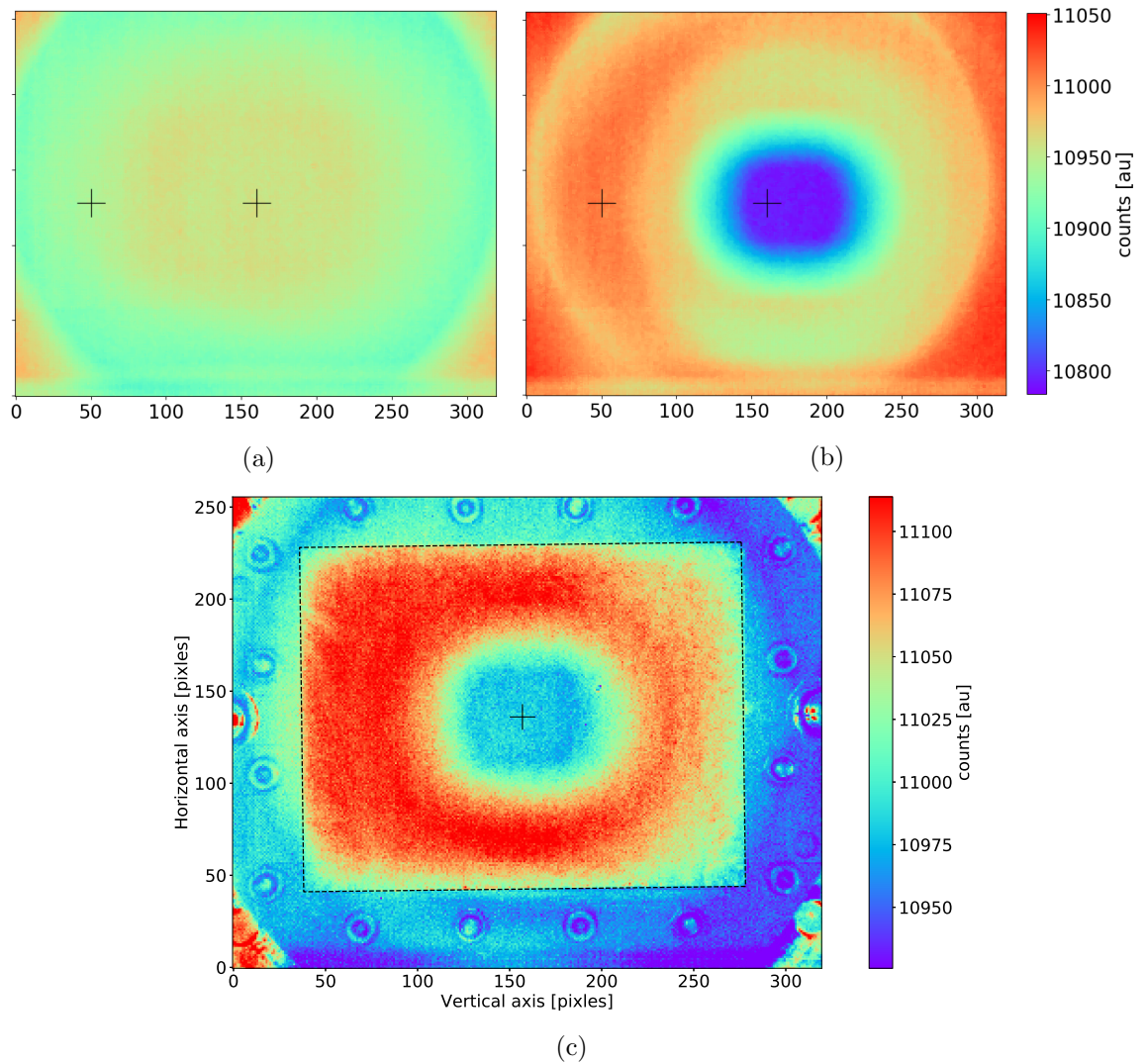
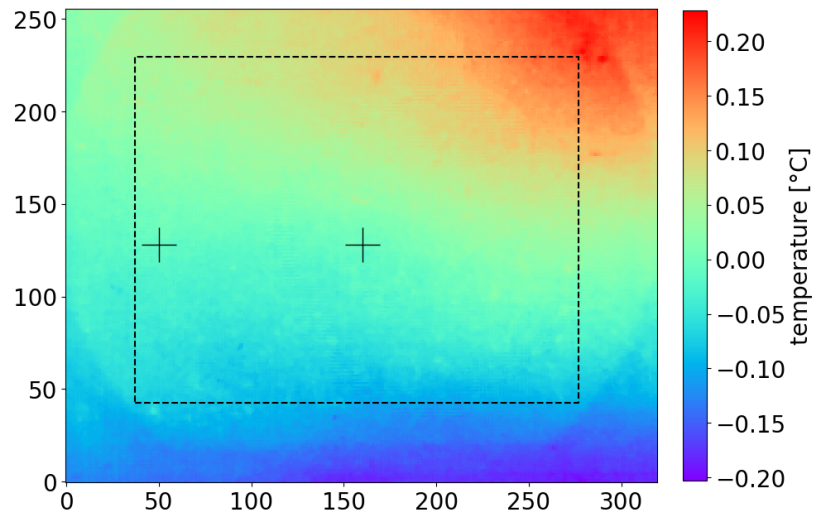
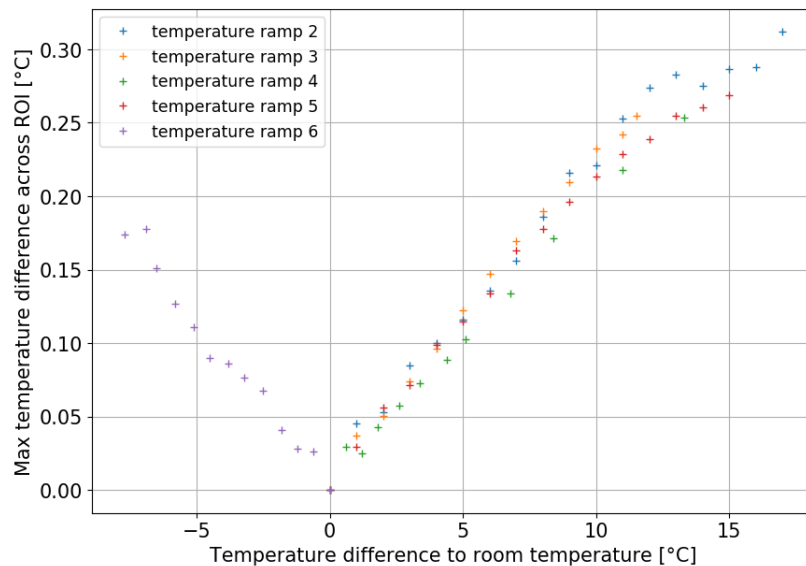


Figure 2.12: Example of non uniformity of the counts of the IR camera when aimed at the NUC plate at room temperature. Shown are the images without the view port (a) and with (b). The same scale is applied to both plots and there was a 2ms integration time. The black cross indicates two reference points (inside/outside the narcissus) that will be used in later analysis. c shows the position of the foil (the red square) inside the camera field of view. Around the foil are the bolts that lock the foil in between the two copper plates, that can be used to identify the foil orientation.

is very slow, with a very minor impact on the spatial and temporal derivative. The effect of the location where the thermocouple is connected to the NUC plate was also investigated by moving it to different corners of the plate. The spread of the temperature around a curve that fits average camera counts and temperature for all the probe positions with the model in Section 2.4.1 is about 0.25°C . There was, though, no pattern found so the difference is most likely due to the connection of the sensor to the plate rather than the actual temperature of



(a)



(b)

Figure 2.13: (a) Shown are the IR camera counts at 41.9°C minus the counts at room temperature, scaled up such that the average across the foil is the same as at high temperature. In black is highlighted the region corresponding approximately to the IRVB foil and the two reference points defined in Figure 2.12. The vertical orientation is here bottom to top, with the top of the image being up. (b) Peak temperature difference between the temperature deriving from the counts at high temperature and the counts at room temperature scaled up as previously mentioned.

the plate.

The result of the scan for the two pixels identified in Figure 2.12, one close to the centre of the narcissus effect and one on its side, are shown in Figure 2.14. Equation 2.3 can reproduce the measurements with high accuracy. As expected the presence of the narcissus

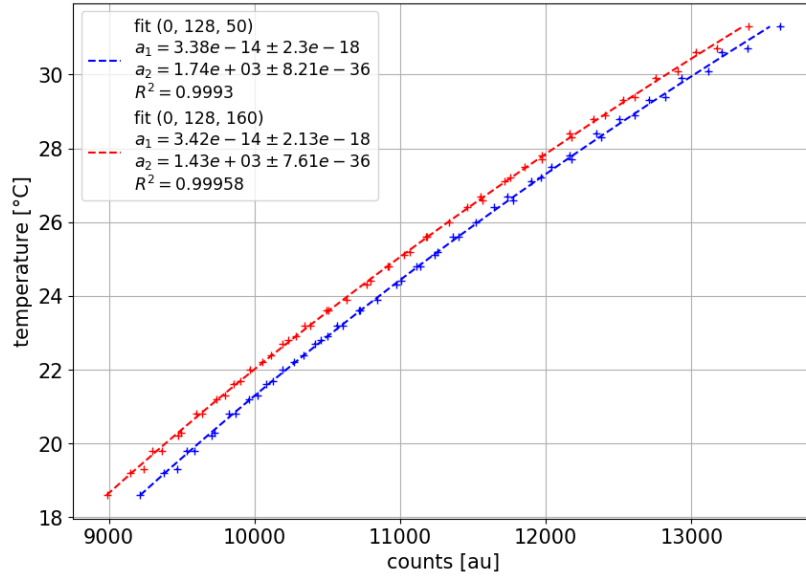


Figure 2.14: Comparison of the temperature calibration curves for a pixel at the centre of the narcissus (red) with one on its side (blue). The legend gives the fit parameters (a_1 proportional and a_2 additive components), their uncertainties, and the coefficient of determination of the fit.

mostly affects the a_2 offset.

The results of the calibration for the entire foil are shown in [Figure 2.15](#). Both coefficients are affected by vignetting and the narcissus effect. It is noteworthy that the ~ 200 counts at the centre of the narcissus are assigned entirely to the constant parameter, as one would expect for a systematic error. Some of the variation in a_1 , especially the red ring around the centre, could be related to the narcissus, meaning that its effect is not completely independent of temperature. The variation in a_1 is very small, however, only $\sim 2\%$ and changes fairly slowly across the FOV, resulting in a small impact on the spatial and temporal temperature derivatives. Both coefficients seem to have a general dependency on the vertical direction (right to left in the figure), possibly due to the slight non-uniformity of the temperature of the NUC plate. The measured difference in fit coefficients between digitizers is small, $< 0.2\%$ and $< 0.5\%$ for a_1 and a_2 respectively, with no particular structure.

For future calibrations, a large flat black body calibration source with the capability to cool below and heat above room temperature could be used to further reduce the uncertainties in the NUC plate temperature.

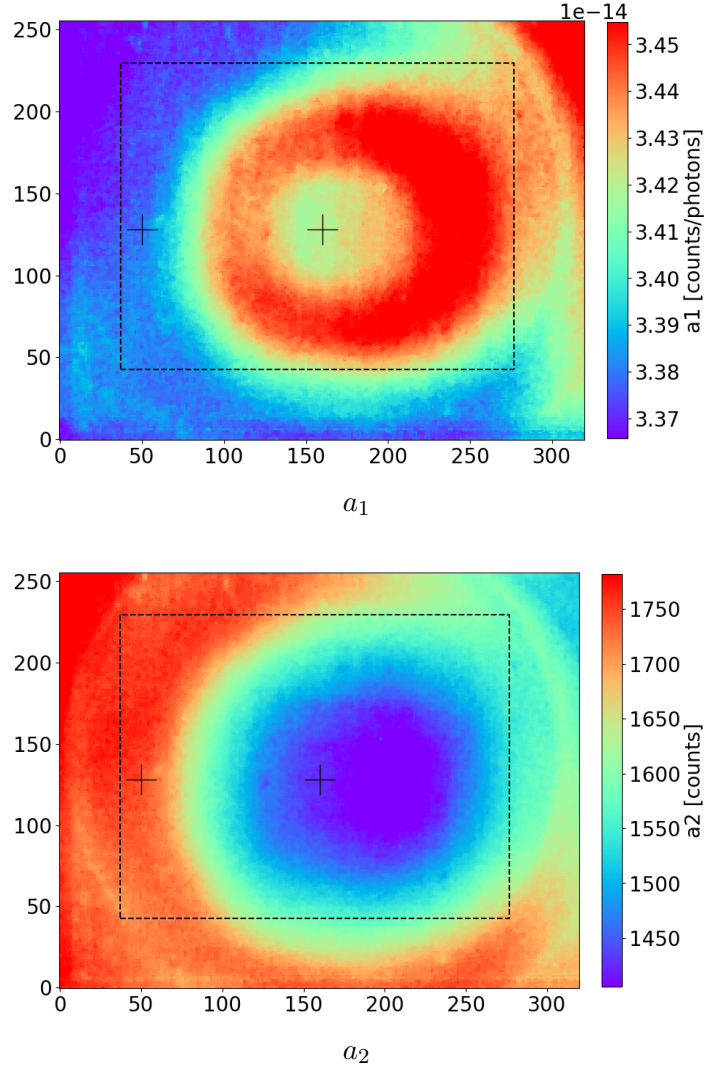


Figure 2.15: a_1 and a_2 coefficients of Equation 2.3 obtained via calibration with the NUC plate. In black is highlighted the region corresponding approximately to the IRVB foil and the two reference points defined in Figure 2.12. The vertical orientation during this calibration is right to left, with the top on the left.

2.4.3 Foil model

The foil thermal response is dictated by heat transport: the source is the radiated power from the plasma reaching the foil (P_{foil}) while the local sinks are its black body radiation (P_{BB}), conduction ($P_{\Delta T}$) and temperature variation ($P_{\frac{\partial T}{\partial t}}$). The foil is very thin and therefore 2D heat transport can safely be considered instead of 3D. Equation 2.5 shows how to calculate the power absorbed by the foil based on its temperature.

$$\begin{aligned}
P_{foil} &= P_{\frac{\partial T}{\partial t}} + P_{\Delta T} + P_{BB} \\
P_{\frac{\partial T}{\partial t}} &= \frac{k t_f}{\kappa} \frac{dT}{dt} \\
P_{\Delta T} &= -k t_f \left(\frac{\partial^2 T}{\partial x^2} + \frac{\partial^2 T}{\partial y^2} \right) \approx -k t_f L \cdot T \\
P_{BB} &= 2 \varepsilon \sigma_{SB} (T^4 - T_0^4)
\end{aligned} \tag{2.5}$$

where k is the thermal conductivity, t_f the thickness, κ the thermal diffusivity, ε the black body emissivity and σ_{SB} the Stefan-Boltzmann constant. L is the matrix containing the coefficients to build the temperature Laplacian via the dot product. It is built such that its dot product with the temperature returns the sum of the second order central finite difference in all directions. In the Laplacian matrix the elements corresponding to the derivative in the diagonal direction are divided by 2, to account for the increase in distance.

Assuming $\alpha(T)$ (from [Equation 2.2](#)) to be slowly varying the uncertainty in the temporal variation, diffusion and radiation terms of the heat equation can be calculated with [Equations 2.6, 2.7 and 2.8](#) respectively for the pixel i :

$$\sigma_{\frac{\partial T}{\partial t}} = \frac{k t_f}{\kappa dt} \sqrt{\left(\frac{\sigma_{C_{i+1}}}{a_1 \alpha(T_{i+1})} \right)^2 + \left(\frac{\sigma_{C_{i-1}}}{a_1 \alpha(T_{i-1})} \right)^2 + \left[(T_{i+1} - T_{i-1}) \frac{\sigma_{a_1}}{a_1} \right]^2} \tag{2.6}$$

$$\sigma_{\Delta T} = \frac{k t_f}{dx^2} \sqrt{L^2 \cdot \left[\left(\frac{\sigma_{C_i}}{a_1 \alpha(T_i)} \right)^2 + \left(\frac{\sigma_{C_0}}{a_1 \alpha(T_0)} \right)^2 + \left((T_i - T_0) \frac{\sigma_{a_1}}{a_1} \right)^2 \right]} \tag{2.7}$$

$$\sigma_{T_i} = \frac{1}{\alpha(T_i)} \sqrt{\frac{(\sigma_{C_i}^2 + \sigma_{C_0}^2)}{a_1^2} + \left[\left(\frac{C_i - C_0}{a_1} \right) \frac{\sigma_{a_1}}{a_1} \right]^2 + (\alpha(T_i) \sigma_{T_0})^2} \tag{2.8}$$

$$\sigma_{BB} = 4 \varepsilon \sigma_{SB} \sqrt{(T_i^3 \sigma_{T_i})^2 + (T_0^3 \sigma_{T_0})^2}$$

2.4.4 Foil calibration

In this section the calibration procedure followed to obtain the foil properties will be detailed. To calibrate the foil its thickness t_f , thermal κ diffusivity and black body emissivity ε must be determined (assuming nominal Platinum thermal conductivity $k = 71.6W/mK$). A set of spatially resolved parameters was supplied together with the foil of which the average and variability across the foil corresponds to $\varepsilon = 0.85 \pm 0.04$, $t_f = 1.29 \pm 0.17 \mu m$. Nominal platinum thermal diffusivity is assumed $\kappa = 2.5 \cdot 10^{-5} m^2/s$. These values were obtained with a single exposure of a laser of known power, pulse and and spatial shape by monitoring the

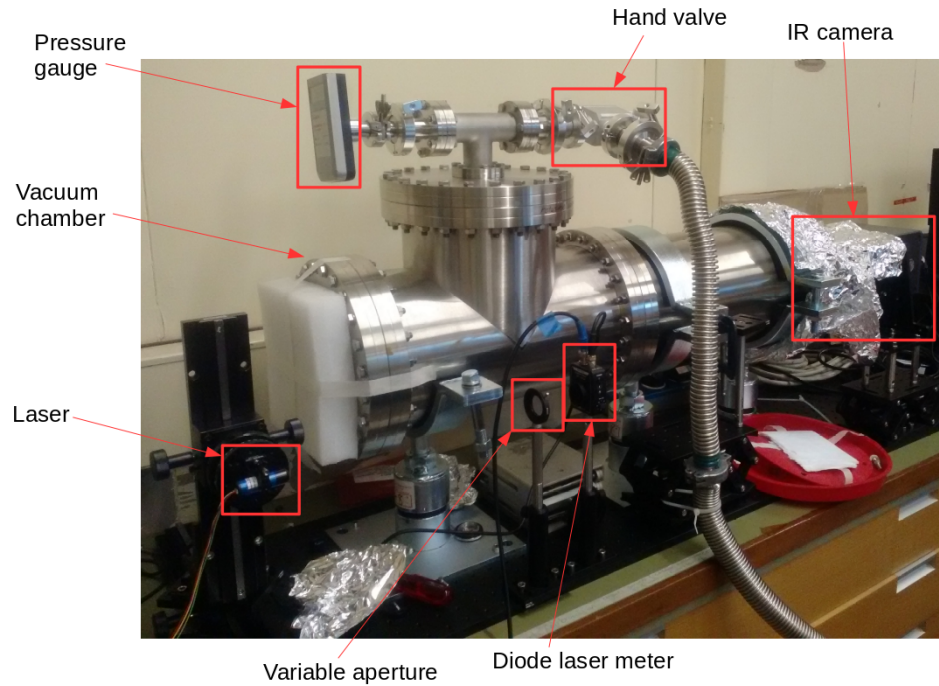
cooling down phase of the foil in vacuum as described in [106]. There are different ways to find the foil parameters, all reliant on shining a laser on the foil (see references [106,108,109]).

Rather than using a single laser exposure, the method of choice relied upon varying the laser intensity, frequency and focus as done by Reinke. [84] With slow pulses, the time variation component tends to become irrelevant such that only black body radiation and diffusion remain. With a defocused laser (low laser power density), the temperature increase is low and the spatial distribution slowly varying, increasing the relevance of the black body radiation. With a fast pulsed laser the time dependent component is dominant.

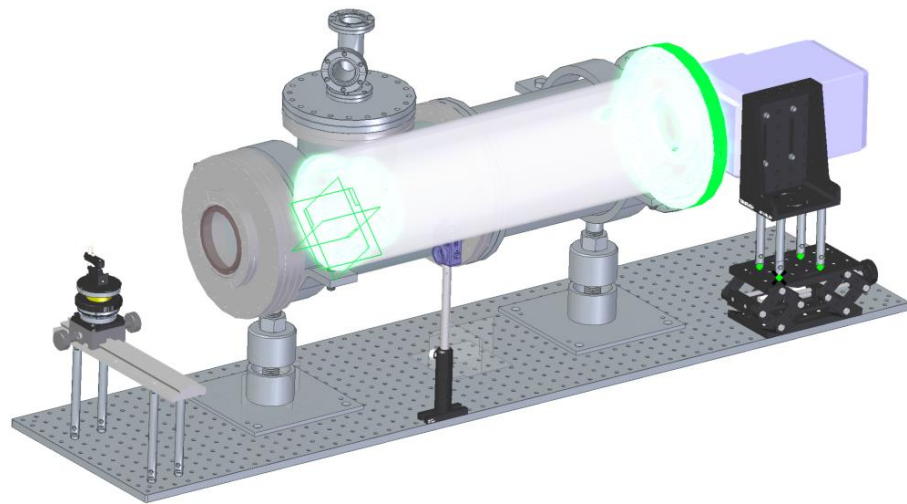
A bench top vacuum system was built for the foil calibration, shown in Figure 2.16. The vacuum is necessary to eliminate convection as a heat loss mechanism, as it is also absent during the experiments. The pressure during calibration was $\sim 3 \cdot 10^{-5} \text{bar}$, compared to $\sim 10^{-8} \text{bar}$ during MAST-U experiments. A 5mW, 655nm BlueLyte laser was used, capable of gradually reducing the total power output to zero and with a maximum modulation up to 750kHz. The laser was equipped with an adjustable lens to change the focus. The laser was calibrated with a Thorlabs PDA100A2 diode in combination with a variable aperture. The maximum laser intensity was measured to be about $1200 \text{W}/\text{m}^2$ and $50 \text{W}/\text{m}^2$ when focused and defocused respectively, with a maximum total power of 4.16mW. The laser was controlled with a square wave function generator so that the laser output was modulated in intensity, frequency and focus. The transmission of the vacuum window on the laser side was measured at 93.3% and taken into account. The power delivered to the foil integrated over the pinhole area, P , can be determined with Equation 2.5. To find the foil thermal properties, the running average of P is computed, averaging over the duration of half the square wave duration. The peaks P_h and troughs P_l of the running average are compared to the input values P_{in} .

A scan in laser power from 0 to 100% and frequency from 0.2 to 90Hz with the laser fully focused and fully defocused was carried out in the location of the foil closer to the pinhole. The fit was done with data up to 10Hz returning the following fit parameters: $\epsilon = 1$, $t_f = 2.69 \mu\text{m}$, $\kappa = 1.35 \cdot 10^{-5} \text{m}^2/\text{s}$. The t_f/κ ratio is similar to foil properties measured prior to the installation on NSTX-U, differing significantly from the supplied one. [103] The difference in the t_f and κ values is likely due to the difference in emissivity inferred.

An example of the power calculated in the laser experiments is shown in Figure 2.17 while Figure 2.18 shows the quality of the fit for varying power and frequency and for



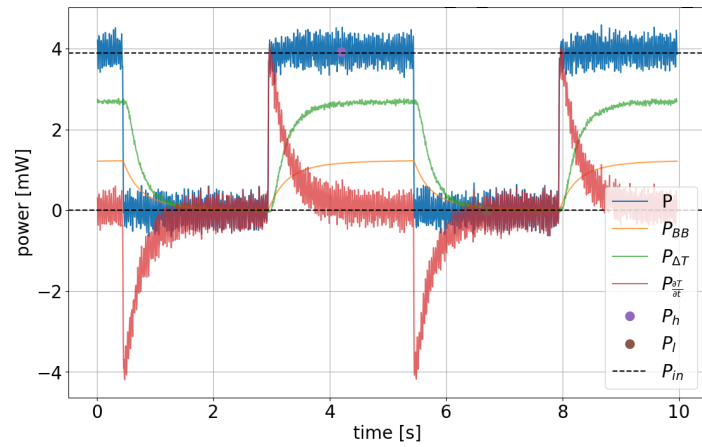
(a)



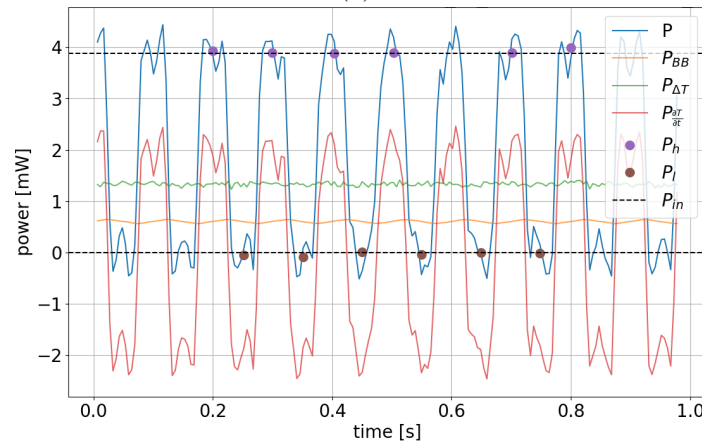
(b)

Figure 2.16: Photograph (a) and CAD model (b) of the bench-top setup used for the foil calibration. In the CAD model the re-entrant tube is shown in white and the foil assembly is on the left side. The photograph, taken on 02/08/2018, shows the laser used to illuminate the foil, as well as the diode and aperture used to calibrate the laser and vacuum system.

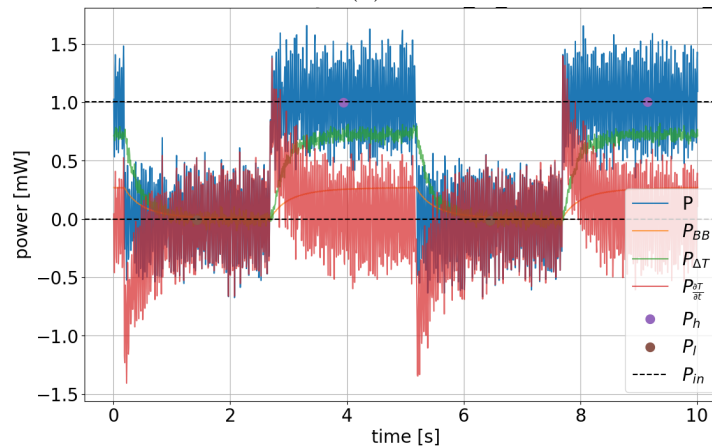
focused and defocused laser light. It can be observed that above 30Hz the inferred power drops, implying a limit in the temporal resolution of the IRVB. The data corresponding to the defocused laser degrades at lower frequencies, as the total delivered laser power is lower.



(a)



(b)



(c)

Figure 2.17: Examples of the power absorbed by the foil and its components (total absorbed power P and its components black body radiation P_{BB} , conduction $P_{\Delta T}$ and temperature variation $P_{\frac{\partial T}{\partial t}}$; peaks and troughs of P running average, P_h and P_l ; peak input power P_{in}) with the laser at maximum intensity for a focused low frequency case (a), a focused high frequency case (b) and a defocused low frequency one (c).

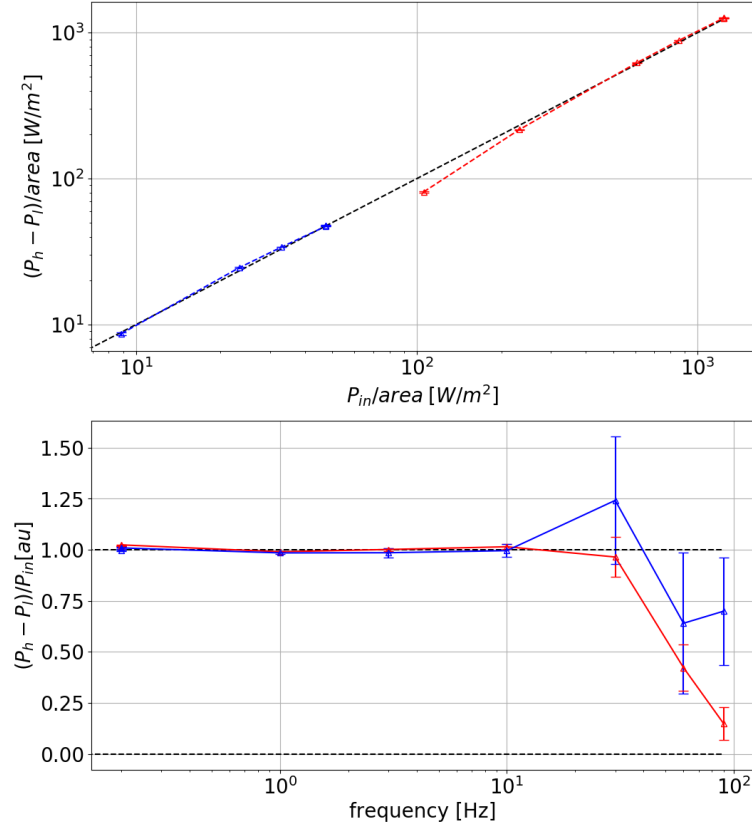


Figure 2.18: Variation of the measured power compared to the expected values with laser intensity (top) and frequency (bottom). The blue colour indicates the defocused cases while the red the focused ones. P_h and P_l are the inferred high and low power level of the laser square wave, $area$ is the area of the foil receiving laser light, P_{in} is the known peak laser power density.

During these experiments it was also observed that a fixed oscillation of $0.01K$ at about $29Hz$ is superimposed on the data so measurements at the same frequency or higher will be affected. The oscillation seems to be independent of the power supply system and the frame rate but proportional to the integration time, ultimately due to the internal operation of the camera.

These foil properties were measured in a single location and were therefore assumed uniform across the foil. To account for the variability across the foil the uncertainty from the fit is increased by the variability of the properties provided to us with the foil. This returns the uncertainties $\sigma_\epsilon/\epsilon = 8.61\%$, $\sigma_{t_f}/t_f = 13.6\%$, $\sigma_\kappa/\kappa = 13.9\%$ (for κ is used the same variability across the foil as for t_f).

2.4.5 Etendue

In order to convert the measurement from the power absorbed by the foil to the brightness at the pinhole, the geometrical configuration of the foil compared to the pinhole has to be considered. This is given by the etendue, that it is calculated here for the section of the foil corresponding to the (i, j) pixel of the IR camera with the simplified formulation in Equation 2.9 [110, 111]

$$U_{i,j} = \frac{A_{i,j} A_{pin} \cos(\psi) \cos(\phi)}{d_{i,j}^2} \quad (2.9)$$

Where $A_{i,j}$ is the area of the pixel, A_{pin} is the area of the pinhole, $d_{i,j}$ is the distance from the centre of the pinhole to the pixel and ψ and ϕ are the angle from the normal to the pinhole to the vector from pinhole to pixel and the angle from the normal to the pixel to the vector from pixel to pinhole respectively. $A_{i,j}$ is considered equal for all pixels (A_{pix}) and is given by the size of the foil as seen from the camera. As it can be seen in Figure 2.3 the foil is parallel to the aperture therefore $\cos(\psi) = \cos(\phi) = d_{fp}/d_{i,j}$ where d_{fp} is the minimum distance from the pinhole to the foil. Equation 2.9 reduces then to Equation 2.10.

$$U_{i,j} = \frac{A_{pix} A_{pin} d_{fp}^2}{d_{i,j}^4} \quad (2.10)$$

The brightness is then simply obtained with Equation 2.11.

$$B = P_{foil} \frac{4\pi}{U} \quad (2.11)$$

2.4.6 Viewing geometry validation

The viewing geometry of the diagnostic as designed in Section 2.3 has to be validated to make sure that each IRVB pixel FOV into the plasma is as expected. For diagnostics where a camera is directly imaging inside the vacuum vessel this is usually done by acquiring long exposure images and matching the observed features on the machine surface with features from CAD models. For bolometers this is not possible as the black body radiation of the vessel surfaces is many orders of magnitude below the detection limit, even when heated up by the plasma. For this reason this spatial calibration has to rely on laser light sources. The size and orientation of the LOS viewing cone is often measured in dedicated laboratory experiments and translated into machine coordinates using some reference point of the diag-

nostic assembly and the vessel. [112,113] If there is good access to the inside of the machine, a laser can be placed in fixed locations to measure the bounds of the light detection region of every LOS. [110] More recently, in the effort to develop the bolometer system for ITER, a robotic arm was developed on AUG which can probe the relation between the origin of the emission and sensor response by moving a laser to various positions in the field of view of the bolometer. [114] An inability to access the interior of MAST-U prevented these types of measurements. For these reasons the geometry of the IRVB was verified by comparing known features of the plasma during operation with their expected locations, adapting methods used for visible imaging. The bright features of interest are fuelling locations, alignment of the centre-column and the flash heating of the foil from disruptions.

2.4.6.1 Spatial calibration using fuelling valves and EFIT++

The plasma can be fuelled via a multitude of entry ports, of which only some are directly visible by the IRVB. The names of the valves corresponding to the visible outlets are indicated in Figure 2.8. If hot plasma is present in the immediate vicinity of the gas outlet, the hot electrons dissociate and then excite and ionise the injected neutrals. If the electron temperature is not too high and the plasma is close enough, a bright non-toroidally-symmetric emission appears in the vicinity of the gas outlet. In all the observed discharges when the gas injection valve PFR_BOT_B01 was employed, a localised bright region never appeared, possibly because the separatrix was too far away or the gas flow too low. The fuelling valves, then, that caused a visible localised emission to appear in the IRVB FOV are HFS_MID_L08 and HFS_BOT_B03, although HFS_BOT_B03 was only used once and thus not very useful to compare across pulses.

The 2 HFS_MID_L08 valve outlets locations at the inner wall can be used as one spatial calibration of the IRVB viewing geometry. The valve is consistently used throughout MU01 and its outlets are both in the field of view of the high speed visible light camera (HSV), shown in Figure 2.19, while only one outlet is in the IRVB FOV. Strong visible light brightness does not necessarily indicate a strong total radiated power, but indicates regions where neutral hydrogen is interacting with the plasma. [115]

Figure 2.20 shows the comparison of the localised emission arising from the use of valve HFS_MID_L08 for HSV and IRVB for the shot 45351. Figure 2.20a shows the brightness from the IRVB while Figure 2.20b shows the brightness from the HSV. The IRVB shows

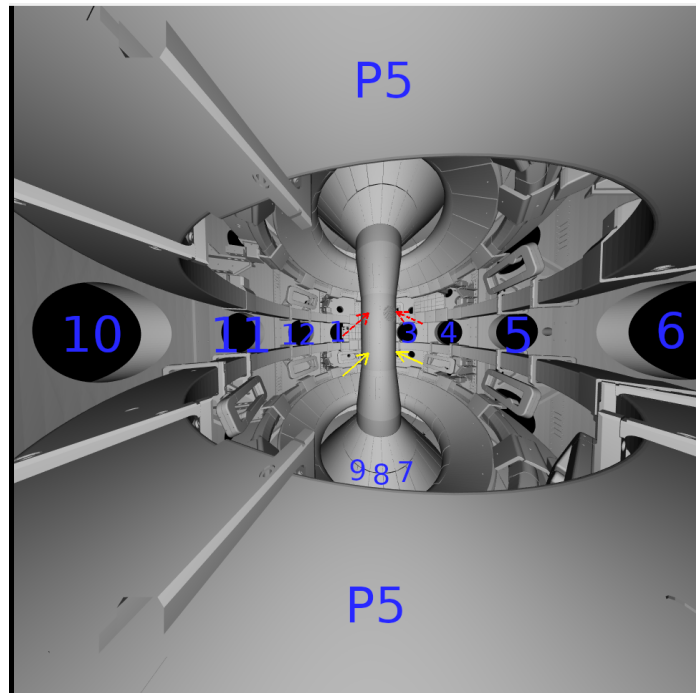


Figure 2.19: Field of view of the high speed visible light camera indicating the sector numbers. In yellow the locations of the outlets of the gas valve HFS_MID_L08 are indicated. In red is shown the location of the outlets of the gas valve HFS_MID_U02, dashed because they are on the other side of the central column, hidden from view.

that the emissivity is clearly non symmetric and localised in the proximity of the outlet. The HSV data is affected by saturation but the bright spot due to both outlets is clearly visible. To further illustrate the validity of the comparison [Figure 2.20b](#) shows the time evolution of the average of the relative brightness around outlets compared to the flow rate of gas programmed for the valve. Both IRVB and HSV measure an increase and decrease of the local emissivity that matches the gas output.

[Figure 2.21](#) shows a later stage of the discharge when the HFS_MID_L08 valve is off. The image, determined with EFIT++ magnetic reconstruction [116], shows that high emissivity regions are present along the inner and outer legs as would be expected in the divertor for a detached target. This consistency is true across all shots providing further indication of the similarity of the real IRVB geometry to the designed one.

2.4.6.2 Spatial calibration using disruptions

During disruptions the core plasma can quickly move towards plasma facing components (PFC). There the ion flux is recycled as neutrals which are then excited through electron-

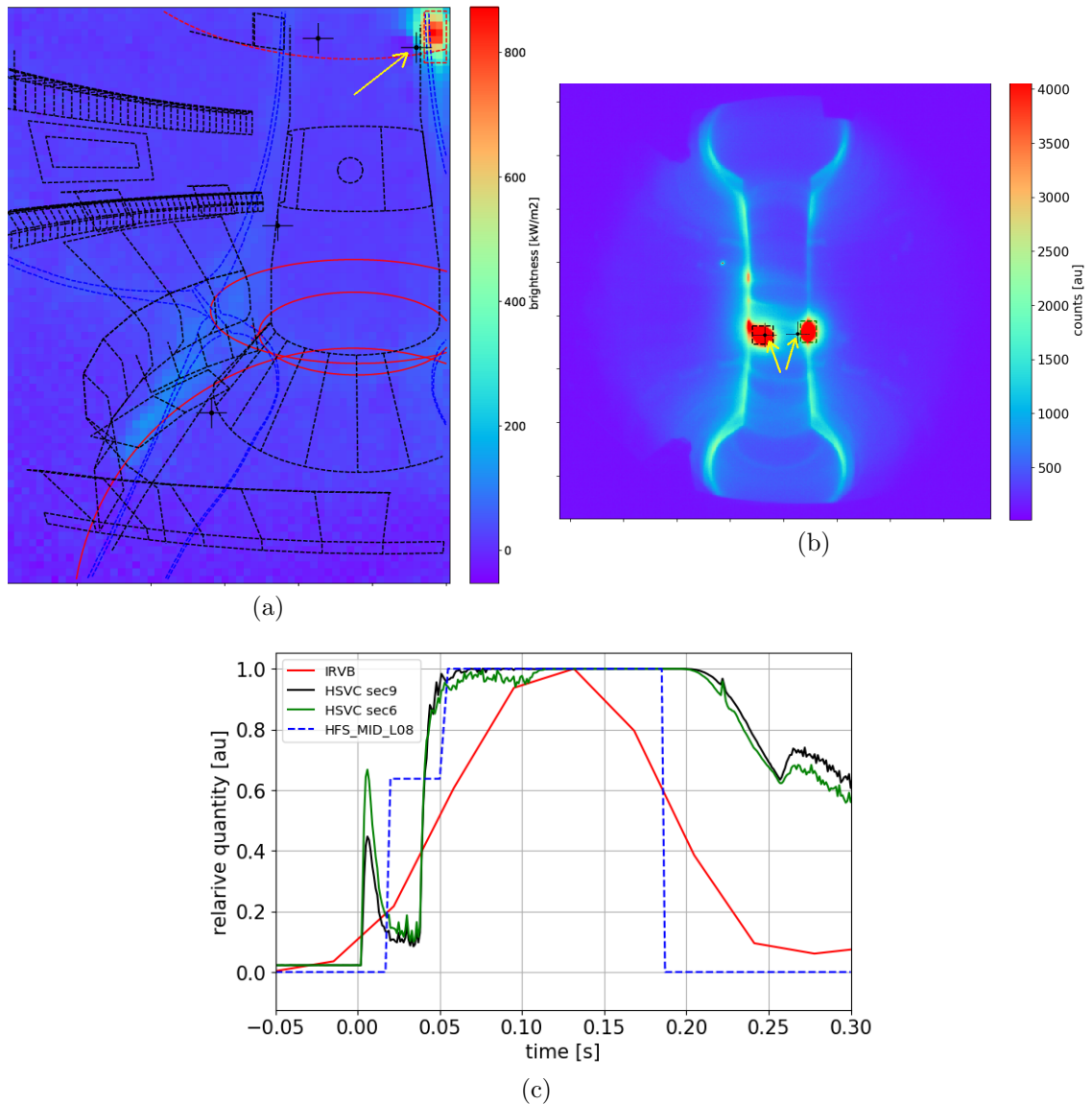


Figure 2.20: Example of the radiation caused by the valve HFS_MID_L08 from shot 45295. (a) brightness data from IRVB at 132ms. Shown in dashed blue is the poloidal projection of the separatrix. The toroidal traces of x-point and strike points are shown in solid red, and in dashed red is the magnetic axis. The outlet of the valve HFS_MID_L08 in the IRVB FOV, marked by a black cross and a yellow arrow, is clearly visible in the IRVB image. In (b) a cropped image of the raw data from the high speed visible light camera (HSV) for the same shot at 50ms. The two bright spots correspond to the two outlets from the valve, both in the HSV FOV, marked as in (a). Note: this data is affected by saturation. In (c), the relative average of the readings inside the dashed regions that are outlined in a and b, and the programmed flow for the HFS_MID_L08 valve.

atom interactions, leading to a strong localised radiation from the proximity of the PFCs in question. Additionally, some carbon can be sputtered from the PFCs because of the sudden

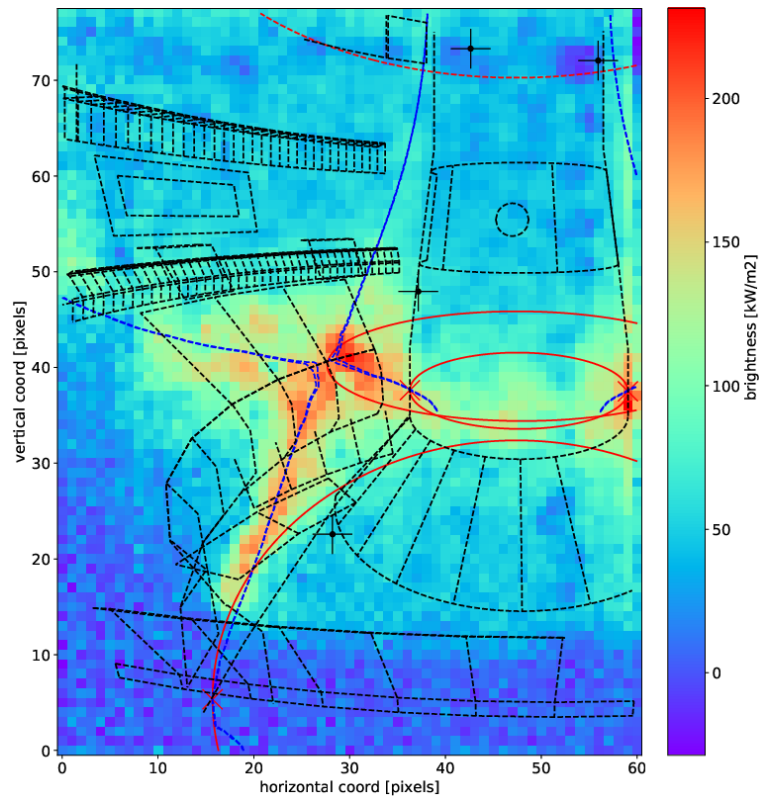


Figure 2.21: IRVB Brightness image of the plasma from shot 45295, 388ms, at a time when high field side valves are off and the target is radiatively detached. In blue a tangential projection the separatrix from EFIT++ magnetic reconstruction overlaid on the image using nominal IRVB design geometry. The toroidal traces of x-point and strike points are shown in solid red, and in dashed red, is the magnetic axis.

increase of particle flux and also lead to radiation from the excited C ions and neutrals. Because of the transient nature of the phenomena it is sufficient to investigate the temporal derivative of the foil temperature, neglecting the other components of the heat transfer equation, to locate regions where a high emission originates.

Figure 2.22 shows the foil temperature increase due to a disruption at the end of shot 45225. The plasma moved towards the lower half of the machine and as a consequence a strong emission comes from regions of the image within close proximity to the tiles. Details of the radiation structure can't be easily interpreted as the source of signal is not necessarily toroidally symmetric. A bright emission is present close to the tiles around the baffle and it is therefore possible to observe the presence of a part of the foil that cannot be illuminated because of the interference of the P6 coil close to the pinhole seen in Figure 2.8. The demarcation line between the region of the foil that can or cannot receive radiation from Figure 2.7a is overlaid, and it lines up well with the observation.

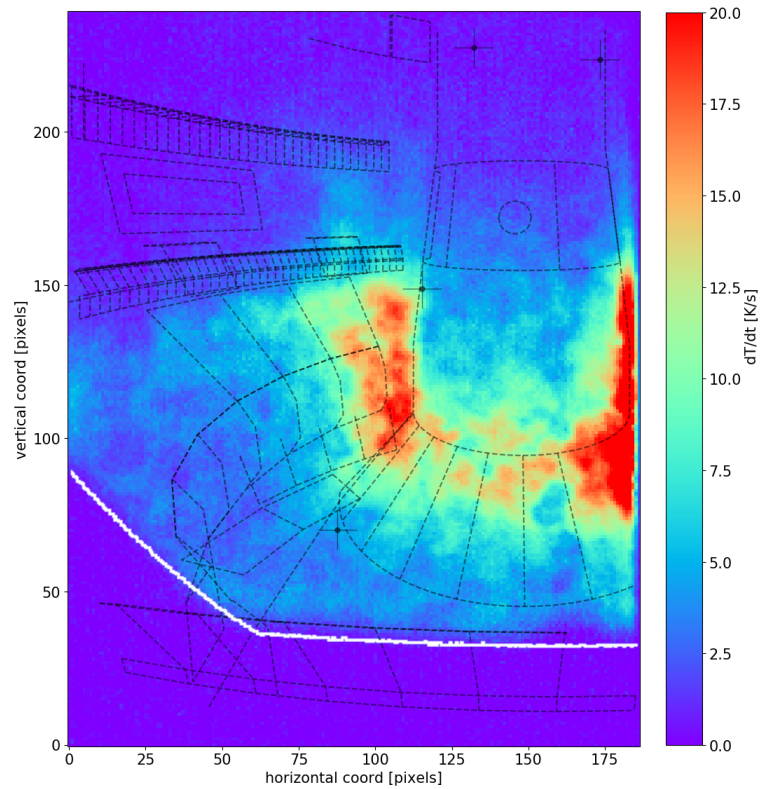


Figure 2.22: Image of foil temperature increase due to the disruption of the plasma in shot 45225. No temporal or spatial binning of the data applied. Indicated in white is the demarcation line between the region of the foil that receives any radiation or none from an homogeneous emitter in the core and divertor region from [Figure 2.7a](#).

From the above observations it can be stated that the IRVB is positioned "close" to what is expected from the design; we cannot be quantitative in determining how accurate the view of each pixel is. The FOV calibration could be further improved by including the valve HFS_MID.L02 and modifying the geometry such that the observation in [Figure 2.7a](#) has an even better match with [Figure 2.22](#), but a confirmation of the geometry as per design is for now sufficient.

2.5 MU01 Line integrated results

Once the IR camera, the foil and the viewing geometry are validated the IRVB can be used to measure the radiation brightness from the plasma during experiments. The data is first split between the two digitizers and the counts converted to temperature as per [Section 2.4.1](#). As mentioned in [Section 2.4.4](#) the camera is affected by a pickup oscillation of the signal at a frequency of about $29Hz$, so the temperature is binned in time over one period of such

oscillation, returning a temporal resolution of about $30ms$. In order to reduce the noise the temperature is also binned spatially over the foil, with a good compromise between resolution and noise being a 3×3 pixel binning, reducing the independent LOS in the plasma from 36700 to about 3900. The binned temperature is then used to calculate the power absorbed by the foil and the result from the two digitizers averaged¹. Finally the power is converted to brightness with Equation 2.11.

In conventionally diverted discharges [117] in which the core density was progressively increased with either fuelling from the midplane or the divertor, it can be observed that the peak brightness is at first close to the targets before moving along the divertor legs to the x-point forming the XPR. On further increase of the density, the radiation moves upstream along the inner separatrix to a region around the midplane where a toroidally symmetric MARFE-like structure forms at the high field side (HFS) of the plasma [56]. From there the structure becomes brighter and moves slowly inwards from the inner wall, correlating with the ensuing disruption.

These phases are shown for the double null low power Ohmic shot 45473 in Figure 2.23. The movement of the radiation can be correlated with other plasma parameters like the core plasma density and with the existing resistive bolometry system for which the chordal views are shown in Figure 2.9. For MU01, multiple LOSs of the resistive bolometers were damaged (including the two poloidal LOS closer to upper and lower x-point) and the measurements were severely affected by noise, but the system was robust enough to return low time resolution data. The two LOS closest to the x-point are not available, but the one just below the midplane (CH9, see Figure 2.9) is.

Figure 2.24 shows the comparison between resistive bolometry CH9 chordal brightness and similar brightness measurements from the IRVB. Figure 2.24a shows the average IRVB brightness inside the regions marked with matching colours in Figure 2.23 vs time. The region with the highest brightness changes with time according to the time development described for Figure 2.23. This is related to a monotonic increase of the core density that causes the plasma to detach from the targets. The brightness from the resistive bolometer CH9 (Figure 2.24d) has to be compared with the midplane data from the IRVB (Figure 2.24a). The absolute value of the brightness is different, with the IRVB recording about two times the brightness of the resistive bolometer (possibly because the LOS of the IRVB is integrated

¹The two digitizers return almost identical results, therefore this averaging results in a $\sqrt{2}$ reduction of the noise.

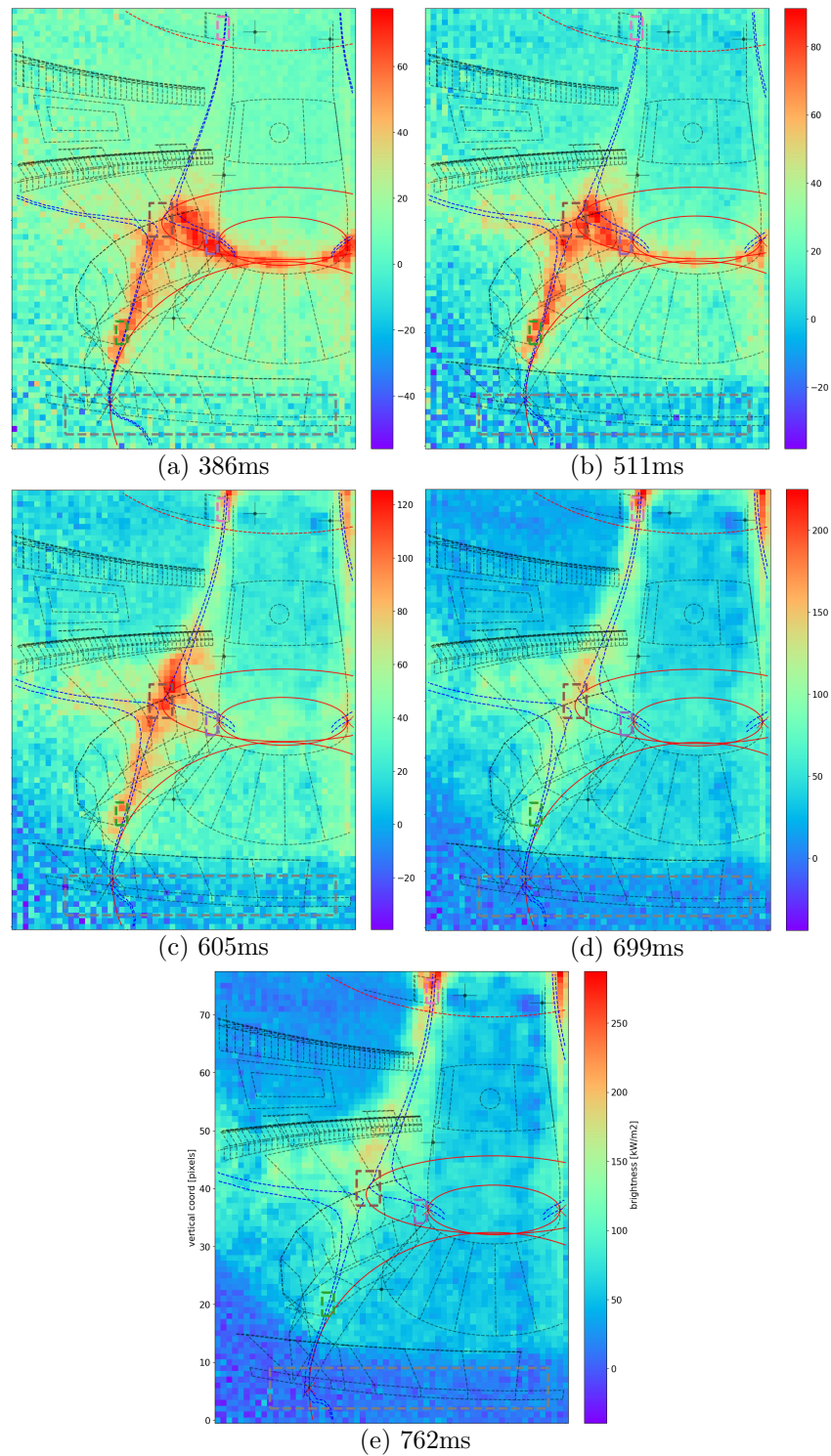


Figure 2.23: Changes in brightness pattern in a density ramp for a conventional divertor, L-mode, Ohmic plasma (shot 45473, Double-null and 650KA). All MU01 shots have ion ∇B drift downward. First the inner target is radiatively attached (a), then it starts detaching (b) to form an x-point radiator (c) and finally a radiation MARFE-like structure on the high field side (HFS) midplane (d). Further increasing the density the structure moves inward (e) leading to a disruption. Note that the all images have different colour bar ranges. The average brightness in the regions marked by the dashed lines (green: outer target, violet: inner target, brown: x-point, pink: midplane, grey: control) will be used for later analysis.

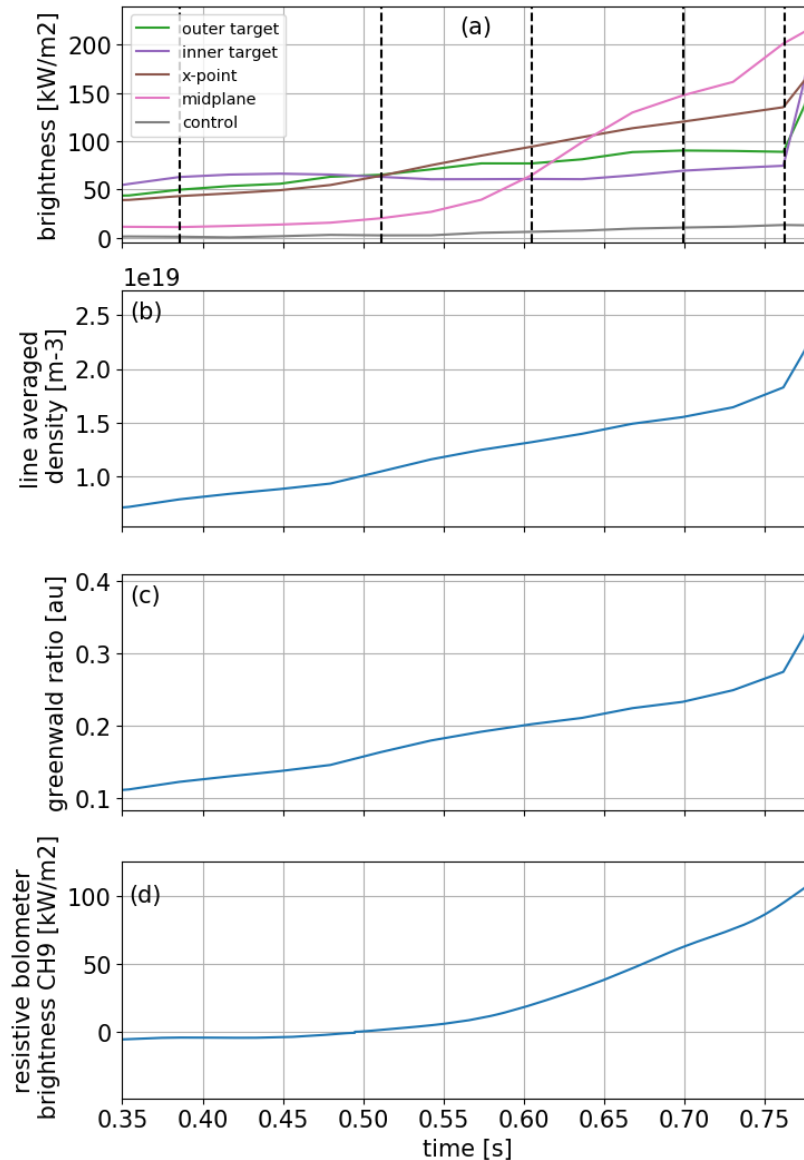


Figure 2.24: Comparison of the measurements from different diagnostics for the shot 45473. In (a) is the IRVB brightness averaged inside the regions indicated with dashed lines of matching colours around the x-point and other regions in Figure 2.23 while the vertical black lines indicate the time corresponding to the images in Figure 2.23. In (b) is the core line averaged density, (c) is the Greenwald density ratio and (d) is the brightness from the resistive bolometer core toroidal channel 9.

over a much longer path through the plasma). Most importantly, though, the emission starts to rise for both at $\sim 550\text{ms}$ and at a similar rate, indicating that both are observing the same phenomena. An important observation to demonstrate the absence of systematic errors is to check the region of the foil that should not receive radiation from the plasma shown in Figure 2.7a. This is labelled as *control* in Figure 2.24 and while drifting upwards in time

it is much smaller than the relevant quantities. This region can also be used to measure the noise level of the diagnostic. The measured NEPD, with the binning mentioned above, is $0.79W/m^2$, close to that indicated by previous models ($0.58W/m^2$ from [118]) and below initial expectations. The uncertainty on the power density with the same binning, whose estimate includes the uncertainty on the foil parameters and the camera calibration, has a minimum of about $10W/m^2$, gradually increasing with a stronger signal up to about $30W/m^2$ in [Figure 2.25d](#).

In higher power discharges, like when the NBI is used and H-mode can be achieved, a similar sequence of events happens to that shown and discussed above for L-mode plasmas and detachment. This is demonstrated in [Figure 2.25](#) which shows the change in IRVB brightness pattern for a conventional divertor beam heated discharge. The sequence proceeds as for the lower power one, except that after the HFS MARFE-like structure is developed, the core density decreases and the peak radiation moves back closer to the x-point. The brightness is much higher than [Figure 2.23](#) because of the increase in heating power. In [Figure 2.25a](#) a region at the top left of the image that shows strong brightness but which does not seem field aligned can be observed. This region typically has strong brightness in beam heated discharges before and after the H-mode phase. Similar behaviour was observed also in resistive bolometry for LOS aimed in the direction opposite to the NBI. The origin of this effect is unclear but it is possible that the heat flux is associated with fast particles escaping the core plasma and undergoing charge exchange. This could be verified by comparing the brightness of the region of interest with data from the fast ion loss detector diagnostic, or results from modelling, but it is outside the scope of this work.

[Figure 2.26](#) shows the relevant time traces for shot 45401. The density is much higher and the Greenwald fraction (a metric of the tokamak performance such that the maximum usually achievable is 1 [119]) corresponding to radiative detachment is around 0.6 rather than 0.15 as for the lower power shot 45473. Here the comparison with resistive bolometry can be done both at the midplane (CH9) as well as close to the location on the separatrix labelled as intermediate, that corresponds to channel 13 and 14 (CH13, CH14). Agreement is good at the midplane but not as good in the intermediate position, where CH13 and CH14 detect significant radiation even before $\sim 850ms$, unlike IRVB. The difference is likely not due to the NBI, as only the leftmost part of the foil is affected, and also only the outermost counter-NBI resistive bolometer LOS is affected (see [Figure 2.9b](#)), while it could be due

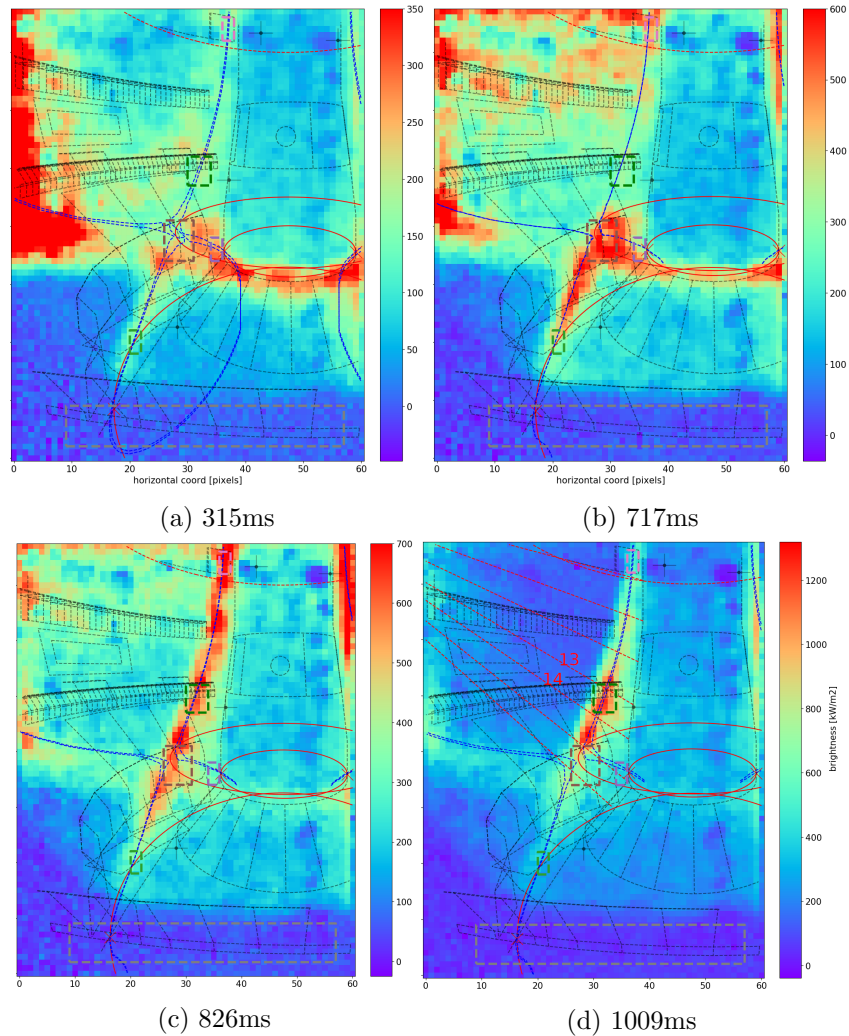


Figure 2.25: Changes in brightness pattern in a density ramp for a conventional divertor, H-mode, beam heated plasma (shot 45401, Double-null and 750kA). All MU01 shots have ion ∇B drift downward. First, the inner target is radiatively attached (a). Then, it detaches and forms an x-point radiator (b) and finally a radiation MARFE-like structure on the HFS midplane (c). In this shot the density was decreased after this point and this resulted in the peak radiation to move back towards the x-point (d). The bright region at the top left of (a) is likely due to the foil being heated by a particle flux rather than radiation from the plasma. In (d) are overlaid in dashed red and numbered, the resistive bolometer LOS through similar regions as included in the IRVB brightness image shown. Note that all images have different colour bar ranges. The average brightness in the regions marked by the dashed lines (green: outer target, violet: inner target, brown: x-point, pink: midplane, grey: control) will be used for later analysis.

to a different length of the resistive bolometer LOS in the emitting region or because it is detecting some radiation from the inner leg (CH14 could be more affected than CH13, hence the higher brightness in CH14).

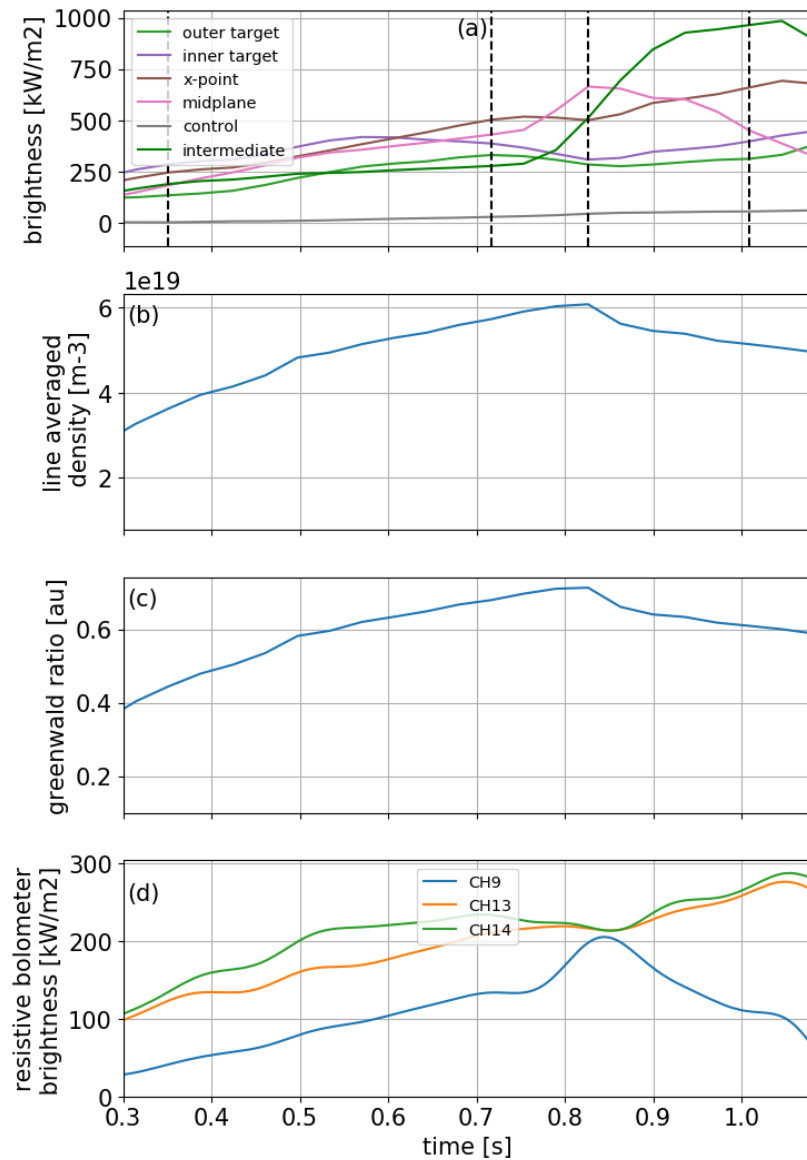


Figure 2.26: Comparison of the measurements from different diagnostics for the shot 45401. In (a) is the IRVB brightness averaged inside the regions indicated with dashed lines in [Figure 2.25](#) while the black lines indicate the time corresponding to the images in [Figure 2.25](#). In (b) is the core line averaged density, (c) is the Greenwald density ratio and (d) is the brightness from the resistive bolometer core toroidal channel 9, 13 and 14, where the first corresponds to the midplane while the others to the intermediate regions of the IRVB.

2.6 Summary

The IRVB diagnostic was successfully deployed in MAST-U. This represents a new implementation of the bolometric diagnostic, not only because it is the first use on a spherical tokamak device, but also because it is aimed at measuring the total radiation emissivity in

the region of the x-point, where significant spatial gradients are expected and a high spatial resolution is necessary. The choices that guided the design of all aspects of the diagnostic are reported, with lessons learned for future implementations.

The calibration procedures for the IR camera and absorbing foil are detailed, in order to calculate the brightness of the radiation from the plasma. Also shown are the methods to verify the qualitative match with the IRVB design of: positioning, viewing geometry and FOV. These can be challenging tasks for bolometers due to the high brightness required for signals to be detected and if there is limited in-vessel access.

The early results from the first MAST-U experimental campaign show that the evolution of detachment in a spherical tokamak, for both L-mode and H-mode conventional discharges and only intrinsic impurities, follows similar trends to low aspect ratio tokamaks: the radiation peaks move along the two divertor legs and the HFS separatrix, depending on the level of detachment. The x-point radiator was observed as an intermediate stage, before the peak of the radiation moves upstream along the inner separatrix up to the HFS midplane forming a toroidally symmetric, poloidally localised, MARFE-like structure. It was also shown that the IRVB measurements are roughly consistent with resistive bolometry, further validating the results.

Chapter 3

MAST-U IRVB scientific exploitation

Once the system is fully characterised, and the general agreement of the line integrated data with the plasma behaviour is verified, it is possible to further the analysis by calculating the plasma emissivity via tomographic inversion. In this chapter different tomographic inversion methods will be illustrated, together with the Bayesian method ultimately developed specifically for the IRVB. This will be validated against SART, a more established one, returning equal or better results. It will be also shown that because only a small portion of the FOV enters the SXD chamber, from a limited solid angle, that the IRVB cannot reconstruct the radiation profile there, but can only determine the integrated power with acceptable precision.

The tomographically inverted data will be used to separate the changes of emissivity in the inner and outer leg, as well as the HFS separatrix. It will be shown that the progression of radiative detachment for increasing density in L-mode discharges is similar to standard large aspect ratio devices: first on the inner leg, then the outer leg and then a MARFE-like structure forms.

H-mode discharges suffered from low repeatability, so one example where both legs detach is shown. Here the progression of radiative detachment happens with a different order than L-mode, but this could be due to fuelling only from the lower divertor. The upper and lower divertors are shown to behave differently, with the lower detaching while the upper being still attached, indicating that thanks to the baffles the two could be controlled independently.

Given the stronger signal in H-mode, the spatial resolution of the inversions is increased.

The IRVB data has been used in combination with line emissivity measurements to infer what processes are important after the onset of detachment in a super-x plasma. It has been found that molecular reactions are important for temperatures too low to cause ionisation and too high to allow for recombination.

3.1 Tomography

A schematic of the entire process is shown in Figure 3.1.

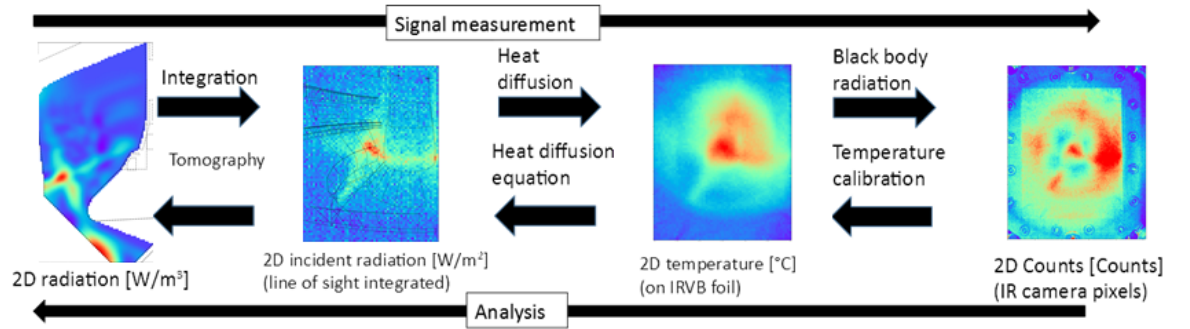


Figure 3.1: Path for forward modeling, left to right, and for experimental data analysis, right to left.

Assuming the radiation from every voxel (a toroidally symmetric 3D volume element) of the plasma is emitted isotropically, the opacity of the plasma itself is neglected (given the relatively low density in MAST-U this should not be a concern [120–122]). Assuming also that reflections are negligible, the relation between the emissivity profile m and power to every pixel of the foil q is linear and can be summarised in the matrix product

$$\mathbf{W}m = q \quad (3.1)$$

To calculate the elements of \mathbf{W} , the geometry matrix, for every voxel, what the power absorbed by the foil would be if the voxel were to have an emissivity of $1W/m^3$ was calculated. This was done with the Monte Carlo ray tracing code CHERAB. The entire volume inside the vacuum vessel was divided into regular toroidal annular voxels of 2cm in both radial and vertical extent, and only the ones that are at least in part inside the IRVB FOV considered. The power absorbed by the foil was calculated assuming:

- no radiation penetrating the IRVB tube apart from the pinhole (the pressure equalisa-

tion cutout close to the vacuum vessel, indicated as vacuum pump plug in [Figure 2.3](#), is neglected)

- no reflection inside the MAST-U vacuum vessel
- no reflection inside the IRVB tube

The result from this method, showing the region of the MAST-U vacuum vessel to which the IRVB is most sensitive, is shown in [Figure 2.9a](#). To obtain the emissivity distribution from the power on the foil, the geometry matrix must be inverted, but this is an ill-posed problem. A problem is well posed if a solution exists, it is unique and it has small changes for small changes of the inputs. [123] In the case of tomographic inversions the last condition often fails. [124] This means additional information has to be added in order to find a solution. In the most famous case of tomographic inversion, MRI scans, the source and detector are moved around the volume of interest so as to collect information from different angles. This decreases the under-determination of the problem and a solution can be found. In our case neither observer or observed object can be moved so additional information is required for a stable solution.

It must be noted that, as mentioned in [Section 2.5](#) and shown in [Figure 2.25](#), some parts of the foil are affected by particle flux from the NBI. This is a heat source not related to the power radiated from the plasma, and would change the inferred emissivity profile. For this reason, for MAST-U shots where NBIs are used, the red section of the foil in [Figure 3.2](#) is not considered. Additionally some parts of the foil near the right and top edge show regular patterns, characterised by spots of lower power density vertically and horizontally aligned. These can cause a variation between neighbouring bright and dim areas of up to a fifth of the peak power density. These features do not change with time or radiation pattern, implying that are likely due to non-uniformities in the foil properties, like a thicker foil or carbon coating. To prevent these affecting the inversion, the edge regions are also not considered, leaving only the region indicated in green in [Figure 3.2](#).

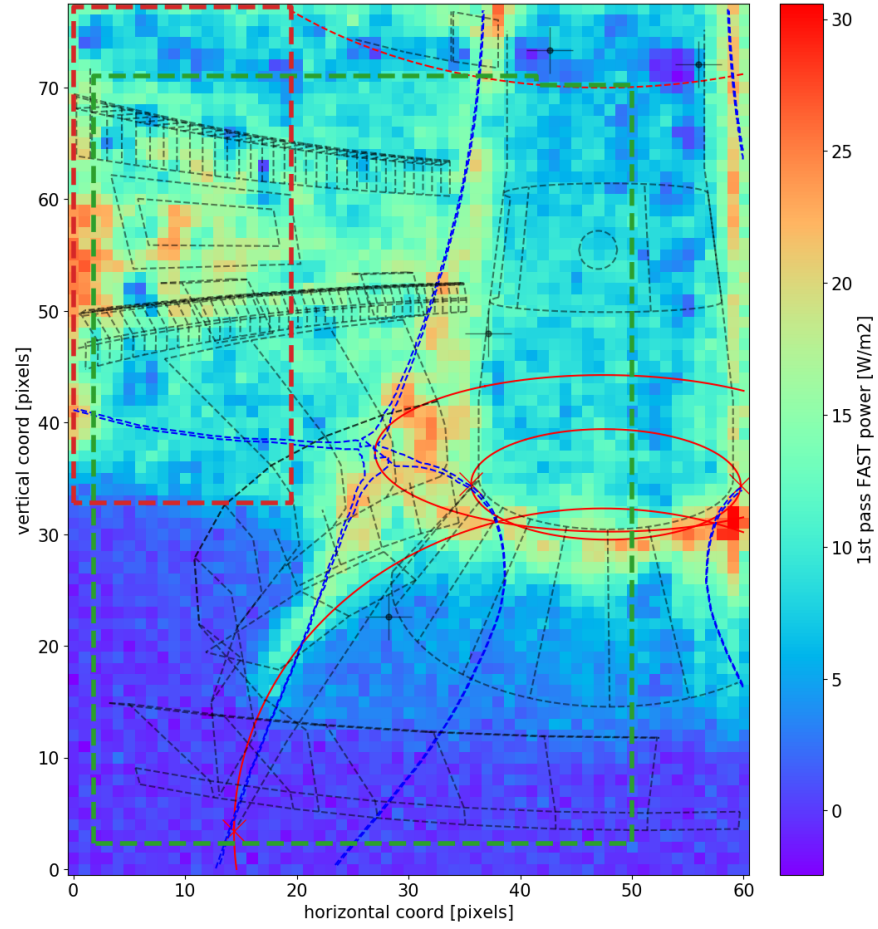


Figure 3.2: Example of power density distribution on the foil from the shot 45401, showing the region of the foil used for Ohmic discharges (green) and that which is excluded when the NBI is used (red)

3.2 Inversion techniques

3.2.1 Truncated singular value decomposition (SVD)

The SVD method for tomographic inversion relies on the direct inversion of the geometry matrix. The inversion is performed by finding the eigenvalues and eigenvectors associated with the geometry matrix. An $m \times n$ matrix, \mathbf{W} , can be written as

$$\mathbf{W} = \mathbf{A}\mathbf{\Sigma}\mathbf{B}^T \quad (3.2)$$

where the columns of \mathbf{A} ($m \times m$) are the eigenvectors of $\mathbf{W}\mathbf{W}^T$, the columns of \mathbf{B} ($n \times n$) are the eigenvectors of $\mathbf{W}^T\mathbf{W}$ and the values on the diagonal of $\mathbf{\Sigma}$ ($m \times n$) are the square roots of the eigenvalues of $\mathbf{W}\mathbf{W}^T$ and $\mathbf{W}^T\mathbf{W}$ [125]. Using singular value decomposition it

is possible to define Σ^+ as a diagonal matrix where the elements on the diagonal are the reciprocal of the elements of Σ , therefore

$$\mathbf{W}^+ = \mathbf{B}\Sigma^+\mathbf{A}^T, m_{SVD} = \mathbf{W}^+q \quad (3.3)$$

where m_{SVD} is the solution of [Equation 3.1](#). The decomposition can often be numerically performed, but the smaller eigenvalues greatly enhance the effect of noise in the measured data and the numerical rounding errors. [17] This can be limited by neglecting the smaller eigenvalues (truncating) and considering only the more significant ones.

3.2.2 Tikhonov regularization

This method relies in replacing the ill conditioned problem in [Equation 3.1](#) with another that is closely related but well conditioned. Rather than finding the solution m that exactly matches the input data and that translates to the residuals

$$r = \|\mathbf{W}m - q\| = 0 \quad (3.4)$$

sought instead is the solution m' that minimizes

$$\|\mathbf{W}m' - q\| + \alpha^2\|\mathbf{L}m'\| \quad (3.5)$$

where the regularisation coefficient α is a scalar and the penalty function L indicates what type of constraint is applied to the solution. There are various choices for the penalty function depending on prior knowledge, but the most common is to limit one of the spatial derivatives of the solution: from the zeroth order (limitation on large values) to the second order (limitation of the Laplacian). For the specific application of tokamaks, the derivative can be limited preferentially along field lines, such to obtain a smoother profile within flux surfaces. [17] In this work a uniform Laplacian penalty is considered. The solutions from this method do not match the input data exactly but are normally more scientifically relevant and less affected by noise. The regularisation coefficient α determines the strength of the regularisation and needs to be determined. This will be shown in [Section 3.2.5](#).

3.2.3 Simultaneous algebraic reconstruction technique

The Simultaneous algebraic reconstruction technique (SART) is an iterative method that aims at minimizing the difference between the measured q and the synthetic image $\mathbf{W}m'$, and the difference at each step informs as to how to correct the previous guess. The emissivity at the step $i + 1$ is calculated from the estimation at the step i with [111, 126]

$$\begin{aligned} \hat{q} &= \mathbf{W}m^i, \quad W_k = \sum_{l=1}^n W_{k,l}, \quad W_l = \sum_{k=1}^m W_{k,l} \\ m_l^{(i+1)} &= m_l^{(i)} + \frac{1}{W_l} \sum_{k=1}^m \frac{W_{k,l}}{W_k} (q - \hat{q}) \end{aligned} \quad (3.6)$$

This method too is affected by the problem being ill conditioned, therefore the use of prior information is required. Similarly to Tikhonov a penalty function mediated by a regularisation coefficient can be added to the scheme returning [Equation 3.7](#).

$$m_l^{(i+1)} = m_l^{(i)} + \frac{1}{W_l} \sum_{k=1}^m \frac{W_{k,l}}{W_k} (q - \hat{q}) - \alpha^2 \left(\sum_{k=1}^m L_{k,l} m_k^{(1)} \right) \quad (3.7)$$

By limiting to the addition of positive values only to $m_l^{(i)}$, SART can also be modified to avoid negative emissivity. [111] Because of its relatively low computational cost, this is often the method of choice when inverting imaging data from plasma. This method also requires other techniques to determine the optimal regularisation or penalty coefficients.

3.2.4 Bayesian method

This approach was developed specifically for the IRVB in MAST-U and it is similar to Tikhonov regularisation in that the aim is to find a solution m' such as to minimize [Equation 3.5](#). Crucially, the residual norm is calculated including the uncertainty σ_k of the measurement in each pixel p_k . This effectively changes the problem into a maximum likelihood optimisation. The practical effect is that power density levels much smaller than the estimated uncertainty (see [Equation 2.6, 2.7, 2.8](#)) are neglected, allowing only the patterns associated with the stronger signals to become apparent.

Here, the Laplacian operator is multiplied by the regularisation coefficient α , divided by the voxel grid resolution d_g squared (so as to return the real second derivative) and divided by an arbitrary factor $10^6 W/m^3$ to avoid floating point precision errors. The addition of this

prior makes the problem Bayesian in nature, because the emissivity profile that maximises the likelihood of generating the observed foil power density, given the probability of observing a specific power density, is found.

In order to penalise negative emissivities a dedicated term is added, mediated via a coefficient. This coefficient should be optimised alongside α but it would be prohibitively computationally demanding, so it is, instead, arbitrarily fixed to $200/(10^6 W/m^3)$. This prior is, unlike the one deriving from the Laplacian of the emissivity, non-linear. This means that an analytic solution to the maximisation problem cannot be found and numerical methods have to be used.

Additionally two variables are included: a uniform power density value over the whole foil (Q_f); and one only over the region of the foil actually affected by the plasma (Q_p , see [Figure 2.7a](#)). This is done to allow for uniform signals arising from a change of the IR camera temperature or sensitivity, sources of radiation close to the pinhole that must be accounted for, or other systematic errors. This did not prove very successful in preventing some non field aligned emissivity features, especially close to the pinhole (an example of SART being affected by this will be shown in [Section 3.2.6.2](#)). To compensate for this, the voxels that are closer to the pinhole and that have the largest impact on the foil as shown in [Figure 2.9a](#), defined as the ones for which $\sum_{k=1}^m W_{k,l} \geq 0.2 \cdot (\sum_{k=1}^m W_{k,l})_{max}$, have been excluded from the Laplacian penalty. This allows for the emissivity associated with slowly varying power density patterns on the foil to be separated out from the emissivity in the region of interest. The emissivity in this small region is then discarded. As will be shown later, this will account for a very minor part of the foil power density.

This approach is similar to the ordinary Maximum Likelihood (ML) reconstruction method, an iterative method that aims at maximising the likelihood of the measurements being generated by the searched emission pattern. [\[127,128\]](#) The differences between ML and the Bayesian method developed here are that in ML the effect of noise is limited by observing the evolution of the iterative solution rather than with a regularisation parameter, the use of a Poisson distribution for the emissivity (that considers only positive values and introduces non linearity) rather than a Gaussian, and that the simple mathematical formulation of Bayesian method allows for specific corrections like the uniform offsets to be added. An even more relevant aspect is that with the Bayesian method the strength of the measured signal is scaled by its modelled uncertainty, while in ML the variance of the Poisson distribution

depends solely on the mean. This should make the Bayesian algorithm more resilient and provide a more rigorous treatment of the uncertainty. In the opinion of the author these are minor differences that, given similar equations are solved, would lead to similar results. A comparison is therefore not provided here. The choice to use a Gaussian distribution was made, beyond the simpler mathematical treatment, to allow for negative values so as to see if any unaccounted systematic error would give rise to negative emissivity patterns. Now that this is verified not to be the case, a probability distribution that considers only positive values could be similarly developed for the IRVB. This would prevent the need of an arbitrarily fixed coefficient to limit the negativity of the inverted emission profile. The feature of weighting the measurements by their estimated uncertainty, not possible with only a Poisson distribution, will need to be conserved. Another possibility is to maximise the same equation but to use an Empirical Bayes method to determine simultaneously the optimal regularisation parameter, as well as the strength, of the negative emissivity penalty. With this method the two coefficients are treated as variables and included in the maximisation of the likelihood, without the need to scan a predefined parameter range. [129]

The Bayesian method results in the maximisation of the log probability in [Equation 3.8](#)

$$\mathcal{L}(m') = -\frac{1}{2} \sum_{k=1}^m \left(\frac{q_k - \hat{q}_k}{\sigma_k} \right)^2 - \alpha^2 \sum_{l=1}^n \left(\sum_{j=1}^n \frac{L_{l,j}}{d_9^2} \frac{m'_j}{10^6 W/m^3} \right)^2 - (200)^2 \sum_{l=1}^n \left(\frac{\min(0, m'_l)}{10^6 W/m^3} \right)^2 \quad (3.8)$$

with

$$\hat{q}_k = \sum_{l=1}^n W_{k,l} m'_l + Q_f + Q_p \cdot F(k) \quad (3.9)$$

$$F(k) = \begin{cases} 1, & k \text{ in area shone by plasma.} \\ 0, & \text{otherwise.} \end{cases}$$

$$L_{lj} = 0 \quad \forall j \text{ if } \sum_{k=1}^m W_{k,l} \geq \max \left(\sum_{k=1}^m W_{k,l} \right) \cdot 0.2$$

where the function $F(k)$ identifies the pixels exposed to light from the plasma as previously identified. This method is very computationally demanding as all emissivities and offsets are independent variables to be optimised. To alleviate the computational cost, the derivative of $\mathcal{L}(m')$ with respect to all variables is generated analytically at each iteration. The maximisation was achieved with the L-BFGS-B algorithm, specifically the Python `scipy.optimize.fmin_l_bfgs_b` package. [130] Like SART this method requires other means to

define α , as will be shown in the next chapter. Differently from SART this method allows direct estimation of the uncertainty of the solution. As mentioned before, the Bayesian method is non linear, so the probability distribution of the solution is not exactly Gaussian and cannot be analytically determined. If $\mathcal{L}(m')$ is close to its maximum, and the problem satisfies certain regularity conditions, the distribution can be approximated as Gaussian. This is called the Laplace approximation and it is widely used in practice. [131, 132] Approximating the posterior distribution as Gaussian, the covariance matrix of standard errors of the parameters can be approximated as the inverse Hessian matrix. [133–135] The Hessian matrix is given by

$$H_{l^*,j^*} = \frac{\partial^2 \mathcal{L}(m')}{\partial m'_{l^*} \partial m'_{j^*}} \quad (3.10)$$

where l^*, j^* means all parameters: not only the n emissivities but also Q_f and Q_p . The covariance matrix is $\mathbf{C} = \mathbf{H}^{-1}$. There is a significant negative correlation between voxels, so in order to correctly propagate the error the uncertainty for the total radiated power in a region is calculated with Equation 3.11

$$\begin{aligned} P &= \sum_{k=1}^n 2\pi r_k d_g^2 V(k) m'_k \\ \sigma_P &= \sqrt{\sum_{k=1}^n \sum_{l=1}^n C_{k,l} \frac{\partial P}{\partial m'_k} \frac{\partial P}{\partial m'_l}} \\ \frac{\partial P}{\partial m'_k} &= 2\pi r_k d_g^2 V(k) \\ V(k) &= \begin{cases} 1, & k \text{ in region of interest.} \\ 0, & \text{otherwise.} \end{cases} \end{aligned} \quad (3.11)$$

where $V(k)$ selects the region of interest.

3.2.5 Regularisation optimisation

The regularisation method depends on the type of inversion technique chosen. The goal is to find the best compromise between a smooth solution with a realistic profile and one that fits best the measured data.

3.2.5.1 Eigenvalues truncation

It is often observed that the eigenvalues associated with the geometry matrix, sorted by amplitude, behave as shown in [Figure 3.3](#).

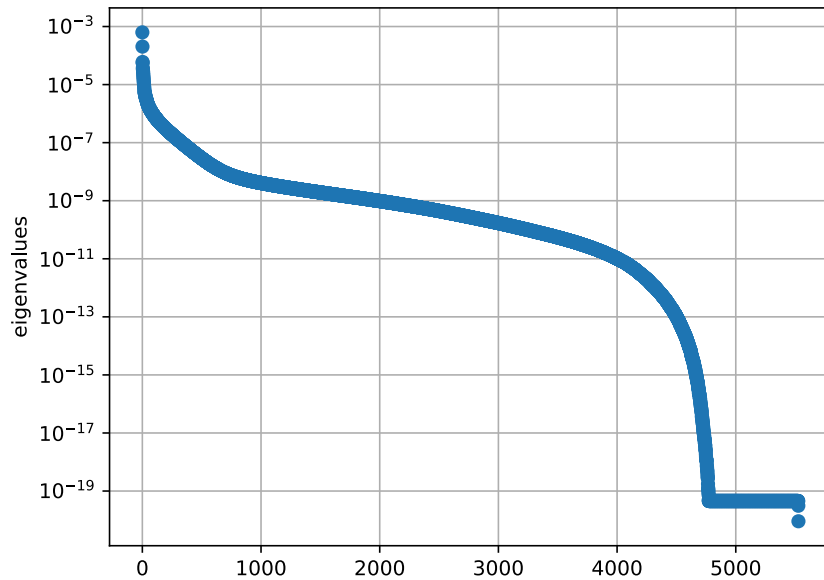


Figure 3.3: Typical amplitude of the eigenvalues in an undetermined inversion problem.

In the process of inverting the geometry matrix, the reciprocal of the eigenvalues is used. This means that the smaller ones, that have the lesser influence on the measured data, have a disproportionate effect on the solution. Small variations due to noise and rounding errors are amplified and the solution can lose physical meaning. To limit this effect the smaller eigenvalues can be neglected. How to find the threshold is not simple and it can depend on the noise level in the input data. In general truncated SVD returns more detailed inversions, but it is more affected by noise than other methods. More detail can be found in [\[17\]](#) and [\[136\]](#).

3.2.5.2 L-curve

For the Tikhonov, SART, and Bayesian algorithms one has to establish the magnitude of the regularisation coefficient and the quantity to regularise. As mentioned before in this work a Laplacian penalty, defined as $\mathbf{L} \cdot m'$, will be used. The elements of \mathbf{L} are such that $L_{i,i}$ is equal to the central element in [Figure 3.4](#) and for the neighbouring cells j , the values around it as per the figure. The more commonly used Laplacian penalties are as shown in [Figure 3.4a](#) and [b](#). [\[16\]](#) Using [Figure 3.4a](#) the derivatives on the diagonals are not calculated, favouring

solutions with larger gradients in the diagonal direction, while the opposite happens for [Figure 3.4b](#). To properly account for the diagonals, important for the IRVB as the LOSs directed towards the x-point are all at a downward angle, the elements of \mathbf{L} are calculated as per [Figure 3.4c](#).

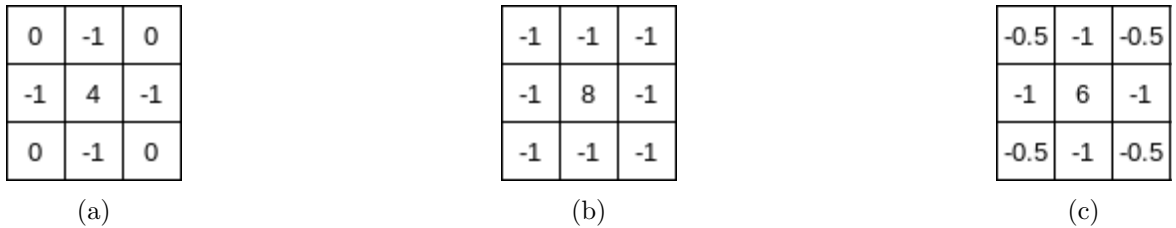


Figure 3.4: (a), (b): types of Laplacian operators commonly used for tomographic inversions. [16] (c): Laplacian operator corresponding to the real 2D second degree derivative used to analyse IRVB data.

A method to determine the regularisation coefficient has then to be defined. A commonly used method is the L-curve. [17] With this approach the emissivity solution is calculated for a range of regularisation parameters. The residuals norm ($\|\mathbf{W}m' - q\|$) and Laplacian penalty norm ($\|\mathbf{L}m'\|$) are plotted in a log-log plot to create the L-curve. A typical L-curve is shown in [Figure 3.5](#).

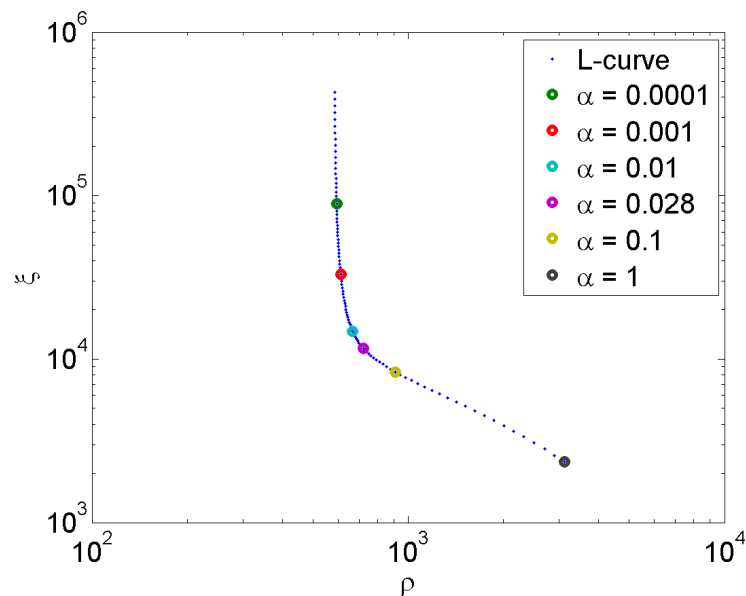


Figure 3.5: Typical L-curve shape. On the horizontal axis is the residual norm, on the vertical the penalty norm. Adapted from [17].

The optimal solution is one that fits the measured data well, but is not dominated by

noise. A good compromise corresponds to the lower left corner of the curve, determined as the region of highest curvature. Rather than calculating the curvature analytically, as in [17], here, a circle is fitted to a number of points that represent a pre-determined portion of the entire L-curve length. The curvature corresponds to the inverse of the fitted circle radius. By fitting different sections of the L-curve one can obtain its curvature smoothed in a similar fashion as a running average. This procedure is computationally demanding as it requires a multitude of solutions to be found for each inversion, but guarantees that the regularisation is always adequate for the signal strength.

3.2.6 Comparison between SART and Bayesian method

One of the most commonly used inversion algorithms for imaging data in fusion is SART. The optimisation of the regularisation coefficient is sometimes neglected with SART, but for a fair comparison with the Bayesian method the L-curve method is adopted for both.

3.2.6.1 SOLPS phantom

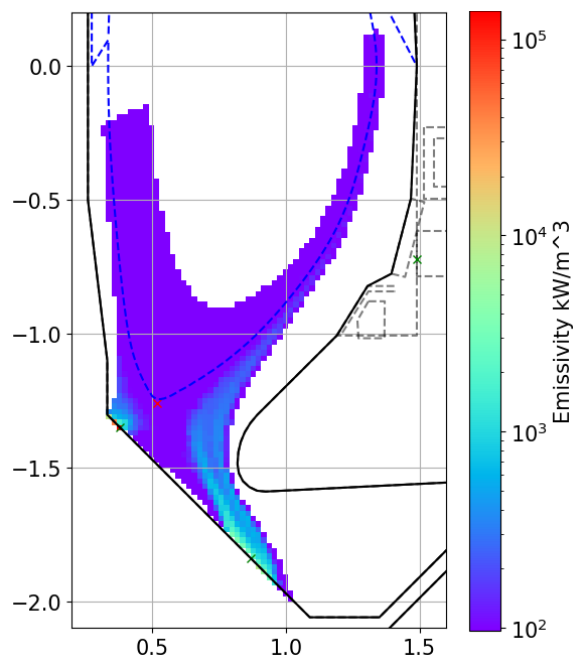


Figure 3.6: Emissivity distribution for the MDS+ SOLPS simulation 69590 corresponding to a MAST-U conventional plasma with the NBIs injecting a total of 10MW (configuration investigated for a future upgrade) characterised by a large radiated power. The approximate location of the separatrix is shown by the dashed blue line.

The radiation pattern from the MDS+ [137] SOLPS simulation 69590, corresponding to

a MAST-U conventional plasma with NBIs injecting a total of 10MW, shown in [Figure 3.6](#), is used for the comparison as it generates strong radiation in the divertor (572kW in the lower half of MAST-U, of which 451kW is below the x-point). The emissivity is multiplied by the sensitivity matrix \mathbf{W} to calculate the power absorbed by the foil. This is used to calculate the temperature increase of the foil from room temperature for a duration, and with time steps equivalent to, what is set during the experiments. For this the foil properties from [Section 2.4.4](#) are used. The temperature is then converted to counts via the coefficients found in [Section 2.4.2](#) and to them is added a random noise of about 5 counts. This dataset is then processed with the same routines used to process experimental data, to determine the power density and uncertainty shown in [Figure 3.7](#).

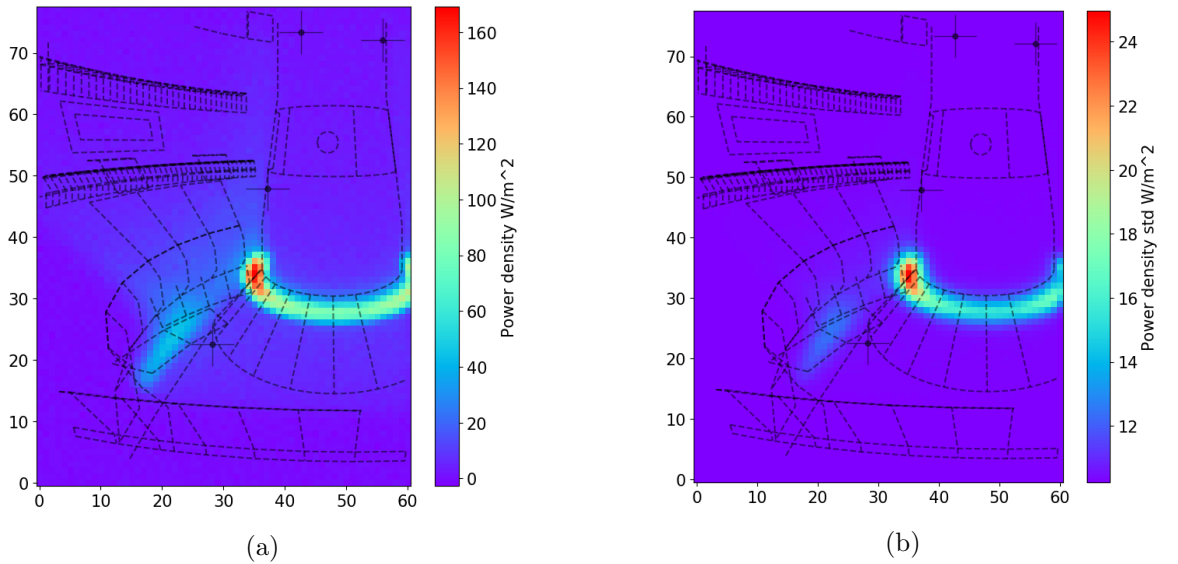


Figure 3.7: Power density (a) and power density uncertainty (b) generated by the emissivity pattern as per [Figure 3.6](#). Of these only the area defined by the green line in [Figure 3.2](#) is used.

This is then inverted using SART and the Bayesian method, scanning a large range of regularisation parameters. The respective L-curves, curvatures and optimal emissivity profiles are determined for both as shown in [Figure 3.9](#).

The power absorbed by the foil that is excluded (partly because of association to the voxels close to the pinhole unbounded by the Laplacian, and partly because of the offsets) is shown in [Figure 3.8](#). Compared to [Figure 3.7a](#) it is clear that it is very low and does not significantly impact the inversion.

Sometimes the L-curve of the Bayesian method can present two concave sections, or it

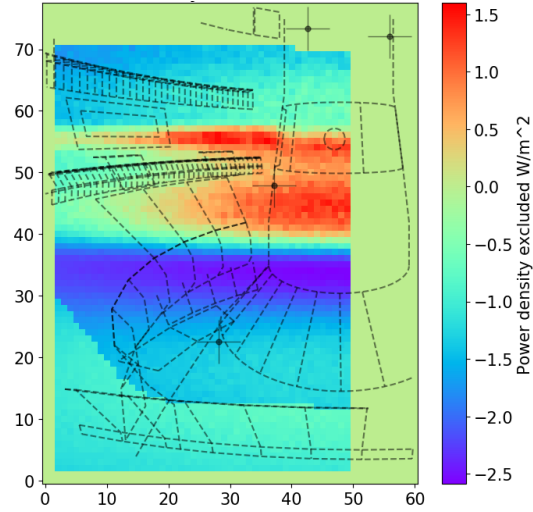


Figure 3.8: Power absorbed by the foil excluded by Bayesian method because it is attributed to the region close to the pinhole (outside the black solid line and close to the green cross in Figure 3.6) or due to offsets (see Equation 3.9). This plot is restricted to the section of the foil used as per Figure 3.2.

can be particularly flat and small deviations could result in erroneous identification of a peak in the curvature. To filter out these anomalies, only the peaks of the L-curve curvature are considered, and of those only the one with $2 \cdot 10^{-4} < \alpha < 10^{-1}$ are considered valid. Of the remaining peaks the highest is then selected.

The difference in the result between the two methods is minor. The Bayesian method seems to return a better match than SART in the SXD chamber (approximately $z < -1.5\text{m}$ and $r > 0.8\text{m}$), but that is of minor importance for the IRVB. From the inner strike point towards the pinhole (both in green), a stripe of higher emissivity not present in the phantom can be observed. This is a common feature for strong signal cases, where the radiation is distributed from its real origin towards the pinhole. This happens because the sensitivity to the poloidal view is higher than to the toroidal (due to a longer integration path in the plasma). In terms of total power, SART is within 1% of the total radiated power (572kW) while the Bayesian method measures $517 \pm 207\text{kW}$. The phantom power is within the uncertainty given by the Bayesian method. Both methods have a very good agreement in the core but return about 33% weaker radiation below x-point and out of the SXD chamber. This is not captured by the uncertainty given by the Bayesian method, which amounts to 6%. This is likely due to the very peaked emissivity of the phantom on the inner target which is difficult to reproduce because of the smoothing induced by the regularisation.

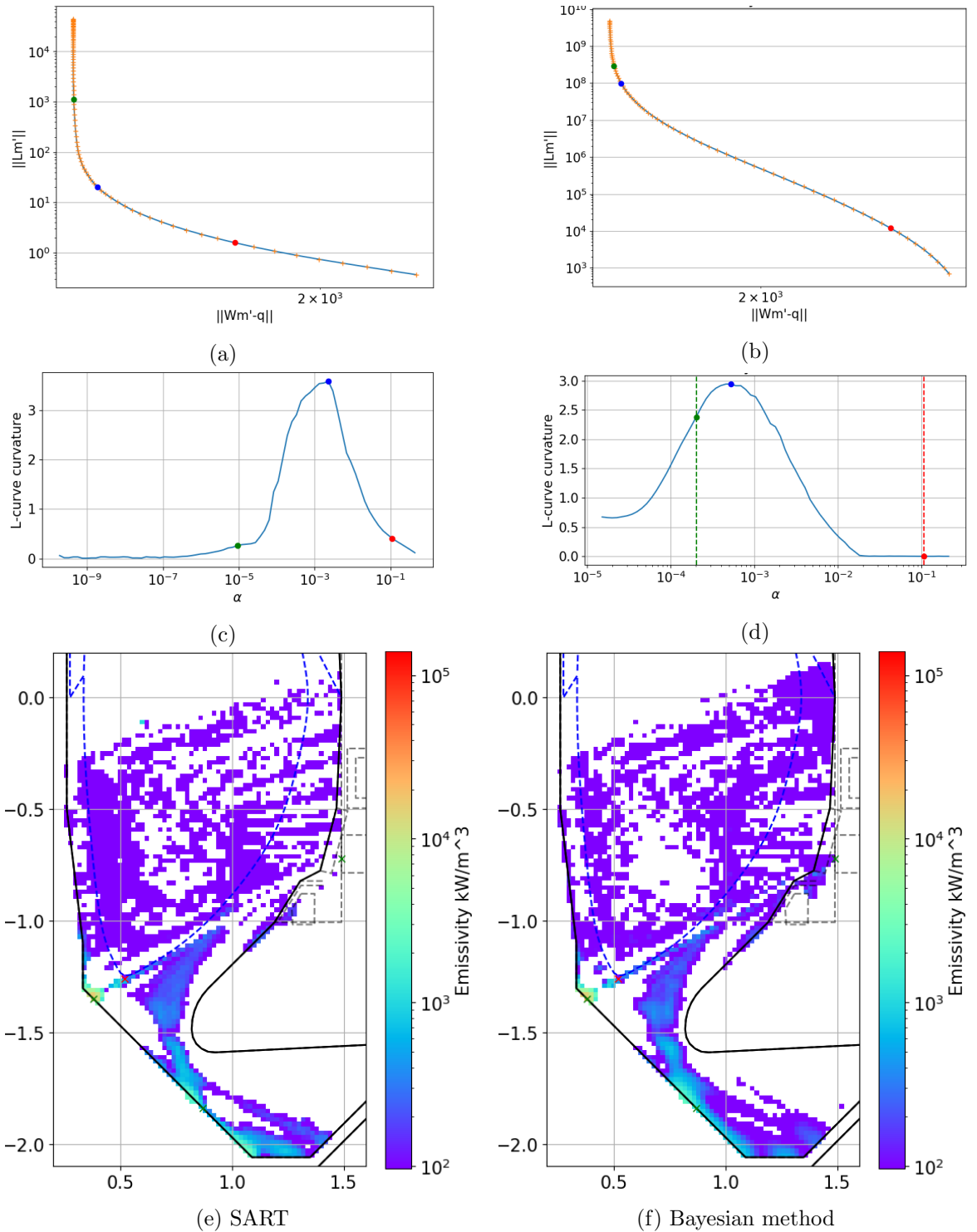


Figure 3.9: Tomographic reconstructions from the SOLPS phantom (Figure 3.7) using SART (left: a, c, e) and the Bayesian method (right: b, d, f). L-curve (a, b) and respective curvature (c, d). The blue point in the L-curve and curvature represent the selected optimal regularisation. The green and red points represent respectively a low and high regularisation coefficient. In (d) the dashed lines indicate the maximum and minimum acceptable regularisation coefficient for the peak of the L-curve curvature. Note that the α regularisation coefficients are not equivalent between SART and the Bayesian method. (e, f) tomographically inverted emissivity. The approximate location of the separatrix is in dashed blue. The same colour scale as Figure 3.6 is used.

3.2.6.2 Experimental data

To compare the performance of the two methods with conditions more typical of the first experimental campaign, the conventional Ohmic shot 45473 shown in [Section 2.5](#) will be used, at the time corresponding to [Figure 2.23b](#) when the radiation peak transitions from close to the inner target to the x-point. The power to the foil and its uncertainty are shown in [Figure 3.10](#). Note that the signal is low enough so as not to affect the uncertainty calculation that is here dominated by the propagation of uncertainty from foil and camera calibration, which is the minimum value it can be.

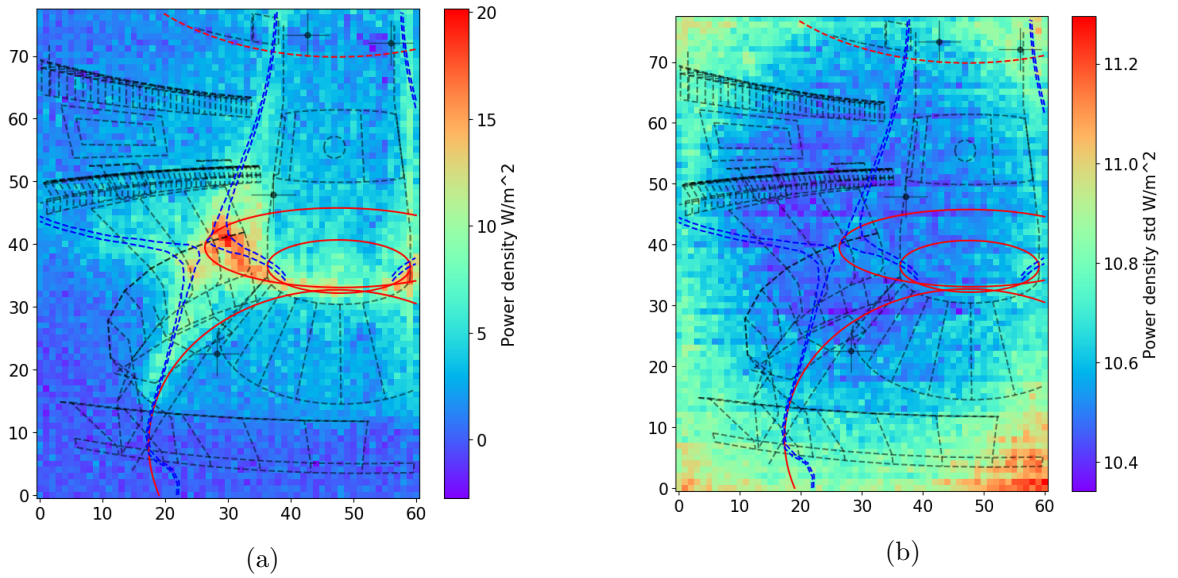


Figure 3.10: Power density (a) and power density uncertainty (b) from the conventional Ohmic shot 45473 at 511ms.

The inversions are performed by scanning the regularisation coefficient and the optimal one is selected. The result is shown in [Figure 3.11](#). The inversions again look similar, but there are some important differences. This time it is possible to observe that the SART inversion is affected by anomalous emissivity close to the magnetic axis and the low field side (LFS) midplane while the Bayesian is not. Also significant are the presence of stripes with higher emissivity converging on the pinhole as observed in [Figure 3.9e](#) and [f](#). They are much less prominent in the Bayesian inversion if not absent. In the SART inversion, at large radius compared to the outer strike point, and below the inner strike point and between it and the HFS midplane, it is possible to observe a series of non field aligned features. These are all reduced or missing from the Bayesian inversion, likely because they

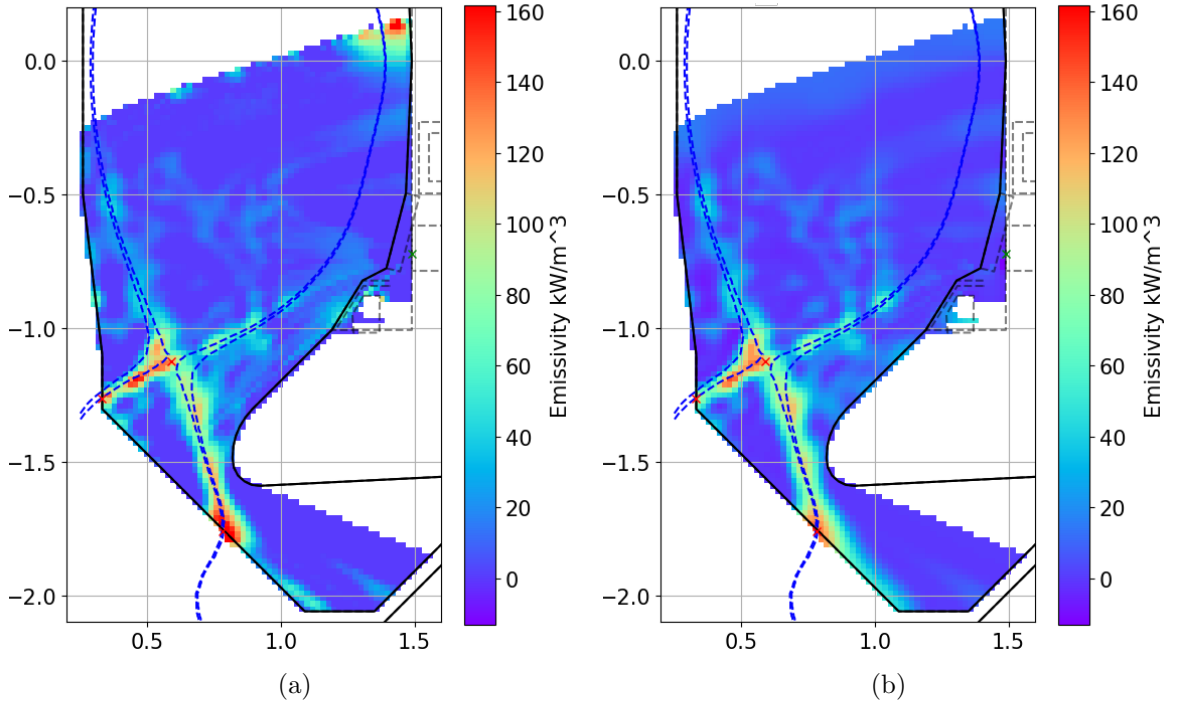


Figure 3.11: Tomographically inverted emissivity using SART (a) and the Bayesian method (b) for data from shot 45473 at 511ms.

are due to low intensity patterns in the power absorbed by the foil, that fall significantly below the uncertainty and are, therefore, penalised. Despite this, the power within 10cm of the x-point ($33kW$ SART, $32 \pm 3kW$ Bayesian) and below the x-point and out of the SXD chamber ($21kW$ SART, $20 \pm 3kW$ Bayesian) is similar between the two. Also the radiation patterns, with strong radiation between the x-point and inner target and at the outer target is maintained, meaning the same physics is captured.

3.2.6.3 Self generated phantom

As a final test, the emissivity in [Figure 3.11b](#) was used as a phantom, to evaluate the difference between the different inversion methods with an emissivity profile similar to what is normally observed in MAST-U. The negative emissivity is set to 0 as well as the region far outside of the plasma (solid black line). The result is shown in [Figure 3.12](#).

Both inversions are close to the phantom even if the emissivity profiles are weaker, corresponding to a measured total power 8.3% (SART) and 6.4% (Bayesian) lower. In the divertor and x-point regions, the power is about 10% less than in the phantom. The SART inversion is less accurate in the SXD chamber and close to the pinhole.

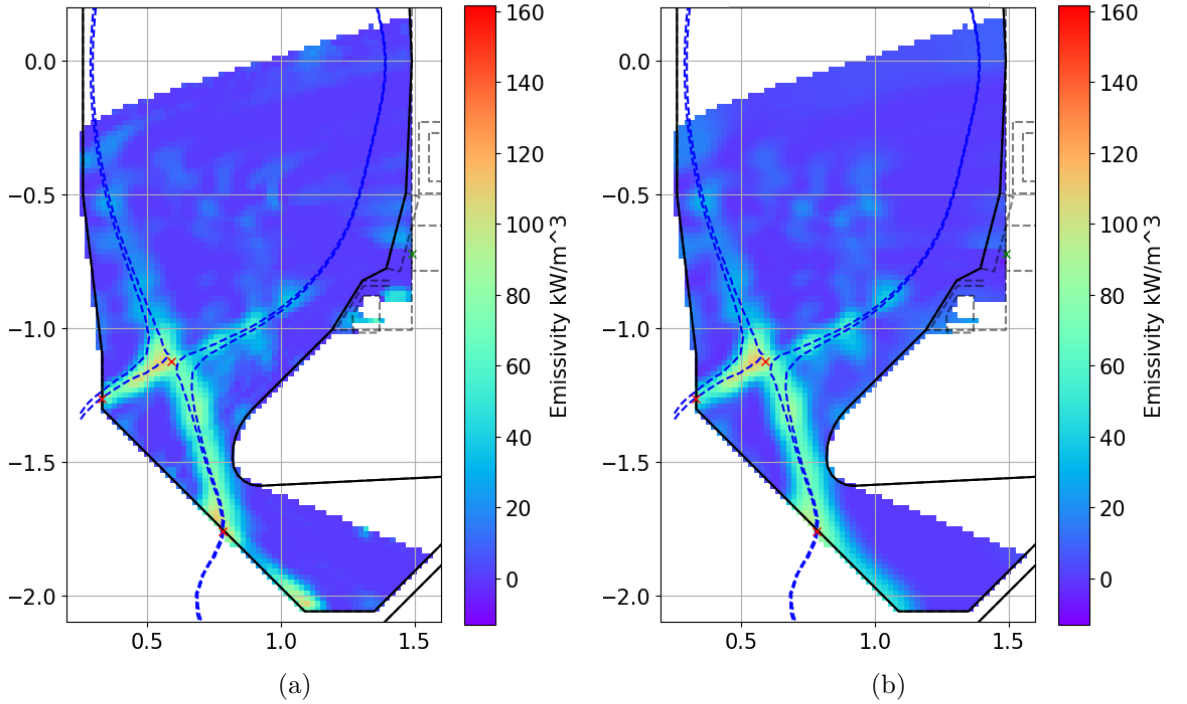


Figure 3.12: Tomographically inverted emissivity using SART (a) and the Bayesian method (b) for data from shot 45473 at 511ms. The same colour scale as Figure 3.11b is used.

Ultimately, being able to measure between 10 and 30% less of the input radiated power, both methods can reliably invert the power absorbed by the foil from a conventional plasma to the emissivity profile. The Bayesian method is preferred to SART because it is less subject to anomalies when inverting real experimental data.

3.2.7 Inversions in the SXD chamber

We only mentioned conventional plasmas before because, during MU01, it was noticed that the radiation for super-x shots could not be properly inverted. In the SXD chamber, the inverted radiation is elongated and moved along the LOS, from the position where it likely to have originated towards the target. To characterise this phenomena, a series of localised toroidal phantoms of constant emissivity of $1.26 MW/m^3$ were forward modelled to the foil and inverted. The centres of the toroidal phantoms were moved along 3 paths indicated by the dashed lines in Figure 3.13: from the outer target to the x-point along the outer leg of a super-x plasma (SXD, black), from the outer target to the x-point along the outer leg of a conventional plasma (CD, green), and along the tiles (surf, magenta). The regularisation coefficient was maintained fixed at $\alpha = 5 \cdot 10^{-3}$, a common value for most experimental

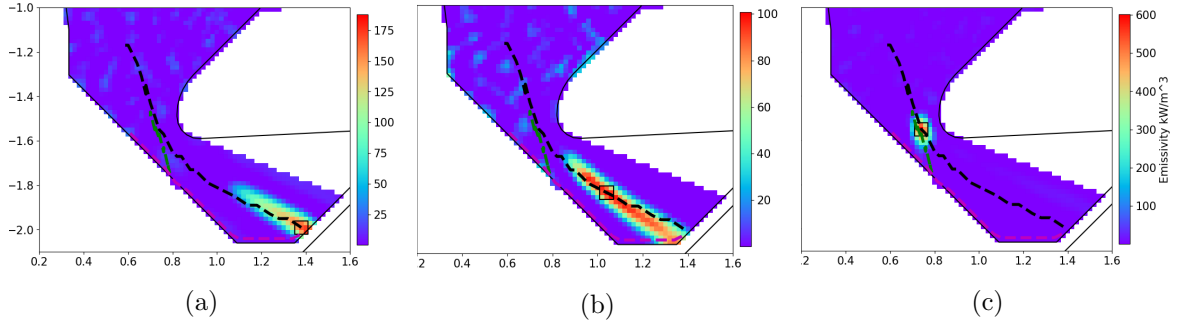


Figure 3.13: Emissivity profiles for 3 toroidal phantoms occupying 9 voxels (indicated by the solid black square) with fixed emissivity of $1.26 MW/m^3$. The radiation from the phantoms is forward modelled to the foil power density, foil temperature and camera counts and then inverted to emissivity with a fixed regularisation coefficient $\alpha = 5 \cdot 10^{-3}$. Inside of the SXD chamber the radiation is elongated along the IRVB LOS. The dashed black line indicates the centre of different phantoms located as to follow the typical shape of the separatrix in a super-x plasma. The green indicates the different shape for a conventional plasma separatrix (the shape at smaller radii is shared with the super-x case so not repeated). In magenta is a scan of location close to the target (surface, surf) to evaluate the precision at the strike point.

conditions. Some of the results moving the centre of the phantom along the super-x separatrix are shown in Figure 3.13. Figure 3.13a and 3.13b show the elongation of the radiation along the IRVB LOS compared to the poloidal extent of the phantom indicated by the square.

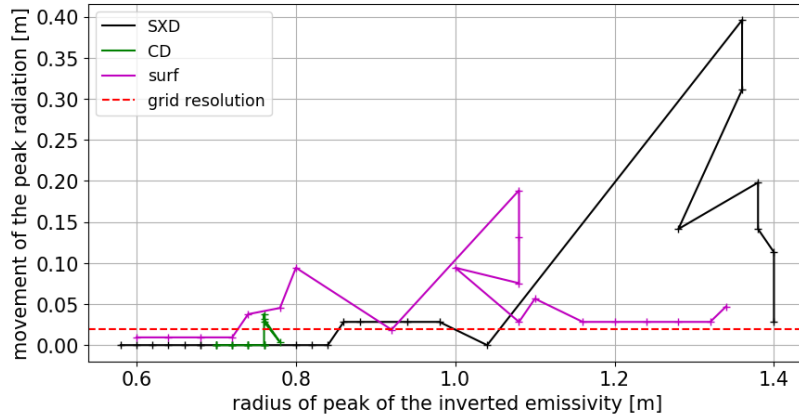


Figure 3.14: Impact of the location of the toroidal phantom centre on the capability to reconstruct its location (distance of peak emissivity and phantom locations). The location of the phantom is moved along 3 paths identified in Figure 3.13.

Important metrics for later discussion are the location of the peak radiation and the radiated power over a larger region. In Figure 3.14 the distance between the centre of the input phantom and the peak of the derived emissivity for the 3 scans is shown. On the x-axis is the radius of the peak of the emissivity profile. In Figure 3.15 the direction and size of the

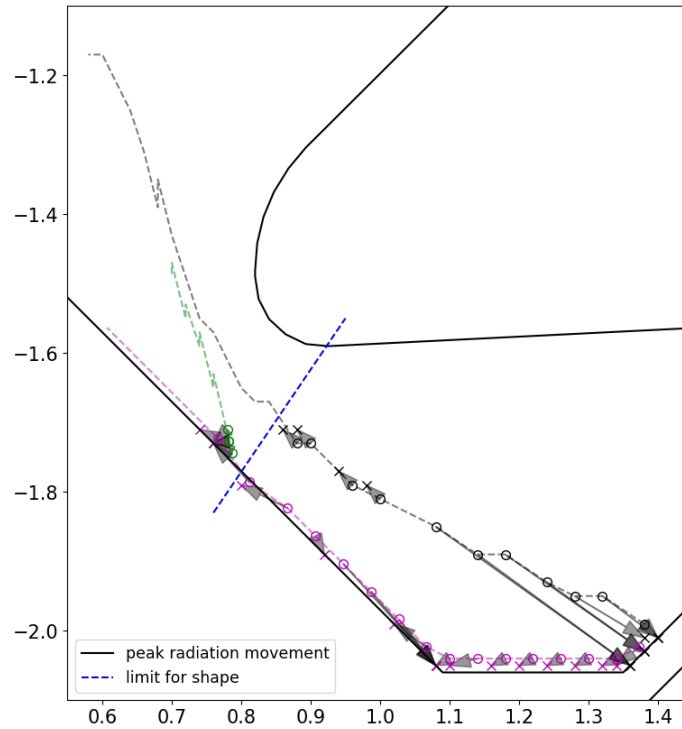


Figure 3.15: Movement of the peak radiation (marked by the 'x') compared to the phantom centre (marked by the circle), indicated by the arrows. In the region right of the blue dashed line the position of the emissivity is considered unreliable.

movement of the peak radiation from the centre of the phantom to the peak of the inverted profiles is shown. A radiator located on the separatrix of a conventional plasma would be marginally affected by the shift in position with an error comparable to the volume grid resolution. Radiators along the super-x separatrix can be located with sufficient precision up to the initial section of the SXD chamber, being pushed towards the strike point afterwards. This is an important finding, as it implies that the IRVB, in the present configuration, cannot directly observe the radiation front detach from the outer target in super-x. A radiator on the tilted tiles (T2, T3) of the *surf* path is significantly affected because it is more closely aligned with the IRVB LOSs, meaning that locating the peak radiator could be difficult in the transition from a conventional to a super-x divertor in an attached regime.

In figure [Figure 3.16](#), the difference with respect to the input of the total radiated power is shown. As observed before in [Section 3.2.6.1](#), when the radiation is concentrated on a surface it is difficult to estimate the total power and this happens too in this case. Radiation at the tiles can be reconstructed with an error up to 60%, while up to 30% in other locations. It is noteworthy that for phantoms that follow the super-x separatrix the error is limited,

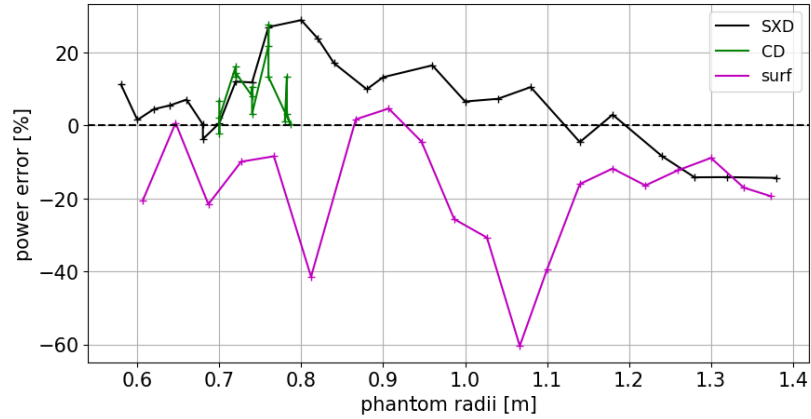


Figure 3.16: Impact of the location of the toroidal phantom centre on the capability to reconstruct its location (error in total radiated power relative to the input). The location of the phantom is moved along 3 paths identified in Figure 3.13.

even when the profile is significantly affected by the elongation. This is an important result as it indicates that even if the local information on the profile is lost, the integrated one about the total radiated losses is still present and can be found with reasonable uncertainty.

It must be noted that these results are valid for the common regularisation coefficient $\alpha = 5 \cdot 10^{-3}$. If the signal level is low and a stronger regularisation is necessary, the radiation is more spread out and this results in the region with insufficient resolution to move towards the x-point. Therefore extra caution should be used in examining data relative to super-x plasmas. Given the above, we can say that the IRVB in the present setup can be used with reasonable uncertainty to determine where high emissivity regions of the plasma are located from the core up to the arbitrarily defined blue dashed line at the entrance of the SxD chamber in Figure 3.15. Beyond that only integrated information like the total radiated power can be obtained.

Now that the Bayesian inversion method is characterised and benchmarked against a commonly used method like SART, we can analyse the inverted data from the first experimental campaign in MAST-U. We will first analyse the same shots from Section 2.5 and compare the results with other diagnostics, then try to find correlations between multiple shots to gain physics understanding and characterise the behaviour of MAST-U plasmas.

3.3 MU01 tomographically inverted results

3.3.1 Metrics from diagnostics

3.3.1.1 Radiator location from IRVB

In order to characterise the change of the radiation distribution along the separatrix a scaling was defined as shown in Figure 3.17. First the poloidal path along the inner (outer) separatrix and inner (outer) leg is found from the EFIT++ magnetic reconstruction. Then the peak of the emissivity within 10cm of the path just defined is found. $(L_{peak} - L_{target})_{sep}$ is the distance along the path between the position on the path closest to the peak radiation and the target. $(L_{x-point} - L_{target})_{sep}$ is the same calculated for the x-point. The scaling \hat{L}_{peak} is the ratio of the two quantities.

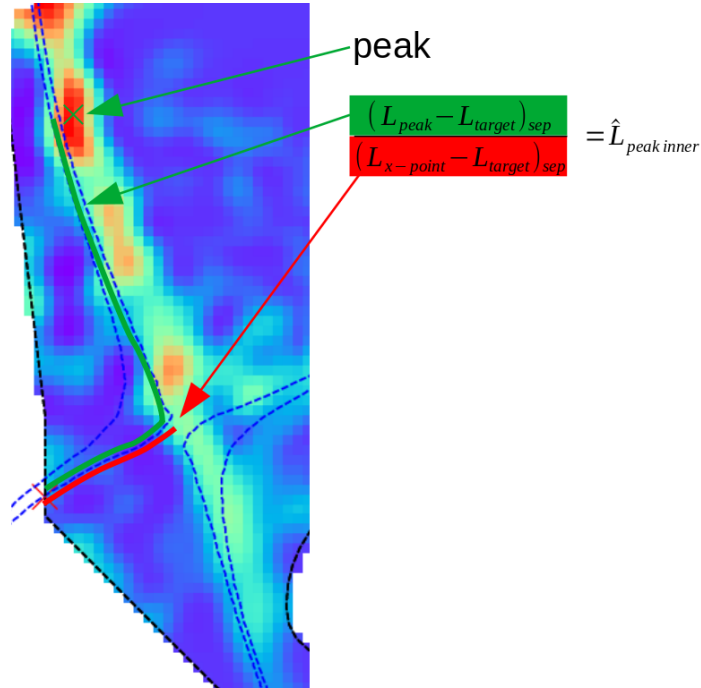


Figure 3.17: How the metric for the movement of the peak radiation along the separatrix is defined. $(L_{peak} - L_{target})_{sep}$ is the distance between the position on the separatrix closest to the peak of the radiation and the target, calculated along the separatrix. $(L_{x-point} - L_{target})_{sep}$ is the same calculated for the x-point. The region where the peak is selected is within 10cm of the inner separatrix. For the radiation at the x-point not to affect the location of the peak radiation, the observed region is first limited to 10cm away from the x-point. When the peak reaches the region of the x-point then the region is extended to the entire separatrix. The same is done on the outer separatrix.

This metric was defined such that when $\hat{L}_{peak} = 0$ the radiator is at the target, referred

to as radiatively attached. When \hat{L}_{peak} increases above 0 the radiation is said to detach from the target. When $\hat{L}_{peak} = 1$ the radiator has moved to the x-point and for numbers greater than 1 it has moved further upstream (the midplane is usually around 5). Radiative detachment is not to be confused with (particle) detachment. With this metric established one can compare its variation with metrics of detachment like target ion flux from Langmuir probes and plasma density.

3.3.1.2 Target current from Langmuir probes

Langmuir probes (LPs) are widely used to diagnose the plasma properties close to solid surfaces. They consist of a small conducting element protruding from a solid surface into the plasma. To this a voltage sweep relative to the rest of the surface is applied and the measured current can be used to infer properties like electron temperature, density and plasma flux to the target. [138] In MAST-U a large number of probes are located in the upper and lower divertor to help characterize the behaviour of the super-x divertor. [139, 140] As explained in [Section 1.7](#) the onset of the detached regime can be identified by the decrease of the target current for increasing upstream density or rollover, so LPs are fundamental. Due to hardware problems a large number of probes were not available during MU01 as shown in [Figure 3.18](#).

This is more severe in the lower divertor which, unfortunately, is the one where most other diagnostics are available. When integrating the current density over the surface of the target bad probes are ignored, while a time step is skipped if a bad probe is within 1cm of the strike point. Nevertheless, the qualitative change of the current to the target can still be used to identify detachment.

3.3.1.3 Resistive bolometers

As mentioned in [Section 3.1](#) the IRVB does not have the HFS midplane in its useful FOV. To examine the change in radiated power there, the resistive bolometer LOSs CH26 and CH27 will be used. As per [Figure 2.9](#) these are part of the tangential midplane fan and correspond to the LOS closer to the central column (CH27) and the one immediately further away from it (CH26), with a tangency radius of 36.5 and 49.6cm respectively, compared to a central column radius of 26.1cm. When the radiator moves upstream along the HFS separatrix it stops at the midplane and from there penetrates further in the core forming the MARFE-like

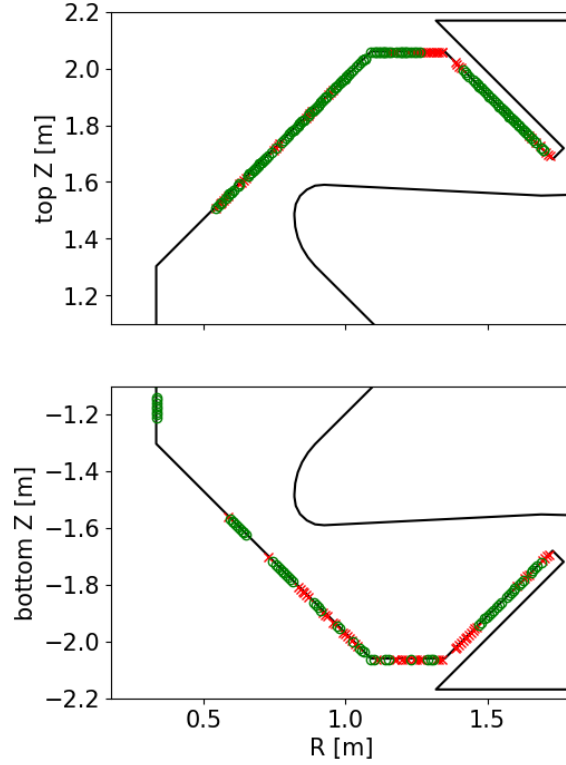


Figure 3.18: Location of the working (green) and broken (red) Langmuir probes for MU01. The probes are in two toroidal locations (sector 4 and 10) but are shown overlapped.

structure. When this happens it is observed that the brightness ratio $CH27/CH26$ increases, indicating strong radiation close to the separatrix. Later when the radiation moves into the core the brightness of $CH26$ is also increased, and the $CH27/CH26$ ratio decreases. The increase in the $CH27/CH26$ ratio can therefore be used to determine when the radiation is increasing at the midplane. $CH26$ has a shorter integration path into the plasma compared to $CH27$, although the difference is small. If the emissivity is uniform, the different path lengths will return different brightnesses. To compensate for this, the brightness of $CH26$ is multiplied by the ratio of L_{CH27}/L_{CH26} .

Additionally, the poloidal view of the resistive bolometer system can be used, even considering the large uncertainty because of the dead channels shown in [Figure 2.9](#), to give an approximate figure for the total core emissivity that can then be compared with the IRVB. In order to calculate the radiated power from the brightness it would be necessary to perform a tomographic inversion, but the resolution is deemed insufficient. Instead, an integral approach, the weighted sum method, is used as done before for the JET resistive bolometer system. [141] Here it is assumed that the line integrated emission from each LOS is generated

at the radial distance of the magnetic axis. A weight, corresponding to the vertical distance between LOSs at the same radius, is applied to the brightness. In JET the result using this approximation is shown to be within 10% of the phantom used and, not requiring an actual inversion, more resilient to noise in the data. In MU01 the LOS close to the x-point are not operational, as shown in [Figure 2.9](#), therefore this estimate is likely an underestimation of the real core emission. As the line integral along the LOS includes regions between the HFS separatrix and the central column and regions outside of the LFS separatrix, this estimate is more representative of the radiation between upper and lower x-points rather than only the core plasma.

The comparison with IRVB is done assuming emissivity up/down symmetry. Even if fuelling is symmetric, up/down symmetry can be affected by the vertical displacement of the plasma and the fact that all shots are run with ion ∇B drift downward. Vertical displacement was maintained very low in most cases, below 1cm. As will be shown later, the direction of the ion ∇B drift downward was expected to have a significant impact on the up/down power sharing (40-60% respectively of the power crossing the separatrix outward). [142] Conversely recent SOLPS simulations indicate that, likely because of the relatively low plasma current in MU01 compared to MAST-U design ($I \leq 0.75MA$ instead of 2MA), the effect of drifts is limited and the errors introduced by the up/down symmetry approximation are marginal.

For ease of analysis the volume in the IRVB FOV is partitioned similar to [143]. The regions are shown in [Figure 3.19](#). Additionally, the radiation around the legs and outside the x-point region is also recorded. In order to compare the emission with the resistive bolometer system, the *core+SOL* region is composed of the core plus both inner and outer SOL region.

3.3.1.4 Upstream density

Lastly an important metric for the characterisation of detachment is the upstream SOL density. During MU01 it is believed that the plasma was effected by MHD modes, that could appear or not during repeats or density scans. The upstream density is preferred here as an indicator for detachment progress rather the core density, as is sometimes done, because there is then no need to assume that a direct proportionality exists between the two. This, however, requires the upstream density to be estimated. The Thomson scattering system (TS) on the midplane can measure the electron density across the LFS separatrix region, but it is characterised by strong gradients (see [Figure 3.29](#) as an example). A small

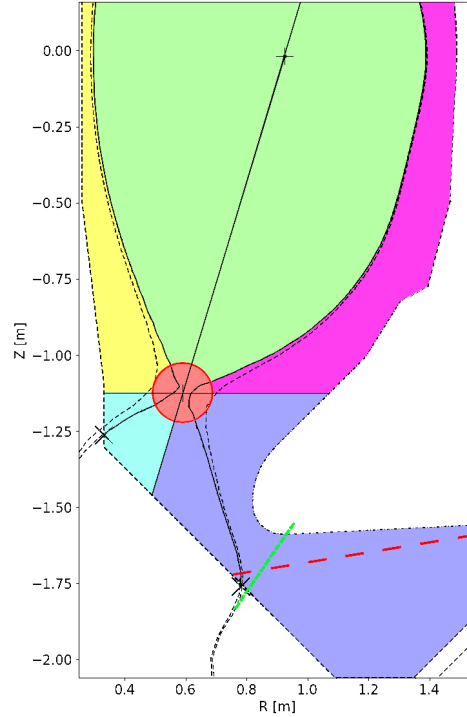


Figure 3.19: Regions in which the plasma volume is divided similar to [14]: red = x-point (radius of 10cm around x-point), green = core, yellow = inner SOL, light blue = inner leg and SOL below the x-point, blue = outer leg and SOL below the x-point, magenta = outer SOL. The distinction between inner and outer leg region is made via the extension of the line between magnetic axis and x-point. The radiation within 10cm of the legs and out of the x-point region is also separately accounted for. The green dashed line indicates the left limit of the SXD chamber region limit; that is also the limit below which the radiation distribution is considered unreliable. The red dashed line indicates the upper limit of the MWI diagnostic FOV.

error in the calculation of the separatrix location can yield a large difference in upstream density, and at the moment the precision of the EFIT++ magnetic reconstructions is yet to be determined.

For these reasons the upstream temperature is here preferred to be estimated with an analytical model and the upstream density is defined as the density at the LFS midplane corresponding to that temperature. The analytical model used is the variation by Cowley [82] of the DLS model [22] as described in Section 1.11.2. The expression for the upstream temperature is Equation 1.19 where the location of the front is assumed to be at the target ($s_{\parallel,f} = 0$). The parallel heat flux at the midplane is calculated as the input power (Ohmic and from NBI, accounting for beam absorption) minus both the core radiated power (from resistive bolometers as mentioned above) and the variation in stored energy, all divided by

the cross section at the midplane. This is obtained using a fixed characteristic SOL power decay length at the midplane (λ_q) of 1cm. q_{\parallel} is then scaled linearly from the midplane to the x-point to account for a progressive power inflow from the core.

3.3.2 L-mode and detachment characteristics

The tomographically inverted emissivity from the shot 45473 is shown in [Figure 3.20](#). As for the line integrated data, it is possible to observe the movement of the inner leg, but also the outer one can now be examined. In these conditions, Ohmic L-mode conventional divertor, the outer leg radiatively detaches after the inner one and it has a lower emissivity. After the formation of the XPR, the radiator moves along the inner separatrix. Here it seems that the radiation is concentrated inside the core, but the resolution is not deemed enough to say it for certain. Conversely, when the HFS MARFE-like structure grows in the later stages of the discharge, a general movement of the radiation inward can be observed. In [Figure 3.20e](#) the radiation is still concentrated at the midplane, only outside the IRVB FOV. This sequence of events is similar to what is expected from [Section 1.8](#). The radiation seems to move forming small continuous spots of higher radiation rather than in a continuous manner. This is most likely due to irregularities of the foil properties that cause similarly irregular changes of the measured foil absorbed power (similar to what observed in [\[99\]](#)).

This shot was fuelled from HFS_MID_U02, a valve on the HFS 26cm above the midplane (see [Figure 2.19](#)), with a usually negligible impact on up/down symmetry. Another factor in up/down symmetry is how close the two separatrices, defined by the upper and lower x-point, are. This is expressed by the δR_{sep} parameter equal to the radial distance between the separatrices at the LFS midplane. It has been shown that a small change around $\delta R_{sep} = 0$ has a significant influence on the up/down and inner/outer leg power balance. [\[142\]](#) For this shot δR_{sep} evolved from -2mm to +5mm, with λ_q of 4-7mm at the midplane (estimated with LPs [\[140\]](#)); in TCV double null (DN) experiments, with a similar $\lambda_q=3-6$ mm, this would have caused a change of about -25 to +50% of the heat flux to the lower divertor. [\[38\]](#) This might not be happening here, as a particle flux difference from LPs is present but limited (see [Figure 3.21c](#)), however up/down particle flux symmetry does not necessarily imply heat flux symmetry. Moreover, beyond some noise caused by a strike point sweep and the presence of bad probes, the difference stays fairly constant. For this shot, also, neither the high speed camera (see [Figure 3.23](#)) or the resistive bolometer display dramatic asymmetries, indicating

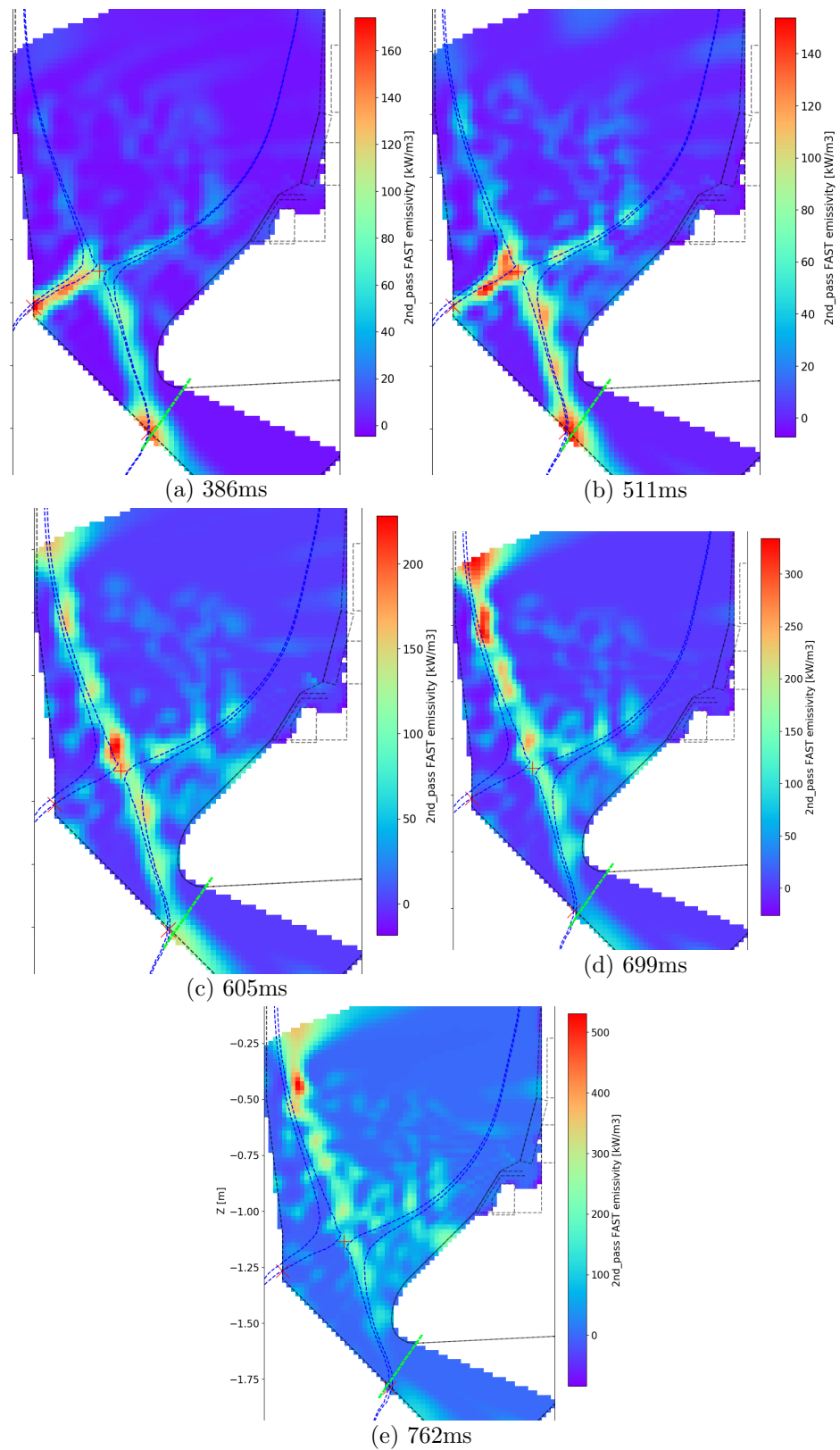


Figure 3.20: Changes in emissivity distribution in a density ramp for a conventional divertor, L-mode, Ohmic plasma (shot 45473, Double-null and 650KA), same as Figure 2.23. First both inner and outer target are radiatively attached (a), then the inner detaches (b) to form an x-point radiator while the outer detaches too (c) and finally a radiation MARFE-like structure on the high field side (HFS) midplane (d). Further increasing the density the structure moves inward (e) leading to a disruption (the radiation peak is here too close to the midplane and out of view). Note that the all images have different colour bar ranges. The limit below which the radiation distribution is considered unreliable is marked in dashed green.

that MAST-U could be less sensitive to δR_{sep} than other devices. An important parameter to assess the quality of the discharge is the inner gap, the distance between the central column and the separatrix. This was maintained higher than 4cm throughout the shot, much larger than λ_q thus guaranteeing no local interaction of the plasma with the central column.

These observations can now be compared with other diagnostics as shown in [Figure 3.21](#). [Figure 3.21a](#) shows again how the inner leg detaches radiatively before the outer. Noteworthy is that the movement of the radiating regions on both legs seems to be gradual, with a progressive movement along the separatrix. This behaviour can be compared with expectations regarding the stability of the thermal front from the DLS model (see [Section 1.11.2](#)). [Figure 3.22](#) shows the profile of C_1 for the inner leg (solid line) and the outer (dashed line) for three reference times during the movement of the radiator. The data shown regards the hottest flux tube in the leg, as it is the harder and last to detach. The C_1 profile is always decreasing on the inner leg, up to a location very close to the x-point. This leads to the prediction that the thermal front should move sharply from target to the x-point as soon as the front forms at the target. This contrasts with the observations, as the radiator on the inner leg moves gradually. A SOLPS simulation that reproduces the evolution of detachment for this shot via an increase of the upstream density indicates that, for the inner leg, the movement of the radiator towards the x-point causes the radial heat transport out of hottest flux tube of the leg to decrease. This equates to an increasing $q_{\parallel,u}$ for increasing degree of detachment, that would have a stabilising effect. Another possibility is the that as the front moves away from the target and the plasma temperature there decreases, carbon sputtering is suppressed, causing a decrease of the carbon fraction, causing a further stabilising effect. The latter, at least, is not confirmed by the simulations. In these simulations, the radiated power in the inner leg is due almost entirely to carbon, but radiation constitutes less than 10% of the total power dissipated in the leg, with the majority being due to ionisation. The carbon fraction in the divertor decreases from 2 to 1% in the divertor as detachment progresses, implying a minor reduction of the power dissipated in the leg due to reduced sputtering.

The C_1 profile is always increasing on the outer leg, indicating that the location of the front is stable and it should move gradually with increasing detachment. This was indeed verified by the IRVB measurements, even if the irregularities of the foil prevent observation of a truly smooth transition.

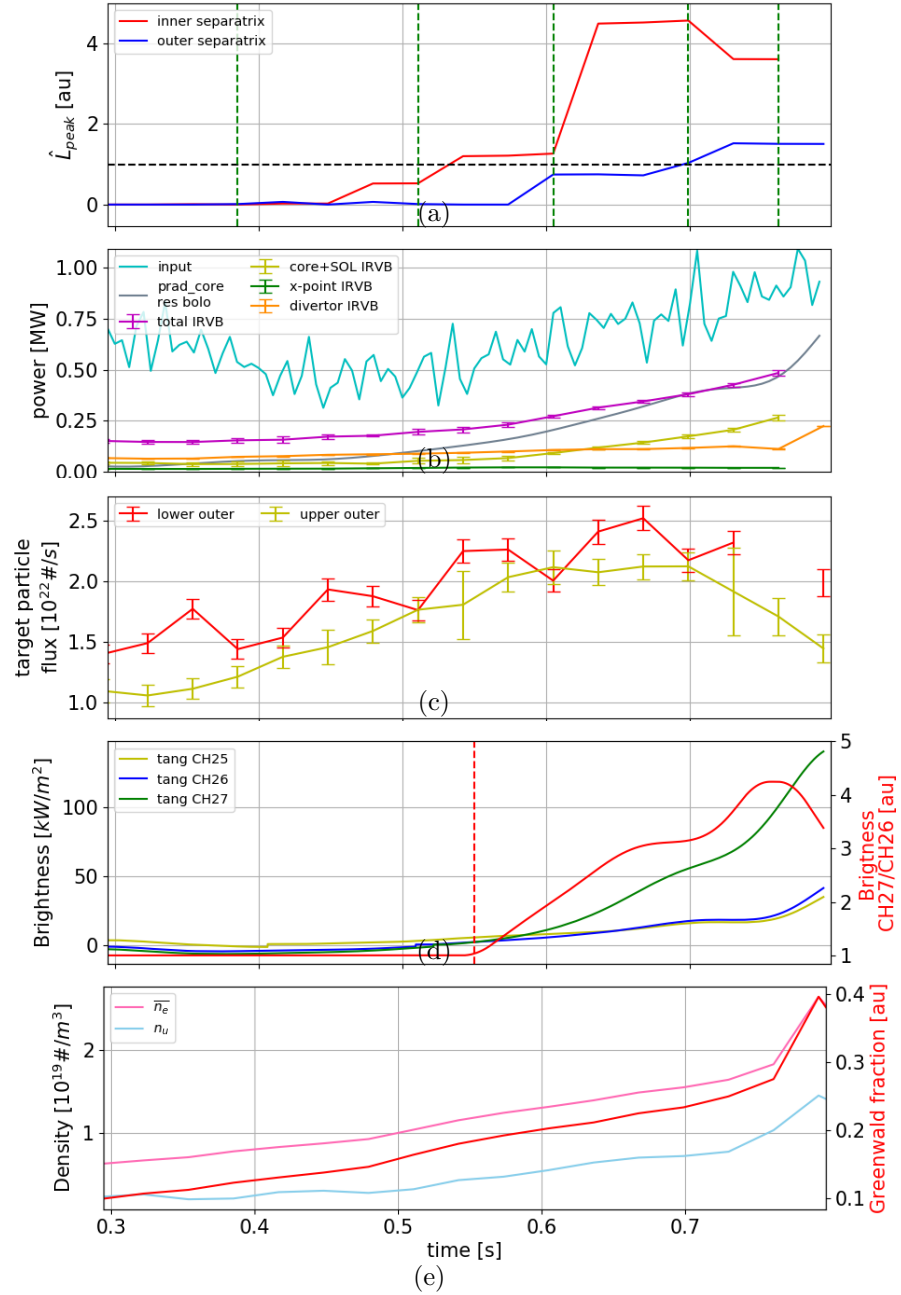


Figure 3.21: Results from different diagnostics related to detachment for a conventional divertor, L-mode, Ohmic plasma (shot 45473, Double-null and 650KA). (a): movement of the peak radiator along the separatrix as per the scaling defined in Section 3.3.1 for the inner and outer separatrix. The vertical dashed lines indicate the time that corresponds to the data in Figure 3.20. (b): Components of the global power balance: input power defined as the sum of Ohmic and NBI minus the variation in stored energy. The IRVB power is obtained by adding all voxels at $Z < 0$ then multiplying by 2, therefore assuming up/down symmetry. The divertor region is obtained adding the inner leg + SOL and outer leg + SOL region (see Figure 3.19). (c): particle flux from Langmuir probes at the outer targets. The oscillation on the lower target is due to a strike point sweep close to a dead probe. (d): brightness for the tangential LOSs CH25, CH26 and CH27 (CH25 and CH26 scaled up to match CH27 integration path length) and (red) the ratio of the two, showing the growth of the MARFE. The vertical red line corresponds to when the CH27/CH26 ratio starts to grow. (e): averaged core density (\bar{n}_e) and upstream density from TS as per Section 3.3.1 (n_u).

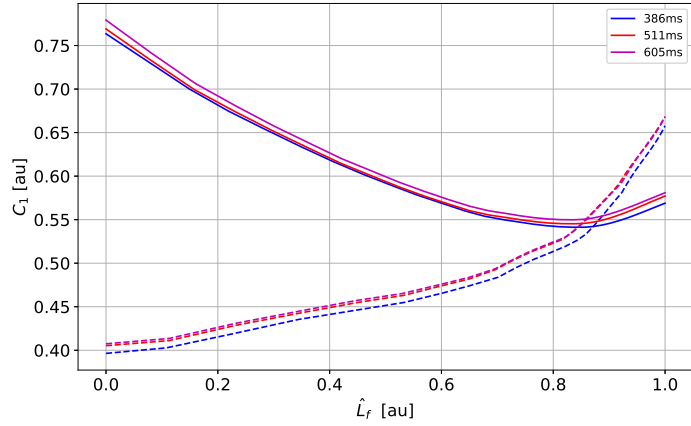


Figure 3.22: Variation of the C_1 parameter as per Equation 1.24 in the shot 45473 for a front position from target ($\hat{L}_f=0$) to x-point ($\hat{L}_f=1$). Solid lines for the inner leg, dashed for the outer.

One point is missing in Figure 3.21c, but the particle flux roll over seems clear, happening at about the same time, or slightly after, radiative detachment.

From Figure 3.21b one can see that the total radiated power from the IRVB is below the input power available to dissipate. The radiated power in the core from resistive bolometry and IRVB match up to the start of the inner leg detachment. From there the resistive bolometer is measuring a higher power in the core. This is not what would be expected. At the beginning of the detachment process the x-point region, and even more the legs, (the outer leg has usually a lower emissivity, but its weight in power is higher because of the larger radius and poloidal spread) dominate radiatively. These regions are out of the FOV of the resistive bolometry system (because of the bad LOSs) so a lower power is to be expected until significant radiation climbs along the separatrix. An explanation for this not happening is that the fuelling location for this shot is above the midplane, out of the IRVB FOV, and in Section 2.4.6.1 it was already noted that strong radiating regions can be localised there. The resistive bolometric LOS CH6 (close to the fuelling location, see Figure 2.9) from ~ 500 ms shows a noticeably higher brightness than the others and could explain the over-prediction from the early stage of detachment. Later in the discharge the MARFE-like structure on the HFS midplane becomes dominant and, because it is outside the IRVB FOV, a higher measured power is to be expected. Figure 3.23 shows high speed visible imaging data showing the visible emission profile at the beginning and end of the MARFE-like structure growth. It can be observed that the visible emission is stronger at the top of the machine and that the strong emission region grows from the plasma fuelling

location. An increase in visible light emission could also be related to the presence of a cold plasma, where molecular and recombination reactions become important. The visible light brightness increase could be therefore contributed by a localised cooling of the plasma in the HFS SOL because of the increasing fuelling of cold gas. The strong visible light emission can also be due to electron ion excitation of the dissociated gas fuelled from the valve. For these reasons it is not clear if the interaction of the fuelled cold gas with the plasma represents a significant contribution to the formation of the MARFE-like structure compared to the radiation-condensation phenomena driven by impurities observed during MARFEs. [56]

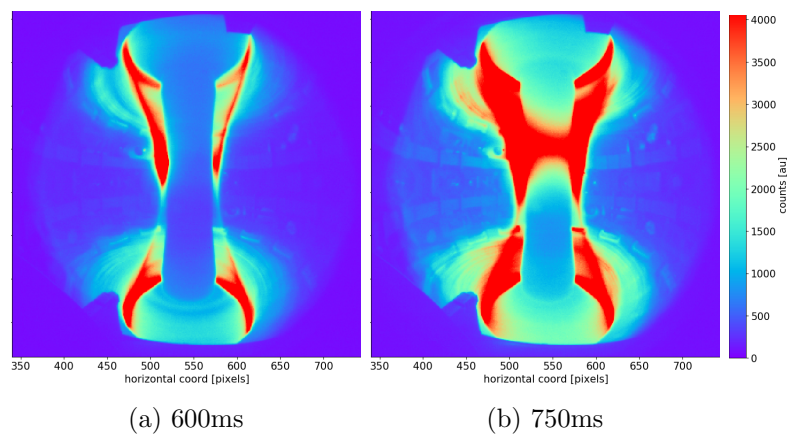


Figure 3.23: Data from the high speed visible camera for shot 45473 showing the minor up/down symmetry in a shot fuelled only by the midplane HFS_MID_U02 valve at the beginning of the formation of the MARFE-like structure (a). At the end of its growth (b) the up/down asymmetry is more significant and centred close to the fuelling location (see Figure 2.19).

The growth of the MARFE-like structure on the HFS midplane can be inferred by the increase of the ratio of CH27 and CH26 brightnesses, shown in Figure 3.21d. The CH27/CH26 ratio starts to rise from the early stages of detachment, after the inner leg radiatively detaches. This is consistent with IRVB and HSV measurements, as the emissivity on the inner separatrix starts to increase early on too. The CH27/CH26 ratio plateaus after the outer leg detaches both radiatively and from LPs. It is hard to tell in this process when a proper MARFE starts, if it does. The growth of the MARFE-like structure is gradual according to resistive bolometry and HSV measurements, consistent with the slow movement of the high density (more than twice the core peak) and low temperature (below 10eV) region towards the magnetic axis, as observed by TS from around 600ms. The presence of an XPR at around 600ms between the divertor leg’s radiative detachment and stronger signs

of a proper MARFE from TS, agrees with analytical predictions that the XPR can more easily be achieved in lower power discharges [74]. This is also supported by recent data from the newly installed x-point imaging system, that shows deeper detachment and the neutrals escaping from the SXD to the main chamber more easily in lower power discharges. The transition to MARFE, though, is fast, requiring a small increase of the upstream density, due to carbon being the dominant impurity in the plasma. This apparent consistency with predictions is only qualitative, requiring further analysis and parameter scans to be confirmed.

Finally [Figure 3.21e](#) shows how the core and upstream density both rise during the discharge. This mirrors the fuelling, that was linearly increased during the discharge from 0.3s.

The consistency in the order in which the legs undergo radiative detachment, the MARFE-like structure formation and their relation with the particle flux roll over and upstream conditions can be verified comparing data from different shots. Within the same session another 3 discharges were performed to complete a density scan from attached to deeply detached by increasing the fuelling. The data from the 4 shots can be combined by using the plasma upstream density as a coordinate. The relation between target particle flux and radiative detachment is shown in [Figure 3.24](#). There is a significant spread in the change of upper particle flux with detachment. This is significant because the upper target is well diagnosed with LPs, so the spread for $n_u > 0.5 \cdot 10^{19} \# / m^3$ is most likely due to imprecision in determining n_u with the method mentioned in [Section 3.3.1](#). The spread on \hat{L}_{peak} and its almost step-wise appearance are most likely due to the non uniformity of the foil mentioned before. Even considering this, it can be observed that the behaviour of 45473 for increasing upstream neutral density is consistent across shots:

- Radiative detachment happens first on the inner target. This is gradual, different to what is expected from the DLS model of the thermal front movement [22, 82]
- Radiative detachment on the outer leg, slightly earlier or at the same time as particle flux roll over, with a gradual movement in agreement with DLS predictions. The emissivity on the HFS separatrix starts increasing.
- The radiation moves upstream along the HFS separatrix towards the midplane and the MARFE-like structure emerges, impacting the core plasma

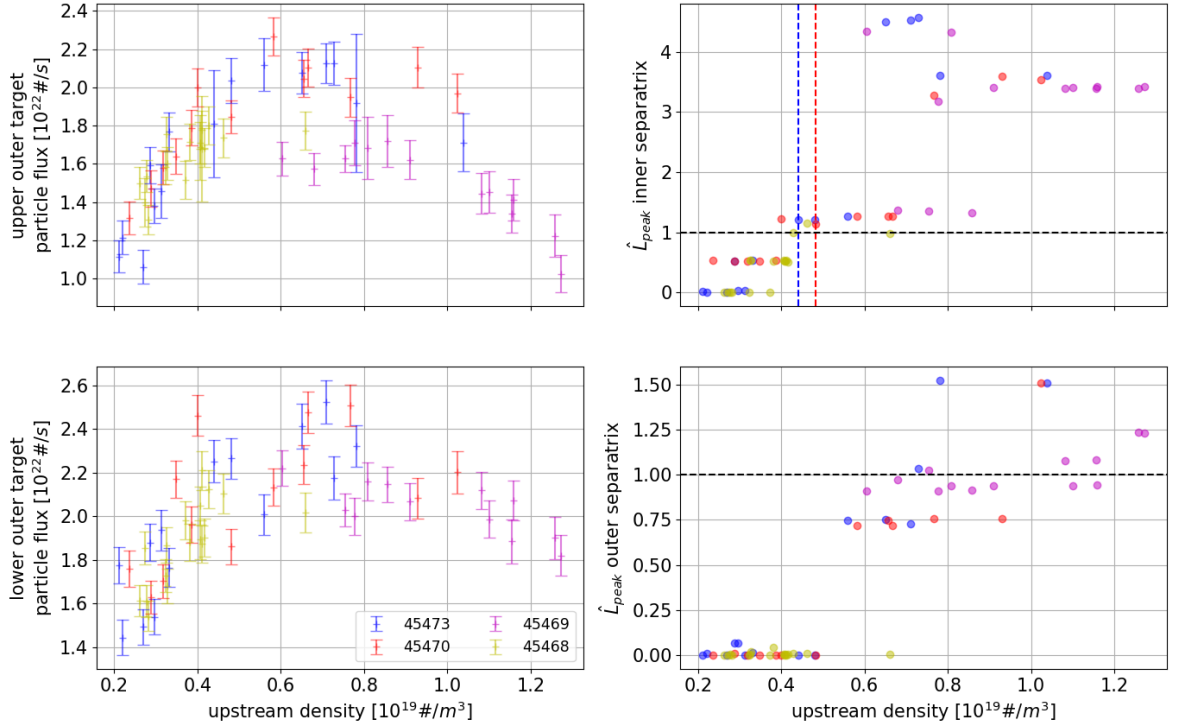


Figure 3.24: Comparison of the target current, providing the detachment condition from particle flux roll over, with the movement of the emission radiator, indicating radiative detachment. The vertical coloured dashed line indicates the beginning of the growth of the MARFE-like structure on the HFS midplane.

3.3.3 H-mode and detachment characteristics

H-mode discharges were obtained in MAST-U by increasing the power injected in the core plasma via NBI, increasing the power traversing the separatrix beyond the threshold for H-mode. H-mode plasmas are characterised by steep temperature and density gradients in the pedestal and ELMs, that can potentially affect the detachment process. The two NBIs (located as per [Figure 2.9](#)) were, for MU01, not capable of running at full nominal power (2.5MW each) and, on top of that, the fraction of the beam energy retained by the plasma was difficult to quantify, due to the beams being still in commissioning. Additionally, it was found after the conclusion of MU01 that the SS beam had been misconfigured for the majority of the campaign, leading to a much lower proportion of the injected neutrals being injected at the full beam energy. For these reasons the beam absorption are estimated to be roughly 40% for the south west (SW) and 80% for the south (SS) of the NBI injected energy.

The data shown in [Figure 3.25](#) and [3.26](#) is in regard to the same high power discharge

as in [Section 2.5](#). Here both NBIs are used and δR_{sep} stays within 2mm but the plasma is mainly fuelled from the valve LFSD_BOT_L0102, located inside the SXD chamber on the flat top wall. This means that the plasma is most likely not up/down symmetric. The inner gap was maintained at around 5cm.

This sequence of events is significantly different than that of the low power case. The outer leg starts detaching first, but then appears to stop 2/3 of the way to the x-point. Then the inner leg detaches completely and the radiation climbs up the HFS separatrix, with the outer leg only fully detaching later. The radiation profiles are sharper than in [Figure 3.20](#) because of the higher signal level and lower regularisation ($\alpha \sim 2.5 \cdot 10^{-3}$ rather than $\sim 4 \cdot 10^{-3}$ in [Figure 3.20](#)) and the poloidal spread seems similar for both legs. As shown in [Figure 3.26e](#) the ratio CH27/CH26 started to grow at the beginning of the shot, but does not provide the same clear marker as in [Figure 3.21e](#), therefore indicating that the MARFE never develops. This is confirmed by the lack of a cold and dense region on the HFS from TS. The initial CH27/CH26 ratio increase could be due to plasma recycling on the inner wall, but the inner gap is much larger than λ_q , suggesting that this early signal might be an artifact due to the relatively low signal level of the two resistive bolometer LOSs. More significant is the increase in the ratio after 800ms, when the signal is much stronger, but this never develops as in [Figure 3.21e](#), indicating that the formation of the MARFE-like structure at the midplane is halted at an early stage. From LPs the current is similar for the upper and lower divertor, indicating minor up/down asymmetry.

Fuelling from the LFSD_BOT_L0102 valve was increased from 400ms throughout the discharge up to 1000ms and then maintained constant. At about 800ms an event occurs such that there is a net separation between the upper and lower divertor. This is confirmed also by comparing the resistive bolometer CH4 and CH13 where CH13, pointing towards the lower part of the separatrix, measures significantly higher radiation after 800ms. From the fast camera images in [Figure 3.27](#) the asymmetry can be observed too, especially in the divertor region, after 800ms.

The core density decreases while the upstream density increases, indicating that the core might start being negatively affected by the fuelling. At this stage a dense region is observed with TS, penetrating the core from the HFS from 800ms, but then does not progress inwards, indicating the initial growth of a MARFE-like structure at the midplane, but which then stops. This is confirmed by the brightness of the tangential resistive bolometer LOSs

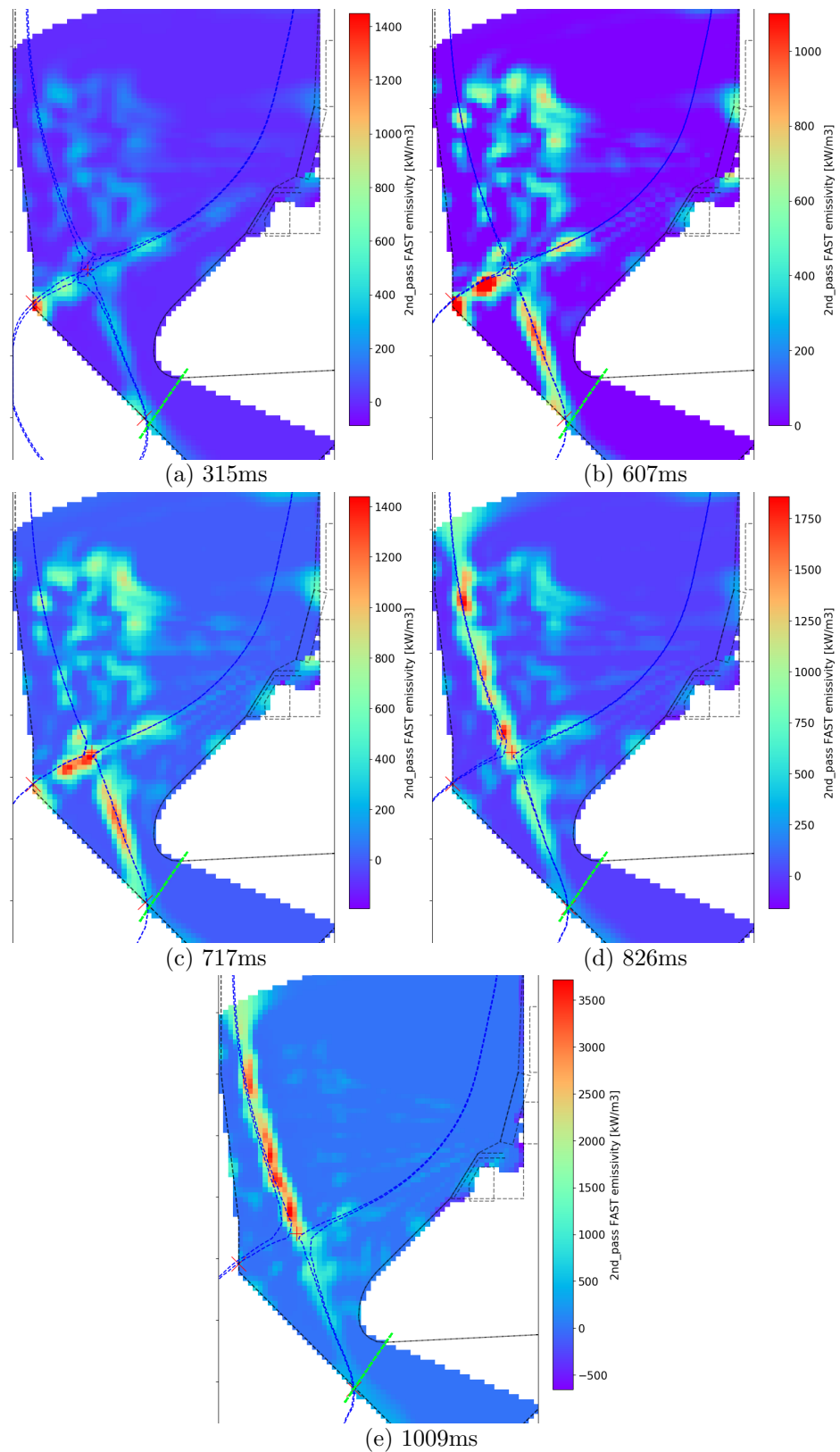


Figure 3.25: Changes in emissivity distribution in a density ramp for a conventional divertor, H-mode, NBI heated plasma (shot 45401, Double-null and 750kA), same as [Figure 2.25](#). First both inner and outer target are radiatively attached (a), then the outer starts detaching (b) and closely after the inner to form an x-point radiator (c). Then a radiation MARFE-like structure forms on the high field side (HFS) just below the midplane (d) and moves slightly back towards the x-point for decreasing core density (e). A disruption then follows. Note that the all images have different colour bar ranges. The colour range in (b) was adapted to show the early detachment of the outer leg. The limit below which the radiation distribution is considered unreliable is marked in dashed green.

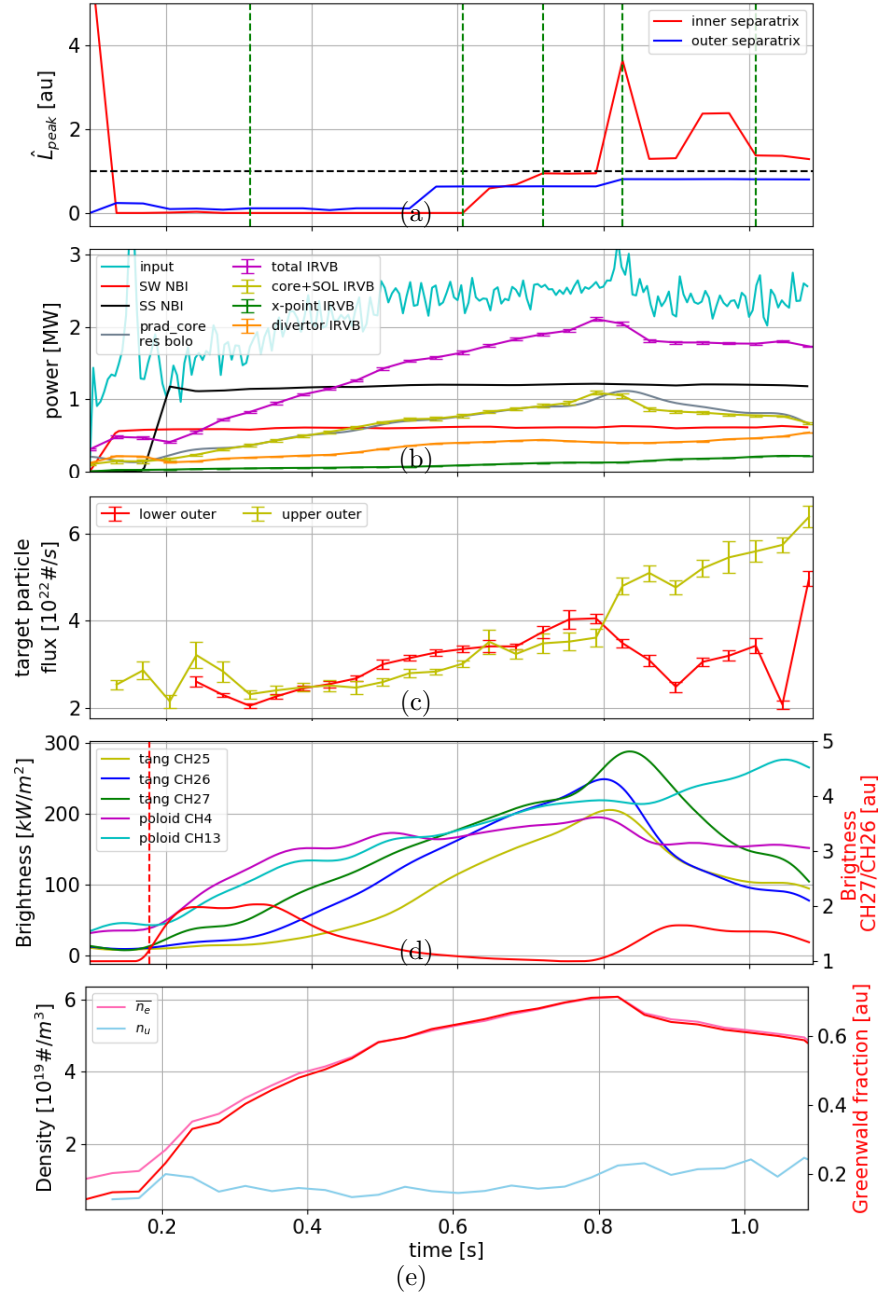


Figure 3.26: Results from different diagnostics related to detachment for a conventional divertor, H-mode, NBI heated plasma (shot 45401, Double-null and 750kA). (a): movement of the peak radiator along the separatrix as per scaling defined in Section 3.3.1 for the inner and outer separatrix. The vertical dashed lines indicate the time that corresponds to the data in Figure 3.25. (b): Components of the global power balance: input power defined as the sum of Ohmic and NBI minus the variation in stored energy. The NBI power is already scaled by the corrective factors 0.4 and 0.8 for SW and SS respectively. The IRVB power is obtained by adding all voxels at $Z < 0$ then multiplying by 2, therefore assuming up/down symmetry. The divertor region is obtained by adding the inner leg + SOL and outer leg + SOL region (see Figure 3.19). (c): particle flux from Langmuir probes at the outer targets. (d): brightness for the tangential LOSs CH25, CH26 and CH27 (CH25 and CH26 scaled up to match CH27 integration path length), (red) the ratio of the two, showing the growth of the MARFE, and poloidal LOSs CH4 and CH13. The vertical red line corresponds to when the CH27/CH26 ratio starts to grow. (e): averaged core density (\bar{n}_e) and upstream density from TS as per Section 3.3.1 (n_u).

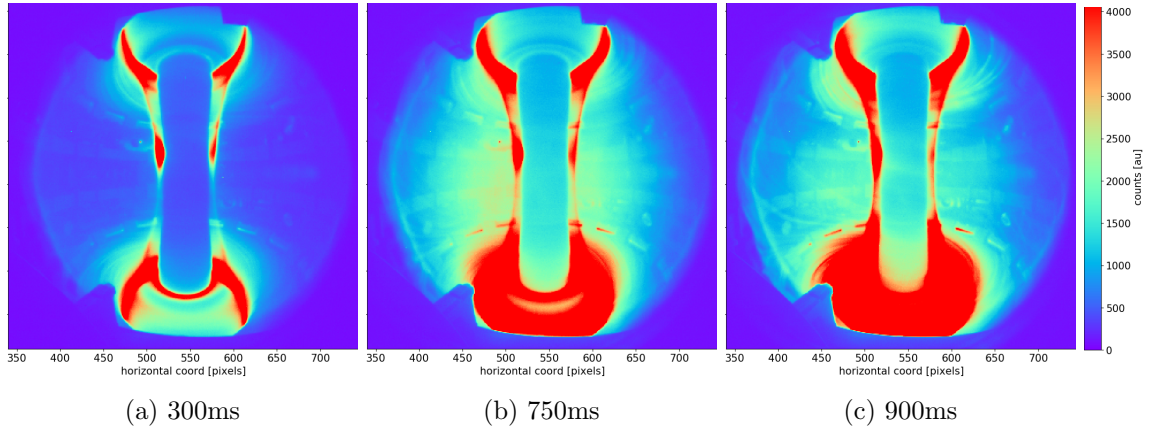


Figure 3.27: Data from the high speed visible camera for shot 45401 showing the level of up/down symmetry when only the midplane HFS_MID_U02 valve is used (a), the valve LFSD_BOT_L0102 is initially used (b) and when the core density decreases (c).

decreasing.

The fact that in the upper divertor the current increases with n_u while it decreases in the lower can indicate that the upper is still attached while the lower is detaching. This could be confirmed by T_e from LPs averaged around the strike point, that steadily decreases from 8 to 4eV from 400 to 1000ms for the lower outer leg while on the upper outer it drops from 12 to 8eV. The current gaps in LPs coverage make, at this moment, this interpretation tentative. This could mean that the detachment of the two divertors could be controlled independently. This will require further examination with a better diagnostic coverage of the upper part of the machine (LPs, radiative, etc.).

From Figure 3.25d and 3.25e it seems that towards the end of the pulse the radiation penetrates into the core of the plasma. This is similar to what is observed in Figure 3.20 but happens here at a much earlier stage of the MARFE-like structure growth. This might indicate that the radiation is indeed still on the separatrix and there is an issue in the exact location of the separatrix itself or IRVB alignment.

From Figure 3.26b it can be observed that the core radiation from IRVB quite accurately matches the estimate from the resistive bolometer up to when the inner leg completely detaches radiatively. This is a fair comparison, as up to that point no significant radiation from the detachment process reached the resistive bolometer FOV. After 800ms strong radiation is observed close to the x-point, missed by the resistive bolometer, and close to the mid-plane, missed by the IRVB, and the two coincidentally compensate. Because of the strong asymmetry, the radiation is likely overestimated by the IRVB after 800ms. It is noteworthy

that even after the outer leg radiatively detaches there is still significant radiation dissipated in the *divertor* region, mainly due to the outer leg and related SOL, with a significantly larger influence of the x-point than in the low power case. The real total radiated power probably peaks at about 1.5MW, amounting to more than half of the input power of which, even during detachment, the core and especially the region around the separatrix provides the largest component.

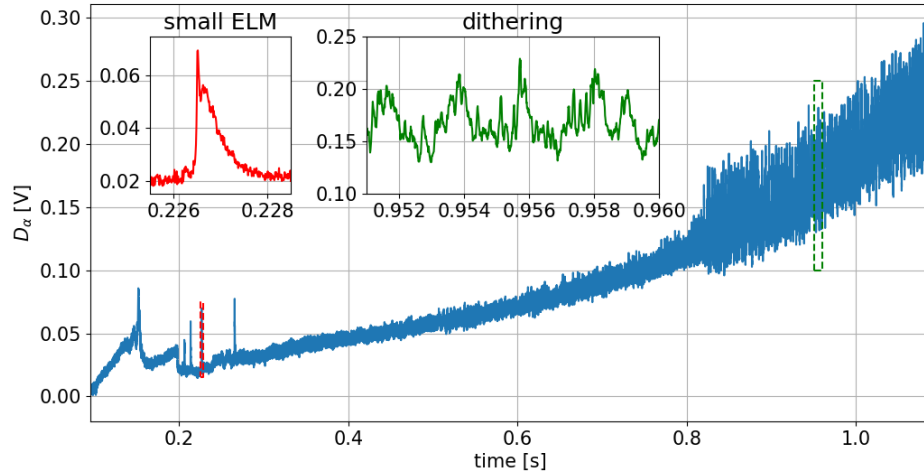


Figure 3.28: Hydrogen D_α emission from the midplane, used to assess the type of ELM regime of the H-mode. Each zoomed section can be identified by the colour.

The core D_α emission can then be used to evaluate the type of ELM regime present during the detachment process, as shown in Figure 3.28. At the beginning of the shot, immediately after the SS NBI is fired, the plasma is in a small ELMs regime, where a negligible fraction of the stored energy is dissipated via ELMs, and the density at the edge of the pedestal quickly decreases by 1/5 during the ELMs as measured by TS, as shown in Figure 3.29 for the same small ELM highlighted in Figure 3.28. Then from 300ms up to the full detachment of the outer leg, the plasma is in a quiescent H-mode, without ELMs and with a stable shoulder. After 800ms, while the MARFE-like structure starts growing on the HFS and the upper and lower divertor diverge, the plasma becomes dithering (meaning switching back and forth between L and H-mode). This happens at the same time as the decrease of the average core density and the radiation reaching the x-point from both legs (see Figure 3.26) further indicating that such a level of detachment on the lower divertor might negatively impact H-mode and confinement.

The event at 800ms could be explained by analytical predictions of XPR stability. [74]

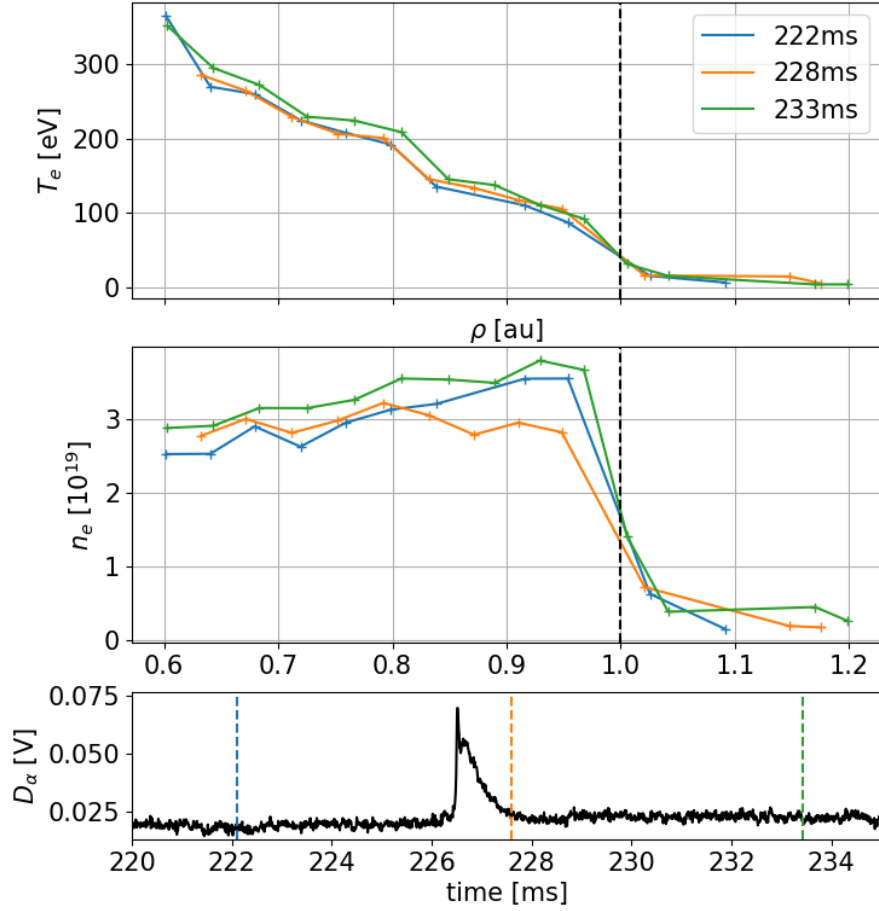


Figure 3.29: Electron temperature and density profiles from core TS before, during and after the small ELM highlighted in Figure 3.28, showing the small decrease of n_e at the outer midplane separatrix. ρ is obtained from EFIT magnetic reconstructions.

It is expected that for higher power discharges, the plasma would transition sharply to a MARFE, skipping the XPR state. From IRVB measurements, the transition between the movement of radiation on the legs (Figure 3.25c) and the appearance of radiation on the HFS separatrix higher than the x-point (Figure 3.25d) seems sharper than in the low power case. The MARFE never fully develops at the HFS midplane, but the radiation is much more spread along the HFS separatrix in Figure 3.25d and 3.25e than in Figure 3.20c. This could imply that the MARFE develops mainly below the midplane after 800ms, possibly due to asymmetric fuelling. After the initial appearance of strong radiation below the midplane, the general performance of the plasma worsens, with core density decreasing and the H-mode becoming dithering, while the density upstream keeps increasing with increasing fuelling and low pump-out due to lack of ELMs. The change in H-mode regime could be related to the MARFE penetrating the core from an intermediate position between the x-point and

midplane, as suggested by the radiation moving slightly inside the separatrix in [Figure 3.25e](#).

Not as many H-mode NBI heated shots were successfully performed as L-mode ones, so it was not possible to identify a significant sample of shots with similar conditions to compare. This data shows that the progress of radiative detachment could be different in H-mode and L-mode, but this could be due to the non symmetric fuelling.

3.3.4 IRVB and MWI correlation in SXD discharges

During MU01 the super-x divertor was investigated, as it is a possible configuration with: improved access to detachment, increased detached operational window [22] and reduced detachment front sensitivity leading to enhanced detachment front position controllability. The hydrogen and carbon line emission in the SXD chamber can be monitored with the MWI diagnostic and compared to the integrated radiated power in the SXD chamber from IRVB, to understand which processes are important with increasing detachment. The results can be compared with a recent interpretation of the evolution of detachment, after its onset, in phases. [86]

As mentioned in [Section 3.2.7](#) the IRVB is incapable of reconstructing the emission profile inside the SXD chamber, but can be used to infer the total emission there with a sufficiently small uncertainty. [Figure 3.30](#) shows some of the emissivity profiles for the shot 45371, an Ohmic 650KA discharge where the outer leg is initially forming a conventional divertor and is then moved inside the SXD chamber to form (starting from ~ 400 ms) the super-x configuration. After this, the plasma is fuelled only in the lower SXD chamber with the valve LFSD_BOT_L0102 for an increasing density scan. The regularisation coefficient for the IRVB inversion is $\alpha \sim 0.4 \cdot 10^{-3}$.

As expected the radiation fades from the SXD chamber as fuelling is increased. In [Figure 3.30a](#) the radiation on the outer leg seems to be peaked at the strike point, but this is not guaranteed to be the case as shown in [Section 3.2.7](#). The change of radiation distribution can be compared with the fuelling level by integrating the region around the outer leg and inside the SXD chamber separately as shown in [Figure 3.31](#). It can be observed that there is a good correlation between the fuelling level, the decrease of the radiation in the SXD chamber and the increase of radiation in the remaining part of the outer leg below the x-point.

This measurement, in particular, can be compared with the diagnostic suite that mon-

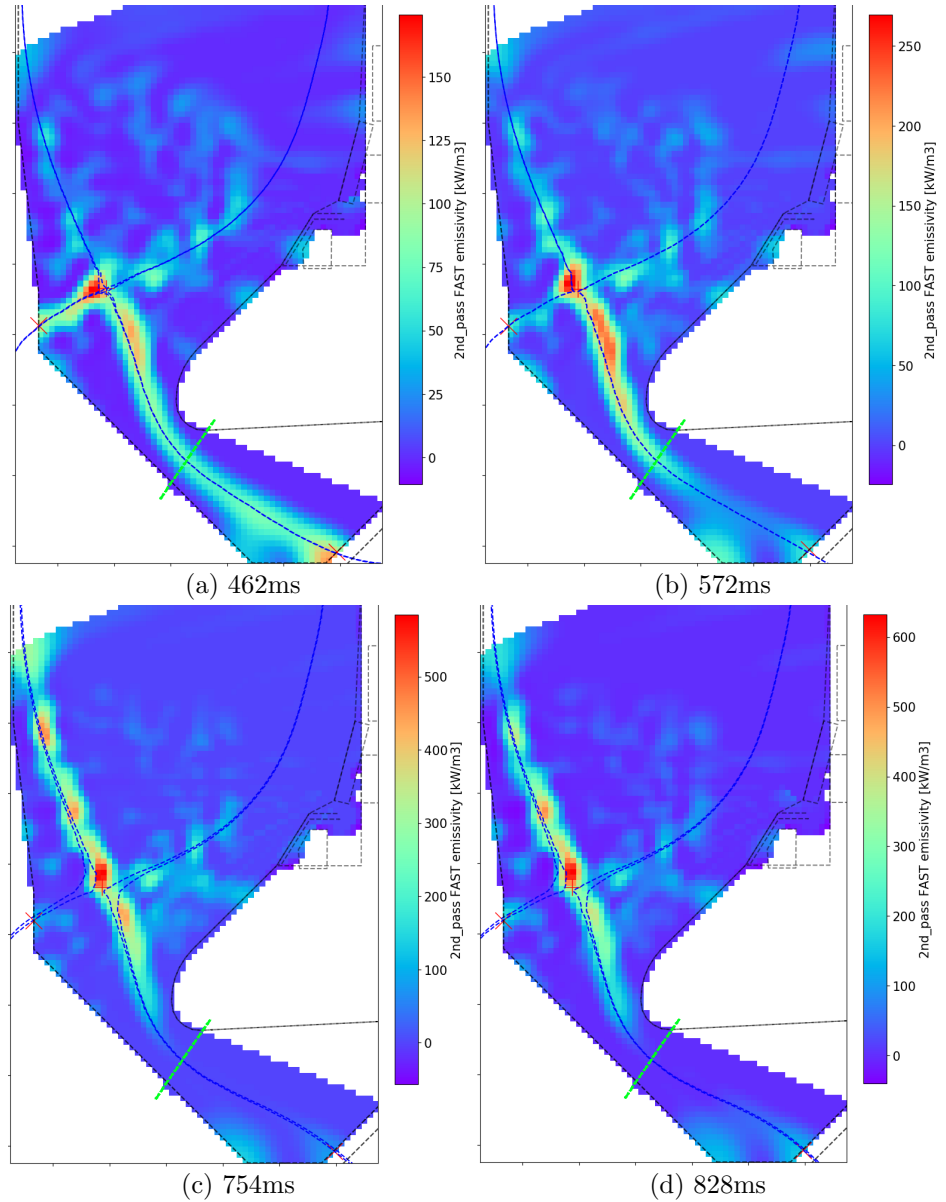


Figure 3.30: Changes of emissivity distribution in a density ramp for a super-x divertor, L-mode, Ohmic plasma (shot 45371, Double-null and 650KA). After the outer leg is moved into the super-x configuration the inner one is already radiatively detached and significant radiation is present in the SXD chamber (a). Then fuelling is increased and radiation inside the super-x decreases (b) up to becoming negligible and the radiation climbs the inner separatrix (c). Then fuelling is cut and the radiation starts to come back towards the strike point (d). Note that the all images have different colour bar ranges. The limit below which the radiation distribution is considered unreliable is marked in dashed green.

itors the plasma inside the SXD chamber. A previous study found that in MAST-U SXD discharges after detachment starts on the outer leg, its progress is in 4 phases, each one corresponding to lower divertor temperatures and dominance of different processes. [86]

Starting from an attached plasma (phase 0), first the ionisation region, where the recy-

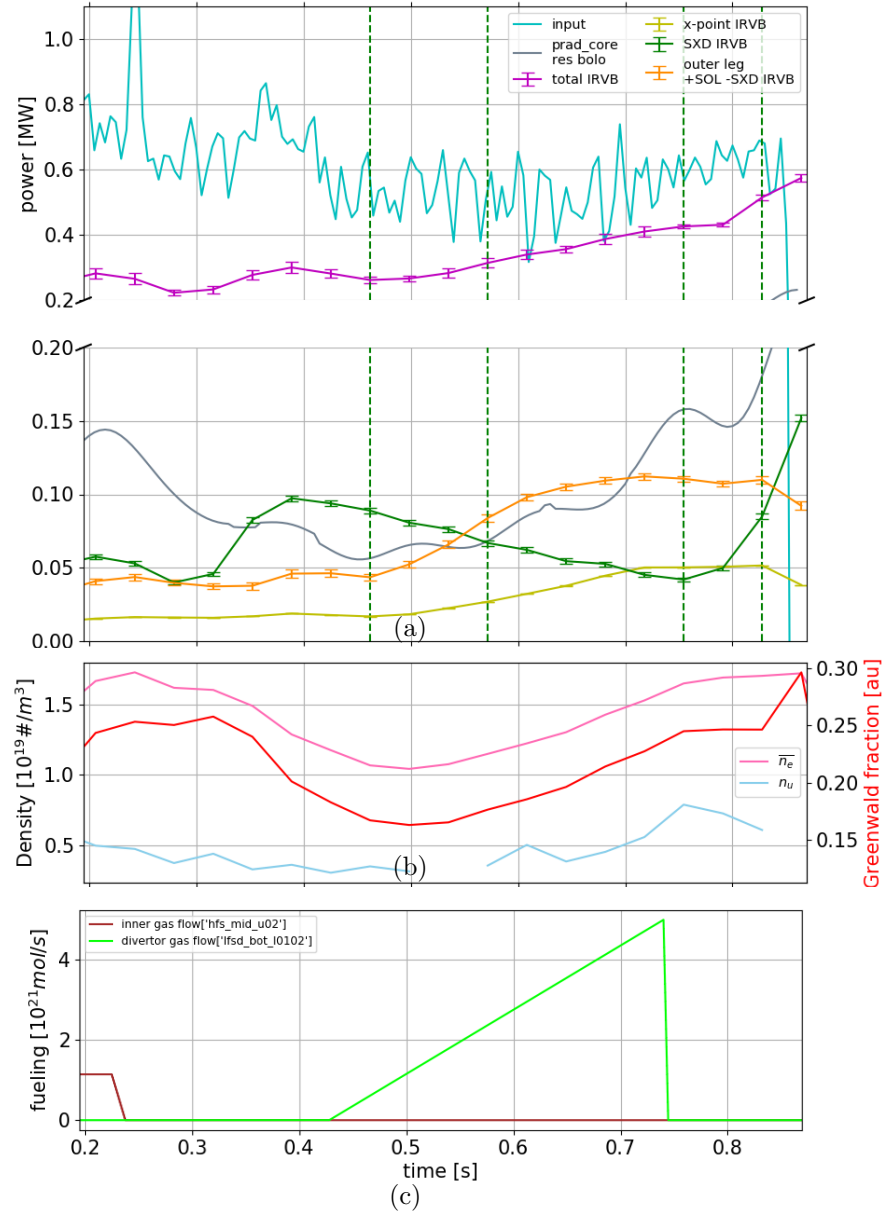


Figure 3.31: Results from different diagnostics related to detachment for a super-x divertor, L-mode, Ohmic plasma (shot 45371, Double-null and 650KA). (a): Components of the global power balance: input power defined as the sum of Ohmic and NBI minus the variation in stored energy. The IRVB power is obtained by adding all voxels at $Z < 0$ then multiplying by 2, therefore assuming up/down symmetry. The regions indicated are defined as per Figure 3.19. The vertical dashed lines indicate the time that corresponds to the data in Figure 3.30. (b): averaged core density (\bar{n}_e) and upstream density from TS as per Section 3.3.1 (n_u). (c): gas flow programmed for the valves used to fuel the plasma. There is no measurement of the effective gas flow produced by a valve setting.

cling deuterium neutrals are converted to plasma via electron-impact ionisation, detaches from the target and moves towards the x-point (phase I). The Fulcher emission arises from molecules being electronically excited by the plasma. Only a plasma hot enough to cause

electron impact dissociation and electron impact ionisation can excite H_2 molecules electronically. Therefore the *movement* of the Fulcher band emission *region* can be used as a proxy for the *movement* of the *ionisation* region, as determined in earlier work. [19] Although a correlation between the Fulcher band intensity and the ionisation source was found in SOLPS simulations, the Fulcher band emission *intensity* is not necessarily a proxy for the ionisation source *magnitude*.

Ionisation also scales with electron impact excitation (EIE) that excites preferentially lower deuterium excited states, leading to low p Balmer lines emission. Then a colder region, where recombination (occurring due to a chain of plasma molecule interactions) dominates, grows near the target and starts to move away from it (phase II). This region is characterised by an increase in emission of $H\alpha$. Then an even colder region dominated by electron ion recombination (EIR) grows at the target (phase III). This is characterised by an increase of the ratio ϵ_x/ϵ_y with $x > y$ and an increase in higher p Balmer lines emissivities. Lastly even this region retracts from the target and the density below it decreases (phase IV).

On top of this picture, that regards molecular and atomic hydrogenic reactions, impurities could be present in the plasma. Impurities can, as mentioned in [Section 1.6](#), greatly increase the radiated power from the plasma, as electrons can be retained on the inner shells at higher temperatures. No impurity was injected in MAST-U in MU01, but the wall is made of graphite, so carbon can play a significant role. In literature, the end of the region with strong Carbon III emission (465 nm) on the outer leg towards the strike point is used as a proxy for the presence of cold plasmas with electron temperatures in the range of 3-11 eV. [143–145] The movement of the point at 50% of the peak CIII emission, on the target side, was used as a proxy for the progress of detachment and to control it. [146]

The multi-wavelength imaging diagnostic (MWI) can record data inside the SXD chamber for 11 wavelength regions. [147, 148] This can then be tomographically inverted and then integrated in the FOV (shown in [Figure 3.19](#)), to return the total number of emitted photons in that volume and given wavelength range. We can then take the total number of photons in the deuterium Fulcher band, from CIII and deuterium Balmer lines $p = 3, 5, 6 \rightarrow 2$ as a proxy for the detachment steps mentioned above. The result is shown in [Figure 3.32](#). Here are shown the number of photons relative to their temporal peak level.

The changes before 400ms are mainly due to the strike point entering the MWI FOV.

The initial rise of SXD chamber power scales well with Fulcher, Balmer $3 \rightarrow 2$ and CIII

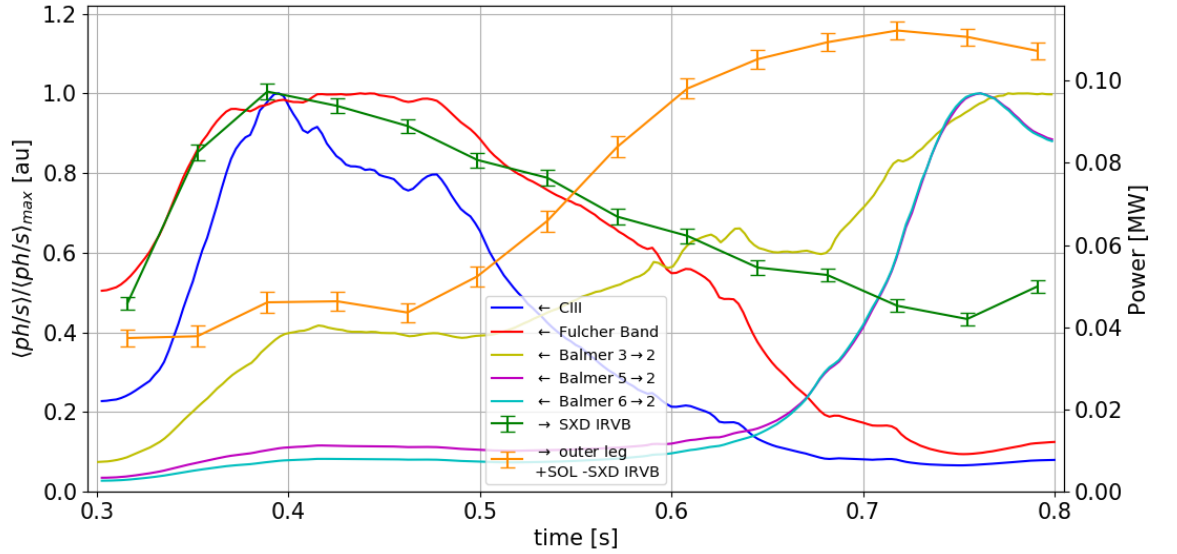


Figure 3.32: Number of photons per MWI target emission line radiated in the SXD chamber relative to the maximum level from MWI, compared to the power radiated in the same region from IRVB. The number of photons is smoothed with a running average of the same length of the temporal resolution of the IRVB data ($\sim 37ms$). The arrow in the legend indicates to which y axis each line refers to. The number of photon axis is scaled so that 1 corresponds to the peak level of the SXD chamber power.

emission, indicating that ionisation and carbon emission might be both important there. While the radiated power decreases after 400ms, when divertor fuelling starts, also Fulcher band and CIII emission decreases. Although tomographic MWI inversions show [85] a movement of both regions, the CIII emission region moves out of the divertor chamber more quickly, consistent with the more rapid decrease of the CIII emission in Figure 3.32. Given the radiated power in the SXD chamber does not decrease as quickly, one might argue that during detachment carbon radiation in the SXD chamber is not the main contributor to the total radiated power. This is consistent with preliminary estimates of the total hydrogenic radiated power (excluding H_2^*) via spectroscopic inference. This is estimated to be 125[70-200]kW at 450ms and 60[30-90]kW at 750ms, while the IRVB measures ~ 90 kW and ~ 45 kW respectively. [86] This is in agreement with interpretative SOLPS-ITER simulations, which indicates the majority of the divertor chamber radiation radiative losses are hydrogenic. This is in stark contrast with previous estimate for TCV, where only 30% of the radiation was hydrogenic. [149, 150]

From 400ms fuelling increases the Fulcher band emissivity, but the total number of photons plateaus, because the emitting region recedes from the target (not shown, previously

observed in [86]).

From 500 to 650ms both the SXD chamber power and the Fulcher band emission decrease in a fairly similar manner, while the power in the leg outside the SXD chamber increases, suggesting that radiative losses due to EIE and ionisation dominate in the outer leg from 400 to 650ms. The Balmer $3 \rightarrow 2$ emission instead increases, while higher lines are still negligible. This might indicate the increase in relevance in the SXD chamber of molecular processes, albeit not necessarily dominating the radiative losses. From 400 to 500ms the plasma in the SXD chamber can be associated with phase 1, while phase 2 up to 650ms. After 650ms the Fulcher band emission becomes negligible and the emission on the outer leg outside the SXD chamber peaks, indicating that the ionisation front has left the SXD chamber completely. The higher p Balmer lines now start to increase up to a maximum at ~ 750 ms, very close to when the fuelling ramp is stopped. The common presence of strong emission from the 3 Balmer lines, combined with the increase of ϵ_x/ϵ_y with $x > y$, indicates that EIR becomes more important, characteristic of phase III. It must be underlined that all the above pertains to observations inside the SXD chamber. In the rest of the leg, SOL and core, the temperature is higher, as the influence of carbon radiation is higher. Preliminary data from the core Survey Poor Resolution Extended Domain (SPRED) VUV spectrometer indicate that carbon radiation is important here. [151]

In this section the detachment characteristics of an L-mode super-x discharge were examined. The integrated emission in the SXD chamber and in the rest of the outer leg, paired with measurement from the multi wave imaging system, was used to infer which processes dominate the IRVB-measured radiation depending on the progress of detachment on the portion of the outer leg inside the SXD chamber. From 400 to 750ms, for increasing fuelling in the SXD chamber, the dominant processes are inferred to be first ionisation and EIE, then molecular reactions and finally EIR. This matches well with a previous analysis that suggests the division of the progress of detachment in phases. [86] In the sequence of phases, the presence of a gap between the dominance of EIE and EIR, where molecular processes dominate, is particularly important, as the relevance of molecular processes is still uncertain in fusion plasmas. The fact that the radiated power in the SXD chamber decreases much slower than the Fulcher band emission after 650ms indicates these processes can cause significant radiative losses when the plasma is deeply detached.

3.4 Summary

To fully exploit the potential of the IRVB, a tomographic inversion algorithm was formulated in parallel to the hardware activities, capable of reconstructing the emissivity profile in the FOV. The method is Bayesian in nature, and allows: accounting for all the known uncertainties arising from the hardware; the highlighting of patterns related to strong signals; and the application of corrective factors tailored to the particular radiation anomalies found. The performance of the Bayesian method was compared with SART, one of the most established tools for tomographic reconstructions, for different radiation phantoms and experimental data, and returned similar or better results. During this analysis it was discovered that the IRVB cannot reliably reconstruct the emissivity profiles inside the SXD chamber, due to a small portion of the FOV observing it and within a small solid angle, but is still capable of detecting the total radiated power in the region.

The IRVB tomographic inversions were used to further distinguish the behaviour of the radiation on the inner and outer leg and to compare it with other metrics of detachment. It was found that in low power Ohmic discharges, the inner leg radiatively detaches at upstream electron density lower than the outer one, and that radiative detachment on the outer leg happens slightly earlier than particle flux roll-over. The movement of the radiation from target to x-point on the inner leg is, appearing to be contrary to expectations for the detachment front from analytical models [22], gradual. An XPR is briefly present before a MARFE-like structure is observed to start growing after the inner leg has completely radiatively detached. Its presence becomes apparent from the radiated power and from the presence of a region of low T_e and high n_e on the HFS midplane. The short duration of the XPR phase matches expectations from an analytical model [74] when carbon is the dominant impurity, as in this case. By increasing the density further, the MARFE-like structure moves towards the magnetic axis. The growth of the structure for HFS fuelling seems to start from fuelling locations.

High power H-mode (NBI heated) discharges in MU01 lacked the repeatability of low power ones, but show a different progression of radiative detachment. First the outer leg starts detaching radiatively, then that process stops and the inner leg detaches completely, and then the outer reaches complete detachment. This observation was obtained with a discharge fuelled from the lower divertor, so this result might differ for an up/down balanced plasma. When fuelling only from the lower divertor, the behaviour of the upper and lower

outer leg diverge with detachment. This potentially indicates that the baffles isolate the divertors and they are only connected through the upstream conditions, allowing to control detachment in the two independently. A MARFE, or its early stage, is possibly observed developing between the x-point and the midplane after both legs radiatively detach, the asymmetry driven by asymmetric fuelling.

Super-x plasmas are difficult for the IRVB to diagnose, since the inverted spatial distribution of the emissivity inside the SXD chamber is not reliable. Nevertheless, the slow decrease of the total radiated power in the SXD chamber due to detachment, in conjunction with spectroscopic observations from the MWI diagnostic, support the progress of detachment as a series of stages as described in [86], and that molecular processes play a significant role.

Chapter 4

Magnum PSI activities

4.1 Motivation

In high performance regimes short (sub ms) bursts of heat and particles from the core (edge localised modes, ELMs) happen cyclically increasing temporarily the heat flux by 2-3 orders of magnitude, and this can hardly be tolerated by large tokamaks. [29] If ELMs happen when the target is detached the plasma temporarily reattaches and loses energy in the process of dissociating and ionising the neutrals. This is beneficial for the reduction of target heat load but computational and experimental investigations are difficult due to the dynamic nature of the phenomena.

The aim of this study, resulting from a collaboration with DIFFER, The Netherlands, in 2019, is to investigate the behaviour of ELM-like pulses on a detached target. During detachment the region in front of the target is cold so neutral and molecular density is high and this might effect the ELM behaviour. Of particular interest is the relevance of molecular assisted processes (ionisation (MAI), recombination (MAR) and dissociation (MAD)) over atomic. This was studied before in tokamaks and linear machines but never during the ELM burn through. [18,120] Another topic is if a regime in which the ELM energy can effectively be fully dissipated in the volume, meaning the energy reaching the target is negligible for its whole duration, exists. This work is also important because different phenomena are at play and have to be correctly understood to gain predictive capability for the ELM burn through in tokamaks. The filamentary nature of the ELM makes a 3D treatment necessary [75,76] while its fast transient nature makes kinetic effects relevant. [77] On top the interaction with cold neutrals, with solid surfaces and the cooling of the plasma to sub eV temperature

require transport and a large number of interactions to be accounted. [78, 79] The presence of molecular precursors like H_2^+ and H^- and their interactions with plasma and neutrals further complicate the picture, so it is necessary to assess if they play a significant role in the burn through process.

To reliably investigate the above phenomena, ELM-like pulses are produced in Magnum-PSI, a linear plasma machine located in the DIFFER laboratory in the Netherlands. Magnum PSI is capable of producing steady state target perpendicular heat fluxes comparable to that at the ITER target. The configuration is different than a tokamak, but the simpler geometry allows for an easier interpretation, better repeatability and diagnostic access. The ELM-like pulses are generated thanks to a capacitor bank (CB) and detachment is induced by increasing hydrogen neutral pressure in the target chamber. The Optical Emission Spectroscopy (OES) setup was improved to increase the time resolution in order to collect data on the ELM-like pulse behaviour. An analysis of the power and particle balance in the plasma column inside the target chamber, separating molecular and atomic contributions to power and particle losses, was performed through a purpose built Bayesian routine that also makes use of the new OES data.

As mentioned before, linear machines are significantly different from the tokamaks. In a tokamak divertor, especially the high recycling regime preceding detachment, the main contributor to the ion target flux is not the flow from upstream but the ionisation of neutrals recycling at the target, while the upstream acts as a power source. The divertor leg, in terms of particle balance, acts more as a closed system being supplied with energy from the upstream boundary [46]. In linear machines, the upstream plasma flow usually dominates, and the ionisation source is minor. The plasma flows from the source to the target, where its temperature and density are usually too low to cause recycling. Another difference is the connection length, of the order of tens of metres in tokamaks while it is less than $1m$ in Magnum-PSI. In tokamaks, the wave of hotter plasma due to the ELM can propagate along field lines, progressively burning through the barrier of cold neutrals generated by detachment. The temporal dynamics of the upstream conditions have comparable timescales to the transport of heat along the magnetic field lines [75, 152]. In linear machines the flow from source to target is much faster than the evolution upstream, so that the discharge behaves more as a succession of steady states. In linear machines it is difficult, therefore, to study the effect of the ELM burning through the gas buffer created by detachment, while

they should be more representative of the cross field neutral transport. The ELM frequency can be high in tokamaks, from fractions to tens of kHz. Considering recycling confines the neutrals at the target, it was postulated from simulations that the neutral pressure in the divertor could progressively increase as more ELMs happen, [75] making it difficult to study a quasi steady state reference state. Due to the lower ELM frequency achievable in Magnum-PSI, and the low ion source, this effect is usually not observed and the effect of repeated ELMs can be studied with respect to the same steady state case. This enables delineating the impact of an ELM on a neutral gas buffer from changes of the neutral gas buffer due to previous ELMs interacting with the target. In tokamaks there is also a strong correlation between ELM frequency and energy released during the ELM, [29] making the independent study of these two aspects difficult, while in linear machines these can be more easily controlled. The presence of impurities likely plays a role in the interactions of ELMs with detachment, both due to increased radiative, and because of the increased sputtering when reaching the target. This is not guaranteed to be reproduced in linear machines unless specific setups are arranged. Even considering these differences, linear machines are still useful tool in understanding the processes happening during tokamak ELMs and the effects of neutral pressure.

It will be shown that by increasing the target chamber neutral pressure, energy is removed from the ELM-like pulses. In some cases, the target is not significantly affected by the ELM-like pulses. The pulse effect on the target is comparable to what is measured in current tokamaks, even if significantly lower than the expectation for large scale devices like ITER, and can be reduced by increasing the neutral pressure. It will also be shown that for increasing neutral pressure, the energy and particles of the ELM-like pulse will increasingly be removed in the Magnum-PSI target chamber volume and that an important role is played by plasma-molecule interactions. The radiated power losses are a significant power loss channel, but elastic collisions with neutrals and exchanges of potential energy dominate in reducing the plasma temperature to levels where recombination becomes important.

4.2 Experimental setup

Magnum-PSI is a linear machine with a superconducting coil surrounding the vacuum chamber to confine the plasma generated by a cascaded-arc source from it to the target. The

vacuum vessel is split in three chambers separated by skimmers to allow differential pumping. This ensures that the conditions in the target chamber are independent from the source and the vast majority of the impurities and neutrals from the source are removed from the plasma column before it enters the target chamber. [153] Magnum-PSI is capable of reproducing ITER steady state orthogonal target heat flux, even if the parallel heat flux is much lower. [153] A capacitor bank is connected in parallel to the plasma source power supply to temporarily increase the heat flux tenfold and simulate ELMs. [154] A schematic of the Magnum-PSI machine is in Figure 4.1.

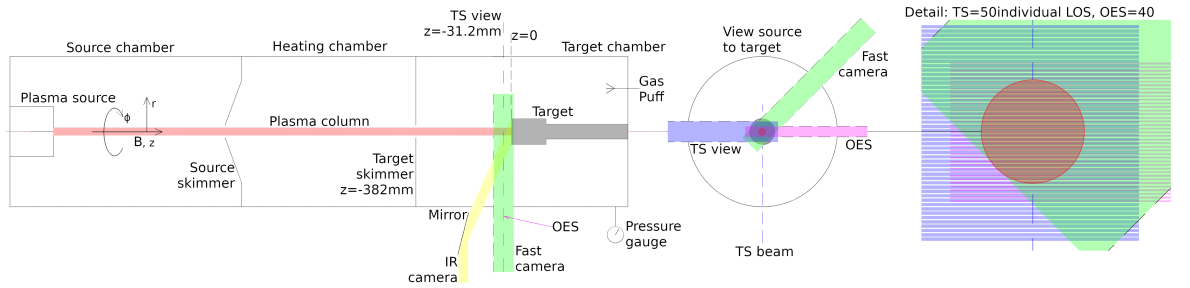


Figure 4.1: Schematic of Magnum-PSI linear plasma machine. $z = 0$ corresponds to the surface of the target, Thomson scattering and Optical Emission Spectroscopy (OES) are located at $z = -31.2\text{mm}$. The TS view is composed of 50 evenly spaced LOS orthogonal to the plasma column length (z). The OES view is composed of 40 LOS perpendicular to the column length. The fast camera, for measuring integrated light emission from the plasma, has a radial view of the plasma through a lateral viewport of the vacuum vessel of diameter $\sim 75\text{mm}$. The IR camera has a radial view that is converted to looking at the target surface by a mirror outside the target chamber. The mirror angle can be adapted to maintain the view of the target when moved in z .

4.2.1 Experimental conditions

Table 4.1 indicates the experimental conditions used on Magnum-PSI for this work, with the detachment stage of the discharge based on the visible light emission defined in Section 4.3. ID 1-4 are referred to as weak pulses: the magnetic field intensity is lower so the steady state and ELM-like pulse input energy is spread over a larger area, making it easier for the background gas to dissipate it. The energy in the capacitor banks is also lower. ID 5-10 are, conversely, referred to as strong pulses, with stronger magnetic field and higher capacitor bank energy.

For every condition two discharges are performed. In each, first the steady state plasma is generated, then a series of ELM-like pulses are generated on top. More detail on the

procedure are given in [Section A.1](#). During weak pulses a small neutral pressure increase was observed from the initial steady state plasma phase to when repeated ELMs are delivered, as is expected in tokamaks [75], but not for strong pulses. This is likely because the lower magnetic field allows the plasma to spread over a larger volume ($\sim 50\%$ more from OES) and can therefore better fill the target skimmer, preventing gas from the target chamber to be removed by the heating chamber pump, that always runs at 82% speed. The pressure increase is from $\sim 1\%$ in ID4 to $\sim 5\%$ in ID1. This is likely due to the increase of the gas temperature in the target chamber due to the heating from the ELM-like pulse, as the more gas is present, the less is the pressure increase.

ID	capacitor voltage [V]	capacitor energy [J]	Magnetic field [T]	Target chamber H_2 feeding [slm]	Target chamber pump speed [%]	Steady state neutral pressure in target chamber [Pa]	Stage (defined in Section 4.3)
1	370	10.3	0.6	0	82	0.223	1
2	370	10.3	0.6	0	25	0.385	1
3	370	10.3	0.6	10	25	5.991	2/3
4	370	10.3	0.6	20	25	10.956	3
5	800	48.0	1.3	0	82	0.296	1
6	800	48.0	1.3	0	25	0.516	1
7	800	48.0	1.3	5	25	4.370	1/2
8	800	48.0	1.3	10	25	8.170	2
9	800	48.0	1.3	15	25	11.847	2
10	800	48.0	1.3	20	25	15.040	2

Table 4.1: Table of the experimental conditions of Magnum-PSI for the experiments presented in this work. Common parameters are: steady state source current 140A to generate the background plasma, 31.2mm target to OES/TS distance, TZM (a molybdenum alloy) target. ID 1-4 are referred to as weak pulse conditions while ID 5-10 are referred to as strong pulses. The stages are 1-3 and correspond to: fully attached (1), partially detached (2) and fully detached (3) as it will be defined in [Section 4.3](#).

4.2.2 Diagnostics

In this section, the diagnostics employed in this study will be described. Some diagnostics have the time resolution to be able to observe individual ELM-like pulses, while others only a limited part of it, so a sampling strategy was adopted to reconstruct the full behaviour of the ELM-like pulse. More detail is given in [Section A.1](#).

The results from the diagnostics used in the experiments are described in the following sections:

- 4.3 Vision Research Phantom v12.1 CMOS camera: axial and radial view of the plasma
 - 4.4 Thomson scattering (TS): electron temperature and density
 - 4.5 Infrared (IR) camera FLIR SC7500MB: target temperature (used with calibration from FAR-Associate Spectro Pyrometer FMPI)
 - 4.6 Jarell-Ash, Czerny-Turner spectrometer OES: Hydrogen atomic line emission (Balmer series $p = 4 - 8 \rightarrow 2$)
- 4.6, A.4.5 Power source (ADC): temporal variation of the power delivered to the plasma

4.2.2.1 Optical emission spectrometer (OES)

The main component is a Jarell-Ash spectrometer connected to a fibre optic bundle with 40 individual cores that view the plasma radially with a spatial resolution of 1.06mm, individual line of sight (LOS) width of ~ 1 mm. See the OES LOS in the target chamber in [Figure 4.1](#), further detail from Barrois. [[155](#)]

Before this work was conducted the camera connected to the spectrometer was a Princeton Instruments PIXIS 2048B, with a shutter speed of the order of seconds. In order to obtain information on the behaviour during the ELM-like pulse this camera was replaced in 2019 by the author and Gijs Akkermans with a Photometrics Prime95B 25mm RM16C with a minimum integration time of $20\mu s$.

The camera has a CMOS sensor with rolling shutter, meaning the exposure of one row happens after the previous row is completed, forcing the accumulation of data on multiple ELM-like pulses to reconstruct the full spatial and temporal brightness profile of the pulse. Details on how to sample all stages of the ELM-like pulse so that one obtains a coherent picture are shown in [Section A.1](#) while the steps from raw images to line emissivity are detailed in [A.2](#). The sensitivity calibration was done using a Labsphere as explained extensively by Barrois. [[155](#)]

During the experiments hydrogen Balmer lines brightness ($p = 4 - \infty \rightarrow 2$) were recorded; only lines $p = 4 - 8 \rightarrow 2$ were considered to have a sufficient signal to noise ratio and were used in this study.

4.2.2.2 Fast Camera

A Vision Research Phantom v12.1 CMOS camera is installed such that it has a radial and axial view of the plasma coming from the source (left) and directed to the target (right). The view is through a lateral viewport of the vacuum vessel so the useful FOV is limited to a diameter of $\sim 75\text{mm}$ (see [Figure 4.2, 4.4.](#)) The camera records visible light and it's not used to deliver quantitative information but it is very useful to establish the qualitative behaviour of the plasma. The frame rate used was 67kHz, enough to resolve individual ELM-like pulses ($\sim 1\text{ms}$ in duration, 67 frames). The information from multiple pulses was then averaged. Thanks to this diagnostic it is possible to identify 3 distinct regimes/stages that are evident as the neutral pressure in the target chamber is increased and therefore increasing the level of detachment.

4.2.2.3 Thomson scattering (TS)

Thomson scattering (TS) is a diagnostic that allows the measurement of T_e and n_e by firing a laser beam through the plasma and collecting the scattered light from a particular measurement volume determine by the intersection of the laser beam with each TS viewing LOS. 50 LOS are measured simultaneously in the radial direction (in the same plane as OES as shown in [Figure 4.1](#)) to reconstruct the profile of the plasma. In Magnum, TS can be used for steady state plasmas but also for time dependent measurements, albeit with reduced performance. For this campaign the system was used in time dependent mode with $50\mu\text{s}$ time resolution and integration time, with an uncertainty $< 3\%$ for electron density and $< 10\%$ in electron temperature for $n_e > 2.8 \cdot 10^{20} \#/\text{m}^3$. The time between consecutive measurements must be equal to the laser frequency, 10Hz, thus forcing us to accumulate data over multiple pulses to reconstruct the whole time evolution. [[156](#)] Details on the sampling strategy is given in [Section A.1](#).

4.2.2.4 IR camera

This data is collected by a FLIR SC7500MB infra red camera that views the surface of the target in the wavelength range $3.97 - 4.01\mu\text{m}$. The camera view is directed towards the target by a mirror and enters the target chamber from a port upstream from the target as shown in [Figure 4.1](#). The temperature calibration is performed with a dedicated FAR-Associate Spectro Pyrometer. The frame rate of the FLIR camera is about 3kHz, which corresponds

to ~ 3 frames per ELM-like pulse and integration time was set to $100\mu s$. To increase the confidence in the measurements, the records for multiple ELM-like pulses are overlapped and averaged once the target reached a thermal steady state in a similar fashion as done by Li. [157] The IR camera results are a 2D temperature profile on the target over time. Due to differences in the triggering system it is not possible to directly relate IR camera time with OES or TS so this results are used independently.

4.2.2.5 Power supply

The steady state power supply regulates the DC plasma source voltage such that its current is equal to the set point. A capacitor bank composed of 28 individual sections consisting of an inductor ($L=160\mu H$) and a capacitor ($C=150\mu F$) is connected in parallel to the DC source. The energy stored in each capacitor (shown in Table 4.1) is given by $\frac{1}{2}CV^2$. These can be individually controlled such that they each charge to a set voltage and discharge at a set time. The current released by the capacitor will be additional to the steady state one. The voltage and current at the plasma source are recorded and data from multiple ELM-like pulses is overlapped to compensate for small differences in each capacitor/inductor pair in a similar fashion as done for the IR camera. The energy transferred into plasma energy was measured to be 92% of the electrical energy dissipated at the plasma source during ELM-like pulses. [154] Some of the energy can additionally be dissipated in the source and heating chambers before the target skimmer. The pressure in those chambers is maintained as low as possible via differential pumping to reduce interaction of the beam with cold gas and consequent energy losses. Energy losses due to the interaction of the plasma with source and target skimmers are here neglected.

The results that can be gathered by the examination of the data from individual diagnostics will now be presented. The fast camera will be used to identify the spatial features of the radiation profile during each pulse, which will be used to characterize the level of detachment and to distinguish the influence of increasing neutral pressure on the burn through of the ELM-like pulse. Thomson scattering allows to measure the main plasma properties so that the plasma pressure losses can be compared with target chamber neutral pressure. The target surface temperature measured with the infrared camera allows to determine the energy delivered to the target by the ELM-like pulse, finding it decreasing with increasing neutral pressure until full dissipation of the pulse energy is achieved. Then the understanding will

be deepened with the use of a Bayesian technique specifically developed to interpret in a self-consistent way results from different diagnostics. This allows to quantify the relevance of molecular assisted processes compared to atomic ones.

4.3 Fast camera

In this section the visible fast camera brightness is used to examine the spatial distribution of the emission in the target chamber and how the ELM-like progression to the target is impacted by increasing neutral pressure. This will allow to define 3 progressive stages of detachment based on the averaged spatial brightness profile.

4.3.1 Steady state

In order to characterise the state of the plasma during the ELM-like pulse from the visible fast camera brightness, the known characteristics of a steady state plasma are shown in [Figure 4.2](#). [18, 158] These images are taken with a $H\alpha$ filter with plasma in similar conditions to the ones in this work (1.2T, 120A) during an experiment by Akkermans. [18] Because of the presence of the filter the images are blurred.

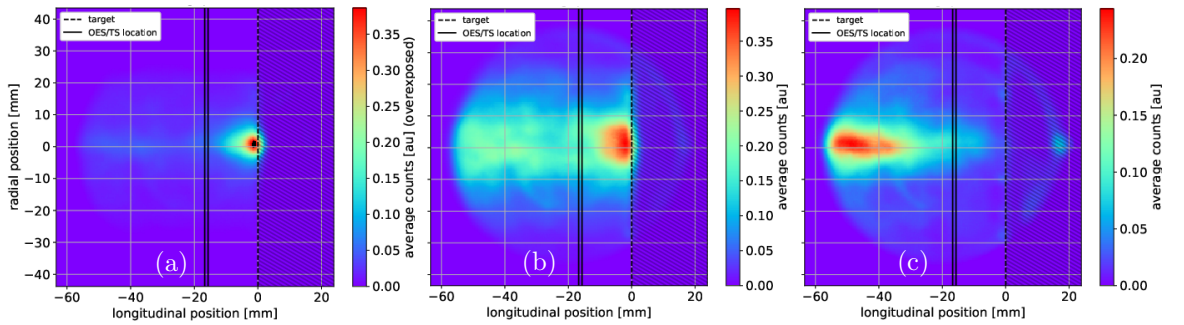


Figure 4.2: Visible fast camera brightness images corresponding to a steady state plasma in conditions similar to this work from an experiment by Akkermans [18] (1.2T, 120A, $H\alpha$ filter present), (a) is affected by overexposure in the black region near the target. The target chamber neutral pressure is increased to induce detachment and corresponds to 0.29Pa (a), 2.01Pa (b) and 17.3Pa (c). The shaded region indicates the position of the target. The OES and TS measurement locations in z are indicated by the 2 vertical lines. The fast camera view is through a lateral viewport, giving a useful FOV of ~ 75 mm diameter.

For low target chamber neutral pressure, the plasma emitting region is concentrated close to the target at the centre of the plasma column ([Figure 4.2a](#)). This indicates that the interactions between plasma and the background gas are weak and the plasma can flow

towards the target mostly unperturbed. This is due both to the low neutral density and to the fact that the high plasma temperature typical of low target chamber neutral pressure causes further neutral hydrogen dilution. [159]

For increased neutral pressure (Figure 4.2b) the radiation in the volume increases while it decreases close to the target; the plasma volume away from the target plays an increasingly important role. By increasing the neutral pressure even further (Figure 4.2c) the radiation near the target is strongly reduced and the bulk of the plasma radiation recedes from the target. The peak plasma density close to the target measured by TS first increases from 1.13 to $1.98 \cdot 10^{20} \text{ #/m}^3$ from 0.29 to 2.01Pa, and then decreases to the point that TS measurement fails at 17.3Pa. The peak plasma temperature conversely decreases from 3.34eV to 1.53eV and becomes undetectable at 17.3Pa. The characteristics of the plasma near the target from TS thus display a monotonic loss of plasma pressure as neutral pressure increases, consistent with the behaviour of a plasma that experiences detachment caused by the increase of neutral pressure. [158] The plasma is classified as attached to the target in Figure 4.2a and b, while detached in Figure 4.2c.

By averaging the visible fast camera brightness over the radial direction one obtains the profiles in Figure 4.3. Those profiles reinforce how the main interactions of the plasma shift from close to the target to the volume of the plasma column for increasing neutral pressure. The increase in visible radiation correlates well with observations from simulations that $\text{H}\alpha$ emission is greatly increased from the detachment onset onward because of the influence of molecular reactions. [78] Using this method of determining the detachment state of the plasma, we can proceed interpreting the visible fast camera brightnesses during the ELM-like pulses.

4.3.2 Effect of ELM-like pulses

For this study, the fast camera was set with a high frame rate of 67kHz and low integration time of 900ns in order to capture the bright ELM-like pulse behaviour. With those settings, the brightness of the steady state is not detectable and only the ELM-like pulses can generate counts. The ELM-like pulse lasts 0.7 to 1ms (equivalent to 67-47 frames) depending on the target chamber neutral pressure and a clear movement of a radiation front from the source to the target could not be clearly identified with this settings. In order to extract information on the behaviour across the ELM-like pulse the camera measurement is averaged in time

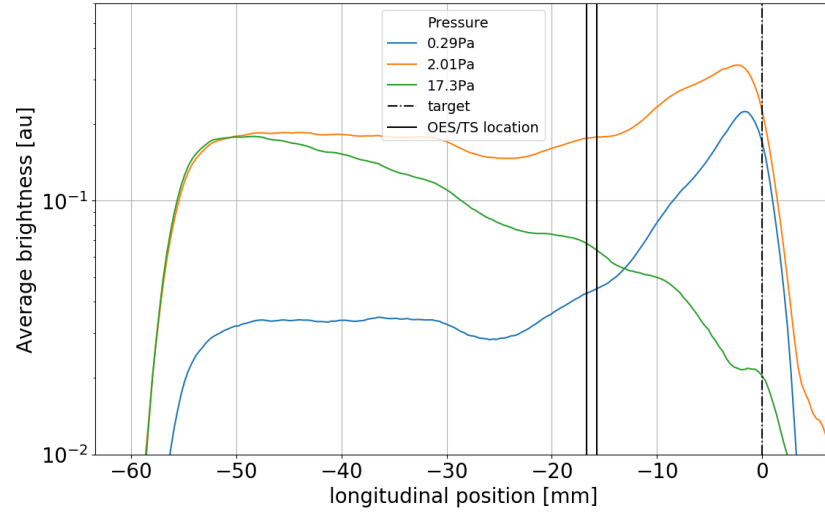


Figure 4.3: Radial average of the visible fast camera brightness for the steady state cases in Figure 4.2. The longitudinal position axis is cut after the target. The brightness decreases towards the source as the plasma exits the field of view of the camera.

over the time interval with non zero data. The data from a few ELM-like pulses in the same conditions is then further averaged. A sample of the results for the plasma conditions in this work are shown in figure Figure 4.4.

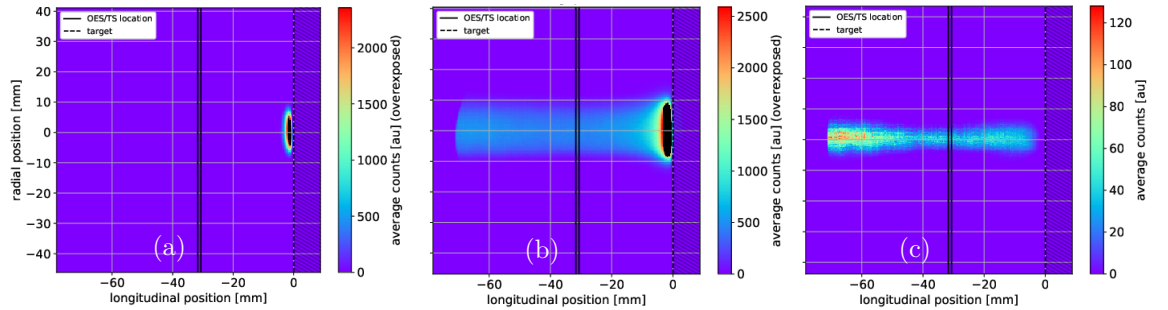


Figure 4.4: Fast visible camera images of the ELM-like obtained by averaging temporally over the pulse duration. The images show a plasma which is increasingly detached and corresponds to ID 5 (a), 10 (b), 4 (c) in Table 4.1 ((a) and (b) are effected by overexposure in the black region near the target). The fast camera view is through a lateral viewport, giving a useful FOV of ~ 75 mm diameter.

Figure 4.4a corresponds to a low target chamber neutral pressure. Under such conditions, it is typical to observe a bright emission in proximity of the target while almost nothing is visible far from it; the vast majority of the plasma-neutral interactions and the resulting emission happens at the target while the plasma is transported, mostly undisturbed, through the bulk of the target chamber. This closely resembles what was observed in Figure 4.2a, indicating that the plasma is, in this case, attached to the target. Another observation

is that, during the ELM-like pulse, the visible fast camera brightness close to the target increases and then decreases, while maintaining the same relative shape (see [Figure 4.5](#)). This points towards the fact that the plasma is attached before, during and after the pulse. This is also confirmed by independent TS and OES measurements away from the target. From the steady state to the peak ELM-like pulse values T_e rises from ~ 5 to 9.4eV and n_e from ~ 1 to $23 \cdot 10^{20} \#/\text{m}^3$ (see [Section 4.4](#) for further details). This experimental condition is the first one encountered starting from low neutral pressure, so it is referred to a Stage 1.

In [Figure 4.4b](#) the neutral density is increased. The light emission in the bulk of the target chamber increases with respect to at the target and is typically quite homogeneous along the magnetic field direction. The emission closely resembles [Figure 4.2b](#), meaning that during the ELM-like pulse the plasma is still attached to the target. This is not the case before and after, where the density is so low that TS measurements fail and no emission is visible from OES. During the ELM-Like pulse, the peak T_e decreases to $\sim 4.6\text{eV}$ while n_e increases to $\sim 52 \cdot 10^{20} \#/\text{m}^3$. This condition is referred to as Stage 2.

If the neutral pressure is further increased from what causes Stage 2 to occur, the baffling in the bulk of the target chamber can be so severe that the strong luminous spot close to the target might not appear. This is shown in [Figure 4.4c](#). In such cases the interaction of the plasma in the volume is so strong as to dissipate the ELM-like pulse almost entirely before it reaches the target. Only luminosity in the volume is present, closely resembling [Figure 4.2c](#) which corresponds to a detached plasma, meaning the plasma is detached before and during the ELM-like pulse. The OES, TS, and visible fast camera brightness is measurable for a much shorter time compared to the ELM-like pulse duration ($\sim 300\mu\text{s}$ compared to the pulse length of $700\mu\text{s}$), meaning most of the ELM-like pulse energy is dissipated in the volume. This is further confirmed by TS as peak T_e drops from 0.63 to 0.58eV and n_e from 12.6 to $4.7 \cdot 10^{20} \#/\text{m}^3$ increasing the neutral pressure from Stage 2 (ID 3 to 4 in [Table 4.1](#)). This regime is referred to as Stage 3.

The information in [Figure 4.4](#) is summarised in two figures: [Figure 4.5](#) and [Figure 4.6](#) (averaged radially and in time for each pressure) which displays the average of the visible fast camera brightness as a function distance from the target. Both figures include analysis for several neutral pressures for the two scans included in this work (ID 1 to 4 and 5 to 10 in [Table 4.1](#)).

[Figure 4.5](#) corresponds to a strong ELM-like pulse. The emission is always peaked at the

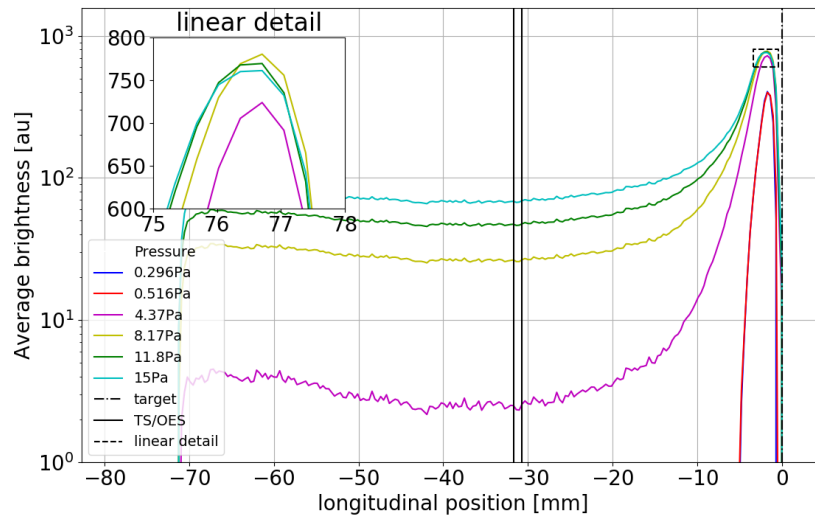


Figure 4.5: Radial and temporal average of the visible fast camera brightness for the neutral pressure scan with strong ELM-like pulses, where we observe the transition from Stage 1 to 2. (ID 5-10 in Table 4.1).

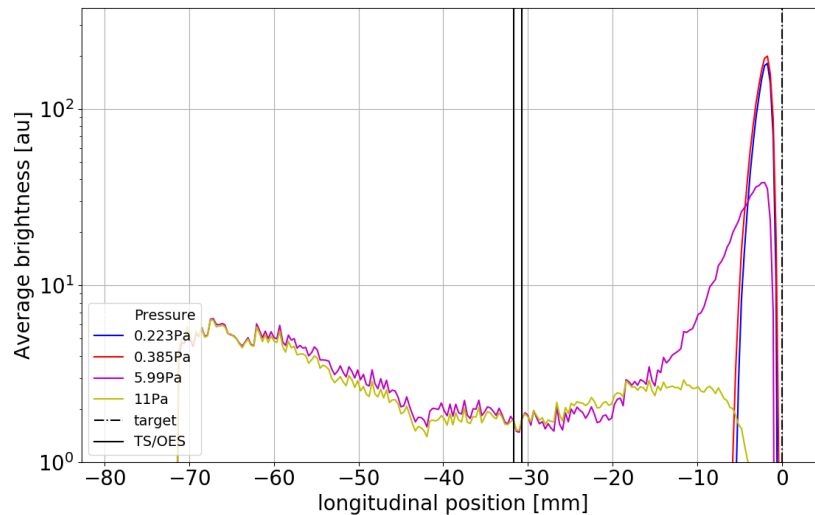


Figure 4.6: Radial and temporal average of the visible fast camera brightness for the neutral pressure scan with weak ELM-like pulses, where we observe the transition from Stage 1 to 3 (ID 1-4 in Table 4.1).

target while the emission away from it increases significantly for increasing pressure. At the two lowest neutral pressure settings the plasma is in Stage 1, it is at an intermediate state for ID7 (with a significantly lower emission in the volume than the other higher pressure cases) while it then transitions to Stage 2 for ID8-10 in Table 4.1. The brightness becomes more homogeneous along the magnetic field for increasing neutral pressure, reducing the signal anisotropy in the longitudinal direction. The emission at the peak in Figure 4.5 initially

increases with neutral pressure but, as shown in the linear detail it then starts to decrease, signalling the start of the transition from Stage 2 to 3 (it must be noted, though, that the peak region is affected by saturation). It will be shown later that the peak plasma pressure measured by TS does not significantly change in the transition from Stage 1 to 2, indicating that the plasma is still attached during all the strong ELM-like pulses.

Figure 4.6 displays the average of the brightness for the neutral pressure scan with weak ELM-like pulses (ID 1-4 in Table 4.1), meaning the pulses are weak compared to the baffling of the background gas. Here we have the transition from Stage 1 (0.223 and 0.385Pa) to 2/3 (5.99Pa) and ultimately 3 (11Pa). The same trend in Figure 4.5 continues here, with an even more uniform light emission at the highest pressures. Note that this dataset is unaffected by saturation. The 5.99Pa case is indicated as Stage 2/3 because even if some emission comes from nearby the target, that is significantly reduced compared to the Stage 1 cases, and looking at the temporal evolution of the brightness, the pulse reattaches to the target only briefly. Later analysis will show that with neutral pressure 5.99Pa no heating is delivered to the target, typical of Stage 3 rather than 2, and the plasma pressure loss is significant, indicating increasing levels of detachment.

The distinction in stages helps to discriminate between types of behaviour of the plasma and its influence on other diagnostics and the power balance. Plasmas in Stage 1 are typically correlated to low volumetric losses, high steady state target temperature and measurable steady state plasma conditions, as it will be clear from analysis of the IR camera and TS data. In Stage 2, the target is cold in between ELM-like pulses but a significant target heating can be provided transiently and volumetric losses dominate as a power loss mechanism. In Stage 3, the lack of emission near the target coincides with negligible target heating, significant plasma losses before reaching the OES/TS location and an increased anisotropy in the plasma column. As previously mentioned the emission is not homogeneous in the whole target chamber. Strong emission is located close to the target and even in the bulk there is a slight increase in emission moving away from the target. The anisotropy in the bulk of the target chamber, though, is weak and decreasing for increasing neutral pressure. *This observation will be used in Section A.4.5 to support the approximation that volumetric power losses can be considered constant from skimmer to target.*

4.4 Thomson scattering

The Thomson scattering diagnostic measures the main plasma properties (T_e , n_e) and allows to determine the temporal evolution of the ELM-like pulse and the transfer of plasma energy from high temperature (and low density) to high density (and low temperature) for increasing neutral pressure. The data collected corresponds to plasma volumes along the path of the laser beam. The lines of sight of the light collection system are centered on the plasma column so data is collected on the plasma above and below the plasma column centre. These are averaged to return the radial profiles. A small time difference between OES and TS is also present so the raw TS T_e and n_e are resampled and smoothed, to match the OES time and spatial bases and obtain the temporal and radial profiles.

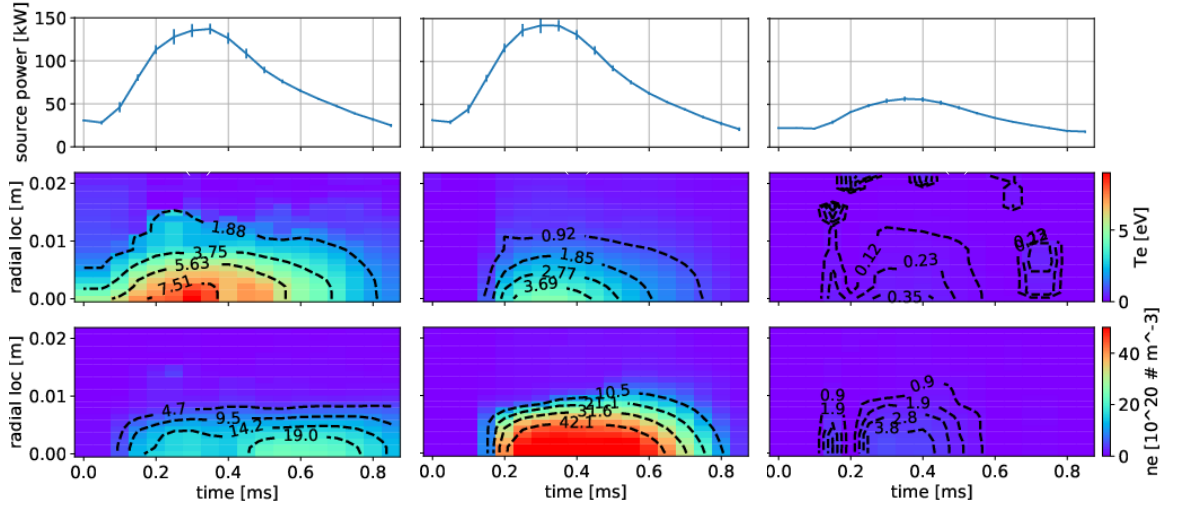


Figure 4.7: Typical source power (top), Thomson scattering T_e (mid) and n_e (bottom) measurement for strong pulses in Stage 1 (a), Stage 2 (b) and weak pulses in Stage 3 (c) (ID 5, 10, 4 in Table 4.1 respectively). TS data is smoothed over time and radius in order to match the same steps of OES.

In Figure 4.7 are shown typical T_e and n_e from TS for experimental conditions in Stage 1, 2 and 3. On top is also shown the power dissipated by the plasma source averaged over multiple ELM-like pulses and aligned with TS. As mentioned before, the weak pulses are obtained via a lower magnetic field and a lower energy of the pulse itself. The lower magnetic field causes the energy of the pulse to distribute over a larger area (radius) and increase the volume of contact between plasma and cold gas. The lower temperature and density also causes the neutral mean free path to increase, allowing them to penetrate deeper inside the

plasma column. For strong pulses T_e decreases while n_e increases as the neutral pressure and the amount of gas available to be ionised increases. The steady state properties become undetectable while the time corresponding to peak density shifts earlier in time. For weak pulses and high neutral pressure peak density is at even earlier times with a very low plasma temperature.

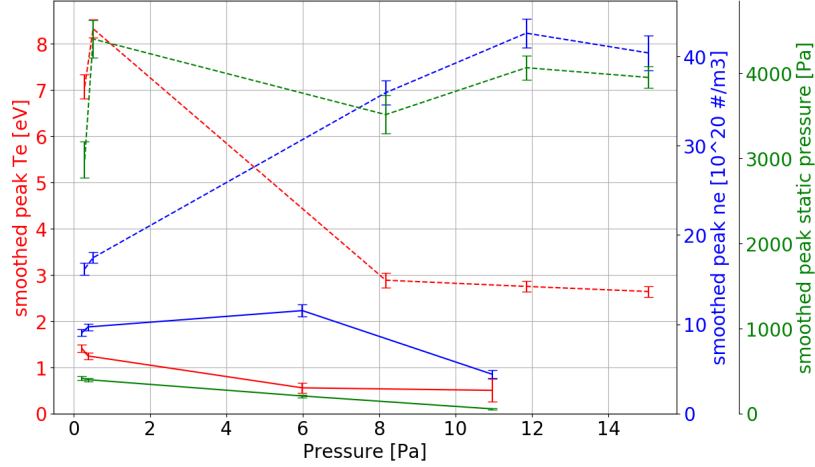


Figure 4.8: Comparison of plasma peak T_e , n_e and p_e smoothed over $700\mu s$ for a neutral pressure scan with strong pulses (dashed lines, $B=1.3T$, pulse energy= $48J$), corresponding to Figure 4.5 and weak (solid lines, $B=0.6T$, pulse energy= $10.3J$), corresponding to Figure 4.6 (ID 5-10 and 1-4 respectively in Table 4.1)

A comparison of the peak T_e , n_e and $p_e (= n_e 2T_e/k_B)$ smoothed over $700\mu s$ (the duration of the ELM pulse) is shown in Figure 4.8. For strong pulses (dashed lines) T_e decreases while n_e increases as the neutral pressure and the amount of gas available to be ionised increases. Only the maximum neutral pressure achievable is high enough to cause a possible decrease of the measured n_e , indicating that the plasma may be starting to transition to a detached state also during the strong ELM-like pulses (as indicated by the fast camera results). This trend can be seen also in the static plasma pressure, that remains at similar levels as the neutral pressure increases. If it could have been further increased, the plasma pressure would likely have decreased as would both n_e and T_e . Similar trends can be seen for weak pulses too (solid lines), but n_e starts decreasing at much lower neutral pressure, indicating that it is easier for the gas to dissipate the weak ELM plasma energy. In the highest pressure case the plasma is significantly depleted in the volume before reaching the TS location, causing the TS measurement itself to fail except at the very peak of the ELM-like pulse, and not be representative of the whole plasma column. For this reason weak pulses are not suited to be

analysed with the Bayesian model in Section 4.6. This situation corresponds to an ELM-like pulse in Stage 3 as defined before.

In summary increasing the neutral pressure (ID 5-10 in Table 4.1) the plasma transitions from Stage 1 to Stage 2: the energy losses before reaching the TS measuring location increase but the ELM-like pulse energy is still enough to maintain the plasma pressure constant. Further increasing the neutral pressure (ID 1-4 in Table 4.1) the energy losses for the weak ELM pulses keep increasing and n_e as well as p_e decrease transitioning to a detached plasma in Stage 3.

4.5 IR camera

The IR camera returns 2D temperature profiles of the target temperature over time. Only 3 frames correspond to a single ELM-like pulse so multiple pulses are overlapped and averaged to increase the resolution aligning all pulses peak as done by Li. [157] To avoid being affected by thermal transients only the last 150 of the 300 pulses within every scan is considered (see Section A.3 for details). From this data, the time dependent peak temperature and the shape of the affected region are extracted. These are used to show that the ELM-like pulse energy delivered to the target decreases with increasing neutral pressure to the point of being negligible therefore achieving the baffling of the ELM-like pulse.

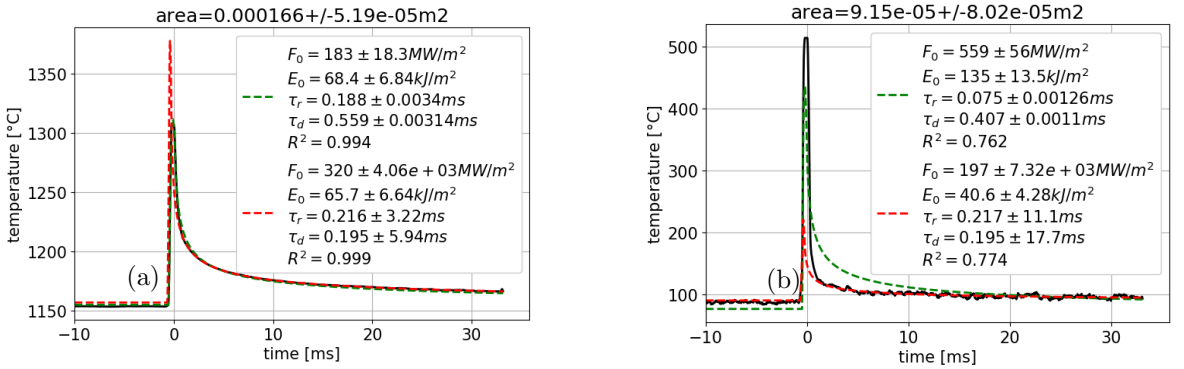


Figure 4.9: Comparison of the measured and fitted time dependence of the peak target temperature: (a) Stage 1 case, (b) Stage 2 case (ID 5 and 10 in Table 4.1 respectively). The black curve is the target peak temperature. The green dashed line (colour online only) is the temperature fit using the entire temperature curve. The red dashed line corresponds to fitting the temperature only for the time 1.5ms after the temperature peak. The curve is then plotted over the entire time domain using the fit parameters. In both cases the analytical model used is Model3 (Equation A.4 in Section A.3). The fit parameters are shown in the figure legend.

To estimate the energy delivered to the target the cooling curve is fitted with an analytical solution of the heat transfer equation. Various analytic solutions are available with different degrees of sophistication of the heat source time and spatial profile. It's important to keep in mind that the quantity of interest is an estimation of the total energy density [J/m^2] of the heat absorbed by the target from the ELM-like pulse. The analytical solutions considered have the following power density profiles in time and space:

- Model1 a temporally square wave delivered uniformly on a semi infinite plane as described by Behrisch [160], commonly used in tokamaks to asses the impact of ELMs because of the large extension of the wetted area.
- Model2 a temporally square wave delivered by a spatially Gaussian beam using a solution from Bäuerle [161, 162] and
- Model3 a temporally triangular wave delivered by a spatially Gaussian beam using methods from Bäuerle that better reproduce the Magnum-PSI conditions.

All the above analysis methods return similar values for the total energy density delivered to the target by each ELM pulse (details of the comparison of the various techniques are given in Section A.3). The total energy delivered to the target by the ELM-like pulse is then obtained by multiplying the peak energy density (E_0) by the affected area found by fitting the temperature profile after the pulse with a Gaussian profile. In Section A.3 the MSC.Marc/Mentat® non linear FEM suite was used to reproduce a heat pulse as close as possible to the typical experimental conditions in terms of temporal and spatial variation and temperature dependent material properties. It was found that fitting the temperature after 1.5ms from the peak temperature returns a value of energy delivered within $\pm 10\%$ of the real one. It was also found that an uncertainty of $\mp 1.5ms$ in the time corresponding to the temperature peak translates to a $\pm 10\%$ variation of the energy detected. This translates to a total uncertainty from the method of about $\pm 20\%$, good enough for our purposes.

Typical time dependent peak temperatures are shown in Figure 4.9. The traces presents a sharp peak followed by a slow cooling period. This fast peak can be caused by emission from the plasma (prompt emission) or an actual temperature increase of the target. For low target chamber neutral pressure the peak temperature matches well with the analytical model: sudden heating of a very thin layer of the surface of the target then the heat quickly

redistributes over a larger thickness and radius, being then more slowly dissipated to the actively cooled back plate. [157, 163]

In high neutral pressure conditions the peak is still present but it is inconsistent with the following slower cooling. The profiles are fit with Model3, fitting for all times or only the times beyond 1.5ms after the peak. For the Stage 1 case both fits return similar energy values and, most importantly, both fit well the curve for $t > 1.5$ ms. This is not the case in Stage 2, where the fit for all time fails appreciably. This demonstrates the inconsistency between the temperature peak and the slowly decreasing curve in high neutral pressure conditions. We attribute the enhanced peak to prompt IR line or continuum emission from the plasma (some hydrogen molecular lines lie inside the band allowed by the IR camera filter [164]). This is further reinforced by examining the spatial temperature distribution at the peak compared to afterwards. Further details on this and other aspects of the estimation of the energy delivered to the target are given in Section A.3. The OES could be used to differentiate between emission from the plasma column and then reflected by the target or emission from its immediate vicinity but because of the different wavelength ($3.97 - 4.01\mu\text{m}$ vs $0.32 - 0.52\mu\text{m}$) a direct comparison is not possible. In order to avoid possible misinterpretations only the temperature after 1.5ms from the peak is used rather than the peak itself. This phenomena is also observed in tokamaks, where IR measurements are routinely found unreliable during strong detached phases [165], and is sometimes used as a marker for detachment itself.

In Figure 4.10, for strong pulses, and Figure 4.11, for weak ones, are shown the results from the analysis of the target temperature. In blue is indicated the surface temperature prior the ELM-like pulse, that decreases for increasing target chamber neutral pressure as it would be expected for increasing volumetric losses in the target chamber and increasing level of detachment in steady state. In red is indicated the average temperature increase 10 to 11ms after the peak. This is done to mitigate the uncertainty in the time of the real temperature peak, hidden by the prompt emission for high neutral pressure cases. This indicates that at low neutral pressure a large portion of the energy of the ELM-like is absorbed by the target, while it is more and more dissipated in the volume for increasing target chamber neutral pressure.

In green are indicated the results from the analytical model. In solid green is indicated the energy absorbed by the target calculated as mentioned above. In 4.10 the delivered energy decreases to an apparent minimum, possibly due to some energy not delivered via plasma

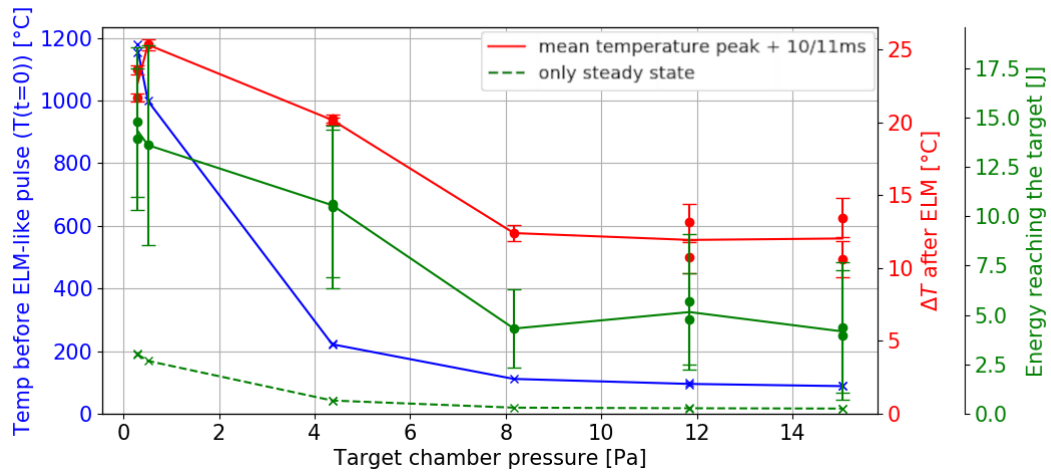


Figure 4.10: Results of analysis of the IR data for the variations in target chamber neutral pressure. In this figure we focus on the case of strong pulses (48J at the source) and higher magnetic field that yields higher plasma pressure background plasma (ID 5 to 10 in Table 4.1). Analysed data displayed are: target temperature before the ELM (blue), temperature increase during the ELM (red), ELM energy reaching the target (solid green) estimated with Model3 fitted after 1.5ms of the temperature peak and the steady state heat flux (dashed green).

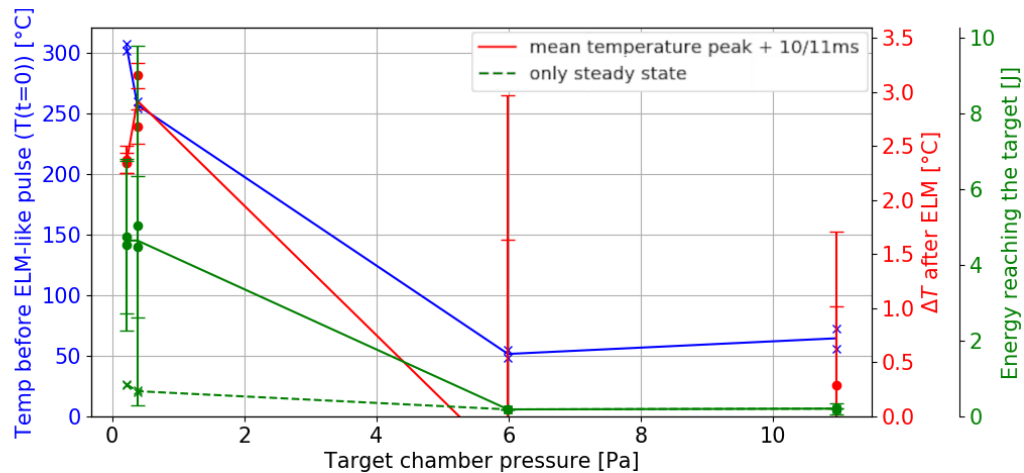


Figure 4.11: Results of analysis of the IR data for the variations in target chamber neutral pressure. In this figure we focus on the case of weak pulses (10.3J at the source) and lower magnetic field that yields lower plasma pressure background plasma (ID 1 to 4 in Table 4.1). Line colours and styles are the same as Figure 4.10.

convection but via neutral heating and radiation, shown later (see Section 4.6.3) to increase with higher pressure. In the extreme case of high target chamber neutral pressure and weak ELM-like pulse shown in Figure 4.11 the energy delivered to the target is negligible, indicating that the pulse energy was mostly dissipated by the gas in the target chamber. In dashed green is indicated the steady state component, always relatively small. The energy delivered

decreases with fuelling in a similar fashion as the temperature increase after the pulse. Most notably the energy delivered is negligible for the case with higher neutral pressure.

The thermal analysis allows us to compare the heat fluxes due to an ELM-like pulse in Magnum with Tokamaks. A metric often used in Tokamaks to estimate effect of ELMs is the heat flux factor, defined as the energy of the ELM divided by the area in which it is delivered divided by the square root of its duration. This metric is derived by the same analytic solution for the temperature increase in Modell and is proportional to the maximum temperature increase. The maximum heat flux factor to prevent tungsten melting is $\sim 50 \text{MJm}^{-2} \text{s}^{-0.5}$ while $\sim 40 \text{MJm}^{-2} \text{s}^{-0.5}$ for the molybdenum target used here. The limit to prevent cracking is about half of the melting one [166] with some studies indicating it as low as $6 \text{MJm}^{-2} \text{s}^{-0.5}$ for tungsten. [167]

The heat flux factor obtained in these experiments was estimated from the pulse energy density from the IR analysis and as pulse duration an arbitrary 0.7ms and 0.3ms for the strong and weak pulses respectively estimated from the fast camera records. In the strong pulses case the heat flux factor is decreased from $\sim 2.5 \text{MJm}^{-2} \text{s}^{-0.5}$ for $p < 6 \text{Pa}$ to $\sim 1.5 \text{MJm}^{-2} \text{s}^{-0.5}$ for $p > 6 \text{Pa}$. For weak pulses the drop in heat flux factor went from $\sim 0.4 \text{MJm}^{-2} \text{s}^{-0.5}$ for $P < 3 \text{Pa}$ to effectively zero for $P > 3 \text{Pa}$. These heat flux factors are higher than what measured in current tokamaks (< 1.3 for JET) but much lower than what could be achieved in ITER ($600\text{-}1100 \text{MJm}^{-2} \text{s}^{-0.5}$ for unmitigated ELMs). [29, 168]

In a tokamak the connection length from target to midplane is of the order of tens of meters on the outer target and the divertor neutral pressure can reach the Pascal range [169]. If the divertor is separated from the main chamber by a baffle, meaning there is a physical restriction of neutral flow between the divertor and the main chamber, the plasma can plug the divertor entrance and the neutrals cannot freely move between the two. The neutrals have to interact with the plasma in the SOL and (in deep detachment) the ionisation front, and the neutral pressure behind the ionisation front can be increased by more than one order of magnitude compared to that in the main chamber. [170–172] In our experiments the connection length in the target chamber is 0.38m and the neutral pressure up to 15Pa. Given the energy delivered to the target by the ELM-like pulse is reduced with neutral pressure and that tokamaks are characterised by potentially longer connection lengths and similar or higher neutral pressures behind the ionisation front, this result implies that a significant reduction of the heat flux factor in tokamaks should be possible thanks to the cold regions

forming close to the target when strongly detached too. The reduction of heat flux factor and heat flux to the target with pressure and connection length could be non linear (see the higher pressure cases in [Figure 4.10](#)) but [Figure 4.11](#) shows that transitioning from stage 2 to 3 via volumetric losses should ultimately be possible. The viability of this method to dissipate the ELM energy will ultimately depend on the neutral pressure required to achieve the needed buffering and its effect on the inter-ELM plasma. Configurations like the super-x divertor could be the most suitable for this approach, as the ionisation front could be maintained relatively close to the x-point while a large volume with high neutral pressure can be maintained in the super-x divertor chamber. Reducing the ELM heat flux factor would improve the safety for long term operations in a tokamak, further showing the benefit of baffling and increasing the neutral chamber pressure in detached scenarios.

In summary, by increasing the target chamber neutral pressure it is possible to cause detachment of the steady state plasma from the target surface. From the visible fast camera brightness in Magnum-PSI, we identify 3 stages for the interaction between the ELM-like pulse and the background gas in the target chamber. By increasing the neutral pressure more interactions happen in the volume rather than in contact with the target, and become more homogeneous in the plasma column. This is true up to Stage 3, where the loss of plasma in the volume becomes dominant. A regime with low-energy ELM-like pulses was found where the gas in the target chamber can effectively prevent all of the pulse energy from reaching the target.

These results are obtained through analysis of one diagnostic at a time. To gain more insight the OES data will be combined with that from TS and the input power source measurement within a Bayesian analysis framework. The purpose is to identify which processes are more relevant in the increase of energy removed in the volume for increasing levels of steady state detachment, driven by target chamber neutral pressure, and possibly their evolution in time.

4.6 Role of molecular assisted reactions

In this section we describe our analysis technique that simultaneously takes into account information from different diagnostics on Magnum-PSI data to gain more insight on the dominant atomic and molecular processes during an ELM-like pulse. A significant aspect of

this analysis is the inclusion of the molecular species H_2 , H_2^+ and H^- . These species interact with the plasma leading to the formation of excited hydrogen atoms, with related power and particle sources/sinks, which have a significant influence on the behaviour of Magnum-PSI target chamber plasmas driving them into detachment. Since the interaction of these species with the plasma causes hydrogen atomic line emission they will be referred to as molecular precursors.

The ordinary method to infer the plasma properties from Balmer emission lines is to consider that the emission from higher- p H excited states is mainly generated via electron-ion recombination (EIR), while the emission from lower excited states is generated via electron impact excitation (EIE), and molecular contributions are generally neglected for simplicity. This normally allows to determine if the plasma is ionising, recombining or in between. [149, 173]. Under conditions like those in this work, on the other hand, molecular contributions can be significant. [18] Plasma molecular interactions lead to excited hydrogen atoms generally excited to low p levels, and their distribution across p is similar to the one of EIE, thus complicating the Balmer line analysis (see Section 4.6.2).

In order to find the set of plasma/molecule/atom characteristics (T_e , n_e , n_H/n_e , n_{H_2}/n_e , $n_{H_2^+}/n_{H_2}$, n_{H^-}/n_{H_2} , one of these quantities is referred to as Θ_i while a set of 6 as Θ) that best match both the line emission (from OES) and the electron temperature and density (from TS), a Bayesian approach is followed. This allows the analysis method to pool together information from different diagnostics in combination with priors from simulations as well as reaction rates to find the best match to experimental data and thus derive an understanding of the dominant processes and effects on the energy and particle balance. The main advantage of this approach is that it can not only account for all uncertainties and non linear rates, but also allows calculating the probability density function (PDF) of the quantities of interest. This implies that multiple non unique solutions, if present, can be found.

Probabilistic approaches have been used before to infer the full state of the divertor plasma in tokamaks but never during the ELM burn through. [19, 174, 175] First, the parameter space of Θ is defined, forming a regular grid. The range and samples of the Θ_i parameter are defined based on Thomson scattering and other priors. Given a certain combination of parameters Θ the outputs of all the quantities of interest can then be calculated, like line emission, power and particle sinks and sources, etc. Those predicted observables can then be compared with the priors to find the probability that the calculated values match

the expected ones. This comparison and the calculation of the observables depend on the specifics of the problem and the simplifications used. For the combination of parameters Θ the probability from the priors is multiplied with the probability from the comparison of the calculated and measured line emission, returning the likelihood of the particular Θ . Starting with this grid one can: add individual Θ searching for the maximum of the likelihood; or refine the grid further around the best Θ . A grid refinement is done here to retain a grid structure and simplify the numerical problem. This is done only twice to limit the computational cost and memory requirements. After the quantities of interest like, for example, terms of the power balance, can then be calculated for each Θ and their probability density function (PDF) found.

Section A.4.5 gives the full list of assumptions used to simplify the physics of the plasma of interest (from the target skimmer to the target, see Figure 4.1). In short, the plasma is considered homogeneous along its length (z) from the target chamber skimmer to the target within each time step, and being poloidally (ϕ in Figure 4.1) symmetric for a given radius (r). This is supported by the relatively uniform visible light emission far from the target found in Stage 1 and 2 in Section 4.3. This means that the ELM-like pulse is not localised at a particular spatial location but happens along the whole plasma column, matching well the fast nature of the transport along field lines (\sim sonic flow, $< 20\mu s$ to flow through the target chamber) compared to the changes in plasma conditions over time (changes well resolved with $50\mu s$ time steps). The conditions at the target chamber skimmer will be considered as the input to the plasma column. The presence of impurities is monitored by a 6-channels Avantes AvaSpec-2048-USM2-RM survey optical emission spectrometer covering the range 299-950nm. [155] The survey spectrometer's channels LOSs are in the target chamber and impurities like metals from the power source or oxygen from cooling water are only detectable in significant amounts when the plasma source fails. This shows that impurities from the source are ordinarily efficiently removed in Magnum-PSI by differential pumping. Carbon can play a significant role when graphite targets are used [176], but this is not a concern in these experiments in which a TZM target was used.

The integral over the ELM-like pulse of quantities of interest, like terms of the power balance, are obtained by summing the contribution from each time step and radial location. In the following section we will explain the method used to determine the probability associated with an output at a given time and radial location.

4.6.1 Analysis steps

We will describe here in more detail the steps to first initialize the parameter space based on TS and other priors (Section 4.6.1.1). Then we will show how to compare the modelled quantities and TS with the priors to obtain the probability of each Θ (Section 4.6.1.2). Lastly the comparison with the measured Balmer lines emission, grid refinement process and determination of the quantity of interest PDFs will be illustrated (Section 4.6.1.3). The numbering of each step corresponds with the numbers in the boxes in Figure 4.12, 4.13, 4.14.

4.6.1.1 Parameter space initialisation

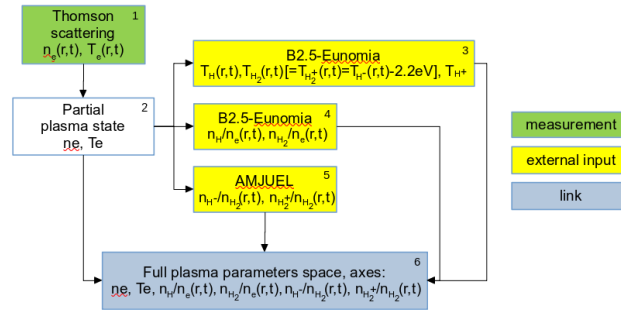


Figure 4.12: Sketch illustrating how the initial guess of each parameter Θ_i is done. With *link* are marked items that link different parts of the global bayesian routine together. *measurement* indicate quantities measured experimentally and *external input* represents inputs from simulations or reaction rates libraries.

Our Bayesian analysis first finds the range of parameters to utilize. This is shown in Figure 4.12. Every point in time and radius (t, r) during the ELM-like pulse is considered independently. Referring to Figure 4.12 the meaning of the steps are as follows:

1,2 Thomson scattering $n_e(r,t)$, $T_e(r,t)$:

The measured T_e and n_e and their uncertainties are used to specify the range and grid elements of T_e and n_e . From every T_e, n_e combination the samples for the other Θ_i are calculated.

4 B2.5-Eunomia $n_H/n_e(r,t)$, $n_{H_2}/n_e(r,t)$:

We utilize B2.5-Eunomia simulations, a multi-fluid plasma code coupled with a non-linear Monte Carlo transport code for neutrals [177–179], to determine scalings for n_{H_2} and n_H with T_e . We utilize these scalings to obtain ranges for n_{H_2}/n_e and n_H/n_e (see Section A.4.1 and A.4.3).

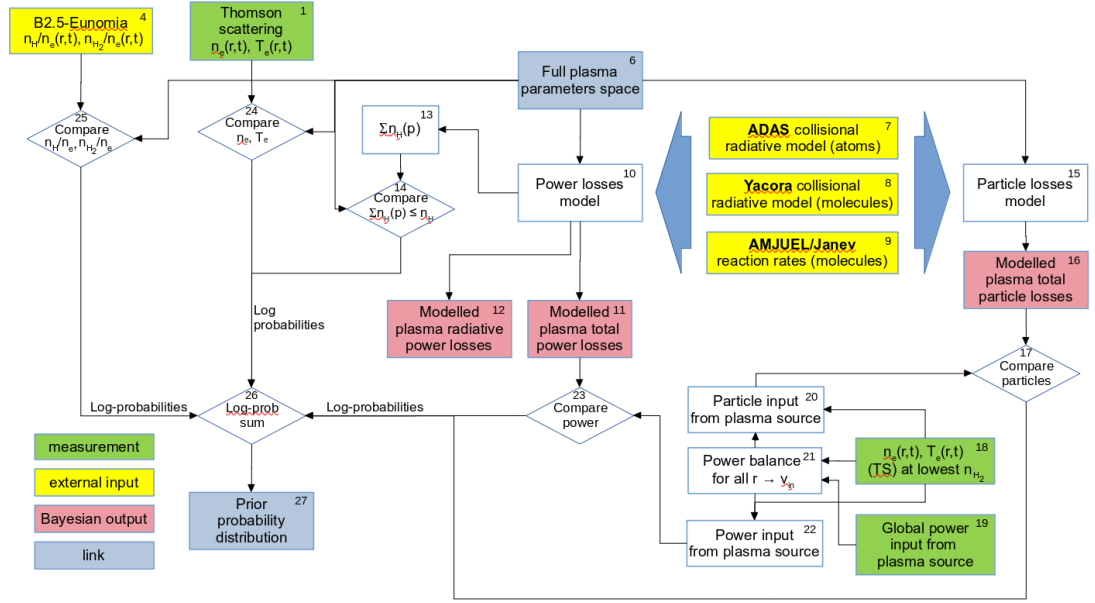


Figure 4.13: Sketch illustrating how the prior probability distribution is determined given the parameter grid. *Bayesian output* indicates groups of quantities that are collected for all the parameter space and with the likelihood will return their PDF.

3 *B2.5-Eunomia* $T_H(r,t)$, $T_{H_2}(r,t)[= T_{H_2^+}(r,t) = T_{H^-}(r,t) - 2.2eV]$, T_{H^+} :

Similarly, values of T_H , T_{H_2} and T_{H^+} are extracted from B2.5-Eunomia simulation scalings with T_e . Given the molecular precursor H_2^+ is predominantly generated from H_2 it is assumed that $T_{H_2} = T_{H_2^+}$. In the creation of H^- from H_2 the ion can get some of the Frank-Condon energy of the H_2 bond (2.2eV per nucleon). For this reason 2.2eV are added to T_{H_2} to estimate T_{H^-} [19] (see Section A.4.1).

5 *AMJUEL* $n_{H^-}/n_{H_2}(r,t)$, $n_{H_2^+}/n_{H_2}(r,t)$:

H_2^+/H_2 and H^-/H_2 density ratios are calculated from the AMJUEL collection of cross sections, reaction rates and ratios [5–7] to determine the n_{H^-}/n_{H_2} and $n_{H_2^+}/n_{H_2}$ ranges used as priors (see Section A.4.2 and A.4.3).

4.6.1.2 Prior probability distribution

Once the initial parameter space is determined the prior probability distribution is calculated. The process for this is shown in Figure 4.13 and the meaning of the steps is as follows:

7 *ADAS collisional radiative model (atoms)*:

The Atomic Data and Analysis Structure (ADAS) collisional radiative model [1, 2]

is used to calculate the line emission (see [Section A.4.4](#)), the power losses (see [Section A.4.6](#)) and the particle balance sources/sinks (see [Section A.4.7](#)) due to atomic processes. The reactions considered and relative coefficients are indicated in [Table A.1](#). This type of analysis is fairly standardised, see for example [\[180\]](#).

8 *Yacora collisional radiative model (molecules):*

The Yacora collisional radiative model [\[3, 4\]](#) is used to calculate the line emission due to molecular precursors via the population coefficients (see [Section A.4.4](#)) and the radiative power losses (see [Section A.4.6](#)). The molecular precursors that will be utilized in this analysis are H_2 , H_2^+ and H^- based on the work by Verhaegh [\[150\]](#) (see the reactions in [Table A.2](#)). H_3^+ could also be considered, but its relevance is expected to be much lower than that of H_2^+ and H^- so it is dropped to limit the number of variables. [\[150\]](#).

9 *AMJUEL/Janev reaction rates (molecules):*

The AMJUEL database and a collection of reaction rates from Janev [\[8\]](#) is used to calculate the rate of reactions involving molecular precursors (see [Table A.3, A.4](#)). The reactions rates are use then to calculate sources and sinks in the power and particle balance in the plasma column (see [Section A.4.6, A.4.7](#))

19 *Global power input from plasma source:*

The power input from the plasma source is calculated from the measurement of voltage and current on the plasma source. From a study by Morgan [\[154\]](#), 92% of the electrical energy is transferred to the plasma during an ELM-like pulse. This value will be considered valid for each time step.

18 *$n_e(r, t), T_e(r, t)$ (TS) at lowest target chamber pressure:*

It is assumed that for the lowest pressure case the interactions between the plasma column and the background gas in the target chamber are negligible, therefore they represent the input conditions for all cases that differ only by the target chamber neutral pressure. They are referred to as $n_{e,in}, T_{e,in}$ and used to determine the input power and particle profiles (see [Section A.4.5](#)).

21 *Power balance for all $r \rightarrow v_{in}$:*

Assuming that the plasma flows from skimmer to target with the same Mach number

($M_{in}(t)$) across different radii it is possible to relate the total input power ($P_{source}(t)$) with the input conditions ($n_{e,in}(r,t), T_{e,in}(r,t)$). It is then possible to determine $M_{in}(t)$ and then $v_{in}(r,t)$. See [Section A.4.5](#) for details.

22 *Power input from plasma source:*

The maximum power input is calculated as the energy flow due to a plasma in the input conditions ($n_{e,in}(r,t), T_{e,in}(r,t)$) at flow velocity $v_{in}(r,t)$ plus the energy associated to the depletion of the plasma at the specific neutral pressure of the experiment ($n_e(r,t), T_e(r,t)$) in one time step. See [Section A.4.6](#) for details.

20 *Particle input from plasma source:*

Similarly to the previous step the maximum particle input is obtained as the input particle flow using $n_{e,in}(r,t)$ and $v_{in}(r,t)$ plus the particle flow associated with the dissipation of the plasma at the specific neutral pressure of the experiment ($n_e(r,t)$) in one time step. See [Section A.4.7](#) for details.

10 *Power losses model:*

The power losses in the annular section of the plasma column of interest are modelled as per [Section A.4.6](#). The effect of impurities is not considered, as it is assumed that most of the impurities introduced by the plasma source anode and cathode are removed by differential pumping in the source and heating chamber.

12 *Modelled plasma radiative power losses:*

The total radiated power from the plasma column is calculated. For atomic processes ADAS coefficients are used. For molecular processes Yacora coefficients are used, summing the line emission for all possible transitions (the highest excited state considered is $p=13$). It is not considered the radiation caused directly by H_2, H_2^+, H^- excited states such as the Werner and Lyman bands, as it should have a negligible contribution. [[181](#), [182](#)]

11 *Modelled plasma total power losses:*

The total power losses are obtained by adding: total radiated power losses, net difference of potential energy from reactants to products and energy loss attributed to the heat carried away from the neutral produced by recombination. This terms and their components are part of the outputs of the Bayesian analysis.

23 *Compare power:*

The modelled net power losses are compared to the power input previously inferred. The net power losses have to be between 0 and the power input. The probability that this is the case is calculated as shown in [Section A.4.6](#) and is one component of the prior density distribution.

15 *Particle losses model:*

The particle sink-sources terms are modelled as per [Section A.4.7](#). We neglect cross field transport when analysing the particle balance. Given the difficulty of accounting for cross field transport only the particle balance of the charged particles (e^- , H^+ , H_2^+ , H^-) that are bound by the magnetic field is operated.

16 *Modelled plasma total particle losses:*

The net particle sink is calculated for e^- , H^+ , H_2^+ , H^-). These terms and their components are part of the outputs of the Bayesian analysis.

17 *Compare particle:*

The modelled net particle losses are compared to the particle input previously inferred. Bounds for physical values of the net particle losses are obtained from the particle input previously inferred as detailed in [Section A.4.7](#). The probability that the particle sinks are within the bounds is calculated and their log-probability summed.

13 $\Sigma n_{H(p)}$:

Within the power losses model the total density of excited states is calculated. ADAS PEC coefficients are used for atomic processes while Yacora coefficients are used for molecular, summing the density for all excited states.

14 *Compare $\Sigma n_{H(p)} \leq n_H$:*

It is checked that the total density of excited states is lower than the density of atomic Hydrogen. At the temperature of interest in this work the density of excited states is always a small fraction compared to the ground state, so a probability of 1 is assigned if the condition is respected and 0 otherwise.

24 *Compare n_e , T_e :*

The measured T_e and n_e and their uncertainties are used to assign the relative probability on the n_e and T_e axis of the parameter space, uniform on the others.

25 Compare n_H/n_e , n_{H_2}/n_e :

The previously mentioned scalings from B2.5-Eunomia simulations are used to assign weakly varying probabilities on the n_H/n_e , n_{H_2}/n_e axis of the parameter space, being uniform on the others, as indicated in Section A.4.1.

26 Log-prob sum:

The log probability from the particle and power balance, amount of Hydrogen excited states, TS and B2.5 Eunomia are summed to return the Log-probabilities for the entire parameter space.

4.6.1.3 Bayesian analysis

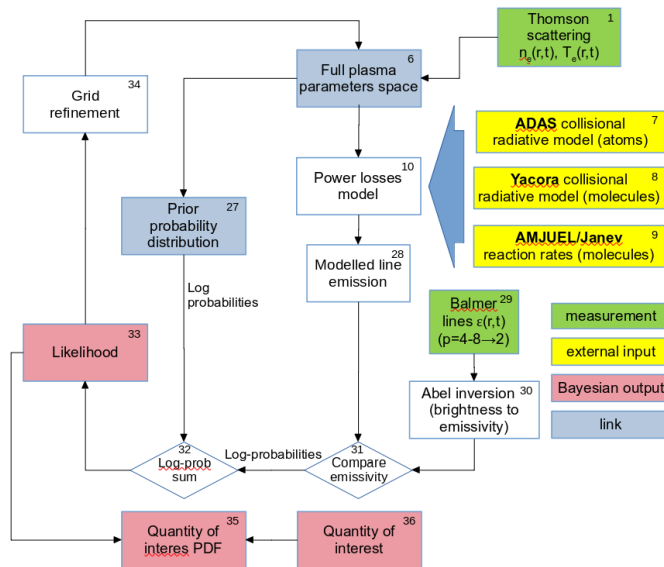


Figure 4.14: Sketch illustrating how the likelihood distribution is determined comparing the line emission with the expected values and adding the prior log-probability, to refine the parameter grid and calculate the outputs PFD.

The expected value of the Hydrogen line emissivity is then compared with the measured one, and the resulting probability combined with the prior to return likelihood, also referred to as the sum of the Log-probabilities. The grid is refined twice around the regions of the grid with high likelihood to improve the resolution of the probability distribution. While keeping a grid structure requires a large amount of memory the numerical procedure is relatively simple. This procedure is shown in Figure 4.14 and the meaning of the blocks here introduced is as follows:

29 *Balmer lines $\epsilon(r, t)(p = 4 - 8 \rightarrow 2)$:*

The Balmer line emission for transitions ($p = 4 - 8 \rightarrow 2$) is measured with OES (see [Section 4.2.2.1](#)). The camera has a rolling shutter so it is necessary to decouple the line of sight from the time information, as detailed in [Section A.1](#) and [A.2](#).

30 *Abel inversion (brightness to emissivity):*

Once the brightness per time step and line of sight is obtained an Abel inversion is operated (see [Section A.2](#)). The process converts the line integrated information to the local emissivity assuming poloidal symmetry and the plasma optically thin.

28 *Modelled line emission:*

As part of the power losses calculation the line emission from atomic and molecular processes the total line emission for the lines of interest ($p = 4 - 8 \rightarrow 2$) is found (see [Section A.4.4](#)).

31 *Compare emissivity:*

The modelled line emissivity is compared to the measured one to return the probability that each combination of priors generated the measured emission (see [Section A.4.4](#)).

32,33 *Likelihood:*

The likelihood for every point of the parameter space is found adding the log probability from the prior and the comparison of the calculated emissivity with the measured one.

34 *Grid refinement:*

To increase the resolution in the region of the parameter space with high likelihood, the grid is refined by adding intermediate steps to the grid elements previously defined for every axis around the marginalised likelihood peak. The grid structure is maintained but it becomes non uniform. The prior probability distribution and comparison with measured emissivity is repeated to recalculate a new likelihood distribution. This loop is repeated twice to limit the computer memory requirements.

35,36 *Quantity of interest PDF:*

The quantity of interest for the plasma column power or particle balance have already been calculated for all the parameter space within [Section 4.6.1.2](#). In order to reduce the size of the outputs the full range is reduced to a smaller number of intervals and the likelihood is summed within each interval.

Once the PDFs for a quantity of interest in all radial and spatial locations are determined they are then convolved over radial steps, to obtain the total over the plasma column, and then in time over the ELM-like period to obtain the global quantities (see details in [Section A.4.8](#)).

When a reaction occurs, energy is transferred between different species (e.g. plasma to molecules or atoms). If charged particles are created they are bound by the magnetic field and are confined to the same radial section of the plasma column. When neutral hydrogen atoms and molecules are generated they can escape the plasma column, carrying with them their kinetic energy. They can also interact with plasma at a different radii on the way out and transfer the energy back in the plasma.

To model the transfer of energy to the neutrals and back to the plasma would require an effort beyond the scope of this work, so for now this component is not considered in the power and particle balance and only hydrogenic radiation is considered as net power leaving the plasma column. For more details see [Section A.4.8](#).

It is important to address whether ignoring the power removed by the plasma column (and possibly transferred back) due to charge exchange (CX) and elastic collisions between H_2 and H^+ (H_2 elastic) is important and compatible with the Bayesian algorithm results. To estimate CX and H_2 elastic power losses we post-process our results as shown in [Section A.4.6](#). The same methodology was employed to reprocess B2.5-Eunomia results, and it returned a CX contribution between a 1% and 150% and H_2 elastic within 18% and 34% of the correct (self consistent) values. In one instance, the simplified method produced a factor of 100 larger CX losses compared to B2.5-Eunomia result. It is observed that in this case, with both high temperature and density, a large fraction of the CX losses are recovered by fast neutrals exchanging back to the plasma their energy before escaping the plasma column. This behaviour can be captured by the Monte Carlo model but not by this simplified method. With these very large uncertainties it is possible to say that CX is likely more important than H_2 elastic for ELM-like pulses, contrary to what shown in [179], but the relevance for the plasma column energy balance is uncertain and would require a more detailed analysis, out of the scope of this work.

4.6.2 Analysis limitations due to restrictions on measured Balmer lines

While it is in general desirable to measure as many transition lines as possible, it became apparent during the setup of the experiment that the $H\alpha$ line ($p = 3 \rightarrow 2$) could not be measured simultaneously with lines $p \geq 4 \rightarrow 2$ due to the grating used. We describe herein how the lack of the $H\alpha$ line prevents the separation of the line emission contribution from H_2^+ and H^- precursors.

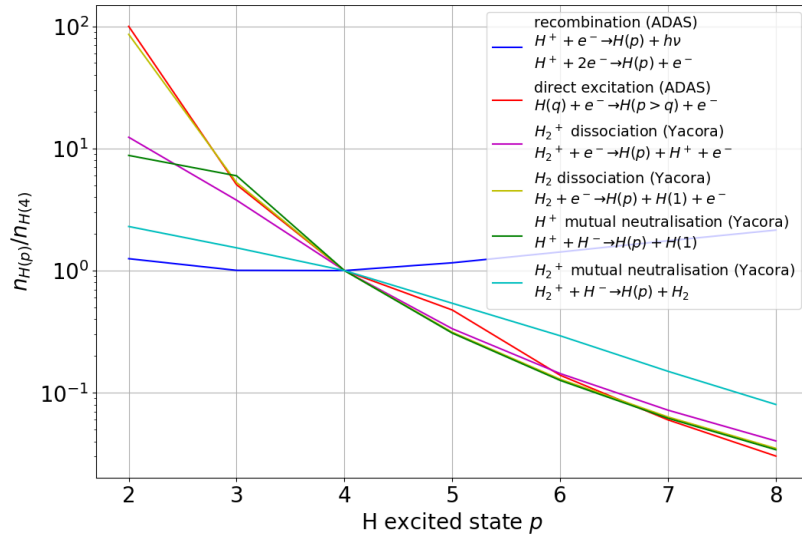


Figure 4.15: Density ratio of hydrogen excited states to $p=4$ for different processes for typical $T_e = 1\text{eV}$, $n_e = 4 \cdot 10^{21} \text{ \#}/\text{m}^2$ plasma. The similarity of the profile shape for H_2^+ dissociation and H^+ mutual neutralisation is maintained for all the T_e, n_e range of interest.

As a reference, [Figure 4.15](#) shows the density ratio of excited states produced by different processes with respect to $p=4$ for typical T_e, n_e values. Restricting Balmer lines to $n \geq 4 \rightarrow 2$ recombination, H_2^+ mutual neutralisation and EIE have a distinctively different profile while H_2^+ dissociation, H_2 dissociation and H^+ mutual neutralisation are fairly similar. H_2 dissociation is usually not problematic because the H_2 density required to match the measured emissivity is excessively high. Conversely, H_2^+ dissociation and H^+ mutual neutralisation can be caused by relatively low molecular precursors densities, making it difficult to distinguish which caused the emission. This could have been alleviated by including $p = 3 \rightarrow 2$ in the analysis [\[120\]](#) but this was not possible with the available gratings. [Figure 4.15](#) illustrates that with the present setup, using only the line ratios available is insufficient to distinguish which molecular precursor, H_2^+ or H^- , is dominant. This could be alleviated by combining matching line intensities with other conditions as

described in [Section 4.6.1](#), as it can help rule out regimes that can well match the emission profile but would be unphysical.

The results of this study and the relevance of molecular interactions during the ELM-like pulse will now be shown.

4.6.3 Bayesian analysis results

In this section the results from the Bayesian analysis will be presented. Only results regarding the strong pulse cases are shown, since the temperature and density falls below the detection capabilities of the TS system for a significant fraction of the duration for weak pulses.

4.6.3.1 Power balance

As explained in [Section 4.6.1.3](#) the results at each time and radial location are a collection of PDFs for the quantities of interest in the volume from target skimmer to target, like the power radiated via EIE. The temporal and spatial distribution of the most likely values can already be useful, as they can inform on the conditions in which some phenomena are important. Our inference shows that ionisation and excitation tend to be more important close to the axis of the plasma column, where and when temperature is highest, but are not peaked on the axis as the atomic hydrogen density profile is hollow. Radiation from EIR is strong for high density and intermediate temperature. Radiation from excited H atoms (H^*) generated from plasma molecular reactions (PMR) is present at similar times and locations as EIR but is significant up to even larger radii (and lower temperatures) than EIR. This is shown for ID 10 in [Table 4.1](#) in [Figure 4.16](#).

The PDFs are convolved over the radial direction to integrate the parameter of interest on the radii. An example of the radial convolution of the power radiated from EIE at 0.4ms for ID 5 in [Table 4.1](#) is shown in [Figure 4.17](#). It can be noted that some PDFs, for example at $r = 11mm$, show multiple peaks. This indicates that multiple possible combinations of the precursors densities with similar likelihood have been found.

The evolution over time of the terms of the local the power balance, as per [Section A.4.6](#), are shown in [Figure 4.18](#) for the lowest and highest pressure cases. In [Figure 4.18a](#) is shown that the energy of the ELM-like pulse is almost entirely used for ionisation, dissociation and molecular processes (MAD, MAI) increasing the plasma potential energy. However these ions recombine at the target, meaning that a larger fraction of the pulse energy will be

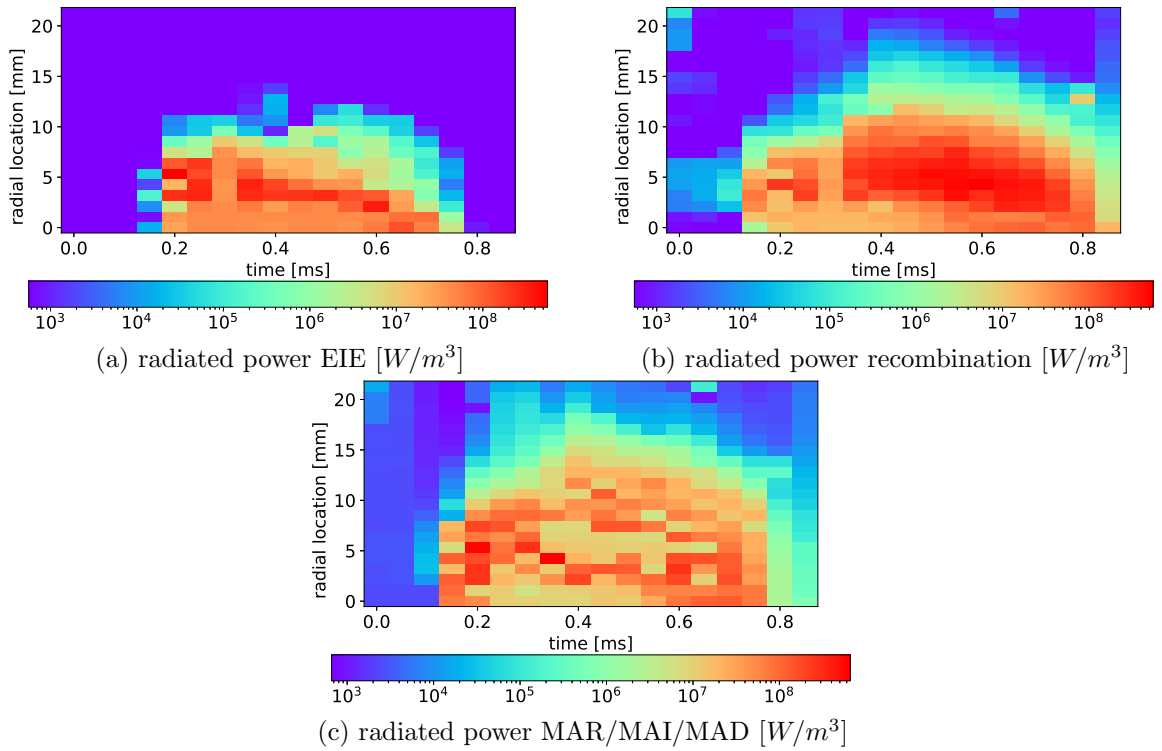


Figure 4.16: Most likely values of the radiated power via EIE (a), recombination (b) and molecular processes (c) for the same conditions of Figure 4.7b, ID 10 in Table 4.1. The noise shown in these figures arises from the fact that the analysis is independent for each radial and temporal location (no regularisation applied).

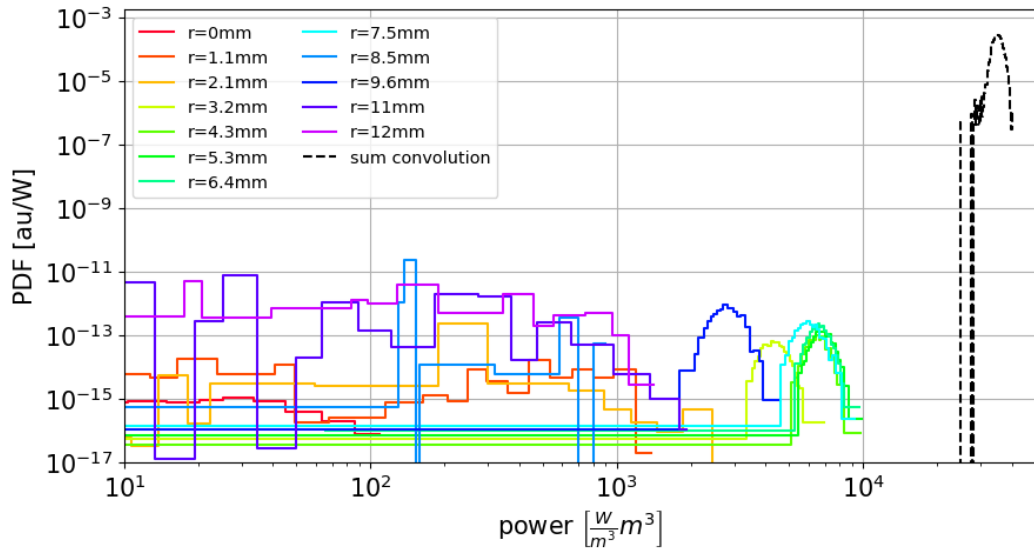
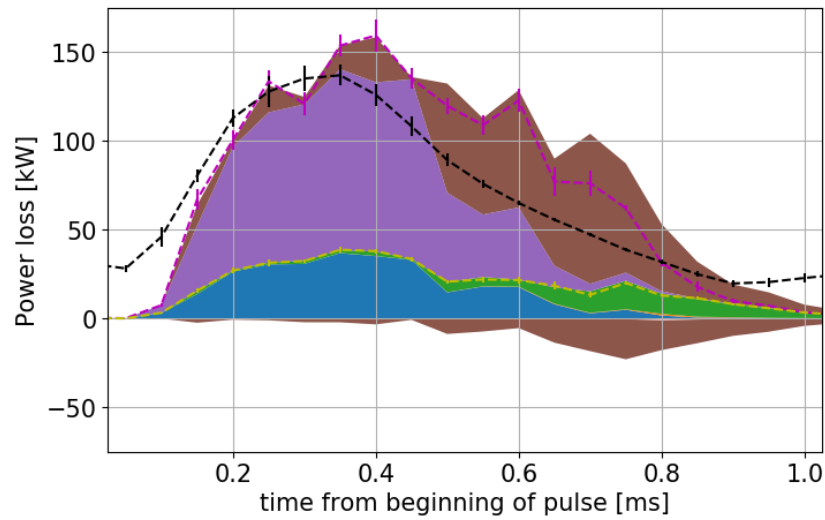
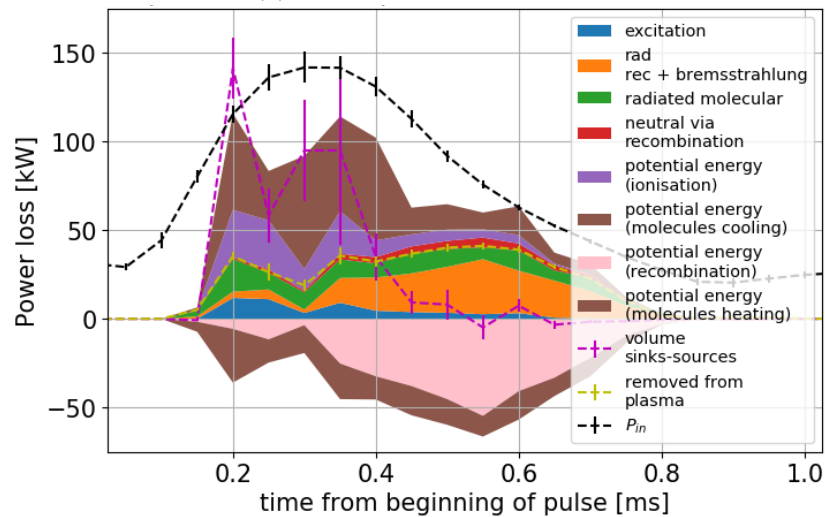


Figure 4.17: Example of the radial sum of the power radiated via excitation for ID 5 in Table 4.1 at 0.4ms. Only the radial locations that are more relevant are here shown. The power density (W/m^3) at each location is multiplied by the volume it pertains to determine the x coordinate.



(a) neutral pressure = 0.3Pa



(b) neutral pressure = 15Pa

Figure 4.18: Stacked area plot of the most likely values for the terms of the power balance as per Section A.4.6 for the lowest (a) and highest (b) pressure conditions for strong pulses. The data below zero corresponds to energy that released by recombination reactions heating the plasma. The potential energy from interactions with molecules is split in its positive and negative components. As *molecules* is here intended any reaction with exchange of potential energy different to EIR and ionisation (see Section A.4.9). *volume sinks-sources* corresponds to the net local power balance while *removed from plasma* indicates the contribution to the plasma column power balance as per Section A.4.8. The colours in the legend of (b) apply to both plots.

able to reach the target, and in fact for this condition the target receives the most heat. The net power sink from the plasma is slightly larger than the input energy after its peak. This can be understood as there is no mechanism to enforce a global power balance since the analysis for every radial and temporal location is independent. The radiated energy is

mostly due to EIE, that is to be expected due to the high temperature. After 0.6ms the temperature decreases below 4eV and the radiative and potential energy losses to the plasma from MAI/MAD and dissociation increases.

For higher neutral pressure (Figure 4.18b) the peak in power input corresponds to the peak of power loss from molecular reactions rather than ionisation (due to the lower temperature) and most importantly, after the input power and temperature peak, there is a strong influence of EIR. Radiative losses and potential energy gains balance such that after 0.4ms the net power sink on the plasma is negligible. [149] The period of peak radiative losses now coincides with the peak in EIR. More energy is radiated then before and recombination in the volume means that the plasma is depleted before reaching the target. The radiative losses are on the expenses of the plasma potential rather than its thermal energy. This causes a reduction of the heat flux just like in deep detachment, matching with the results in Section 4.5. EIR dominates the path to radiative losses but the influence of molecular reactions increases. These results are quite similar to recent studies of detachment in medium size tokamaks including molecular precursors. [86, 150]

The PDFs at each time are further convolved multiplying by the time interval they refer to, returning the total for the quantity of interest over the entire ELM-like pulse. In Figure 4.19 is shown how the total energy radiated by the plasma changes with target chamber pressure. As the target chamber pressure is increased (Stage 1 ($P < 2\text{Pa}$) to 2

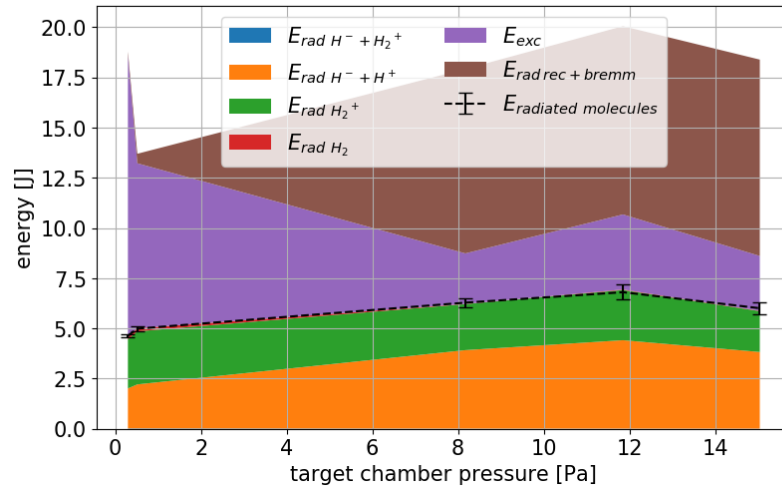


Figure 4.19: Energy dissipated radiatively per mechanism for increasing neutral pressure (ID 5 to 10 in Table 4.1) obtained with the Bayesian analysis.

($P > 2\text{Pa}$) the dominant process changes from EIE to EIR and the impact of molecules

increases reaching up to $\sim 1/3$ of the total radiated power. This is also reflected in the total radiated power in the visible wavelength range (not shown): in Stage 2 it is 3 times higher than in Stage 1, 0.3J and 0.1J respectively (the Lyman series is always responsible for most of the power radiated), largely due to the increase of EIR importance. This is not as a dramatic increase as observed in [Figure 4.5](#), implying that the extrapolated $H\alpha$ emission, from our inferences, could be overestimated. This could imply an overestimation of molecular assisted reactions in Stage 1 (visible radiated power losses due to EIE are 0.005-0.01J in for ID 5 and 6 in [Table 4.1](#) respectively, with a better agreement with [Figure 4.5](#)). An overestimation of $H\alpha$ can also arise from an (over)underestimation of $(H^-)H_2^+$, changing the $H\beta/H\alpha$ ratio as shown in [\[19\]](#). Among radiation due to molecules the precursor that is more important is H^- . This would be against results from previous analysis that show a dominance of the H_2^+ precursor [\[18\]](#) but, as mentioned in [Section 4.6.2](#), the radiation from H_2^+ dissociation and H^+ mutual neutralisation has similar line ratios for the lines used in this study, so cannot be distinguished with certainty.

In [Figure 4.20](#) are shown the variation of the terms in the global plasma column power balance with target chamber pressure. The energy absorbed by the target was determined in [Section 4.5](#). The estimation of CX and H_2 elastic collisions is as per [Section A.4.6](#). The two terms are already multiplied by the corrective factors found by comparing their simplified model with B2.5-Eunomia, identified in [Section 4.6.1.3](#) (CX and H_2 elastic collision losses from B2.5-Eunomia being 1-150% and 18-34% respectively compared to the simplified estimate). The radiative energy losses increase with target chamber neutral pressure, up to $\sim 1/3$ of the input energy, while the energy to the target decreases. This transition corresponds to the transition between Stage 1 and 2 introduced when analysing the visible fast camera brightness. H_2 elastic losses are of the same order of magnitude as radiative and target losses, while CX has a very large range from zero to one order of magnitude higher than P_{in} . These losses are here only estimated. Subtracting the radiative losses from the input energy returns much more than the measured target flux, allowing for other loss channels like CX, H_2 elastic collisions or the losses associated with plasma surface interactions, that are here not inferred.

From this very crude balance it seems that losses due to radiation and energy transfer to the target can account for about 1/3 of the input energy and H_2 elastic collisions for another 1/3. From fast camera observations, for high pressure conditions the energy dissipated at

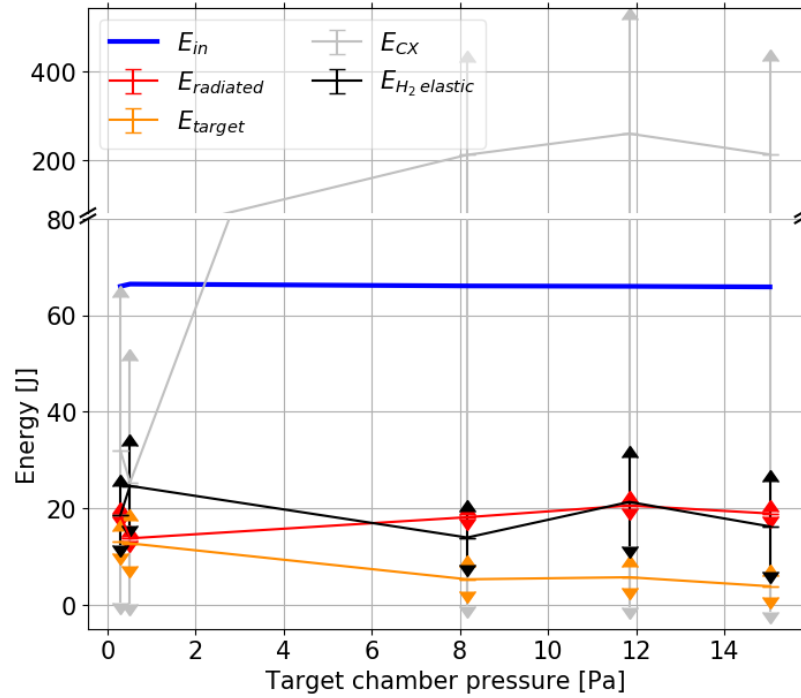


Figure 4.20: Results from the Bayesian analysis for strong ELM-like pulses with increasing neutral pressure (ID 5 to 10 in Table 4.1). Total energy input (blue), energy removed from the plasma column (approximated with the hydrogenic radiative losses, red), energy absorbed by the target from IR camera analysis in Section 4.5 (orange), estimated maximum energy removed from CX (grey) and H_2 elastic (black) collisions. CX and H_2 elastic have already been multiplied by the corrective factors found in Section 4.6.1.3 by comparison with B2.5-Eunomia.

the target could be less relevant, leaving more room for CX losses, while the opposite for low pressure.

4.6.3.2 Particle balance

During the experiment there was no direct measurement of any part of the particle balance, so it is not as well constrained as the power balance. Nevertheless thanks to the assumptions and approximations in Section A.4.5 it is possible to perform a rough particle balance on the plasma column. Only the charged particles' particle balance is utilised, as only these are confined to a certain poloidal location by the magnetic field. Only H^+ , e^- are introduced by the plasma source, using the flow velocity estimated from the power input in Section A.4.5. The volumetric particle sources and sinks are calculated together with the power ones and the target particle losses are treated as an unknown in a similar way as in the power balance. To calculate the prior probability, the balance of H^+ and e^- has a large uncertainty, as the

plasma can potentially accumulate in the plasma column, while the balance of H_2^+ and H^- has a smaller uncertainty due to their short lifetime. More detail on the particle balance is given in A.4.7.

The procedure to convolve the data from time and spatial dependent PDFs to a global one for the whole pulse is the same as previously mentioned for the power. In order to better understand the influence of molecular reactions on the plasma the individual reaction rates are divided in MAR, MAI and MAD. These are defined as the paths composed of a first reaction that converts a neutral specie (H_2 , H) into a molecular precursor (H_2^+ , H^-) then a second one where the precursor is used. The final result of the two reactions combined can either be the recombination of the plasma that participated to the reactions (MAR) the ionisation of the original neutral (MAI) or the dissociation of H_2 (MAD). Here paths that cause ionisation or recombination and dissociation are not accounted in MAD to avoid double counting. All of the possible combinations of reactions that achieve the mentioned goals via a molecular precursor are added together to form the MAR, MAI and MAD rates. [19]

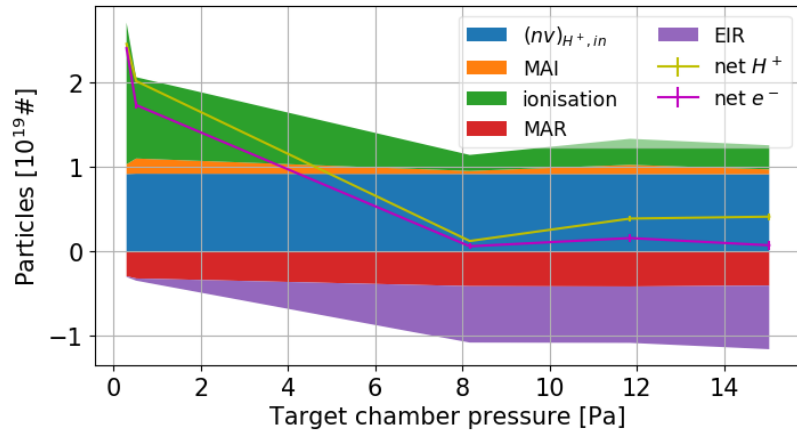


Figure 4.21: Plasma particle balance on the plasma column from the Bayesian analysis for strong ELM-like pulses with increasing neutral pressure (ID 5 to 10 in Table 4.1). Total particle input from the plasma source estimated from Section A.4.5 and A.4.7 ($(nv)_{H^+,in}$). Number of plasma particles created during the duration of the ELM-like pulse by type of reaction. MAR and MAI are defined as ensemble of multiple reactions that, starting from neutrals, first create a molecular precursor (H_2^+ , H^-) then further react with the end result of the two consecutive reactions being plasma recombination or ionisation respectively. [19] We note that there can be a discrepancy between $\text{net}H^+$ and $\text{net}e^-$, which appears to be an analysis artefact.

The particle balance on the plasma is shown in Figure 4.21. Here are shown the plasma particle input, constituted by the source, the ionisation source and the recombination sink.

MAI increases at lower pressure but is not very important representing a small fraction of the total ionisation. With the considered reactions H_2^+ is the only precursor that can cause MAI. MAR increases with pressure, but it dominates at low pressure (high temperature), and amounts to $\sim 1/3$ of the total plasma particle sink at high pressure (low temperature). It is mainly due to the H^- precursor.

An important observation is that for low pressure conditions the ionisation source is higher than the estimated particle input from the source. The main difference between linear machines and tokamak divertors is that in a divertor, especially in high recycling, most of the particle source for the plasma comes from the recycling neutrals while the upstream plasma acts as the energy source. Conversely in linear machines the external source usually dominates. For low pressure conditions this does not happen here. If the neutrals predominantly come from plasma recycling at the target surface, this might be evidence of recycling in a similar fashion as in a tokamak. [Figure 4.21](#) shows a decrease in net balance of protons and electrons in the plasma column (net H^+ and net e^-) for increasing neutral pressure due to a transition from an ionising to a recombining plasma. This is in agreement with both the analysis of power losses as per [Section 4.6.3.1](#) and the target heating analysis shown in [Section 4.5](#). The potential energy exchanges in the plasma like ionisation, dissociation, MAI and MAD are important to lower the plasma temperature enough for MAR and EIR to become important and reduce the particle flux to the target. MAD is more efficient than electron impact dissociation (EID) in converting H_2 to H and MAR can effect the plasma at higher temperature than EIR, therefore the inclusion of the chemistry from H_2^+ and H^- is important in describing the ELM burn through processes.

The particle balance for atomic hydrogen is shown in [Figure 4.22](#). It must be kept into account that this balance is not directly constrained and that transport is not considered, so the balance is very tentative. Hydrogen from molecular reactions, and MAD within it, represent the largest contribution to the source. Considering also that MAI is less than 10% of MAD reaction rate, this means that most of the power losses due to molecules in the local power balance ([Figure 4.18](#)) are due to MAD. Molecular reactions are responsible (integrating the local power balance) for about half of the potential energy exchange while up to a third of the radiative power losses. Molecular reactions seem to not have a strong impact in the plasma particle balance while dominating the neutral's particle balance. This is in agreement with previous findings in tokamaks such as TCV [[120](#)], JET [[183](#)], and TCV SOLPS-ITER

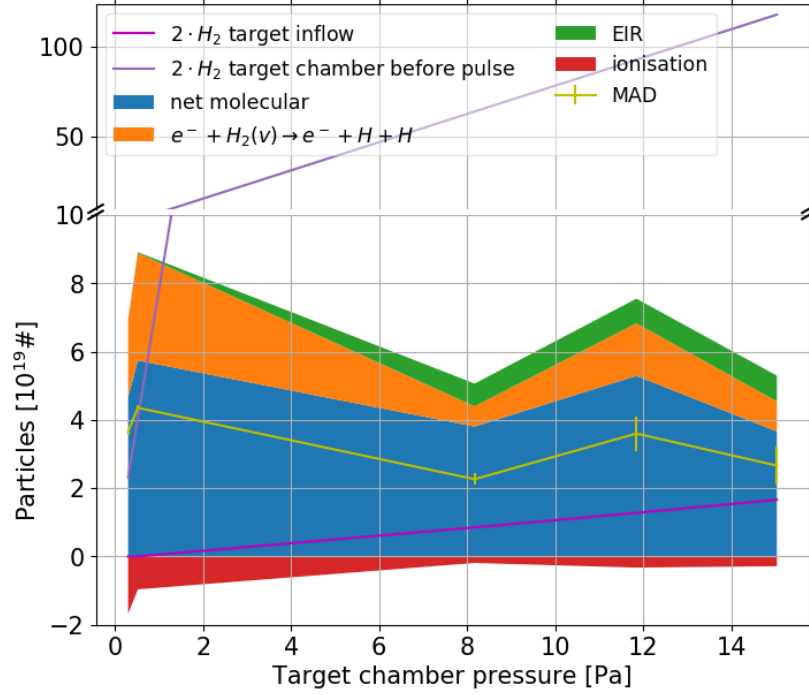


Figure 4.22: Atomic hydrogen particle balance on the plasma column from the Bayesian analysis for strong ELM-like pulses with increasing neutral pressure (ID 5 to 10 in Table 4.1). It is assumed no atomic hydrogen enters the plasma column from the source thanks to differential pumping so only volumetric sources/sinks and interactions with the surface (not inferred here) are possible. Number of particles created during the duration of the ELM-like pulse by type of reaction. MAD is defined as ensemble of multiple reactions that, starting from neutrals, first create a molecular precursor (H_2^+ , H^-) then further react with the end result of the two consecutive reactions being exclusively H_2 dissociation. [19]

modeling with reaction rates modified to properly assess molecular contributions [184]

It must be noted that impact of molecular reactions on the particle balance, radiated power, and potential energy is heavily dependent on the rates used. For this work the Yacora rates have been used to determine the radiative power losses due to molecular precursors. To determine the reaction rates and the potential energy losses, other rates from AMJUEL and Janev have been used, with no guarantee of the consistency with Yacora (in terms of approximations used, consideration of different ro-vibrational states for H_2 and H_2^+ and other parameters used in the collisional radiative codes). For typical plasma conditions in this study ($T_e = 2eV$, $n_e = 10^{21} \# / m^3$), the average radiative power losses per molecular reaction are:

- $H_2^+ + H^- \rightarrow H(p) + H_2 : 0.17eV$
- $H^+ + H^- \rightarrow H(p) + H : 8.2eV$

- $H_2^+ + e^- \rightarrow H(p) + H(1)$ and
 $H_2^+ + e^- \rightarrow H(p) + H^+ + e^- : 0.72\text{eV}$
- $H_2 + e^- \rightarrow H(p) + H(1) + e : 0.026\text{eV}$

The molecular rates are less established than atomic ones, so these numbers can change and significantly effect the power balance.

In low pressure conditions volume recombination is negligible and the vast majority of atomic hydrogen is produced by volumetric dissociation of H_2 . Here the total volumetric source is higher than the total number of hydrogen atoms present in the target chamber before the ELM-like pulse and the neutrals that can be produced by surface recombination at the target (see [Figure 4.21](#)). This points to the source being over estimated, that can be expected being H_2 and H particle balances not constrained. Both the hydrogen in the target chamber before the pulse and the possible neutrals generated at the target are larger than the volumetric ionisation sink. It is therefore unclear if what observed at low pressure is evidence of recycling or just dissociation and ionisation of a significant fraction of the gas in the target chamber.

A metric which is potentially significant for tokamaks is the average energy loss per interaction with the neutrals. The plasma enters the target chamber at about 10eV , so Magnum-PSI can be thought as comparable to the section of a tokamak SOL from the region where the temperature the peak temperature is $\sim 10\text{eV}$ to the target. Above this temperature molecular effects become much less relevant, so the interactions between plasma and neutrals are easier to model. In Magnum-PSI, especially in Stage 2 where EIE is low, the importance of recycling appears to be very limited and the vast majority of the atomic hydrogen is produced via dissociation of H_2 , that therefore can be considered the main neutral precursor causing the cooling of the plasma. The quantity of neutral gas that has a chance to interact with the plasma can be roughly estimated from the neutral pressure, assuming sonic inflow at room temperature over a cylinder or a conventional 2cm radius. In Stage 2 the H_2 that reacts with the plasma is about a fifth of what enters from the sides. This is likely a product of the geometry of the plasma and elastic collisions heating the neutrals and causing dilution. [159] The average power losses via radiation due to plasma interaction with H_2 (then H) neutrals (EIE and MAD/MAR/MAI), calculated as $(P_{rad} - P_{rad\ recomb})/(2\dot{n}_{H_2, sinks})$, correspond to $0.9 - 1.7\text{eV}/\#$ per interaction. Considering the overestimation of the MAD reaction rate mentioned before, this metric is likely slightly higher. Including the potential energy losses

due to ionisation and molecular reactions the energy losses per nucleon are $\sim 4.5eV$ in Stage 1 and $\sim 6eV$ in Stage 2. Of these the fraction due to ionisation and MAI, that converts plasma thermal energy to potential and therefore requires recombination or MAR not to effect the target, is $1eV$ and $2.5eV$ respectively. For comparison in Stage 2 the estimated energy losses due to CX and H_2 elastic collisions are $0.04 - 12eV$ and $0.15 - 0.5eV$ per nucleon entering the reference plasma volume. Another useful metric is the energy cost per ionisation [150,185]: as temperature decreases and the plasma becomes more detached more excitation happens before ionisation occurs. In our case the radiation due to EIE increases from $\sim 5eV$ in Stage 1 to $\sim 7eV$ in Stage 2, while it was $\sim 22eV$ in TCV at particle flux roll-over. [149] The radiation due to molecular reactions per ionisation increases from $\sim 2eV$ in Stage 1 to $\sim 15eV$ in Stage 2, showing the relevance of molecular reactions and bringing the total closer to TCV estimations. Considering then that not all the hydrogen produced via dissociation is ionised, the total cost including the potential energy losses for molecular reactions and ionisation itself increase from $\sim 35eV$ to $\sim 60eV$. It must be considered that while radiative losses are in part constrained by matching the line emission, an absolute measure, the potential ones are only inferred, and could change significantly if elastic collisions and CX are accounted for properly. Recycling, potentially significant in Stage 1, can cause an increase of the radiative losses via EIE at the target but also a local increase in plasma density, therefore only moderately reducing the heat flux to the target.

The results from particle balances are here tentative and obtained with strong approximations, so further investigations will be necessary to better understand the respective roles of the various sources and sinks.

4.7 Summary

The effect of ELM-like pulses on a detached target in Magnum-PSI was studied with the help of various diagnostics. It was found that the ELM-like pulse energy can be effectively dissipated through a high level of detachment before the ELM energy reaches the target. The decreasing power reaching the target is inferred to be due to higher volumetric power losses in the volume between target and source. The volumetric power losses, inferred from the visible light emission, for low neutral pressure are fairly constant along the magnetic field, presenting a strong peak close to the target due to plasma surface interactions indicating

an attached plasma. The volumetric power losses become more uneven along field lines as neutral pressure is increased, with the region close to the target decreasing its brightness and expanding towards the plasma source. This change is correlated with increased loss of plasma before reaching the measuring location. This behaviour can be divided in stages. In Stage 1 the plasma is attached before and during the ELM-like pulse and the energy losses in the volume are at a minimum and predominantly not radiative. In Stage 2 the target chamber neutral pressure is such that the plasma is detached from the target in steady state but can reattach during the ELM-like pulse, and energy losses in the volume increase. Detachment during the steady state is correlated with a strong increase of the visible hydrogenic line emission, similar to what is inferred from simulations. [78] In Stage 3 the plasma is detached before and during the pulse and the losses in the volume are such that the plasma cannot reach the target.

The power delivered to the target by the ELM-like pulse is independently calculated by measuring its temperature via an infrared camera. This data set shows a reduction of the power to the target in agreement with the progress in stages mentioned above. In the most extreme cases the power is not detectable, meaning the energy of the ELM-like pulse is completely dissipated in the volume. For the neutral pressure scan with strong pulses the heat flux factor, a metric often used to qualify the damage to the target given by ELMs pulses in tokamaks, is decreased by about half with increasing neutral pressure, becoming negligible at high pressure for weak pulses. This effect could be used in tokamaks, as they can have longer connection length between ionisation front and target, and potentially similar neutral pressures, to reduce the risk of ELMs damaging the target.

The optical emission spectrometer was upgraded to acquire temporally and poloidally resolved brightness in the visible range. Dedicated routines were developed to separate the spatial and temporal dependence in the raw data given by the rolling shutter, and an Abel inversion was performed on the brightness to give the line emissivity. Hydrogen Balmer line emission from OES ($p = 4-8 \rightarrow 2$) was used to develop a Bayesian routine that incorporates the results from multiple diagnostics to return the power balance in the plasma column in the target chamber. Various approximations to extrapolate the results from a single location in the target chamber to its entirety were adopted. The routine incorporates priors from numerical simulations (B2.5-Eunomia) and collisional radiative codes (Yacora, ADAS). The goal is to understand what drives the volumetric losses previously identified and what is the

role of atomic and molecular assisted reactions.

It was found that radiation from the plasma due to molecular assisted reactions is an important but not dominant energy loss mechanism. Radiation from excited hydrogen atoms created from plasma molecular interactions is found to be the about the same for Stage 1 and 2, but this is likely due to overestimation in Stage 1. Mutual neutralisation of H^- seems to dominate radiative losses, but it was established that this could not be determined from OES alone with the present setup. Molecular assisted reactions significantly effect the local plasma power balance exchanging kinetic to potential energy, limiting what is available for ionisation and recycling. This is somewhat analogous to tokamaks, where power limitation of the ionisation source can induce detachment [180].

Molecular reactions predominantly lead to MAD, as it is a more efficient path to H_2 dissociation than EID. These losses could be overestimated here due to an unconstrained particle balance for H_2 and H . Molecular processes are mostly dominant in an intermediate temperature range around 3eV, between ionisation and EIR dominant regions. The radiated power losses can be responsible for significant plasma power losses, but exchanges of potential energy like ionisation, EID, MAI, MAD, and collisional processes like CX and H_2 H^+ elastic collisions are expected to dominate the plasma power balance. Ionisation is more important at high temperature, >5eV, while at lower temperatures MAD/MAR increases significantly. When these processes cause the temperature of the plasma to go below ~ 1.5 eV EIR occurs, reducing significantly the plasma flow to the target and the relative heat flux. The importance of radiated power losses could be different if impurities like carbon or nitrogen are present. These results indicate that for highly detached regimes in linear machines molecular interactions are important and need to be accounted, something that is not yet fully done in many codes used for Tokamak edge plasma studies.

Chapter 5

Overall summary

In this work different aspects of detachment have been investigated. A new diagnostic was developed for the MAST-U spherical tokamak (IRVB) to study the changes in total emissivity distribution depending on the plasma conditions and level of detachment. An algorithm for tomographic reconstruction was developed and applied to the IRVB data to further examine the change in the radiated power distribution in the divertor. The resilience to ELM-like pulses of a detached plasma produced in a linear device was analysed, in order to understand the processes involved with burn through, as part of a collaboration with DIFFER.

5.1 MAST-U

The activities in MAST-U are aimed at characterising radiative detachment, which occurs in parallel to detachment as observed from particle flux roll over, for various experimental conditions in a spherical tokamak. This is important as the spherical tokamak configuration is expected to allow reaching higher plasma pressure than large aspect ratio tokamaks for the same magnetic field strength. A disadvantage is that the available target area to absorb the exhaust from the core is smaller, so heat management becomes even more important. It is rare in large aspect ratio tokamaks to have a diagnostic with such a high spatial resolution in the divertor as in this work (IRVBs are usually deployed to monitor core radiation) and it is unique for spherical tokamaks.

[Chapter 2](#) describes the steps to develop the IRVB diagnostic for MAST-U. The goal of the IRVB is to monitor the changes of total radiated power around the x-point, a region where strong gradients of emissivity are expected, and relate them to detachment. Focusing

on the x-point also allows us to fill the gap between the core and SXD chamber resistive bolometry systems. The IRVB original geometry optimisation and hardware is designed by Matthew Reinke, based on previous work for NSTX-U. [21]

The design for the first MAST-U experimental campaign featured a large FOV so as to almost reach the HFS midplane, including both a poloidal and a tangential view of the plasma. The design was optimised using the ray tracing code *CHERAB* to have the best spatial resolution around the x-point while maintaining a sufficient SNR. The FOV was verified, a particularly difficult task for foil bolometers, by using the plasma from MU01 itself as a light source. During disruptions the increase of foil temperature highlights the silhouette of the central column, while fuel locations cause strong localised emissivity. In both cases, their location on the foil matched the expectation from design. The observed changes in brightness was also well matched with the location of the separatrix from *EFIT*. This is particularly relevant in situations where in vessel access is restricted or a full characterisation of the field of view would be too onerous.

To obtain the power absorbed by the foil, the system was fully characterised, from camera counts to foil temperature and foil power. In this process the uncertainties were estimated so that a full propagation of the errors could be performed and used in later analysis. An ad hoc vacuum bench top setup was built in order to characterise the foil.

The resulting brightness shows the movement along the separatrix of a region with high emissivity, from the inner target to the x-point, and then to the HFS midplane, that is expected from detachment. The changes of brightness are compared with the resistive bolometry system and the two show similar trends, validating the IRVB diagnostic.

The noise levels are shown to be better than expectations, with the largest uncertainty due to the variability of the foil and coating properties.

In parallel to the hardware work, an inversion routine to convert the line integrated data to local emissivity was developed, as shown in [Chapter 3](#). Various methodologies were considered and a Bayesian method was implemented to make full use of the previous characterisation of the uncertainty, to compensate for the foil non uniformity, and to adapt to the changing signal strength. The inversion algorithm was checked against a more established method, *SART*, returning similar or better results.

The results from MU01 show that for low power L-mode discharges the movement of the radiator is as would be expected from ordinary large aspect ratio tokamaks, with the inner leg

detaching before the outer. These changes are related to the particle flux roll over measured by LPs (the onset of detachment) with radiative detachment on the outer leg happening at about the same time, or slightly earlier. Once the region of high emissivity reaches the x-point, it then moves upstream following the HFS separatrix up to the midplane, forming a MARFE-like structure localised on the HFS midplane that can then move into the core. This structure is often elongated along flux surfaces, being more localised and less elongated with HFS fuelling.

The integrated emissivities (radiated power) in the regions in which MAST-U is divided are in agreement with resistive bolometry measurements, and show a radiated power fraction reaching $\sim 50\%$ after the emergence of the MARFE-like emissivity peak. This progression of radiative detachment for increasing upstream density is confirmed across multiple shots of this type.

Radiation on the inner leg is observed to gradually move from the target to the x-point. This is different from expectations from theory that, because the movement is in the same direction as the toroidal field gradient, suggests a rapid jump with no solutions in between. This measurement was possible only because of the high spatial resolution achieved.

The radiation and level of detachment is observed not to be significantly affected by δR_{sep} , a metric of how close the plasma geometry is to a single or double null, contrary to what is observed in other experiments where it can significantly impact up/down power sharing for changes of the order of λ_q . The reason for this is inferred from SOLPS simulations to be a relatively low plasma current in MU01 compared to the MAST-U design ($I \leq 750\text{kA}$ instead of 2MA), limiting the influence of drifts.

High power NBI heated H-mode discharges were performed but the shots were less successful, so a set of similar discharges to compare the behaviour for different stages of detachment could not be found. The results for one shot were shown, where detachment is caused by increased fuelling from the lower divertor. Given the non up/down symmetric fuelling, the up/down radiation balance was also not symmetric, so the total radiated power cannot be inferred by only observing the lower half of the machine. Due to the higher power being radiated the inversion algorithm returned emissivity profiles with a higher spatial resolution.

Radiative detachment first starts at the outer target, then stops at an intermediate location between target and x-point, then the inner target then fully detaches and finally, the outer leg fully detaches. The particle flux roll over is observed on the lower outer target

at about the same time as full radiative detachment is achieved. After the radiation on both legs has detached up to the x-point, the radiation peak moves upstream on the HFS separatrix to form the MARFE-like structure on the HFS midplane.

Given the higher power injected in the plasma in H-mode, a much higher density can be reached compared to L-mode before incurring disruptions, increasing the peak Greenwald fraction from 30% up to 70%. As mentioned before, the upper and lower divertors behave differently due to asymmetric fuelling, with the lower reaching detachment while the upper is still attached. This different behaviour could be due to the baffles. They enhance neutral compression between the divertors and the main chamber, limiting the equalisation of the neutrals between the volumes. This might suggest the possibility to independently control the two divertors.

The total radiated power, accounting for the asymmetry, likely peaks at about 60% of the input power, showing that even in H-mode, and without extrinsic impurities, a large fraction of the input power can be dissipated via radiation.

In MU01 only a small fraction of the IRVB lines of sight enter the SXD chamber, and the solid angle between them is small. It was demonstrated that it is not therefore possible to accurately reconstruct the radiation distribution in the SXD chamber. This prevents, with the current IRVB geometry, the characterisation of the progress of radiative detachment in the SXD chamber, needed for super-x plasmas. It is still possible to use the IRVB to determine the integrated power radiated in the SXD chamber with sufficient precision. This, compared to the power radiated in the rest of the outer leg, was used in conjunction with data from the multi wave imaging diagnostic (MWI), to infer the atomic and molecular processes that dominate the IRVB-measured radiation for increasing levels of detachment.

Given the relatively low power available in MU01 in the super-x configuration (no NBI, L-mode), the outer target at the beginning of the shot is already partially detached, showing the ease of achieving detachment in this configuration. Most of the radiation from the outer leg, in the early stages of detachment, is inferred to be due to hydrogen electron impact excitation (related to ionisation), rather than carbon line emission. For decreasing temperature in the SXD chamber the importance of molecular processes increases and then at even lower temperatures EIR becomes dominant. This implies that molecular processes play a role in deep detachment and, if accurate simulations are needed, they have to be included, especially when the temperature decreases below $\sim 5\text{eV}$.

5.2 Magnum-PSI

Chapter 4 shows the work regarding the resilience of the detachment to ELMs. ELM-like pulses were reproduced in the linear plasma machine Magnum-PSI with the use of a dedicated capacitor bank in parallel to the steady state power source supply. The ELM-like pulses increase the power to the plasma source for ~ 0.5 ms by about 5 times, with a similar increase of the heat flux through the plasma and to the target. Thanks to differential pumping among three separated chambers, it was possible to maintain the same upstream conditions while increasing the neutral pressure in the target chamber in order to cause detachment of the steady state plasma.

It is observed that 3 distinct stages of the burn through develop. In stage 1 the plasma is attached in steady state and during the ELM-like pulse, the interactions in the volume are minor and a high heat flux is deposited on the target. Increasing the neutral pressure, the plasma transitions to stage 2, detaching in steady state and reattaching during the ELM-like pulse. The heat flux to the target is reduced but still significant, while the increase of Balmer α emission observed is characteristic of a colder plasma. Increasing the pressure further the plasma reaches stage 3, in which the ELM-like pulse energy is dissipated entirely in the volume and no significant heat is transferred to the target.

In the transition from stage 1 to 2, the target heat flux factor, a metric used to assess the effect of ELMs on the target, is reduced by about half, becoming negligible in stage 3. In a tokamak the connection length from the ionisation front to the outer target can be (in deep detachment) of the order of meters and the divertor neutral pressure can reach the Pascal range, while in these experiments the connection length in the target chamber was 0.38m and the pressure up to 15Pa. If divertor neutral compression is enhanced by baffling, the divertor neutral pressure can be increased by more than one order of magnitude compared to the main chamber, limiting the negative effects on the core due to a high neutral pressure. These results imply that a significant reduction of the heat flux factor in tokamaks could be possible thanks to the high neutral density region forming close to the target when it is strongly detached, improving the long term performance of the target in H-mode.

The existing optical emission spectroscopy diagnostic, observing the plasma in the target chamber, was upgraded to increase the time resolution and perform intra-ELM measurements by the author and Gijs Akkermans. The diagnostic has a series of LOS observing the plasma tangentially so that the local line emissivity can be inferred assuming poloidal

symmetry. From the change in the hydrogen Balmer line emission ratio, the importance of atomic processes (ionisation, recombination, dissociation) and molecular processes (reactions involving the plasma and neutral interactions with H_2^+ and H^- precursors) can be assessed using coefficients from collisional radiative models. The setup did not allow the measurement $H\alpha$, implying that the analysis of the line ratios alone could not help in distinguishing between the effect of H_2^+ and H^- . In order to improve the physical consistency of the results, a Bayesian algorithm and a very crude model of the plasma column were developed to combine the data from different diagnostics and limit the parameter space of the variables considered.

The results from this analysis show that, as expected, the type of process that dominates in the plasma depends mainly on the plasma temperature. For temperatures above $\sim 5\text{eV}$, ionisation and dissociation (both via electron impact and molecular precursors) dominate. At lower temperatures molecular reactions are more important, and below $\sim 1.5\text{eV}$ electron ion recombination dominates. The power losses due to radiation account for $\sim 1/3$ of the input power at high pressure, and $1/3$ of this portion is due to molecular reactions.

Most of the thermal energy of the plasma is exchanged to potential energy. At low pressure, the plasma generated via ionisation during the part of the ELM-like pulse with the higher temperature is more than that produced by the plasma source, a unique case in linear machines. At higher pressure recombination, both via molecules ($\sim 1/3$ of the total) and EIR, dominates particle and power balance, and the particle flux to the target is greatly reduced. This is in accordance with direct heat flux measurements.

The impact of molecular reactions on the radiative losses is significant but not dominant while, as observed in previous research, molecular activated recombination and especially dissociation play an important role in the power balance. This implies that if the burn through process with a strongly detached target has to be modelled, or the (low temperature) far SOL has to be accounted for, the inclusion of molecular reactions is required to capture the behaviour at $5\text{eV} > T_e > 1.5\text{eV}$ and to estimate H_2 dissociation correctly.

Chapter 6

Conclusions

The aim of this work is a better understanding of the progression and processes involved with divertor detachment.

6.1 MAST-U

The activities in MAST-U were aimed at characterising the role and dynamics of total radiation during detachment in a spherical tokamak. This was made possible with the development of the IRVB diagnostic. The IRVB field of view (FOV) is aimed at the x-point, and the diagnostic was used to reconstruct the radiation profile in the lower half of MAST-U. With a single IRVB, a spatial resolution of the order of few cm was achieved, a level difficult to achieve with resistive bolometers, allowing for clear differentiation of the radiative detachment of the inner from the outer leg. The IRVB could also be reactor relevant, as the only component significantly exposed to neutron irradiation is the foil, contrary to the resistive bolometer where some elements are glued to the back of the foil. The IRVB foil characteristics can be adjusted to reduce its degradation over time, and the camera can be located in a safer location looking through a periscope system.

The high IRVB spatial resolution allowed monitoring of the radiation profile on the inner leg. It was found that radiative detachment happens gradually, with the radiator gradually moving from the target to the x-point, appearing to be contrary to expectations from analytical models of detachment stability. This has beneficial implications for controlling the heat flux to the target.

Radiative detachment was observed, for L-mode conventional divertor discharges, to

evolve in MAST-U in the same fashion as in a large aspect ratio tokamak. The inner target detaches first followed by the outer divertor. Once the radiation peak reaches the x-point, rises along the inner separatrix and can then evolve into a high field side midplane MARFE-like structure.

This particular implementation of the IRVB did not allow for the reconstruction of the radiation profile in the SXD chamber, but it is nevertheless useful for estimating the total radiated losses in that volume. For a super-x divertor shot the change in integrated radiated power in the SXD chamber and in the rest of the outer leg (below the x-point) were compared with changes in MWI-derived measures of ionization and recombination and radiated power estimates derived from spectroscopy. The radiation in the SXD chamber is observed to decrease in correlation with the movement of the ionisation front (end of the Fulcher band emitting region towards the target) out of the SXD chamber, while in the rest of the outer leg (between SXD chamber entrance and x-point) it increases. Additionally the radiation in the SXD chamber didn't scale as the carbon related emission, indicating that most of the plasma radiative losses are hydrogenic in the SXD chamber. This is in contrast with another device of similar size, TCV, where during detachment most of the radiation from the legs is due to carbon (intrinsic impurity in both tokamaks).

It was also inferred that between the detachment phases where ionisation and then EIR dominate, there is another phase where plasma interactions with molecular precursors like H_2^+ and H^- become important. This points to the relevance of these interactions and the need to clarify their role in tokamaks.

6.2 Magnum-PSI

The activities on Magnum-PSI have been dedicated to understanding the ELM burn through process in a detached divertor. Magnum-PSI is a linear device, so it does not compare exactly with a tokamak divertor. The magnetic field geometry is linear rather than toroidal, with a much shorter connection length, meaning the propagation of the wave of hot plasma cannot be studied. The ion source is mostly provided by the external source rather than recycling in the divertor leg, and the ELM repetition rate is much lower, however diagnostic access is much better and it is far easier to consistently repeat the same conditions to accumulate data. Therefore linear machines can still provide useful data on the processes happening in

the plasma and the effects of high neutral pressure.

It was found that, indeed, it is possible to fully dissipate in the volume the energy in ELM-like pulses, meaning that essentially no measurable fraction of the ELM-like pulse energy reaches target. This was achieved with pulses with an ELM heat flux factor comparable to what is measured in current tokamaks like JET, albeit much smaller than is expected in ITER. Considering that, in ITER, a much longer connection length is possible between the target and the edge of the ionisation front compared to the Magnum-PSI target chamber size, and the similar neutral pressures, it might be possible to significantly reduce the ELM energy to the target via deep detachment. This has to be balanced with the potentially negative effects of deep detachment on the core plasma. The connection length and the neutral density behind the ionisation front can be increased with a limited effect on the core with baffling and advanced divertor configurations like the super-x. All of that can be tested in MAST-U.

Interpreting the data from an upgraded optical emission spectrograph via a Bayesian framework, it was found that radiative losses in Magnum-PSI are important in reducing the plasma energy ($\sim 1/3$ of the ELM-like pulse energy input), but the dominant energy losses are due to potential energy exchanges. Ionisation is dominant for a hot ($T_e > 5\text{eV}$) plasma, molecular processes are important at lower temperatures and electron ion recombination becomes dominant below 1.5eV .

Molecular assisted dissociation is estimated to be the reaction path, through molecular precursors H_2^+ and H^- , with the biggest impact to the particle and power balance, being more efficient than H_2 electron impact dissociation. This causes potential energy losses, limiting what is available for ionisation, in a process analogous to "power limitation" in tokamaks.

If detailed simulations of the ELM burn through are needed, it is necessary to include molecular reactions, especially if deeply detached conditions are of interest, as they can provide a significant reduction of the heat flux to the target. The understanding gained from the analysis of the simulated ELM burn through in linear devices, like Magnum-PSI, can help to improve the predictive capability of the fraction of ELM energy that can be removed before it reaches the target.

6.3 Outlook

The design, calibration and verification of the IRVB diagnostic, still classified as a prototype in MAST-U, has allowed best practices and improvements for future implementations to be found, such as:

- Orient the camera and viewport such to avoid self reflection
- Perform the temperature calibration of the IR camera with a large black body source encompassing the whole FOV
- Use a foil with the coating applied via chemical vapour deposition rather than sprayed to reduce its non uniformity
- Aim the FOV in the co-NBI direction to prevent neutrals from charge exchange to enter through the pinhole and effect measurements
- Use an infrared camera in the wavelength range $8 - 14\mu m$, that is more sensitive to temperature changes around room temperature

Given the lower than expected noise level observed in MU01, the IRVB geometry was modified ahead of MU02 to concentrate the FOV even more around the x-point and divertor. This should provide an even greater spatial resolution, allowing a better assessment of the penetration of the radiator inside the core and possibly the radiation distribution in the SXD chamber.

It is also planned, by the ORNL collaborators with MAST-U, to add a new IRVB aimed at the upper x-point. Together with an additional resistive bolometry system for the upper divertor and the refinement of the current core and lower divertor resistive systems, this will allow monitoring of the radiated power profile in the entire machine. This is necessary for power balance studies and will allow a full characterisation of the evolution of radiation with detachment for all divertor configurations possible in MAST-U.

Further improvements will also come from better data analysis, like implementing the Empirical Bayes method for the simultaneous estimation of regularisation and negative correction coefficients. Another avenue is to try merging the resistive system and IRVBs to perform a tomographic inversion of the entirety of the MAST-U plasma. This could return even more accurate estimates of the integrated radiated power.

Regarding the study of ELM burn through, implementing a spectroscopic setup capable of measuring intra-ELM line emission in tokamaks is very challenging, so a better understanding could still come from linear machines. The crude plasma column model detailed in this work could be improved allowing a gradual change of the plasma properties along the plasma column. This could be achieved by defining an analytical radial and axial (in z and r) profile shape for parameters like n_e , T_e , n_{H_2} , n_H , $n_{H_2^+}/n_{H_2}$, n_{H^-}/n_{H_2} and then finding the most likely values for the parameters of the analytical expressions in a similar fashion as done in [186]. This could be coupled with a model for the neutrals capable of accounting for transport such as Eunomia. Additionally, other experimental data like the total radiated power from bolometry and the flow velocity from collective Thomson scattering (which was later added to the Magnum-PSI diagnostic suite) could be added to the Bayesian analysis.

It might also be important to repeat the experiment with extrinsic impurities, to establish the impact on the radiated power losses and if they facilitate the ELM baffling.

Appendix A

Details on the Magnum-PSI study

I will here expand in more detail on the models, approximations and assumptions that have been used in [Chapter 6](#).

A.1 Sampling strategy

As mentioned above, of all diagnostics only the fast camera has a time resolution high enough to resolve individual ELM-like pulses. The TS laser is fired at a fixed frequency of 10Hz from a dedicated timing system. The CB can be triggered at an arbitrary time compared to the 10Hz clock so that information on different parts of the pulse can be collected. The OES is triggered with the same 10Hz signal as TS and, due to the rolling shutter, acquires data with a time shift between rows pairs of $20\mu s$ for a total of $22ms$ required for exposure and acquisition of a single frame. For all experimental conditions it was decided to record TS/OES data from $0.5ms$ before the ELM-like pulse to $2.5ms$ after. A desired time resolution of $50\mu s$ determines $(22 + 3)/0.05 = 500$ ELM-like pulses, rounded to 600, are required. A phenomena often observed was that one capacitor failed to be triggered at the requested time, instead being trigger together with the next. This means that rather than 600 identical ELM-like pulses, one would be missing and the one after would be with a released energy twice the others. To reduce the effect of the missing data the required 600 pulses are split in two 300 pulses scans with the CB delayed of $100\mu s$ at the time. The two scans are shifted of $50\mu s$ to obtain the desired $50\mu s$ resolution for all the OES rows. With this strategy the maximum time separation between two ELM-like pulses with good data is $100\mu s$ rather than $150\mu s$. The missing data is obtained by interpolating between the good

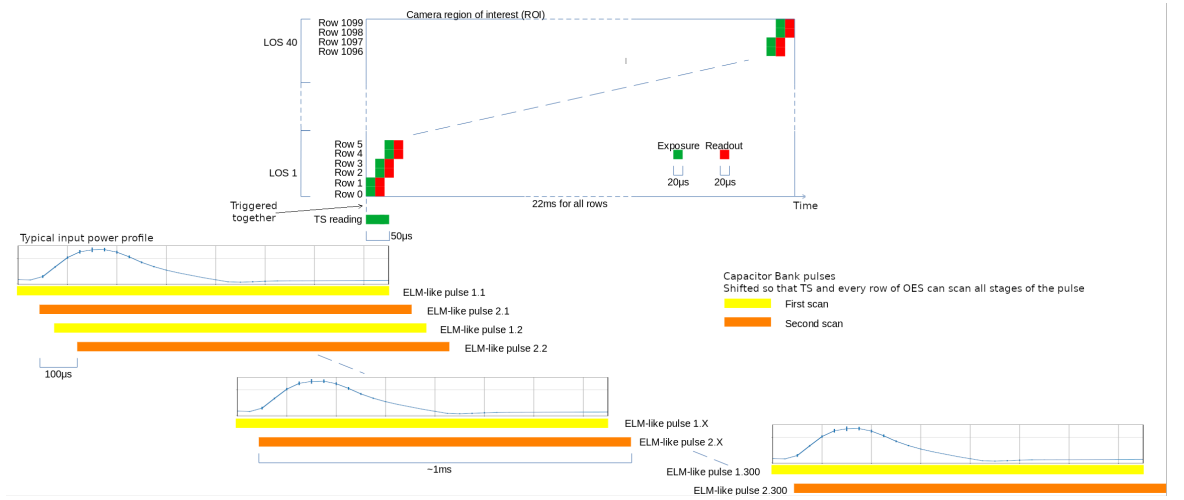


Figure A.1: Sampling strategy for TS and OES. At the top is indicated the progressive reading of the camera rows, with the integration time of TS is indicated. Below are each of the ELM-like pulses. It is shown how the trigger of the capacitor bank is shifted in time and all the pulses are split in two scans. Dashed lines indicate an interruption of the space or time scale.

data. In Figure A.1 is represented the sampling strategy adopted. At the top is indicated how the camera exposure and readout are shifted in time due to the rolling shutter.

The rows are managed two at the time and during the readout of the rows $i - 1/i$ the rows $i + 1/i + 2$ are exposed. Each OES LOS is composed of ~ 24 rows, so the time shift within would be $240\mu s$, much larger than the desired $50\mu s$. Just below is indicated the TS integration time. OES and TS are synchronised such that the trigger to start data acquisition is sent to the two diagnostics simultaneously. The time difference between CB and OES/TS trigger is initially such that OES and TS reading correspond to the end of the ELM-like pulse. From this the CB trigger is progressively delayed by $100\mu s$ so that TS and OES can acquire data about progressively earlier stages of the pulse. For TS this sampling procedure returns directly T_e and n_e while for OES additional steps are required to: reconstruct frames with row data corresponding to the same time slice, bin the LOS, obtain the emission line brightness, calculate radial emissivity from the line integrates brightness. Further details are given in Section A.2. The final result is a map of the line emissivity in both space (radius) and time. The plasma is assumed poloidally symmetric with a radial coordinate of interval 1.06mm dictated by the OES resolution.

A.2 OES data interpretation

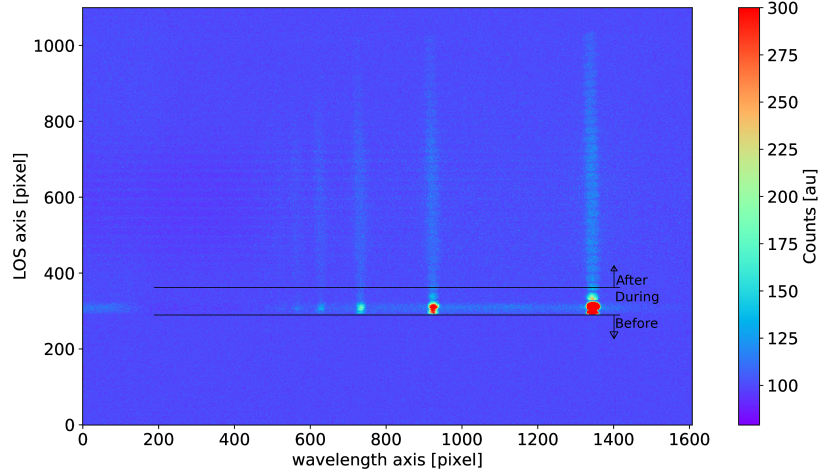


Figure A.2: Example of a raw image from the OES. The readout starts from the bottom so higher rows represent later times. In the figure are indicated rows/times corresponding to different stages of the ELM-like pulse

In this section it will be detailed how the OES measurements are processed to obtain the local radially and temporally resolved emissivity used to estimate the relevance of molecular processes. The camera that was selected for the purpose of collecting time resolved OES data was a Photometrics Prime95B 25mm RM16C, because of the relatively high signal to noise in low light conditions and large size of the sensor. In [Figure A.2](#) is shown the typical picture collected during an experiment when on top of a steady state plasma an ELM-like pulse is fired. The rows are read sequentially from the bottom, with a time shift equal to the integration time, minimum $20\mu s$. This means that for the particular example shown the rows indicated as *Before* represent times before the effect of the ELM-like pulse propagated to the OES location. *During* represents the pulse and *After* is for times after the ELM-like pulse, characterised by homogeneous line emission from the hot gas filling the target chamber. From [Figure A.2](#) it is also possible to distinguish part of the 40 line of sight that are available.

The first effect that is compensated is the sensitivity of the camera at low signal levels. The counts/light intensity correlation of the pixels is mostly linear, but deviates significantly below 6 counts and negative counts are returned at very low signal. A routine was developed to compensate for this thanks to dedicated measurements to find the correlation between light intensity and counts.

In order to decouple spatial and temporal information a scan is operated such that the ELM-like pulse is shifted in time respect to the start of the camera image record and TS measurement. More details on the sampling strategy in [Section A.1](#). The presence of ELM-like pulses effected by capacitor bank misfires (see [Section A.1](#)) is found analysing the plasma source power and the data corresponding to those pulses is excluded. To separate the time and row dependency, for every row, column and time of interest the data in a range of $100\mu s$ and 8 rows is fit with a second degree polynomial in time and one in row. To avoid over smoothing the image a smaller weight is assigned for increasing times and row difference from the one that is being examined. In [Figure A.3](#) is shown the time/row decoupled image. The output time step has a $50\mu s$ resolution to match TS data.

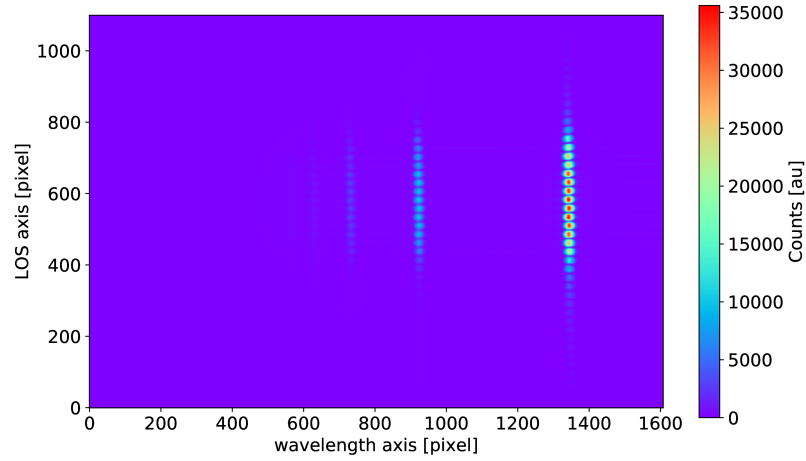
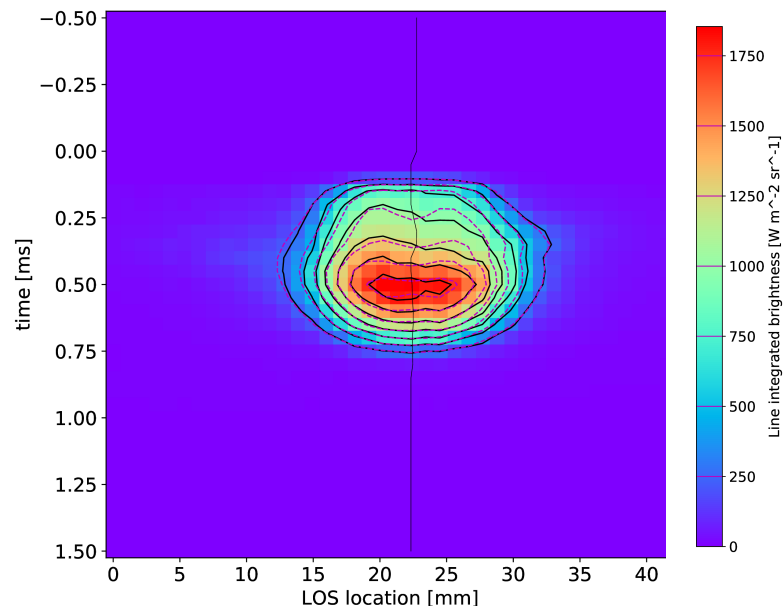
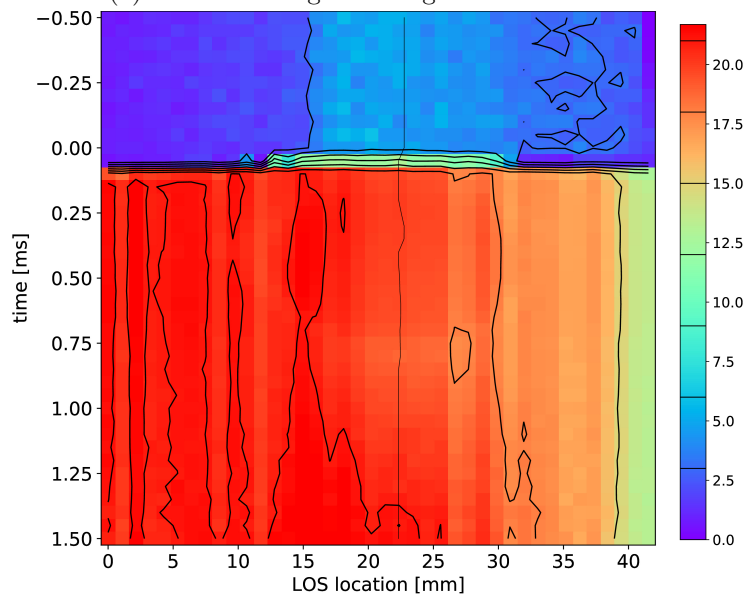


Figure A.3: Example of decomposed time frame showing the symmetry of the image to the vertical pixel ~ 600 , likely representing the location of the plasma column axis.

The counts are summed among the rows composing each LOS and the line intensity is calculated by integrating above the background level. Brightness is then converted to emissivity via Abel inversion. The line emission is supposed poloidally symmetric and the plasma optically thin. In order to avoid unrealistic discontinuities given by noise, the superimposition of 3 Gaussian is fitted to the brightness profile as done by Barrois. [155] Each Gaussian can then be Abel inverted analytically and summed to obtain the total emissivity. In this process the uncertainties are propagated to be used in subsequent steps in the analysis. An example of the inversion process is shown in [Figure A.4](#). Given the signal to noise ratio and the available lines it is decided to use Balmer lines $p = 4 - 8 \rightarrow 2$.



(a) OES line integrated brightness



(b) OES line integrated brightness SNR

Figure A.4: (a): example of a fit of the OES line integrated brightness and relative SNR with 3 Gaussians for the $n = 4 \rightarrow 2$ line. In magenta the profile of the fitted Gaussians, in thin black the found location of the plasma column centre. (b): SNR of the line integrated brightness.

A.3 Target temperature profile interpretation

In this section the mathematical models used in the interpretation of the target temperature data will be examined in more detail.

The heat delivered by the plasma to the target during an ELM-like pulse is shaped in time

and space. The power density is spatially peaked at the centre of the plasma beam due to the peak in plasma density and temperature. It temporally follows the power evolution dictated by the discharge of the capacitor bank as measured by the plasma source (see [Figure 4.7](#) for an example). The full spatial and temporal power density distribution of the target heat source is difficult to obtain from the surface temperature for all experimental conditions but analytical solutions that can approximate the peak temperature are available. As mentioned in [Section 4.5](#) the ones considered in this work are:

Model1 a temporally square heat wave delivered uniformly on a semi infinite plane: the surface temperature increase in the heating and cooling phases are respectively [[160](#)]

$$\begin{aligned}\Delta T(t)_r &= F_0 \frac{2}{\sqrt{\pi \rho c_p k}} \{\sqrt{t-t_0}\} = \frac{E_0}{\tau} \frac{2}{\sqrt{\pi \rho c_p k}} \{\sqrt{t-t_0}\} \\ \Delta T(t)_c &= F_0 \frac{2}{\sqrt{\pi \rho c_p k}} \{\sqrt{t-t_0} - \sqrt{t-t_0-\tau}\}\end{aligned}\tag{A.1}$$

with τ the duration of the heat pulse and t_0 its start, F_0 the peak power density, E_0 the energy density, ρ the density, c_p the specific heat capacity and k the thermal conductivity

Model2 a temporally square heat wave delivered by a spatially Gaussian beam: the surface temperature evolution in the heating and cooling phases are respectively [[161](#)]

$$\begin{aligned}\Delta T(t)_r &= \frac{2}{\pi} \Theta_c \tan^{-1}(2\sqrt{\tilde{t}}) \\ \Delta T(t)_c &= \frac{2}{\pi} \Theta_c \tan^{-1}\left(\frac{2\sqrt{\tilde{t}} - 2\sqrt{\tilde{t} - \tilde{\tau}}}{1 + 4\sqrt{\tilde{t}}\sqrt{\tilde{t} - \tilde{\tau}}}\right)\end{aligned}\tag{A.2}$$

with

$$\Theta_c = \frac{\sqrt{\pi} F_0 \omega_0}{2 k}, \tilde{t} = \frac{(t-t_0)D}{\omega_0}, \tilde{\tau} = \frac{\tau D}{\omega_0}, D = \frac{k}{\rho c_p}\tag{A.3}$$

and ω_0 the $1/e$ size of the spatial heat distribution on the target

Model3 a temporally triangular heat wave delivered by a spatially Gaussian beam: the surface temperature evolution in the heat rise, heat decreasing and cooling phases are respectively

$$\begin{aligned}
\Delta T(t)_r &= \frac{2}{\pi} \Theta_c \frac{1}{\tilde{\tau}_r} \left\{ \tilde{t} \tan^{-1}(2\sqrt{\tilde{t}}) - \frac{1}{4} [2\sqrt{\tilde{t}} - \tan^{-1}(2\sqrt{\tilde{t}})] \right\} \\
\Delta T(t)_d &= \Delta T(t)_r - \frac{2}{\pi} \Theta_c \left(\frac{1}{\tilde{\tau}_r} + \frac{1}{\tilde{\tau}_d} \right) \left\{ (\tilde{t} - \tilde{\tau}_r) \tan^{-1}(2\sqrt{\tilde{t} - \tilde{\tau}_r}) \right. \\
&\quad \left. - \frac{1}{4} [2\sqrt{\tilde{t} - \tilde{\tau}_r} - \tan^{-1}(2\sqrt{\tilde{t} - \tilde{\tau}_r})] \right\} \\
\Delta T(t)_c &= \Delta T(t)_d + \frac{2}{\pi} \Theta_c \frac{1}{\tilde{\tau}_d} \left\{ (\tilde{t} - \tilde{\tau}_r - \tilde{\tau}_d) \tan^{-1}(2\sqrt{\tilde{t} - \tilde{\tau}_r - \tilde{\tau}_d}) \right. \\
&\quad \left. - \frac{1}{4} [2\sqrt{\tilde{t} - \tilde{\tau}_r - \tilde{\tau}_d} - \tan^{-1}(2\sqrt{\tilde{t} - \tilde{\tau}_r - \tilde{\tau}_d})] \right\}
\end{aligned} \tag{A.4}$$

with $\tilde{\tau}_r$ the time to rise the power density from 0 to F_0 and $\tilde{\tau}_d$ the time to decrease to 0 again.

These have been obtained assuming homogeneous and constant thermal properties and a semi infinite target. With these assumptions the heat equation is linear and the superposition principle could be employed.

An important observation from these analytical solutions is that in all cases in the limit $t \gg \tau$ the surface temperature cooling is proportional to $t^{-3/2}$. For pulses with a significant energy delivered, the target surface is still cooling when the next ELM-like pulse comes, so the temperature has to be corrected. The temperature before the pulse is fit with

$$T = \frac{a}{(t + \Delta t)^{3/2}} + T_0 \tag{A.5}$$

with Δt the time between consecutive ELM-like pulses. The time dependent component is then subtracted.

The result can be seen in the black dashed line in [Figure A.5](#) and in the increase of the peak temperature from the thin solid black line to the thick one. This correction is significant only for low neutral pressure conditions. In this cases it has to be taken also into account that it takes time to reach a thermal equilibrium after the ELM-like pulse train is started. To minimize this slow variation only the second 150 of the ELM-like pulses within a 300 strong scan is used to construct the average profile as it can be seen from [Figure A.6](#).

Considering all this a fit of the ELM-like pulse with the lowest neutral pressure can be used to compare the performance of the different models. As shown in [Figure A.7](#) all models fit well the slowly decreasing peak temperature slope and return a power density within 10% of each other. Model3 fits best also the peak when the entire time axis is used.

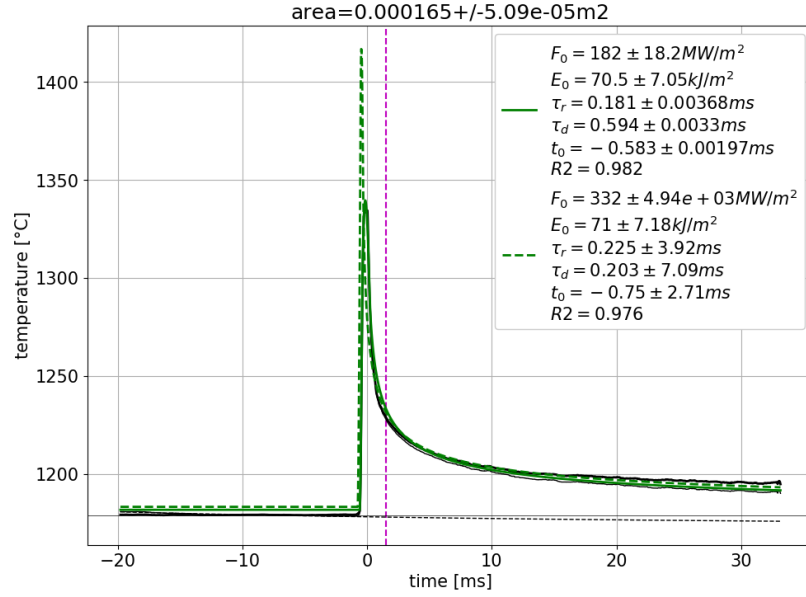


Figure A.5: Measured and fitted peak target temperature for a discharge in Stage 1 (ID 5 in Table 4.1). In dashed green the fit of the temperature profile using the triangular Gaussian pulse model for $t > 1.5 \text{ ms}$ and in solid green the whole profile. The black dashed line indicates the cooling from the previous pulse and the thin solid black one is the peak target temperature not corrected for this.

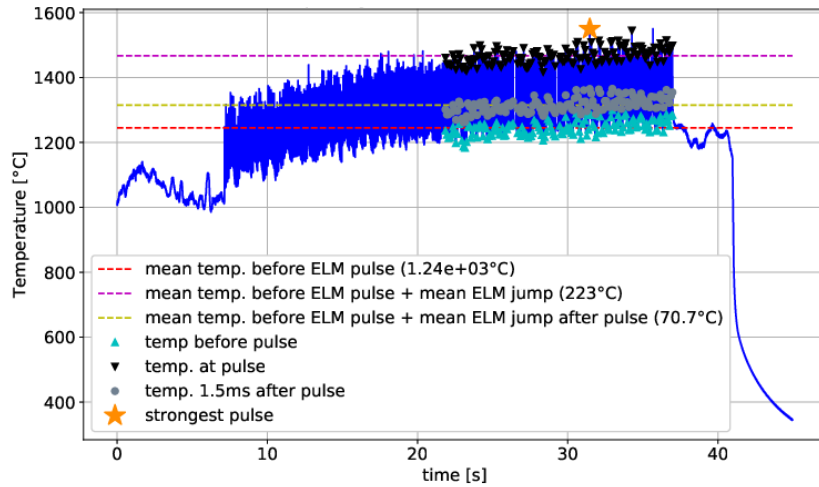


Figure A.6: Peak temperature of the target for low neutral pressure (ID 5 in Table 4.1). To estimate the effect of the ELM-like pulse only the second half of the pulses is used, when the target is close to a steady state.

The same comparison can be done with a simulated temperature rise obtained from a known input power profile. The MSC.Marc/Mentat® non linear FEM suite was used to reproduce a heat pulse similar to the one generated by the CB in terms of temporal and spatial variation and with temperature dependent material properties. The spatial

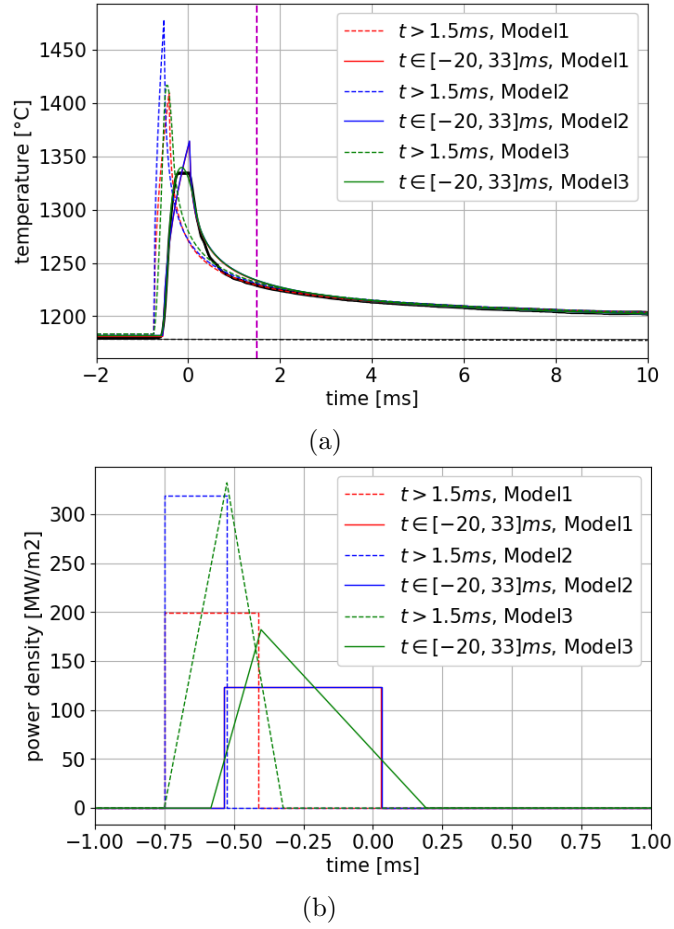


Figure A.7: Comparison of the peak power density profiles (b) result of fitting the peak temperature curve (a) the with different analytical solutions for the lowest available neutral pressure conditions (ID 5 in Table 4.1). All find adequate values for the energy density even with radically different peak durations. Dashed lines are obtained fitting from 1.5 to 30ms while solid ones from -20 to 30ms. In magenta 1.5ms after the temperature peak.

distribution of the heat pulse was set as a Gaussian of radial extent consistent with what measured with TS ($1/e^2 \sim 1\text{cm}$) while the temporal variation was reproduced by fitting two Gaussians to the power profile from the plasma source. The comparison of the fits using the 3 models is shown in Figure A.8.

Model3 is capable of better reproducing the full temperature profile returning, for the full fit, with a power density shape very close to the input one. Even if the pulse duration when fitting only after 1.5ms is quite different from the input, the energy density is within 10% of the input one for all cases and, as mentioned before, the uncertainty on the energy delivered to the target is $\sim 20\%$, good enough for the purpose of this work.

To reinforce the argument on the origin of the prompt emission for high neutral pressure

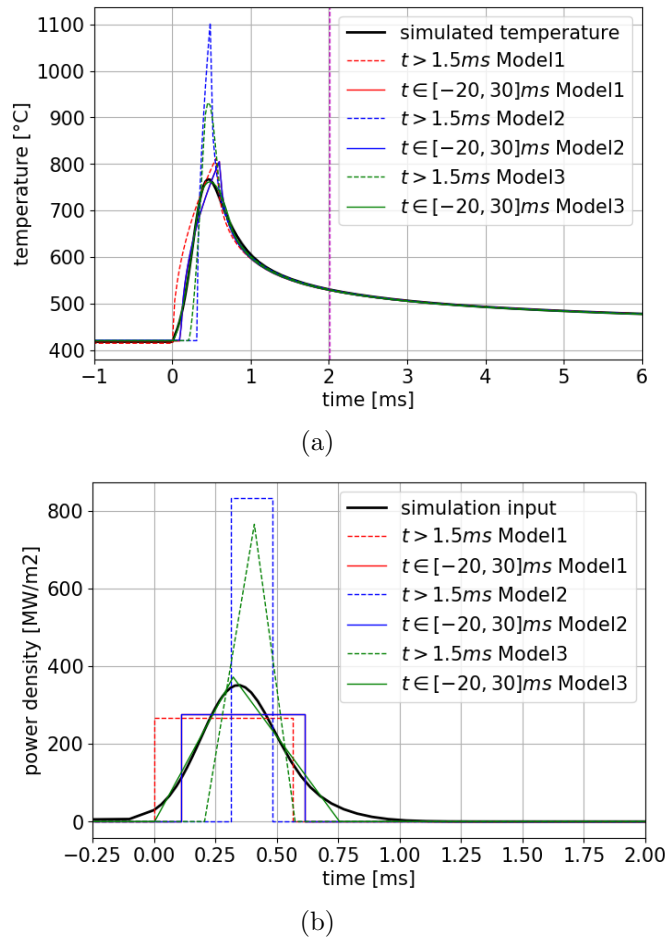


Figure A.8: Peak target temperature evolution (a) calculated with the MSC.Marc/Mentat[®] code from a known heat flux profile made to be similar to the one caused by the CB in Magnum-PSI (b) (solid black lines). That is fit with different analytical solutions and the inferred heat flux compared to the input. Dashed lines are obtained fitting from 1.5 to 30ms while solid ones the entire time axis. In magenta 1.5ms after the temperature peak.

cases it is shown in Figure A.9 the temperature profile at its peak for a low and high neutral pressure case. The low neutral pressure case (a) shows a well defined peak with a radially symmetric decreasing profile. The high neutral pressure case (b) is very different, with a much wider peak and a high temperature shadow from the peak to the edge of the target (marked in black). Note also the higher temperature outside the target itself. Considering the camera looks at the target at an angle and that the source is at the left of the field of view (see Figure 4.1), it is possible that the prompt peak could be due to radiation from the plasma itself reflected by the target. A definitive answer on what the origin of this radiation is cannot be given at this stage, but this observation further strengthen the case for only fitting the slowly decreasing temperature profile after the pulse.

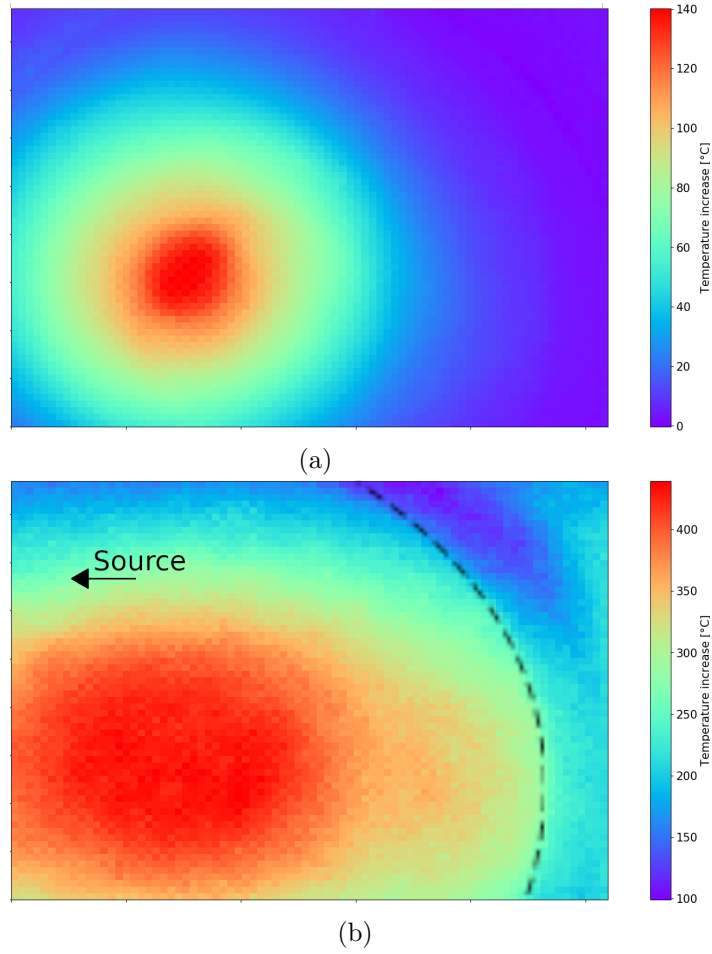


Figure A.9: Peak temperature increase distribution over the steady state on the target. (a) low neutral pressure conditions showing a clear confined peak (ID 5 in Table 4.1). (b) high neutral pressure case showing the temperature increase is not localized, possibly consistent with reflections of volumetric radiation or radiation of other origin (ID 10 in Table 4.1). The black dashed line is the circular side of the cylindrical target. The arrow indicates where the source is outside the camera view.

A.4 Details on the Bayesian calculations

It will be detailed here how the expected properties of a plasma given a set of priors are calculated, compared with the measurements and used in the particle and power balance.

A.4.1 Priors from B2.5 Eunomia

In order to define the initial parameter space and the prior it is necessary to define the range and probability associated with all the axis of the parameter space.

For T_e and n_e the TS values are used and the range is defined as 6 times the uncer-

tainty. The probability is calculated as a linear normal distribution with the uncertainty corresponding to 1 sigma.

The range and probabilities for n_{H_2}/n_e are obtained from B2.5-Eunomia simulations for a steady state neutral pressure scan with 2 plasma source settings, ranging from attached to detached via increasing neutral hydrogen target chamber neutral pressure, carried out by Chandra. [178, 179] The simulations consider the whole plasma column source to target, but only data inside the target chamber and within 2cm of the axis are considered here (marked with x , versus other regions marked by a point in Figure A.10, A.11, A.12, A.13, A.14, A.15).

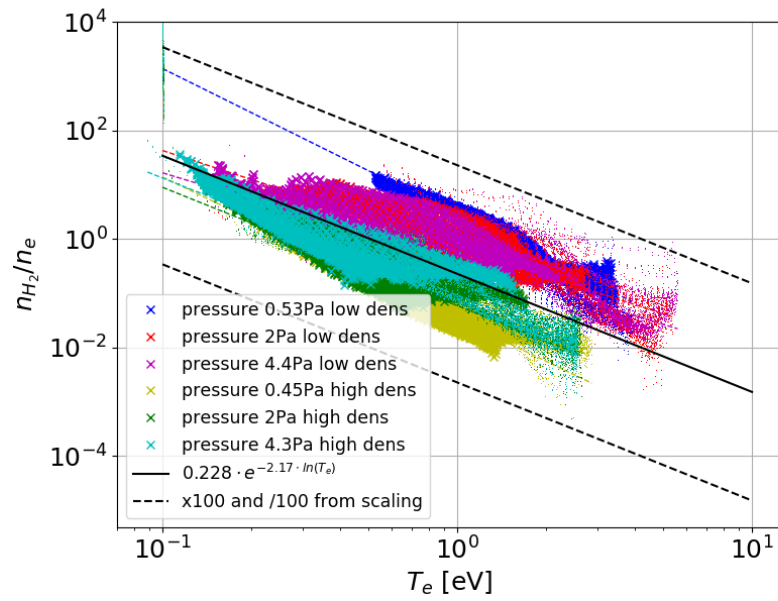


Figure A.10: Correlation between molecular hydrogen and plasma density with temperature from B2.5-Eunomia modelling. The coloured dashed lines are obtained with a linear log log fit for the single cases. The solid black line is obtained averaging the fitting parameters obtained.

As demonstrated by Den Harder [159] the density decrease of H_2 in the plasma is mainly driven by rarefaction due to the high temperature of the plasma itself. For this reason a quite strong correlation between molecular hydrogen and plasma density ratio and plasma temperature exists, shown in Figure A.10. The most likely ratio is obtained by fitting each simulation's results with a linear log log function and then averaging the fit parameters as shown in Figure A.10. The probability is defined as a normal distribution where 2 sigma corresponds to the black dashed lines, 100 and 1/100 times the fit value. The range is a significantly larger window around the dashed lines, to account for the large uncertainty coming from the fact that B2.5-Eunomia only simulates steady state conditions while the

ELM-like burn through is a very dynamic one.

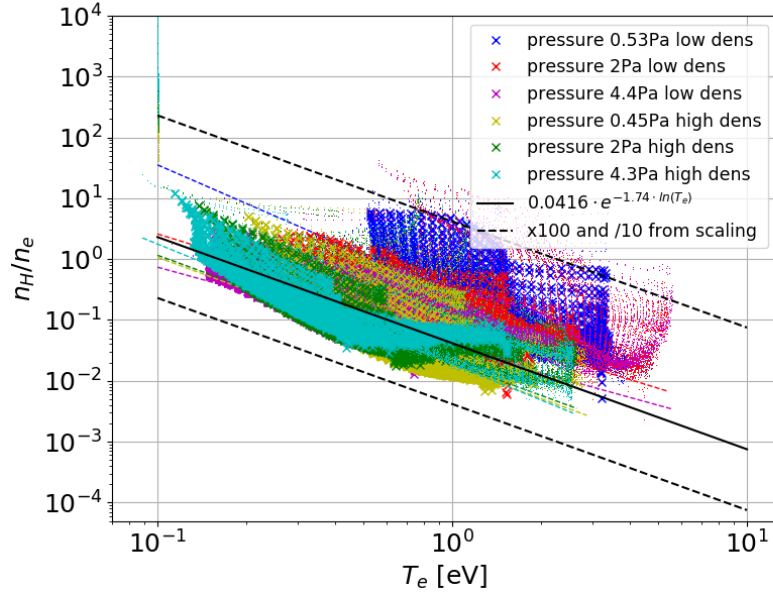


Figure A.11: Correlation between atomic hydrogen and plasma density with temperature from B2.5-Eunomia modeling. The coloured dashed lines are obtained with a linear log log fit for the single cases. The solid black line is obtained averaging the fitting parameters obtained.

The simulations are used to provide also range and probability for n_H/n_e . Atomic hydrogen is generated from recombination and from H_2 interaction with plasma and various molecules, so its density is only weakly correlated with plasma temperature and density, as shown in Figure A.11. The probability was calculated with a linear normal distribution with nominal value from the fit (calculated in the same fashion as for n_{H_2}/n_e) and 2 sigma arbitrarily assigned as per the dashed line in Figure A.11.

Other quantities that are part of the plasma state and had to be determined to calculate reaction rates and other coefficients are the temperatures of all species. To reduce the number of variables in the Bayesian algorithm their uncertainty is in this work not considered and only the nominal values are used. The correlations are shown in Figure A.12, A.13, A.15 for H , H_2 and H^+ temperature respectively where the black dashed lines indicates the values used. For T_H and T_{H_2} the fit is obtained in the same fashion as n_H/n_e while for T_{H^+} it is assumed $T_{H^+} = T_e = T_{plasma}$. For T_{H_2} in particular a weak dependence on the plasma density is present, whose estimate is shown in Figure A.14 and can be due to an increase of the collisionality for higher density and a better coupling with the neutrals, resulting in a correction factor to apply to the dependency on T_e alone. Given H_2^+ is mostly originated

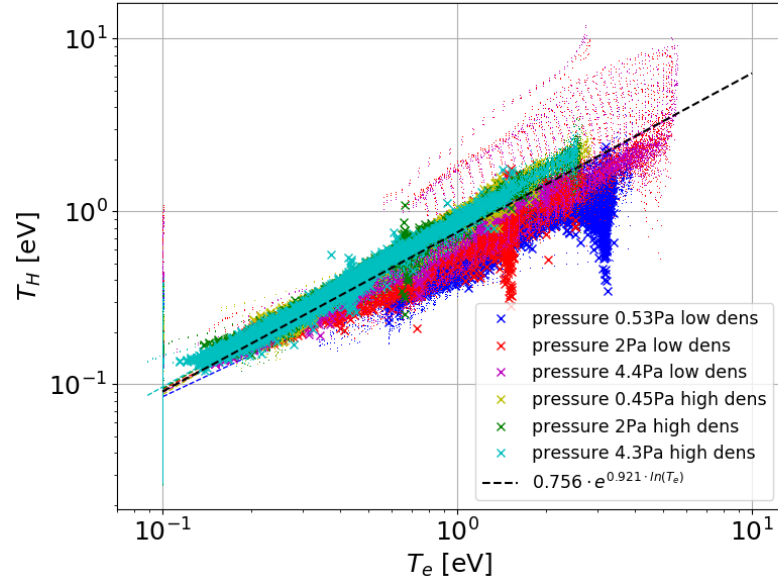


Figure A.12: Correlation between atomic hydrogen and electron temperature from B2.5-Eunomia modeling

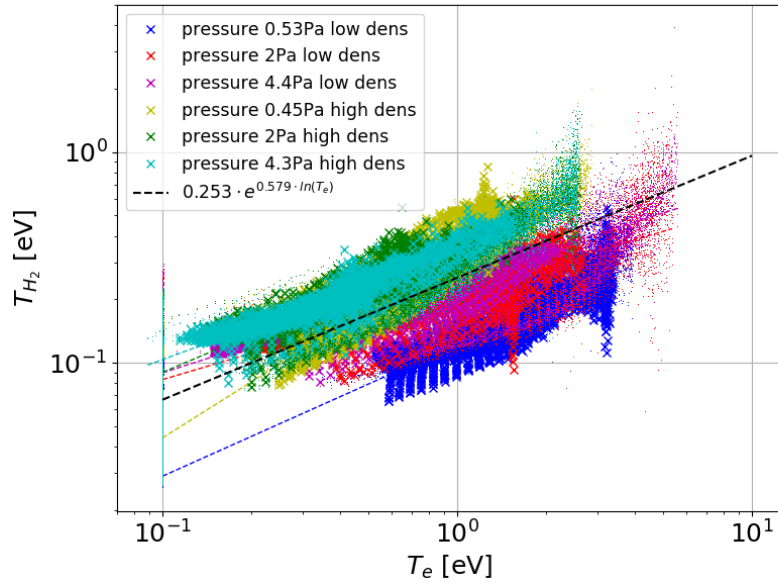


Figure A.13: Correlation between H_2 and electron temperature from B2.5-Eunomia modelling. The coloured dashed lines are obtained with a linear log log fit for the single cases. The solid black line is obtained averaging the fitting parameters obtained. This is assumed to be the same as H_2^+ temperature, while to obtain H^- temperature 2.2eV are added to account for the H_2 dissociation energy.

from H_2 it is considered $T_{H_2} = T_{H_2^+}$. This is valid for H^- too, but because it can get some of the H_2 binding energy (2.2eV per atom) 2.2eV are added to T_{H_2} to estimate T_{H^-} . [19]

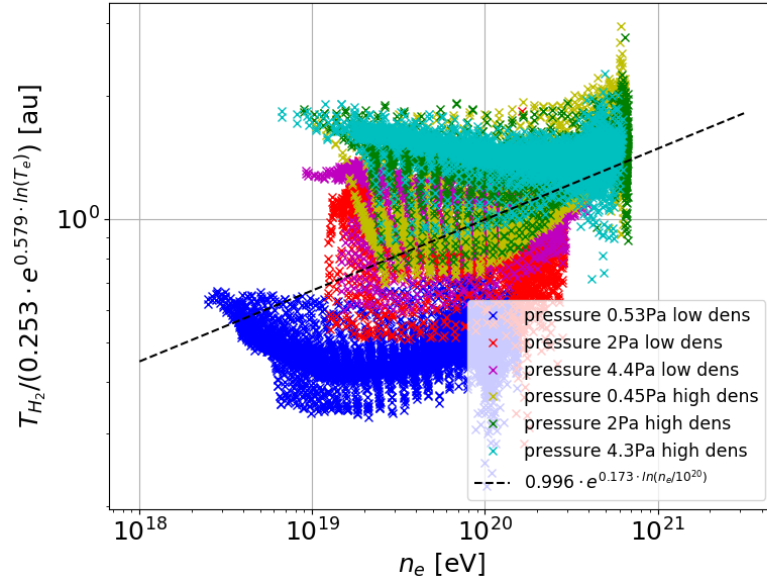


Figure A.14: Residuals from fitting T_{H_2} with the scaling from Figure A.13 and their weak dependence on the plasma density. The linear log log scaling in black is obtained by fitting all points at once.

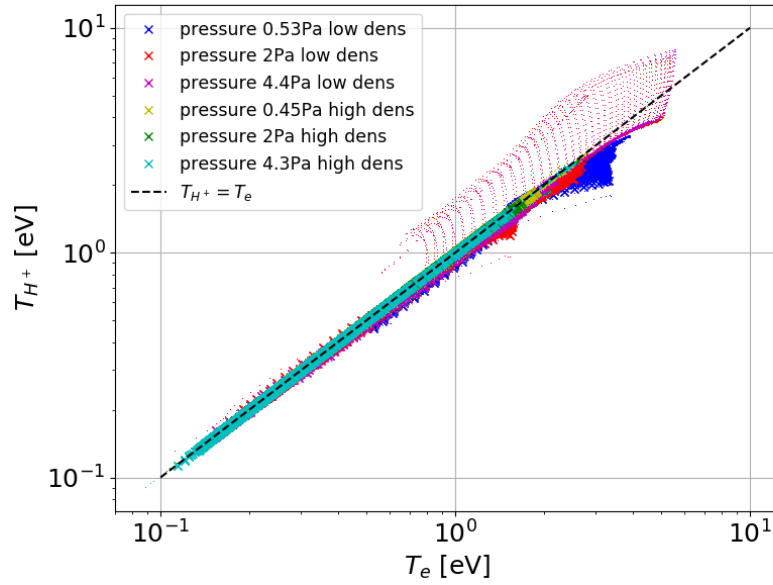


Figure A.15: Correlation between H^+ and electron temperature from B2.5-Eunomia modelling. The dashed line indicates $T_{H^+} = T_e$.

A.4.2 Priors from AMJUEL

Ionised hydrogen molecules are generated mainly from H_2 so their density prior is calculated with AMJUEL [5], a library that, among others, contains n_{H^-}/n_{H_2} and $n_{H_2^+}/n_{H_2}$ density ratios in an equilibrium plasma for given plasma temperature and density (Section 12.58,

12.59, 11.11, 11.12). The conditions of an ELM-like pulse can potentially deviate significantly from equilibrium, so a wide range around equilibrium is considered as prior and a linear uniform distribution as likelihood.

A.4.3 Priors range optimization

In order to optimize the n_H/n_e range to only useful values a combination of the information from [Figure A.10](#) and the OES measurement is used. For each T_e / n_e combination it is calculated what is the emission from EIR via the ADAS PEC coefficients and subtracted from the OES measurement. It is then calculated what is the n_H/n_e required to recreate via EIE each residual line emission plus its uncertainty. The largest n_H/n_e , limited by a predefined multiplier times the value from the B2.5-Eunomia fit, will be the highest value considered for that particular T_e / n_e combination. The lower limit will be taken as a small fraction of the maximum value, again limited by a predefined multiplier times the value from the B2.5-Eunomia fit. In this way parts of the range of n_H/n_e that would cause an excessive line emission are automatically excluded and the prior range is assigned efficiently.

The same process is applied to the n_{H_2}/n_e prior. For each $T_e / n_e / n_H/n_e$ the total emission from EIR and EIE is subtracted from the OES measurement and the n_{H_2}/n_e required to match the residual is calculated with the Yacora coefficients for the H_2 dissociation reaction. For the $n_{H_2^+}/n_{H_2}$ prior the emission from EIR, EIE, H_2 dissociation is considered. Consequently for the n_{H^-}/n_{H_2} prior also the emission from H_2^+ is considered.

A.4.4 Emissivity

The emissivity is calculated for known precursors densities via the ADAS PECs and Yacora population coefficients. [19] The Photon Emission Coefficients (PEC, photons m^3/s) coefficients are defined as the number of photons generated per second per unit of the precursors density. The number of photons for the transition $p \rightarrow q$ is equal to the product of density of the excited state p and the Einstein coefficient A_{pq} so the emission generated by atomic excitation and recombination can be expressed as per [Equation A.6](#) and [A.7](#), where it is also highlighted what is intended as population coefficient (PC_i).

$$\epsilon_{pq}^{exc} = PEC_{pq}^{exc}(T_e, n_e) n_e n_H = A_{pq} \underbrace{\frac{n_H(p)}{n_e n_H}}_{PC_{exc}} n_e n_H \quad (\text{A.6})$$

$$\epsilon_{pq}^{rec} = PEC_{pq}^{rec}(T_e, n_e) n_e n_{H^+} = A_{pq} \underbrace{\frac{n_H(p)}{n_e n_{H^+}}}_{PC_{rec}} n_e n_{H^+} \quad (\text{A.7})$$

The line emission due to molecular reactions is similarly calculated via the Yacora population coefficients as per Equation A.8, A.9, A.10 and A.11. It is also shown which reaction was considered in building the coefficients, and the variables necessary to calculate the coefficients. As mentioned T_H , T_{H_2} are determined from the B2.5-Eunomia simulation while $T_{H_2} \approx T_{H_2^+} \approx T_{H^-} - 2.2eV$.

$$\begin{aligned} \epsilon_{pq}^{H_2^+} &= A_{pq} PC_{H_2^+}(T_e, n_e) n_e n_{H_2^+} \\ \text{reactions : } H_2^+ + e^- &\rightarrow H(p) + H^+ + e^- \\ H_2^+ + e^- &\rightarrow H(p) + H(0) \end{aligned} \quad (\text{A.8})$$

$$\begin{aligned} \epsilon_{pq}^{H_2} &= A_{pq} PC_{H_2}(T_e, n_e) n_e n_{H_2} \\ \text{reaction : } H_2^+ + e^- &\rightarrow H(p) + H(1) + e^- \end{aligned} \quad (\text{A.9})$$

$$\begin{aligned} \epsilon_{pq}^{H^-+H_2^+} &= A_{pq} PC_{H^-+H_2^+}(T_e, T_{H_2^+}, T_{H^-}, n_e) n_{H_2^+} n_{H^-} \\ \text{reaction : } H^- + H_2^+ &\rightarrow H(p) + H_2 \end{aligned} \quad (\text{A.10})$$

$$\begin{aligned} \epsilon_{pq}^{H^-+H^+} &= A_{pq} PC_{H^-+H^+}(T_e, T_{H^+}, T_{H^-}, n_e) n_{H^+} n_{H^-} \\ \text{reaction : } H^- + H^+ &\rightarrow H(p) + H(1) \end{aligned} \quad (\text{A.11})$$

The total calculated emissivity and its uncertainty are determined as per Equation A.12 with σ_{ADAS} and σ_{Yacora} the uncertainty on the coefficients mentioned before.

$$\begin{aligned} \epsilon_{pq}^{calc} &= \epsilon_{pq}^{exc} + \epsilon_{pq}^{rec} + \epsilon_{pq}^{H_2^+} + \epsilon_{pq}^{H_2} + \epsilon_{pq}^{H^-+H_2^+} + \epsilon_{pq}^{H^-+H^+} \\ \sigma_{\epsilon_{pq}}^{calc} &= \left\{ \sigma_{ADAS}^2 (\epsilon_{pq}^{exc2} + \epsilon_{pq}^{rec2}) + \right. \\ &\quad \left. + \sigma_{Yacora}^2 (\epsilon_{pq}^{H_2^+2} + \epsilon_{pq}^{H_2^2} + \epsilon_{pq}^{H^-+H_2^+2} + \epsilon_{pq}^{H^-+H^+2}) \right\}^{1/2} \end{aligned} \quad (\text{A.12})$$

The line emissivity measurement is compared with the expectation. For each precursor combination and line is calculated what is the likelihood that $y_{pq} = 0$ with Equation A.13

$$\begin{aligned} y_{pq} &= \epsilon_{pq}^{calc} - \epsilon_{pq}^{measure}, \sigma_{y_{pq}} = \sqrt{\sigma_{\epsilon_{pq}}^{calc2} + \sigma_{\epsilon_{pq}}^{measure2}} \\ L(y_{pq} = 0 | \Theta) &= \frac{1}{\sigma_{y_{pq}} \sqrt{2\pi}} e^{-\frac{1}{2} \left(\frac{y_{pq}}{\sigma_{y_{pq}}} \right)^2} \end{aligned} \quad (\text{A.13})$$

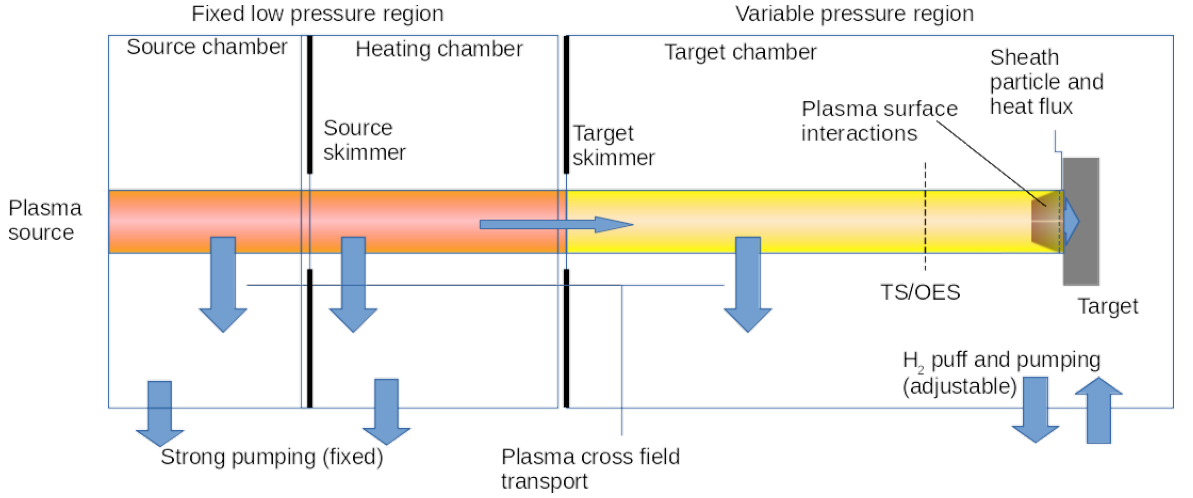


Figure A.16: Schematic of the plasma column model used. This schematic is useful to correlate local properties (at TS/OES location) to global ones like the total input power. Simplifications as constant densities and temperatures along the magnetic field and constant flow speed are used.

where Θ represent the specific combination of precursors that lead to the emission ϵ_{pq}^{calc} .

Following Bayes theorem the posterior (probability of the combination of precursors generating the measurements) is calculated as the likelihood of the measurement being generated by the precursors times the probability associated with the precursors themselves divided by the probability of the measured data. For the case in which only one emission line is included in the model this is expressed in [Equation A.14](#)

$$P(\Theta|y_{pq} = 0) = \frac{L(y_{pq} = 0|\Theta)P(\Theta)}{P(y_{pq} = 0)} \quad (\text{A.14})$$

Where $P(y_{pq} = 0)$ acts as a normalisation factor. The final product of all probabilities will be anyway normalised, so this term can be neglected. $P(\Theta)$ is the product of the probability associated with every combination of precursors (see [Section A.4.1](#), [A.4.2](#) and [4.6.1.2](#)). The probability of fitting all the lines P_ϵ is then determined with [Equation A.15](#).

$$P_\epsilon = P(\Theta) \prod_{p=4, q=2}^{p=8} P(\Theta|y_{pq} = 0) \quad (\text{A.15})$$

For this calculations σ_{ADAS} and σ_{Yacora} were assumed 10% and 20% respectively.

A.4.5 Balance over the plasma column

To avoid to consider precursor densities that could well match the line spectra but would lead to unrealistic power or particle losses a balance on the plasma column is performed. The definition of plasma column allows also to extract global information on the ELM-like pulse from the local TS/OES measurements and compare them with other global measurements like the power input from power supply. A schematic of the model of plasma column used is in [Figure A.16](#).

Fundamental assumptions are:

1. Given the neutrals density in source and heating chamber is low thanks to differential pumping it is assumed that the plasma is transported undisturbed from the plasma source to the target skimmer. Here T_e, n_e are equal to what is measured by TS in the target chamber for the lowest neutral pressure setting, that corresponds to the lowest possible volumetric losses.
2. The plasma enters the target chamber without any molecular precursor. This is justified by the fact that from source to target chamber skimmer the neutral pressure is at it lowest while the temperature is at its highest and this conditions are the least favourable for reactions involving molecules.
3. The neutral pressure is fixed throughout the ELM-like pulse to its steady state value.
4. All plasma properties such as: temperatures, densities, reaction rates, radiated power, depend on radial and temporal coordinates only and are spatially constant from target skimmer to target. This is justified by the fact that the fast camera shows that in Stage 1 and 2 the radiation is mostly constant from a short distance off the target. Given the OES measuring location, only the properties of the bulk of the plasma can be analysed¹. That means that the power losses in the visible light brightness peak between the OES and the target observed in [Section 4.3](#) cannot be accounted, so the volumetric power losses from the analysis will likely be an underestimation. The extent of the non uniform region close to the target, likely including sheath and a region with strong plasma surface interactions, is typically ≤ 1 cm, small compared to the 38 cm from target to skimmer, so this underestimation should be minor. Increasing

¹Measurements specific to the region close to the target have been attempted but failed possibly due to reflections or obstructions by the target itself.

neutral pressure from Stage 1 to 2 (the cases we are most interested in) the visible light brightness becomes stronger in the plasma column, making the anisotropy at the target even less relevant. The approximation also neglects anisotropy in the visible light brightness in the bulk for very high neutral pressure. This is especially dominant in Stage 3, so its importance should be minor for Stages 1 and 2.

5. The plasma behaviour in the sheath and in the region with strong plasma surface interactions is neglected.
6. The flow velocity of the plasma is constant from the source to the target.
7. Cross field transport is negligible (mostly true for charged particles due to the high magnetic field and additionally for molecular ions due to their short life time)

Given these assumptions one can calculate the components of the power and particle balance on the whole plasma column. The OES/TS measurements from a single location can be applied to the whole column and the contribution from atomic and molecular processes can be found.

A quantity that will be used later is the flow velocity (v_{in}), the velocity of the plasma in its flow from the target skimmer to the target. It is here mainly used to subdivide the power from the plasma source (a global value) to what is provided to each radial location and to estimate the local particle inflow. It is also used to estimate the kinetic energy of the plasma, but the relevance of this term is minor. There is no direct measurement of v_{in} yet as collective Compton scattering measurements will be available in the future. v_{in} is then approximated by imposing, for the experimental condition with the lowest target chamber neutral pressure, that the power from the source matches the energy flow measured at the TS location. The flow is assumed having a single Mach number for all radial locations. Applying this conditions to [Equation A.18](#) this translate to [Equation A.16](#) that is then solved to find the Mach number.

$$\begin{aligned}
& \sum_r \left\{ \left(\frac{1}{2} m_i v_{in}^2(r, t) + 5k_B T_{e,in}(r, t) + E_{ion} + E_{diss} \right) \cdot \right. \\
& \left. \cdot n_{e,in}(r, t) v_{in}(r, t) A \right\} = P_{source}(t) \\
& v_{in}(r, t) = M_{in}(t) c_{s,up}(r, t) \\
& c_s = \sqrt{\frac{(T_e + T_{H^+} (\approx T_e)) k_B}{m_H}}
\end{aligned} \tag{A.16}$$

In calculating P_{source} as product of voltage and current an efficiency of 92% is considered in the conversion from electric to plasma energy. [154] M_{in} is ≈ 1 during the ELM-like pulse. It must be noted that at the beginning and end of the pulse TS is incapable of accurately measuring across the whole plasma because of the low density, and the energy conversion from electric power to plasma potential is lower, resulting in the calculated $M_{in} > 1$. The effect of the overestimation, though, is to allow for larger energy and particle budgets, widening the possible parameter space, so it is acceptable. I will now detail how to calculate the likelihood associated with the power and particle balance.

A.4.6 Power balance

In this chapter it will be detailed how the power (energy) balance equation is obtained and how all the terms are defined. The 1D energy and particle balance equations are obtained from the 1D Fokker-Planck collisional kinetic equation (Equation A.17) as per derivation from Stangeby [150] and are adapted using the mentioned approximations for the region from target skimmer to target. This results for every time step and radial location in Equation A.18

$$\frac{\partial f}{\partial t} + v_z \frac{\partial f}{\partial z} + \frac{eE}{m} \frac{\partial f}{\partial v_z} = \left(\frac{\partial f}{\partial t} \right)_{coll} + S(x, v) \tag{A.17}$$

$$\begin{aligned}
& \frac{\partial E}{\partial t} + \frac{d}{dz} \left[\left(\frac{1}{2} m_i v^2 + 5kT_e + E_{ion} + E_{diss} \right) n_e v \right] = \\
& \quad - \underbrace{P_{ext\ source}}_{=0} + P_{volume\ sinks-sources} \\
& \frac{\partial E}{\partial t} + \left(\frac{1}{2} m_i v_{in}^2 + 5kT_{e,in} + E_{ion} + E_{diss} \right) n_{e,in} v_{in} = \\
& \quad + P_{target} + P_{volume\ sinks-sources} \\
P_{diss\ max} &= \underbrace{\left(\frac{1}{2} m_i v_{in}^2 + 5kT_e + E_{ion} + E_{diss} \right) \frac{n_e V}{\Delta t}}_{P_{\partial t}} + \\
& \quad + \underbrace{\left(\frac{1}{2} m_i v_{in}^2 + 5kT_{e,in} + E_{ion} + E_{diss} \right) n_{e,in} v_{in} A}_{P_{in}} \geq \\
& \geq P_{volume\ sinks-sources}
\end{aligned} \tag{A.18}$$

with v the flow velocity, E_{ion} and E_{diss} the ionisation and dissociation energy for hydrogen. The inequality arises from not accounting the power delivered to the target and to neglect plasma interactions with neutrals such as elastic collisions and charge exchange. All quantities marked with the subscript $_{in}$ refer to the input conditions, otherwise the conditions inside the plasma column are intended. $P_{\partial t}$ represents the power deriving by depleting all the energy associated with the plasma in the volume of interest (V) in a single time step (Δt), P_{in} is the power entering the volume of interest from the plasma source through the area A . $P_{diss\ max}$ is the maximum power that can be depleted in a radial portion of the plasma column in a time step. As an additional constrain on the power balance it will be required to $P_{volume\ sink-source}$ to be positive, as otherwise it would mean that the plasma is externally heated on its way to the target.

Let's investigate now the volumetric sinks-sources term. There are roughly three ways in which a hydrogen plasma can undergo power losses:

1. Radiative losses. This mostly comes from the relaxation of excited hydrogen atoms, which can arise from both plasma-atom as well as plasma-molecule interactions. The radiative losses associated with H_2 molecular band radiation are expected to be of insignificant. [182]
2. Power transfer from kinetic energy to potential energy. Several plasma species have a relative potential energy associated with it (for instance, H^+ has a potential energy of 13.6eV compared to atomic hydrogen). Converting a neutral into an ion thus ‘‘converts’’

13.6eV of kinetic plasma energy to potential energy.

3. Power transfer from CX and elastic collisions. CX as well as elastic collisions between the plasma and neutral atoms and molecules can lead to transfer of power from the plasma to the neutrals (and vice versa). This includes collisions between particles of the same specie but at different temperatures like the cold proton generated from ionisation and the hot one part of the plasma.

OES combined with collisional radiative models is used to estimate the magnitude of both path 1 and 2, which is employed in this work. For path 1, the Balmer line emission is measured facilitating, through the Bayesian inference of the plasma properties, a full estimate of the hydrogenic line radiation from excited atoms arising both from plasma-atom as well as plasma-molecule interaction. For path 2, ionisation and recombination rates are estimated to account for the power transfer between potential and kinetic energy. In the recombination reaction a hot H^+ is converted into a neutral. That neutral has a kinetic energy equal to the temperature of the plasma that generated it, significantly higher than all other molecular and neutral species. For this reason the energy removed by the plasma assuming the neutrals from recombination escape is accounted in the local power balance. Additionally a series of molecular reactions are considered, see [Section A.4.9](#) for which the difference in potential energy between reactants and products is calculated and accounted.

Note that paths 2 and 3 do not strictly represent power lost from the plasma column but can be power transfer mechanisms. Such transfer mechanisms often lead to an effective loss of kinetic energy by the plasma, but can also cause it to increase.

In the power balance that regards the limitation of the power transferred from the plasma at a single radial location, [Equation A.18](#), pathway 2 is considered. It is in fact impossible for the plasma to transfer energy from kinetic to potential for more more than it is available. Differently when the quantity of interest are the components of the global power balance, [Equation A.26](#), only terms where the energy is removed from the plasma column entirely will be considered. Internal power transfer will not be considered as it is energy that remains in the plasma.

Pathway 3 cannot be readily analysed experimentally but can be analysed in detail in simulations. The importance of this is currently discussed in literature and it could be significant especially in low temperature conditions in tokamak divertors and linear machines. [[179](#), [187](#), [188](#)] Further code investigations on this and detailed comparisons against

experiments are required, which is outside of the scope of this work. To check that neglecting CX and H_2 elastic collisions, the ones to have the largest impact [179], does not have a negative impact on the consistency of the solution a crude estimation was done in post processing. This is done by first calculating the ADAS CCD reaction rate for CX and AMJUEL 3.5 rate for H_2 elastic. These are multiplied by the density of the reactant species interested and by the maximum energy that can be transfer with a single collision. The energy of the reactants are equivalent to their temperature from TS and A.4.1. This results in Equation A.19.

$$\begin{aligned} P_{CX} &= \frac{3}{2}(T_{H^+}(=T_e) - T_H)RR_{CX}(T_e, n_e)n_{H^+}n_H \\ P_{H_2\text{elastic}} &= \frac{3}{2}\frac{8}{9}(T_{H^+} - T_{H_2})RR_{H_2\text{elastic}}(T_{H^+}, T_{H_2})n_{H^+}n_{H_2} \end{aligned} \quad (\text{A.19})$$

These quantities PDFs are calculated as one of the outputs of the Bayesian algorithm.

The sinks/sources terms for Equation A.18 are taken from different sources, to encompass the best knowledge available at the time of writing, see Section A.4.9. Grouping them by type and precursor the power balance sinks/sources term is then defined as per Equation A.20

$$\begin{aligned} P_{\text{sinks-sources}}^{\text{volume}} &= P_{\text{radiated}} + P_{\text{neutral via recombination}} + P_{\text{potential energy}} \\ P_{\text{radiated}} &= P_{\text{radiated atomic}} + P_{\text{radiated molecular}} \\ P_{\text{neutral via recombination}} &= \frac{3}{2}\Delta V T_e RR_{\text{rec}} \\ P_{\text{potential energy}} &= \Delta V \sum_i \Delta E_i \cdot RR_i \\ P_{\text{radiated atomic}} &= \underbrace{P_{\text{excitation}}}_{\text{ADAS PLT}} + \underbrace{P_{\text{rec+bremstrahlung}}}_{\text{ADAS PRB}} \\ P_{\text{radiated molecular}} &= P_{\text{rad } H_2^+} + P_{\text{rad } H_2} + P_{\text{rad } H^-+H_2^+} \\ &\quad + P_{\text{rad } H^-+H^+} + P_{\text{rad } e^-+H \rightarrow H^-+h\nu} \\ P_{\text{rad},i} &= \Delta V \sum_{p=2, q < p}^{p=13} \epsilon_{pq}^i \end{aligned} \quad (\text{A.20})$$

where ΔV represent the volume corresponding to the radial location of the plasma considered, ΔE_i is the energy difference between products and reactants of the reaction i and RR_i is its reaction rate. The $p=13$ comes from the fact that only atomic hydrogen excited states up to 13 are here considered. The probability that the inequality in Equation A.18 is

true and that $P_{volume\ sinks-sources}$ is positive is calculated with [Equation A.21](#)

$$\begin{aligned}
 y &= P_{diss\ max} - P_{s-s}, \sigma_y = \sqrt{\sigma_{P_{s-s}}^2 + \sigma_{P_{diss\ max}}^2} \\
 L_P &= L(y \in [0, P_{diss\ max}]) = \\
 &= \frac{1}{2} \left[\operatorname{erf}\left(\frac{P_{diss\ max} - y}{\sqrt{2}\sigma_y}\right) - \operatorname{erf}\left(\frac{-y}{\sqrt{2}\sigma_y}\right) \right]
 \end{aligned} \tag{A.21}$$

where $P_{volume\ sinks-sources}$ is shortened with P_{s-s} .

The power sinks/sources are calculated by adding all the radiative losses to the potential energy contribution. The latter is itself composed by positive and negative contributions that tend to cancel out. This causes the uncertainty of the sinks/sources to greatly dominate over the input one, making the effective use of this balance very difficult. To solve this issue σ_y considered as equal to $\sigma_{P_{diss\ max}}$ and that is assumed to be 50% of $P_{diss\ max}$ (using the fixed nominal T_e , n_e values from TS).

A.4.7 Particle balance

The derivation of the particle balance equation from Stangeby [72] results in Equation 14

$$\begin{aligned}
 \frac{\partial n_j}{\partial t} + \frac{d}{dz}(n_j v) &= Sinks - Sources \\
 (nv)_{j,diss\ max} &= \underbrace{\frac{n_j V}{\Delta t}}_{(nv)_{j,\partial t}} + \underbrace{n_{j,in} v_{in}}_{(nv)_{j,in}} \geq \\
 &\geq (nv)_{j,Sinks-Sources} = \Delta V \sum_i f_{ij} R R_i \\
 &= \sum_i \dot{n}_{i,sinks} - \dot{n}_{i,sources}
 \end{aligned} \tag{A.22}$$

with f_{ij} the multiplicity and sign in the reaction i for the specie j and $n_{H_2\ in} = n_{H\ in} = n_{H_2^+\ in} = n_{H^-\ in} = 0$. The inequality comes from not including the particles lost due to surface processes happening at the target and cross field transport. Charged particles are bound by magnetic fields while neutrals can more easily move across. For this reason the particle balance, that considers each radial location independently, is calculated only for charged particles as e^- , H^+ , H_2^+ , H^- . In the case of H_2^+ , H^- the lifetime is very short so even in a single time step it is not physical to allow for its accumulation. [180] For this reason for them $(nv)_{i,Sinks-Sources}$ is limited to be $\geq -(nv)_{i,diss\ max}$. For e^- and H^+ the

net rate of production is limited to their density the next time step. This term, referred as $(nv)_{j,next}$ is defined similarly to $(nv)_{j,\partial t}$ in Equation A.22. The likelihood that the particle balance is verified is given by Equation A.23 and A.24

$$\begin{aligned}
y_j &= (nv)_{j,diss\ max} - (nv)_{j,Sinks-Sources} \\
\sigma_{y_j} &= \sqrt{\sigma_{(nv)_{j,diss\ max}}^2 + \sigma_{(nv)_{j,Sinks-Sources}}^2} \\
L(y_{e^-} \in [0, (nv)_{e^-,diss\ max} + (nv)_{e^-,next}]) &= \\
&= \frac{1}{2} \left[\operatorname{erf} \left(\frac{(nv)_{e^-,diss\ max} + (nv)_{e^-,next} - y_{e^-}}{\sqrt{2}\sigma_{y_{e^-}}} \right) + \right. \\
&\quad \left. - \operatorname{erf} \left(\frac{-y_{e^-}}{\sqrt{2}\sigma_{y_{e^-}}} \right) \right] \tag{A.23}
\end{aligned}$$

$$\begin{aligned}
L(y_{H^+} \in [0, (nv)_{H^+,diss\ max} + (nv)_{H^+,next}]) &= \\
&= \frac{1}{2} \left[\operatorname{erf} \left(\frac{(nv)_{H^+,diss\ max} + (nv)_{H^+,next} - y_{H^+}}{\sqrt{2}\sigma_{y_{H^+}}} \right) + \right. \\
&\quad \left. - \operatorname{erf} \left(\frac{-y_{H^+}}{\sqrt{2}\sigma_{y_{H^+}}} \right) \right]
\end{aligned}$$

$$\begin{aligned}
L(y_{H_2^+} \in [0, 2(nv)_{H_2^+,diss\ max}]) &= \\
&= \frac{1}{2} \left[\operatorname{erf} \left(\frac{2(nv)_{H_2^+,diss\ max} - y_{H_2^+}}{\sqrt{2}\sigma_{y_{H_2^+}}} \right) + \right. \\
&\quad \left. - \operatorname{erf} \left(\frac{-y_{H_2^+}}{\sqrt{2}\sigma_{y_{H_2^+}}} \right) \right]
\end{aligned}$$

$$\begin{aligned}
L(y_{H^-} \in [0, 2(nv)_{H^-,diss\ max}]) &= \\
&= \frac{1}{2} \left[\operatorname{erf} \left(\frac{2(nv)_{H^-,diss\ max} - y_{H^-}}{\sqrt{2}\sigma_{y_{H^-}}} \right) + \right. \\
&\quad \left. - \operatorname{erf} \left(\frac{-y_{H^-}}{\sqrt{2}\sigma_{y_{H^-}}} \right) \right] \tag{A.24}
\end{aligned}$$

$$\begin{aligned}
L_{nv} &= L(y_{e^-} \geq 0) \cdot L(y_{H^+} \geq 0) \cdot \\
&\quad \cdot L(y_{H_2^+} \in [0, 2(nv)_{H_2^+,diss\ max}]) \cdot \\
&\quad \cdot L(y_{H^-} \in [0, 2(nv)_{H^-,diss\ max}])
\end{aligned}$$

Similarly to what mentioned for the power balance, here too the sinks/sources term is composed of positive and negative factor, so rather than using it a large uncertainty on $(nv)_{i,diss\ max}$ of 100% for e , H^+ (using the fixed nominal n_e value from TS) and 5% of TS

n_e for H_2^+ , H^- is assumed. The uncertainties are here adopted so large because differently from power and emissivity there is no direct measurement of the particle input. As part of the particle balance one has also to include that the density of excited states obtained with ADAS and Yacora coefficients is lower than the density of total atomic hydrogen in the volume. This is calculated with [Equation A.25](#).

$$y = n_H - \sum_{q,i} n_{iH(q)}, \sigma_y = \sqrt{\sum_{q,i} (\sigma_i n_{iH(q)})^2}$$

$$L_{H^{exc}} = L(y \geq 0) = \frac{1}{2} \left[1 - \operatorname{erf} \left(\frac{-y}{\sqrt{2}\sigma_y} \right) \right] \quad (\text{A.25})$$

A.4.8 Plasma column power balance

The definition of the plasma column volume and the power balance allows to evaluate the global performance of the detached target to the ELM-like pulse. The parameter of interest is, in this case, how much power is removed from the plasma column and how much is due to atomic versus molecular effects. In considering this the potential energy exchange due to EIR, for example, was not considered because it represent a transfer mechanism and not a net loss, while the radiative component due to radiation (ADAS PRB coefficient, returning the losses due to line radiation and Bremsstrahlung) was. Bremsstrahlung radiation is present also in the wavelength range of the IR camera and could be related to the observed prompt emission but this was not investigated. Similarly all other exchanges of potential energy are not considered. The generated neutrals while travelling out of the plasma can react with the neighbouring plasma and the energy they carry be reintroduced. Because evaluating this would require a significant effort this component is for now excluded.

The terms considered for the global power removed from the plasma column are indicated in [Equation A.26](#).

$$E_{\substack{\text{removed} \\ \text{from} \\ \text{plasma}}} = E_{\text{radiated}} = \underbrace{E_{exc} + E_{rad \text{ rec+bremm}}}_{\text{atomic}} +$$

$$+ E_{rad \text{ H}_2} + E_{rad \text{ H}} + E_{rad \text{ H}_2^{++}} \quad (\text{A.26})$$

$$+ \underbrace{E_{rad \text{ H}^-} + E_{rad \text{ e}^- + \text{H} \rightarrow \text{H}^- + \text{pv}}}_{\text{molecular}}$$

Once all the likelihoods associated with each combination of priors are calculated they are

multiplied to return the total likelihood as per [Equation A.27](#)

$$L = P_\epsilon L_p L_{nv} L_{H^{exc}} \quad (\text{A.27})$$

The PDFs of all the components of the power and particle balance previously calculated are built by portioning their range to a smaller number of logarithmic intervals, summing the probability within. For each additive term of interest the PDFs are then convolved in space and in time to obtain the PDF for the whole ELM-like pulse. For each radial and time location and for each output required (for example the total radiated energy) is defined a large list of the possible energy losses in that section of the plasma. The list is randomly distributed according on the PDF of that output at that location. The contribution for all radii is summed to generate a list of possible values of the total radiated energy at one time step. A histogram is built based on that to represent the PDF of the quantity of interest at that time step. This operation is repeated to sum the contribution from all the time steps to return the PDF of the quantity of interest for the whole ELM-like pulse.

A.4.9 Reactions

Reaction rates and other coefficients used in the Bayesian calculations are obtained from ADAS [1, 2] for the atomic reactions while from Yacora [3, 4], AMJUEL [5–7] or a collection of reaction rates from Janev [8] for the molecular reactions. The reactions considered in this work are listed in [Table A.1](#), [A.2](#), [A.3](#), and [A.4](#).

Reaction:	Chapter / type
$H^+ + e^- \rightarrow H(p) + h\nu$	ADC,PRB,PEC
$H^+ + 2e^- \rightarrow H(p) + e^-$	
$H + e^- \rightarrow H^+ + 2e^-$	SCD
$H(q) + e^- \rightarrow H(p > q) + e^-$	PLT,PEC

Table A.1: Reactions whose rates and reference coefficients were sourced from the ADAS database. [1, 2]

Reaction:
$H_2^+ + H^- \rightarrow H(p) + H_2$
$H^+ + H^- \rightarrow H(p) + H$
$H_2^+ + e^- \rightarrow H(p) + H(1)$
$H_2^+ + e^- \rightarrow H(p) + H^+ + e^-$
$H_2 + e^- \rightarrow H(p) + H(1) + e$

Table A.2: Reactions whose rates and reference coefficients were sourced using the Yacora collisional radiative code. [3,4]

Reaction:	Chapter / type
$e^- + H_2 \rightarrow 2e^- + H_2^+$	4.11 Reaction 2.2.9
$e^- + H_2 \rightarrow 2e^- + H + H^+$	4.12 Reaction 2.2.10
$e^- + H_2^+ \rightarrow 2e^- + H^+ + H^+$	4.13 Reaction 2.2.11
$e^- + H_2^+ \rightarrow e^- + H + H^+$	4.14 Reaction 2.2.12
$e^- + H_2^+ \rightarrow H + H$	4.15 Reaction 2.2.14
$e^- + H_2 \rightarrow e^- + H_2(v) \rightarrow H + H^-$	2.23 Reaction 2.2.17
$H^+ + H_2(v) \rightarrow H + H_2^+$	3.28 Reaction 3.2.3
$H^+ + H^- \rightarrow H + H$	4.52 Reaction 7.2.3a
$e^- + H_2(v) \rightarrow e^- + H + H$	4.10 Reaction 2.2.5g

Table A.3: Reactions whose rates and reference coefficients were sourced from the AMJUEL database. [5-7]

Reaction:	Chapter / type
$H_2^+(vi) + H^- \rightarrow (H_3^*) \rightarrow$ $\rightarrow H_2(X1\Sigma_g; v_0) + H(n \geq 2)$	7.4.1
$H_2^+(vi) + H^- \rightarrow (H_3^*) \rightarrow$ $\rightarrow H_2(N1, 3\Lambda_\sigma; v_0) + H(1), N \leq 4$	7.4.1

Table A.4: Reactions whose rates and reference coefficients were sourced from the Janev database. [8]

List of References

- [1] H. P. Summers. The ADAS User Manual, version 2.6, 2004. <<http://www.adas.ac.uk>>. 7, 172, 231
- [2] M. OMullane. Adas: Generalised collisional radiative data for hydrogen Tech. rep., 2013. <<http://www.adas.ac.uk>>. 7, 172, 231
- [3] D. Wunderlich and U. Fantz. Evaluation of state-resolved reaction probabilities and their application in population models for He, H, and H₂. *Atoms*, 4(4), 2016. 7, 173, 231, 232
- [4] D. Wunderlich, M. Giacomini, R. Ritz, and U. Fantz. Yacora on the Web: Online collisional radiative models for plasmas containing H, H₂ or He. *Journal of Quantitative Spectroscopy and Radiative Transfer*, 240, 2020. 7, 173, 231, 232
- [5] D. Reiter. The data file AMJUEL : Additional Atomic and Molecular Data for EIRENE. Technical report, FZJ, Forschungszentrum Julich GmbH, Julich, Germany, 2020. 7, 172, 218, 231, 232
- [6] D. Reiter, M. Baelmans, and P. Börner. The eirene and B2-eirene codes. *Fusion Science and Technology*, 47(2):172, 2005. 7, 172, 231, 232
- [7] V. Kotov, D. Reiter, and A. S. Kukushkin. *Numerical study of the ITER divertor plasma with the B2-EIRENE code package*. Ph.D. thesis, Forschungszentrum Julich, 2007. 7, 172, 231, 232
- [8] R. K. Janev, D. Reiter, and U. Samm. Collision Processes in Low-Temperature Hydrogen Plasmas. *Sciences-New York*, page 190, 2003. 7, 173, 231, 232
- [9] N. Yan, V. Naulin, B. Wan, and G. Xu. *Coherent structures in the boundary plasma of EAST Tokamak*. Ph.D. thesis, Technical University of Denmark, 2014. 8, 36, 38

- [10] Culham Centre for Fusion Energy. Schematic of the main components of a tokamak, 2018. <http://www.ccfе.ac.uk/How_fusion_works.aspx>. 8, 38
- [11] M. V. Umansky, M. E. Rensink, T. D. Rognlien, B. LaBombard, D. Brunner, J. L. Terry, and D. G. Whyte. Assessment of X-point target divertor configuration for power handling and detachment front control. *Nuclear Materials and Energy*, 12:918, 2017. 8, 41
- [12] H. Lux, R. Kemp, D. J. Ward, and M. Sertoli. Impurity radiation in DEMO systems modelling. *Fusion Engineering and Design*, 101:42, 2015. 8, 42
- [13] S. Wiesen, et al. Modelling radiative power exhaust in view of DEMO relevant scenarios. Technical report, 2nd IAEA Technical Meeting on Divertor Concepts, Suzhou, China, 2017. 8, 33, 49
- [14] J. R. Harrison, S. W. Lisgo, K. J. Gibson, P. Tamain, J. Dowling, and M. Team. Characterisation of detached plasmas on the MAST tokamak. *Journal of Nuclear Materials*, 415(1 SUPPL), 2011. 8, 16, 51, 124
- [15] J. F. Rivero-Rodriguez, et al. Development and installation of a scintillator based detector for fast-ion losses in the MAST-U tokamak. In *45th EPS Conference on Plasma Physics, EPS 2018*, volume 2018-July, pages 233–236. European Physical Society, 2018. 10, 72
- [16] R. Fisher, S. Perkins, A. Walker, and E. Wolfart. Image processing learning resources hipr2, 2004. 14, 108, 109
- [17] A. S. Jacobsen. *Methods to determine fast-ion distribution functions from*. Ph.D. thesis, Technical University of Denmark, 2015. 14, 103, 108, 109, 110
- [18] G. R. A. D. Akkermans, I. G. J. Classen, R. Perillo, H. J. Van Der Meiden, F. Federici, and S. Brezinsek. The role of hydrogen molecular effects on detachment in Magnum-PSI The role of hydrogen molecular effects on detachment in Magnum-PSI. *Physics of Plasmas*, 102509(June), 2020. 21, 147, 155, 169, 184
- [19] K. H. Verhaegh, et al. A novel hydrogenic spectroscopic technique for inferring the role of plasma-molecule interaction on power and particle balance during detached conditions. *arXiv*, 2, 2020. 24, 25, 142, 169, 172, 184, 186, 188, 217, 219

- [20] F. Federici, M. L. Reinke, B. Lipschultz, A. J. Thornton, J. R. Harrison, J. J. Lovell, and M. Bernert. Design and implementation of a prototype infrared video bolometer (IRVB) in MAST Upgrade. *Review of Scientific Instruments*, **94(3):033502**, 2023. [31](#)
- [21] G. G. Van Eden, et al. Design and characterization of a prototype divertor viewing infrared video bolometer for NSTX-U. *Review of Scientific Instruments*, **87(11)**, 2016. [32](#), [57](#), [63](#), [194](#)
- [22] B. Lipschultz, F. I. Parra, and I. H. Hutchinson. Sensitivity of detachment extent to magnetic configuration and external parameters. *Nuclear Fusion*, **56(5)**, 2016. [33](#), [45](#), [47](#), [48](#), [54](#), [55](#), [56](#), [58](#), [124](#), [131](#), [139](#), [145](#)
- [23] G. Miley, H. Towner, and N. Ivich. Fusion cross sections and reactivities, 1974. <<http://www.osti.gov/servlets/purl/4014032/>>. [35](#)
- [24] F. F. Chen. *Introduction to Plasma Physics and Controlled Fusion*. PLENUM PRESS - NEW YORK AND LONDON, 1974. [37](#)
- [25] C. Gormezano, et al. Internal transport barriers in jet deuterium-tritium plasmas. *Physical Review Letters*, **80(25):5544**, 1998. [37](#)
- [26] E. Gibney. Nuclear-fusion reactor smashes energy record. *Nature*, **602(7897):371**, 2022. [37](#)
- [27] F. Rytter, W. Suttrop, B. Brüsehaber, M. Kaufmann, V. Mertens, H. Murmann, A. G. Peeters, J. Stober, J. Schweinzer, and H. Zohm. H-mode power threshold and transition in ASDEX Upgrade. *Plasma Physics and Controlled Fusion*, **40(5):725**, 1998. [39](#)
- [28] H. Zohm. Edge localized modes (ELMs). *Plasma Physics and Controlled Fusion*, **38(2):105**, 1996. [39](#)
- [29] S. Jachmich, et al. Power and particle fluxes to plasma-facing components in mitigated-ELM H-mode discharges on JET. *Journal of Nuclear Materials*, **415(1 SUPPL):S894**, 2011. [39](#), [147](#), [149](#), [167](#)
- [30] T. Pütterich, R. Dux, M. A. Janzer, and R. M. McDermott. ELM flushing and impurity transport in the H-mode edge barrier in ASDEX Upgrade. *Journal of Nuclear Materials*, **415(1 SUPPL):334**, 2011. [39](#)

- [31] A. W. Leonard. Edge-localized-modes in tokamaks. *Physics of Plasmas*, [21\(9\):1](#), 2014. [39](#), [40](#)
- [32] M. Faitsch, T. Eich, G. F. Harrer, E. Wolfrum, D. Brida, P. David, M. Griener, and U. Stroth. Broadening of the power fall-off length in a high density, high confinement H-mode regime in ASDEX Upgrade. *Nuclear Materials and Energy*, [26](#), 2021. [40](#)
- [33] D. Silvagni, T. Eich, M. Faitsch, T. Happel, B. Sieglin, P. David, D. Nille, L. Gil, and U. Stroth. Scrape-off layer (SOL) power width scaling and correlation between SOL and pedestal gradients across L, i and H-mode plasmas at ASDEX Upgrade. *Plasma Physics and Controlled Fusion*, [62\(4\)](#), 2020. [40](#)
- [34] A. Q. Kuang, et al. Divertor heat flux challenge and mitigation in SPARC. *Journal of Plasma Physics*, 2020. [40](#)
- [35] R. A. Pitts, et al. Physics basis for the first ITER tungsten divertor. *Nuclear Materials and Energy*, [20\(July\):100696](#), 2019. [40](#)
- [36] B. Lipschultz. Lecture notes on Fusion Thechnology, 2018. [40](#)
- [37] S. Wiesen, M. Groth, M. Wischmeier, S. Brezinsek, A. Jarvinen, F. Reimold, and L. Aho-Mantila. Plasma edge and plasma-wall interaction modelling: Lessons learned from metallic devices. *Nuclear Materials and Energy*, [12:3](#), 2017. [40](#), [49](#)
- [38] S. Potzel, M. Wischmeier, M. Bernert, R. Dux, H. W. Müller, and A. Scarabosio. A new experimental classification of divertor detachment in ASDEX Upgrade. *Nuclear Fusion*, [54\(1\)](#), 2014. [41](#), [45](#), [57](#), [125](#)
- [39] H. D. Pacher, A. S. Kukushkin, G. W. Pacher, V. Kotov, and D. Reiter. Modelling of the ITER reference divertor plasma. *Journal of Nuclear Materials*, [415\(1 SUPPL\):S492](#), 2011. [42](#)
- [40] F. Reimold, M. Wischmeier, M. Bernert, S. Potzel, A. Kallenbach, H. W. Müller, B. Sieglin, and U. Stroth. Divertor studies in nitrogen induced completely detached H-modes in full tungsten ASDEX Upgrade. *Nuclear Fusion*, [55\(3\)](#), 2015. [43](#), [45](#), [47](#), [57](#), [60](#)

- [41] M. Greenwald, J. L. Terry, S. M. Wolfe, G. H. Neilson, M. G. Zweibelben, S. M. Kaye, and G. H. Neilson. A new look at density limits in tokamaks. *Nuclear Fusion*, [28\(12\):2207](#), 1988. [43](#)
- [42] B. Lipschultz, B. LaBombard, J. L. Terry, C. Boswell, and I. H. Hutchinson. Divertor physics research on alcator C-Mod. *Fusion Science and Technology*, [51\(3\):369](#), 2007. [43](#)
- [43] A. Kallenbach, et al. Partial detachment of high power discharges in ASDEX Upgrade. *Nuclear Fusion*, [55\(5\)](#), 2015. [43](#), [46](#), [47](#), [48](#)
- [44] A. W. Leonard. Plasma detachment in divertor tokamaks. *Plasma Physics and Controlled Fusion*, [60\(4\)](#), 2018. [44](#)
- [45] S. I. Krasheninnikov, A. S. Kukushkin, and A. A. Pshenov. Divertor plasma detachment. *Physics of Plasmas*, [23\(5\)](#), 2016. [44](#), [50](#), [53](#)
- [46] S. I. Krasheninnikov and A. S. Kukushkin. Physics of ultimate detachment of a tokamak divertor plasma. *Journal of Plasma Physics*, [83\(05\):155830501](#), 2017. [44](#), [45](#), [148](#)
- [47] B. Lipschultz, et al. The role of particle sinks and sources in Alcator C-Mod detached divertor discharges. *Physics of Plasmas*, [6\(5 I\):1907](#), 1999. [44](#)
- [48] K. Jesko, Y. Marandet, H. Bufferand, J. P. Gunn, H. J. van der Meiden, and G. Ciruolo. Soledge2D-Eirene simulations of the Pilot-PSI linear plasma device compared to experimental data. *Contributions to Plasma Physics*, [58\(6-8\):798](#), 2018. [44](#)
- [49] Y. Hayashi, K. Ješko, H. J. Van Der Meiden, J. W. M. Vernimmen, T. W. Morgan, N. Ohno, S. Kajita, M. Yoshikawa, and S. Masuzaki. Plasma detachment study of high density helium plasmas in the Pilot-PSI device. *Nuclear Fusion*, [56\(12\)](#), 2016. [44](#)
- [50] P. C. Stangeby. The plasma boundary of magnetic fusion devices - Ch6. ... *Plasma Boundary of Magnetic Fusion Devices. ...*, 2000. [44](#)
- [51] R. J. Goldston, M. L. Reinke, and J. A. Schwartz. A new scaling for divertor detachment. *Plasma Physics and Controlled Fusion*, [59\(5\)](#), 2017. [44](#)

- [52] S. I. Krasheninnikov, M. E. Rensink, T. D. Rognlien, A. S. Kukushkin, J. A. Goetz, B. LaBombard, B. Lipschultz, J. L. Terry, and M. V. Umansky. Stability of the detachment front in a tokamak divertor. *Journal of Nuclear Materials*, **266:251**, 1999. [45](#), [53](#)
- [53] I. H. Hutchinson. Thermal front analysis of detached divertors and MARFEs. *Nuclear Fusion*, **34(10):1337**, 1994. [45](#), [54](#)
- [54] A. Loarte, et al. PLasma detachment in JET mark I divertor experiments. *Nuclear Fusion*, **38(3):331**, 1998. [45](#), [53](#)
- [55] M. Bernert, et al. X-point radiation, its control and an ELM suppressed radiating regime at the ASDEX Upgrade tokamak. *Nuclear Fusion*, **61(2)**, 2021. [46](#), [57](#)
- [56] V. P. Lipschultz, R. La Bombard, P. Marmor, R. Pickrell, R. R. Terry, R. R. Watterson, and S. M. Wolfe. Marfe: An edge plasma phenomenon. *Nuclear Fusion*, **24(8):977**, 1984. [46](#), [57](#), [92](#), [130](#)
- [57] E. J. Doyle, et al. Chapter 2: Plasma confinement and transport. *Nuclear Fusion*, **47(6)**, 2007. [46](#)
- [58] S. Kaye and I. C. D. w. Group. ITER L mode confinement database. *Nuclear Fusion*, **37(11):1657**, 1997. [46](#)
- [59] S. M. Kaye, M. G. Bell, R. E. Bell, E. D. Fredrickson, B. P. Leblanc, K. C. Lee, S. Lynch, and S. A. Sabbagh. Energy confinement scaling in the low aspect ratio National Spherical Torus Experiment (NSTX). *Nuclear Fusion*, **46(10):848**, 2006. [46](#)
- [60] S. M. Kaye, J. W. Connor, and C. M. Roach. Thermal confinement and transport in spherical tokamaks: A review. *Plasma Physics and Controlled Fusion*, **63(12)**, 2021. [46](#)
- [61] A. Salar Elahi and M. Ghoranneviss. Time evolution of the energy confinement time, internal inductance and effective edge safety factor on IR-T1 tokamak. *Physica Scripta*, **81(5)**, 2010. [47](#)
- [62] J. I. Wilson. *Tokamaks*, volume 53. Springer-Verlag, Berlin/Heidelberg, fourth edition, 2012. [47](#)

- [63] B. Lipschultz, J. L. Terry, C. Boswell, A. Hubbard, B. La Bombard, and D. A. Pappas. Ultrahigh densities and volume recombination inside the separatrix of the alcator C-Mod tokamak. *Physical Review Letters*, [81\(5\):1007](#), 1998. [47](#)
- [64] M. L. Reinke. Challenges to Radiative Divertor/Mantle Operations in Advanced, Steady-State Scenarios. In *7th IAEA Technical Meeting on Steady State Operation of Magnetic Fusion Devices*. 2013. [47](#), [48](#)
- [65] M. Bernert, et al. Power exhaust by SOL and pedestal radiation at ASDEX Upgrade and JET. *Nuclear Materials and Energy*, [12:111](#), 2017. [47](#)
- [66] G. D. Hobbs and J. A. Wesson. Heat flow through a Langmuir sheath in the presence of electron emission. Technical report, United Kingdom Atomic Energy Authority, Culham, Abingdon, Oxfordshire, 1966. [48](#), [51](#)
- [67] G. D. Hobbs and J. A. Wesson. Heat flow through a Langmuir sheath in the presence of electron emission. *Plasma Physics*, [9\(1\):85](#), 1967. [48](#), [51](#)
- [68] M. A. Mahdavi, J. C. Deboo, C. L. Hsieh, N. Ohyaabu, R. D. Stambaugh, and J. C. Wesley. Particle exhaust from plasma discharges with an expanded-boundary divertor. *Physical Review Letters*, [47\(22\):1602](#), 1981. [48](#), [51](#)
- [69] M. Keilhacker, K. Lackner, K. Behringer, H. Murmann, and H. Niedermeyer. Plasma boundary layer in limiter and divertor tokamaks. *Physica Scripta*, [1982\(T2B\):443](#), 1982. [48](#), [51](#)
- [70] P. J. Harbour. Thickness of the scrape-off layer of a large tokamak with a poloidal divertor. *Nuclear Fusion*, [24\(9\):1211](#), 1984. [48](#), [51](#)
- [71] K. Lackner, R. Chodura, M. Kaufmann, J. Neuhauser, K. G. Rauh, and W. Schneider. Control of particle and energy transport across the boundary of a tokamak plasma. *Plasma Physics and Controlled Fusion*, [26\(1 A\):105](#), 1984. [48](#), [51](#)
- [72] P. Stangeby. *The Plasma Boundary of Magnetic Fusion Devices*, volume 43 of *Series in Plasma Physics*. CRC Press, 2000. [48](#), [51](#), [52](#), [53](#), [54](#), [228](#)
- [73] C. Theiler, et al. Results from recent detachment experiments in alternative divertor configurations on TCV. *Nuclear Fusion*, [57\(7\)](#), 2017. [48](#)

- [74] U. Stroth, M. Bernert, D. Brida, M. Cavedon, R. Dux, E. Huett, T. Lunt, O. Pan, and M. Wischmeier. Model for access and stability of the X-point radiator and the threshold for marfes in tokamak plasmas. *Nuclear Fusion*, **62(7)**, 2022. [49](#), [58](#), [131](#), [137](#), [145](#)
- [75] S. F. Smith, S. J. Pamela, A. Fil, M. Hölzl, G. T. Huijsmans, A. Kirk, D. Moulton, O. Myatra, A. J. Thornton, and H. R. Wilson. Simulations of edge localised mode instabilities in MAST-U Super-X tokamak plasmas. *Nuclear Fusion*, **60(6)**, 2020. [50](#), [147](#), [148](#), [149](#), [151](#)
- [76] S. F. Smith. *Simulations of edge localised mode instabilities in MAST-U Super-X tokamak plasmas*. Ph.D. thesis, UNIVERSITY OF YORK, 2019. [50](#), [147](#)
- [77] S. Mijin, F. Militello, S. Newton, J. Omotani, and R. J. Kingham. Kinetic and fluid simulations of parallel electron transport during equilibria and transients in the scrape-off layer. *Plasma Physics and Controlled Fusion*, **62(9)**, 2020. [50](#), [147](#)
- [78] Y. Zhou, B. Dudson, F. Militello, K. H. Verhaegh, and O. Myatra. Investigation of the role of hydrogen molecules in 1D simulation of divertor detachment. *Plasma Physics and Controlled Fusion*, **64(6):065006**, 2022. [50](#), [148](#), [156](#), [191](#)
- [79] D. Tskhakaya, R. A. Pitts, W. Fundamenski, T. Eich, S. Kuhn, and JET EFDA Contributors. Kinetic simulations of the parallel transport in the JET scrape-off layer. *Journal of Nuclear Materials*, **390-391(1):335**, 2009. [50](#), [148](#)
- [80] L. Spitzer and C. J. Cook. Physics of Fully Ionized Gases. *Physics Today*, **10(1):133**, 1957. [52](#)
- [81] P. C. Stangeby. Basic physical processes and reduced models for plasma detachment. *Plasma Physics and Controlled Fusion*, **60(4)**, 2018. [53](#)
- [82] C. Cowley, B. Lipschultz, D. Moulton, and B. D. Dudson. Optimizing detachment control using the magnetic configuration of divertors. *Nuclear Fusion*, **62(8)**, 2022. [54](#), [56](#), [58](#), [124](#), [131](#)
- [83] M. L. Reinke. Heat flux mitigation by impurity seeding in high-field tokamaks. *Nuclear Fusion*, **57(3)**, 2017. [54](#)

- [84] M. L. Reinke, J. L. Terry, G. G. Van Eden, B. J. Peterson, K. Mukai, T. K. Gray, and B. C. Stratton. Experimental tests of an infrared video bolometer on Alcator C-Mod. *Review of Scientific Instruments*, [89\(10\):1](#), 2018. [57](#), [60](#), [67](#), [75](#), [82](#)
- [85] T. Wijkamp, et al. Characterisation of detachment in the MAST-U Super-X divertor using multi-wavelength imaging of 2D atomic and molecular emission processes. *Nuclear Fusion*, [63\(5\):056003](#), 2023. [58](#), [143](#)
- [86] K. H. Verhaegh, et al. Spectroscopic investigations of detachment on the MAST Upgrade Super-X divertor. *Nuclear Fusion*, 2022. [58](#), [139](#), [140](#), [143](#), [144](#), [146](#), [183](#)
- [87] J. M. Gao, Y. Liu, W. Li, J. Lu, Y. B. Dong, Z. W. Xia, P. Yi, and Q. W. Yang. Minimum Fisher regularization of image reconstruction for infrared imaging bolometer on HL-2A. *Review of Scientific Instruments*, [84\(9\)](#), 2013. [60](#)
- [88] B. J. Peterson, S. Konoshima, H. Parchamy, M. Kaneko, T. Omori, D. C. Seo, N. Ashikawa, and A. Sukegawa. Observation of divertor and core radiation in JT-60U by means of bolometric imaging. *Journal of Nuclear Materials*, [363-365\(1-3\):412](#), 2007. [60](#)
- [89] J. Jang, W. Choe, B. J. Peterson, D. C. Seo, K. Mukai, R. Sano, S. Oh, S. H. Hong, J. Hong, and H. Y. Lee. Tomographic reconstruction of two-dimensional radiated power distribution during impurity injection in KSTAR plasmas using an infrared imaging video bolometer. *Current Applied Physics*, [18\(4\):461](#), 2018. [60](#)
- [90] B. J. Peterson, S. Oh, D. Seo, J. Jang, J. S. Park, K. Mukai, and W. Choe. Signal to noise ratio of upgraded imaging bolometer for KSTAR. *Review of Scientific Instruments*, [89\(10\)](#), 2018. [60](#)
- [91] B. J. Peterson. Infrared imaging video bolometer. *Review of Scientific Instruments*, [71\(10\):3696](#), 2000. [60](#)
- [92] B. J. Peterson, E. A. Drapiko, D. Seo, and N. Ashikawa. Upgrade of Imaging Bolometers on LHD. *Plasma and Fusion Research*, [5:S2095](#), 2010. [60](#), [67](#)
- [93] A. Miyashita, et al. First Application of an InfraRed Imaging Video Bolometer to Heliotron J Plasma. *Plasma and Fusion Research*, [16:1202079](#), 2021. [60](#)

- [94] K. F. Mast, J. C. Vallet, C. Andelfinger, P. Betzler, H. Kraus, and G. Schramm. A low noise highly integrated bolometer array for absolute measurement of VUV and soft x radiation. *Review of Scientific Instruments*, [62\(3\):744](#), 1991. [60](#)
- [95] S. N. Pandya, B. J. Peterson, R. Sano, K. Mukai, E. A. Drapiko, A. G. Alekseyev, T. Akiyama, M. Itomi, and T. Watanabe. Calibration of a thin metal foil for infrared imaging video bolometer to estimate the spatial variation of thermal diffusivity using a photo-thermal technique. *Review of Scientific Instruments*, [85\(5\)](#), 2014. [62](#), [68](#)
- [96] K. Mukai, B. J. Peterson, N. Ezumi, N. Shigematsu, S. Ohshima, A. Miyashita, and R. Matoike. Sensitivity improvement of infrared imaging video bolometer for divertor plasma measurement. *Review of Scientific Instruments*, [92\(6\)](#), 2021. [62](#)
- [97] G. G. Van Eden, M. L. Reinke, S. Brons, G. van der Bijl, B. J. Krijger, R. Lavrijsen, S. Huber, R. Perillo, M. van de Sanden, and T. W. Morgan. Plasma radiation studies in Magnum-PSI using resistive bolometry. *Nuclear Fusion*, [58\(10\):106006](#), 2018. [62](#), [67](#), [68](#)
- [98] B. L. Henke, E. M. Gullikson, and J. C. Davis. X-Ray Interactions: Photoabsorption, Scattering, Transmission, and Reflection at $E = 50\text{-}30,000$ eV, $Z = 1\text{-}92$. *Atomic Data and Nuclear Data Tables*, [54\(2\):181](#), 1993. [62](#), [67](#), [68](#)
- [99] K. Mukai, B. J. Peterson, S. Takayama, and R. Sano. In situ calibration of the foil detector for an infrared imaging video bolometer using a carbon evaporation technique. *REVIEW OF SCIENTIFIC INSTRUMENTS*, [87:2014](#), 2016. [62](#), [69](#), [125](#)
- [100] C. Giroud, A. Meakins, M. Carr, A. Baciero, and C. Bertrand. CHERAB spectroscopy modelling framework, 2018. <<http://doi.org/10.5281/zenodo.1206142>>. [64](#)
- [101] M. Carr, et al. Towards integrated data analysis of divertor diagnostics with ray-tracing. In *44th EPS Conference on Plasma Physics*, June 2017, page 2017. European Physical Society, 2017. [64](#)
- [102] A. Meakins, Carr M. Raysect Python raytracing package, 2017. <<http://doi.org/10.5281/zenodo.1205064>>. [64](#)

- [103] M. L. Reinke. Experimental Tests of an Infrared Video Bolometer on Alcator C-Mod. In *22nd Topical Conference on High Temperature Plasma Diagnostics*. Oak Ridge National Laboratory, San Diego, USA, 2018. 65, 82
- [104] F. Federici, J. Harrison, T. Farley, and A. J. Thornton. Analysis routines for the paper "Design and Implementation of a prototype infrared video bolometer (IRVB) in MAST Upgrade", 2022. <<https://zenodo.org/record/7108499>>. 65
- [105] U. A. Sheikh, B. P. Duval, B. Labit, and F. Nespoli. A novel carbon coating technique for foil bolometers. *Review of Scientific Instruments*, 87(11):11D431, 2016. 67
- [106] M. Itomi, B. J. Peterson, Y. Yamauchi, R. Sano, K. Mukai, and S. N. Pandya. Improvement on infrared imaging video bolometer by laser calibration method. *Plasma and Fusion Research*, 9(SpecialIssue2):3406080, 2014. 68, 82
- [107] E. Havlíčková, J. Harrison, B. Lipschultz, G. Fishpool, A. Kirk, A. J. Thornton, M. Wischmeier, S. Elmore, and S. Allan. SOLPS analysis of the MAST-U diverter with the effect of heating power and pumping on the access to detachment in the Super-x configuration. *Plasma Physics and Controlled Fusion*, 57(11), 2015. 69
- [108] R. Sano, B. J. Peterson, E. A. Drapiko, D. Seo, Y. Yamauchi, and T. Hino. Foil calibration for IR imaging bolometer by laser irradiation. *Plasma and Fusion Research*, 7(SPL.ISS.1):3, 2012. 82
- [109] F. Cernuschi, A. Russo, L. Lorenzoni, and A. Figari. In-plane thermal diffusivity evaluation by infrared thermography. *Review of Scientific Instruments*, 72(10):3988, 2001. 82
- [110] M. L. Reinke. *Experimental Tests of Parallel Impurity Transport Theory in Tokamak Plasmas*. Ph.D. thesis, Massachusetts Institute of Technology, 2011. 86, 87
- [111] M. Carr, A. Meakins, M. Bernert, P. David, C. Giroud, J. Harrison, S. Henderson, B. Lipschultz, and F. Reimold. Description of complex viewing geometries of fusion tomography diagnostics by ray-tracing. *Review of Scientific Instruments*, 89(8):1, 2018. 86, 104

- [112] K. McCormick, A. Huber, L. C. Ingesson, F. Mast, J. Fink, W. Zeidner, A. Guigon, and S. Sanders. New bolometry cameras for the JET Enhanced Performance Phase. *Fusion Engineering and Design*, [74\(1-4\):679](#), 2005. [87](#)
- [113] A. Huber, et al. Upgraded bolometer system on JET for improved radiation measurements. *Fusion Engineering and Design*, [82\(5-14\):1327](#), 2007. [87](#)
- [114] F. Penzel, H. Meister, M. Bernert, T. Sehmer, T. Trautmann, M. Kannamüller, J. Koll, and A. W. Koch. Automated in situ line of sight calibration of ASDEX Upgrade bolometers. *Fusion Engineering and Design*, [89\(9-10\):2262](#), 2014. [87](#)
- [115] N. R. Walkden, J. Harrison, S. A. Silburn, T. Farley, S. S. Henderson, A. Kirk, F. Militello, and A. J. Thornton. Quiescence near the X-point of MAST measured by high speed visible imaging. *Nuclear Fusion*, [57\(12\)](#), 2017. [87](#)
- [116] L. L. Lao, H. S. John, R. D. Stambaugh, A. G. Kellman, and W. Pfeiffer. Reconstruction of current profile parameters and plasma shapes in tokamaks. *Nuclear Fusion*, [25\(11\):1611](#), 1985. [88](#)
- [117] W. Morris, J. R. Harrison, A. Kirk, B. Lipschultz, F. Militello, D. Moulton, and N. R. Walkden. MAST Upgrade Divertor Facility: A Test Bed for Novel Divertor Solutions. *IEEE Transactions on Plasma Science*, [46\(5\):1217](#), 2018. [92](#)
- [118] S. N. Pandya, B. J. Peterson, M. Kobayashi, S. P. Pandya, K. Mukai, and R. Sano. A reconsideration of the noise equivalent power and the data analysis procedure for the infrared imaging video bolometers. *Review of Scientific Instruments*, [85\(12\)](#), 2014. [95](#)
- [119] M. Greenwald. Density limits in toroidal plasmas. *Plasma Physics and Controlled Fusion*, [44\(8\)](#), 2002. [95](#)
- [120] K. H. Verhaegh, et al. A study of the influence of plasma–molecule interactions on particle balance during detachment. *Nuclear Materials and Energy*, [26](#), 2021. [100](#), [147](#), [179](#), [187](#)
- [121] J. L. Terry, B. Lipschultz, A. P. Pigarov, S. I. Krasheninnikov, B. LaBombard, D. Lumma, H. Ohkawa, D. A. Pappas, and M. V. Umansky. Volume recombination and opacity in Alcator C-Mod divertor plasmas. *Physics of Plasmas*, [5\(5\):1759](#), 1998. [100](#)

- [122] V. A. Soukhanovskii, A. I. Khrabry, H. A. Scott, T. D. Rognlien, D. Moulton, and J. R. Harrison. Modeling of deuterium and carbon radiation transport in MAST-U tokamak advanced divertors. *Nuclear Fusion*, **62(6)**, 2022. 100
- [123] P. C. Hansen. *Rank-Deficient and Discrete Ill-Posed Problems*. SIAM, 1998. 101
- [124] P. C. Hansen. *Discrete Inverse Problems: Insight and Algorithms*. Society for Industrial and Applied Mathematics, Lyngby, Denmark, 2010. 101
- [125] P. C. Hansen. Analysis of Discrete Ill-Posed Problems by Means of the L-Curve. *SIAM Review*, **34(4):561**, 1992. 102
- [126] A. H. Andersen and A. C. Kak. Simultaneous Algebraic Reconstruction Technique (SART): A superior implementation of the ART algorithm. *ULTRASONIC IMAGING* **6**, **1:81**, 1984. 104
- [127] T. Craciunescu, G. Bonheure, V. Kiptily, A. Murari, S. Soare, I. Tiseanu, and V. Zoita. The maximum likelihood reconstruction method for JET neutron tomography. *Nuclear Instruments and Methods in Physics Research, Section A: Accelerators, Spectrometers, Detectors and Associated Equipment*, **595(3):623**, 2008. 105
- [128] T. Craciunescu, E. Peluso, A. Murari, and M. Gelfusa. Maximum likelihood bolometric tomography for the determination of the uncertainties in the radiation emission on JET TOKAMAK. *Review of Scientific Instruments*, **89(5)**, 2018. 105
- [129] B. P. Carlin and T. A. Louis. Empirical Bayes: Past, Present and Future. *Journal of the American Statistical Association*, **95(452):1286**, 2000. 106
- [130] J. L. Morales and J. Nocedal. Remark on "algorithm 778: L-BFGS-B: Fortran subroutines for large-scale bound constrained optimization". *ACM Transactions on Mathematical Software*, **38(1):2**, 2011. 106
- [131] K. Friston, J. Ashburner, S. Kiebel, T. Nichols, and W. Penny, editors. *Statistical Parametric Mapping*. Elsevier, 2007. 107
- [132] D. J. Mackay. Choice of Basis for Laplace Approximation. *Machine Learning*, **33(1):77**, 1998. 107

- [133] N. Thacker, D. Prendergast, and P. Rockett. B-Fitting: An Estimation Technique with Automatic Parameter Selection. In *Proceedings of the British Machine Vision Conference 1996*, pages 1–58. British Machine Vision Association, 1996. 107
- [134] D. H. Rhodri, N. A. Thacker, and C. J. Taylor. Model Fitting using the Bhattacharyya Measure. <https://homepages.inf.ed.ac.uk/rbf/CVonline/LOCAL_COPIES/DAVIES1/rd_bhatt_cvonline/>. 107
- [135] O. M. Shir and A. Yehudayoff. On the covariance-Hessian relation in evolution strategies. *Theoretical Computer Science*, 801:157, 2020. 107
- [136] P. C. Hansen. Computational inverse problems in electrocardiography. Technical report, Department of Mathematical Modelling, Technical University of Denmark, Lyngby, Denmark, 2005. 108
- [137] MDS+, 2020. <<https://www.mdsplus.org/index.php/Introduction>>. 110
- [138] I. H. Hutchinson. *Principles of Plasma Diagnostics*. CAMBRIDGE UNIVERSITY PRESS, 2nd edition, 2002. 121
- [139] J. Lovell, et al. A compact, smart Langmuir Probe control module for MAST-Upgrade. *Journal of Instrumentation*, 12(11), 2017. 121
- [140] P. J. Ryan, S. D. Elmore, J. R. Harrison, J. Lovell, and R. Stephen. Overview of the MAST Upgrade Langmuir Probe System. *Review of Scientific Instruments*, (to be submitted), 2023. 121, 125
- [141] L. C. Ingesson. Comparison of Methods to Determine the Total Radiated Power in JET. Technical Report 99, JET Joint Undertaking, Abingdon, 2000. 122
- [142] O. Février, et al. Detachment in conventional and advanced double-null plasmas in TCV. *Nuclear Fusion*, 61(11), 2021. 123, 125
- [143] J. R. Harrison, et al. Detachment evolution on the TCV tokamak. *Nuclear Materials and Energy*, 12:1071, 2017. 123, 142
- [144] H. Reimerdes, et al. TCV experiments towards the development of a plasma exhaust solution. *Nuclear Fusion*, 57(12), 2017. 142

- [145] A. Smolders, et al. Comparison of high density and nitrogen seeded detachment using SOLPS-ITER simulations of the tokamak α configuration variable. *Plasma Physics and Controlled Fusion*, [62\(12\)](#), 2020. [142](#)
- [146] T. Ravensbergen, et al. Real-time feedback control of the impurity emission front in tokamak divertor plasmas. *Nature Energy*, [Submitted\(2021\):1](#), 2020. [142](#)
- [147] X. Feng, et al. Development of an 11-channel multi wavelength imaging diagnostic for divertor plasmas in MAST Upgrade. *Review of Scientific Instruments*, [92\(6\)](#), 2021. [142](#)
- [148] A. Perek, et al. MANTIS: A real-time quantitative multispectral imaging system for fusion plasmas. *Review of Scientific Instruments*, [90\(12\)](#), 2019. [142](#)
- [149] K. H. Verhaegh, et al. An improved understanding of the roles of atomic processes and power balance in divertor target ion current loss during detachment. *Nuclear Fusion*, 2019. [143](#), [169](#), [183](#), [190](#)
- [150] K. H. Verhaegh, et al. The role of plasma-molecule interactions on power and particle balance during detachment on the TCV tokamak. *Nuclear Fusion*, [61\(10\)](#), 2021. [143](#), [173](#), [183](#), [190](#), [224](#)
- [151] I. Lehane, M. W. D. Mansfield, H. Meyer, P. G. Carolan, E. R. Arends, and S. Korsholm. Impurity Radiation & Transport in the MAST Tokamak. In *43rd Annual Meeting of the APS Division of Plasma Physics*, pages 1–056. American Physical Society, Long Beach, California, 2001. [144](#)
- [152] A. W. Leonard, A. Herrmann, K. Itami, J. Lingertat, A. Loarte, T. H. Osborne, and W. Suttrop. Impact of ELMs on the ITER divertor. *Journal of Nuclear Materials*, [266:109](#), 1999. [148](#)
- [153] J. Scholten, et al. Operational status of the Magnum-PSI linear plasma device. *Fusion Engineering and Design*, [88\(9-10\):1785](#), 2013. [150](#)
- [154] T. W. Morgan, T. M. De Kruif, H. J. Van Der Meiden, M. A. Van Den Berg, J. Scholten, W. Melissen, B. J. Krijger, S. Bardin, and G. C. De Temmerman. A high-repetition rate edge localised mode replication system for the Magnum-PSI and Pilot-PSI linear devices. *Plasma Physics and Controlled Fusion*, [56\(9\)](#), 2014. [150](#), [154](#), [173](#), [224](#)

- [155] R. D. Barrois, W. A. J. Vijvers, I. G. J. Classen, R. Jaspers, and R. Engeln. *Multi-cord spectroscopy during detachment-experiments in Magnum-PSI*. Ph.D. thesis, Technische Universiteit Eindhoven University of Technology, 2017. [152](#), [170](#), [207](#)
- [156] H. J. Van Der Meiden, et al. Advanced Thomson scattering system for high-flux linear plasma generator. *Review of Scientific Instruments*, **83**(12), 2012. [153](#)
- [157] Y. Li, T. W. Morgan, J. A. W. Van Dommelen, S. Antusch, M. Rieth, J. P. M. Hoefnagels, D. Terentyev, G. C. De Temmerman, K. Verbeken, and M. G. D. Geers. Fracture behavior of tungsten-based composites exposed to steady-state/transient hydrogen plasma. *Nuclear Fusion*, **60**(4):046029, 2020. [154](#), [163](#), [165](#)
- [158] R. Perillo, R. Chandra, G. R. A. Akkermans, I. G. J. Classen, and S. Q. Korving. Investigating the effect of different impurities on plasma detachment in linear plasma machine Magnum-PSI. *Physics of Plasmas*, **26**(10), 2019. [155](#), [156](#)
- [159] N. Den Harder, D. C. Schram, W. J. Goedheer, H. J. De Blank, M. C. Van de Sanden, and G. J. Van Rooij. Residual gas entering high density hydrogen plasma: Rarefaction due to rapid heating. *Plasma Sources Science and Technology*, **24**(2), 2015. [156](#), [189](#), [215](#)
- [160] R. Behrisch. Evaporation for heat pulses on Ni, Mo, W and ATJ graphite as first wall materials. *Journal of Nuclear Materials*, 93 / 94(1):498, 1980. [164](#), [209](#)
- [161] D. Bäuerle. *Laser Processing and Chemistry*. Springer, 2nd edition, 1996. [164](#), [209](#)
- [162] J. Yu, G. D. Temmerman, R. P. Doerner, and M. v. d. Berg. Study of temporal pulse shape effects on W using simulations and laser heating. *Physica Scripta*, **014033**, 2016. [164](#)
- [163] T. W. Morgan, M. Balden, T. Schwarz-Selinger, Y. Li, T. H. Loewenhoff, M. Wirtz, S. Brezinsek, and G. C. De Temmerman. ITER monoblock performance under lifetime loading conditions in Magnum-PSI. *Physica Scripta*, **2020(T171)**, 2020. [165](#)
- [164] A. Sternberg. The excitation of molecular hydrogen and its significance. In B. Kaldeich, editor, *22nd Eslab Symposium*, pages 269–280. Infrared Spectroscopy in Astronomy, Salamanca, Spain, 1989. [165](#)

- [165] O. Février, et al. Nitrogen-seeded divertor detachment in TCV L-mode plasmas. *Plasma Physics and Controlled Fusion*, **63**, 2020. [165](#)
- [166] G. Pintsuk, W. Kühnlein, J. Linke, and M. Rödiger. Investigation of tungsten and beryllium behaviour under short transient events. *Fusion Engineering and Design*, **82(15-24):1720**, 2007. [167](#)
- [167] J. Linke, J. Du, T. Loewenhoff, G. Pintsuk, B. Spilker, I. Steudel, and M. Wirtz. Challenges for plasma-facing components in nuclear fusion. *Matter and Radiation at Extremes*, **4(5)**, 2019. [167](#)
- [168] T. Eich, B. Sieglin, A. J. Thornton, M. Faitsch, A. Kirk, A. Herrmann, and W. Suttrop. ELM divertor peak energy fluence scaling to ITER with data from JET, MAST and ASDEX upgrade. *Nuclear Materials and Energy*, **12:84**, 2017. [167](#)
- [169] A. Kallenbach, H. J. Sun, T. Eich, D. Carralero, J. Hobirk, A. Scarabosio, and M. Siccinio. Parameter dependences of the separatrix density in nitrogen seeded ASDEX Upgrade H-mode discharges. *Plasma Physics and Controlled Fusion*, **60(4)**, 2018. [167](#)
- [170] D. Galassi, H. Reimerdes, C. Theiler, M. Wensing, H. Bufferand, G. Ciruolo, P. Innocente, Y. Marandet, and P. Tamain. Numerical investigation of optimal divertor gas baffle closure on TCV. *Plasma Physics and Controlled Fusion*, **62(11)**, 2020. [167](#)
- [171] C. S. Pitcher, C. J. Boswell, J. A. Goetz, B. Labombard, B. Lipschultz, J. E. Rice, and J. L. Terry. The effect of divertor baffling on Alcator C-Mod discharges. *Physics of Plasmas*, **7(5):1894**, 2000. [167](#)
- [172] A. Niemczewski, I. H. Hutchinson, B. LaBombard, B. Lipschultz, and G. M. McCracken. Neutral particle dynamics in the alcator C-MOD tokamak. *Nuclear Fusion*, **37(2):151**, 1997. [167](#)
- [173] S. Potzel. *Experimental classification of divertor detachment*. Ph.D. thesis, Universitat Bayreuth, 2012. [169](#)
- [174] K. H. Verhaegh, et al. Spectroscopic investigations of divertor detachment in TCV. *Nuclear Materials and Energy*, **12:1112**, 2017. [169](#)

- [175] C. Bowman, J. R. Harrison, B. Lipschultz, S. Orchard, K. J. Gibson, M. Carr, K. H. Verhaegh, and O. Myatra. Development and simulation of multi-diagnostic Bayesian analysis for 2D inference of divertor plasma characteristics. *Plasma Physics and Controlled Fusion*, **62(4)**, 2020. [169](#)
- [176] H. J. N. Van Eck. *The linear plasma generator Magnum-PSI*. Ph.D. thesis, Technische Universiteit Eindhoven, 2013. [170](#)
- [177] R. C. Wieggers, D. P. Coster, P. W. C. Groen, H. J. De Blank, and W. J. Goedheer. B2.5-Eunomia simulations of Pilot-PSI plasmas. *Journal of Nuclear Materials*, **438(SUPPL):S643**, 2013. [171](#)
- [178] R. Chandra, H. J. d. Blank, P. Diomede, H. J. N. v. Eck, H. J. v. d. Meiden, T. W. Morgan, J. W. M. Vernimmen, and E. Westerhof. Magnum-PSI detachment experiments : I . Quantitative comparisons with. *Plasma Phys. Control. Fusion*, **63(9):14**, 2021. [171](#), [215](#)
- [179] R. Chandra, H. J. D. Blank, P. Diomede, and E. Westerhof. Magnum-PSI detachment experiments : II . Collisional processes and their. *Plasma Phys. Control. Fusion*, **64(1):16**, 2022. [171](#), [178](#), [215](#), [226](#), [227](#)
- [180] K. H. Verhaegh. *Spectroscopic investigations of detachment on TCV*. Ph.D. thesis, University of York, 2018. [173](#), [192](#), [228](#)
- [181] A. McLean. Understanding Plasma Divertor Detachment in Fusion Power Reactors. Technical report, Lawrence Livermore National Laboratory (LLNL), Livermore, CA (United States), 2019. [174](#)
- [182] M. Groth, et al. EDGE2D-EIRENE predictions of molecular emission in DIII-D high-recycling divertor plasmas. *Nuclear Materials and Energy*, **19(March):211**, 2019. [174](#), [225](#)
- [183] J. Karhunen, A. Holm, S. Aleiferis, P. Carvalho, M. Groth, K. D. Lawson, B. Lomanowski, A. G. Meigs, A. Shaw, and V. Solokha. Spectroscopic camera analysis of the roles of molecularly assisted reaction chains during detachment in JET L-mode plasmas. *Nuclear Materials and Energy*, **34(May 2021):10**, 2023. [187](#)

- [184] K. H. Verhaegh, A. C. Williams, D. Moulton, B. Lipschultz, B. P. Duval, O. Fevrier, A. Fil, N. Osborne, H. Reimerdes, and C. Theiler. Investigating the impact of the molecular charge-exchange rate on detached SOLPS-ITER simulations. 2023. [188](#)
- [185] B. D. Dudson, J. Allen, T. Body, B. Chapman, C. Lau, L. Townley, D. Moulton, J. R. Harrison, and B. Lipschultz. The role of particle, energy and momentum losses in 1D simulations of divertor detachment. 2018. [190](#)
- [186] D. S. Gahle, J. R. Harrison, S. S. Henderson, M. G. O. Mullane, C. Bowman, K. H. Verhaegh, A. Perek, M. Wensing, T. Team, and E. M. Team. Bayesian Inference of the Impurity Concentrations and Ion Confinement Times in the TCV Divertor. In *4th Asia-Pacific Conference on Plasma Physics*. Remote e-conference, 2020. [203](#)
- [187] O. Myatra. *Numerical modelling of detached plasmas in the MAST Upgrade Super-X divertor*. Ph.D. thesis, University of York, 2021. [226](#)
- [188] A. Smolders, et al. Comparison of high density and nitrogen seeded detachment using SOLPS-ITER simulations of the tokamak \dot{a} configuration variable. *Plasma Physics and Controlled Fusion*, [62\(12\)](#), 2020. [226](#)